Aluminium alloys and nanocomposites manufactured via friction stirring and 3D printing processes

Du, Zhenglin

2018

Du, Z. (2018). Aluminium alloys and nanocomposites manufactured via friction stirring and 3D printing processes. Doctoral thesis, Nanyang Technological University, Singapore.

https://hdl.handle.net/10356/88687

https://doi.org/10.32657/10220/45968

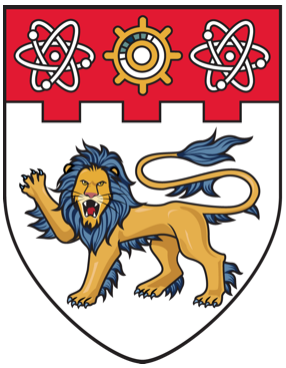

NANYANG TECHNOLOGICAL UNIVERSITY

SINGAPORE

Aluminium Alloys and Nanocomposites Manufactured via Friction Stirring and 3D Printing Processes

DU ZHENGLIN

SCHOOL OF MECHANICAL AND AEROSPACE ENGINEERING

2018

Aluminium Alloys and Nanocomposites Manufactured via Friction Stirring and 3D Printing Processes

DU ZHENGLIN

SCHOOL OF MECHANICAL AND AEROSPACE ENGINEERING

A thesis submitted to the Nanyang Technological University in partial fulfilment of the requirement for the degree of Doctor of Philosophy

2018

Abstract

In recent years, fabricating aluminium matrix composites (AMCs) reinforced with nanoparticles via Selective laser melting (SLM) has drawn attention due to the potential in improving mechanical properties. However, the formation of undesirable intermetallic phases and porosity defects are challenging to overcome. Also, joining of AMCs is also important for industrial applications. Friction stir welding (FSW) is a solid-state joining technique capable of producing good mechanical properties. This study paves the way for the fabrication of new novel AMCs via FSP as well as the joining of SLM fabricated AMCs.

The main findings are:

i. A new Al-based nano-composite reinforced with uniformly dispersed Al_2O_3 and carbon nanotubes (CNTs) have been successfully fabricated using FSP. Grain refinement was observed in friction stir processing with/ without the addition of nano-sized reinforcement particles. The presence of nano-sized reinforcement led to more pronounced grain refinement as pinning effect of the nano-particles have retarded the grain growth rate in the dynamic recrystallisation process. The micro-hardness and tensile strengths were increased significantly through the addition of Al_2O_3 and CNTs nanoparticles. In particular, the yield strength of the composites increased 70% compared with that of FSPed Al when both Al_2O_3 and CNTs were added in the matrix. Multiple reinforcements with different shapes can be an effective method to increase the tensile strengths, especially yield strength of metal matrix composites.
ii. SLM fabricated $AlSi_{10}Mg$, and $AlSi_{10}Mg$-nAl_2O_3 composites were studied. The addition of nAl_2O_3 resulted in the increasing formation of porosity in SLM fabricated AMCs. Hence, higher laser energy input was required to improve the wettability properties. Columnar grain structure along the thermal

gradient was observed. Significant grain refinement was achieved with the addition of nAl_2O_3 via Zener pinning effect by exerting pinning pressure. The use of $AlSi_{10}Mg$ has resulted in the fabrication of $AlSi_{10}Mg$-nAl_2O_3 composites with superior mechanical properties compared to Al-nAl_2O_3 composites using pure aluminium.

iii. FSW had successfully joined SLM fabricated $AlSi_{10}Mg$ parts together without the presence of welding defects with rotational speed = 1200 rpm, travel speed = 1 mm/s, tilt angle = 4.5°. Grain refinement was observed in the FSW region due to dynamic recrystallisation process together with a significant increase in the fraction of high-angle grain boundaries during FSW. Significant decreases in the hardness and tensile strength were observed in the weld region due to the precipitation of Si. The increase in rotation speed or reduction in travel speed increased in grain size and slight reduction of hardness. Ductility was improved after FSW, and tensile strength is comparable to FSW of AA6061-T6 rolled sheets.

iv. FSW was successfully used to joined SLM fabricated $AlSi_{10}Mg$ and its composites together achieving fine grains in the FSW region. Agglomerated and sintered nAl_2O_3 was observed to have broken down and dispersed in the matrix after FSW. It was observed that the use of higher tool rotational speed resulted in larger grains. The addition of nAl_2O_3 contributed to finer grains and higher hardness due to Zener pinning effect. FSW can generate porosity-free welds while 18% porosity density was received from as-printed substrates.

These favourable findings ascertained the feasibility of using FSW to join SLM fabricated Al-Al_2O_3 composites and contributed to the scientific knowledge that FSW can produce a weld with desirable results for actual applications.

Acknowledgement

I would like to express my immersed gratitude and appreciation to my supervisor Associate Professor Tan Ming Jen for his valuable guidance, patience, faith and support during my PhD candidature at Nanyang Technological University (NTU). As well, my other two co-supervisors, Dr. Chen Hui-Chi and Dr. Guo Jun Feng at SIMTech have played a big role in my studies and researches. I want to thank them sincerely for their constant support, encouragement and guidance during my studies and researches in NTU.

I would like to thank my Thesis Advisory Committee members, Associate Professor Li Peifeng and Dr. Song Xu. Their insightful comments have been helpful in refining my research from various perspectives to write this thesis.

I would like to acknowledge the research funding and scholarship received from Singapore Centre for 3D Printing (SC3DP) and SIMTech (Joining Technology Group). I would also like to thank Professor Chua Chee Kai and Dr. Bi Guijun for the great opportunity in pursuing this research project from these institutions.

I am very blessed with friendly and helpful fellow researchers, laboratory mates and technical staffs from SC3DP and NTU. Their technical support, help and companionship have made my PhD an enjoyable and smooth journey.

Last but not the least, I would like to express my heartfelt gratitude to my parents, family and friends for their love, and constant support that has propelled me throughout the candidature life. With these, attaining PhD has been more meaningful.

Table of Contents

List of Figures

List of Tables

List of Abbreviations

AM	Additive manufacturing
Al	Aluminium
AMCs	Aluminium matrix composites
CAD	Computer aided design
Cu	Copper
EDM	Electrical discharge machining
EBSD	Electron backscattered diffraction
EM	Electron beam
EDS	Energy Dispersive X-ray spectroscopy
FESEM	Field emission scanning electron microscopy
FSP	Friction stir processing
FSW	Friction stir welding
GTA	Gas tungsten arc
GP	Guinier-Preston
HAZ	Heat affected zone
Mg	Magnesium
Mn	Manganese
MMCs	Metal matrix composites
Micro CT	Micro-Computerized Tomography
MWCNTs	Multi-walled carbon nanotubes
nAl_2O_3	Nano-sized alumina
LBW	Nd-YAG continuous wave laser beam welding
PSN	Particle stimulated nucleation
RS	Rotation speed
SLM	Selective laser melting
Si	Silicon
WI	The Welding Institute
TMAZ	Thermomechanical affected zone
TA	Tilt angle
TS	Travel speed
VED	Volumetric energy density
XRD	X-ray diffraction
Zn	Zinc

CHAPTER 1

Introduction

1.1 Background

Particulate-reinforced metal matrix composites (MMCs) have drawn much attention in the automobile, aerospace and defence industries due to its superior high elastic modulus, stiffness and wear resistance [1-3]. Significant strengthening effects can be achieved by using small concentrations of reinforcement particles [3]. MMCs could be fabricated using various suitable types of metal. Light metals such as aluminium, cobalt, cobalt-nickel, magnesium, titanium alloys as well as superalloys were found to be more attractive due to their possibility to make strong and light composites. Aluminium alloy has been a preferred choice for research among the light metals due to its wider application, machinability as well as its relatively lower cost. More recently, researchers have grown interested in the use of nano-particles as reinforcement due to their ability to further enhance strength as compared to micro-sized reinforcements [4, 5]. In general, the use of reinforcement in aluminium matrix composites (AMCs) contributes to the improved strength, stiffness, wear resistance as well as mechanical performances at elevated temperature [6-9].

Recently, much attention has been shifted to additive manufacturing (AM) processes due to its ability to fabricate complex components which are challenging and costly via traditional manufacturing processes. In the past, AM plays a crucial role in rapid prototyping, rapid tooling and manufacturing industries. The use of layerwise fabrication technique has enabled fast and relatively lower cost prototype fabrication. In the past five years, the global revenue for AM services and products has experienced remarkable growth with 42.6% coming from AM of metals with a 50% increase from USD 48.7 million

in 2014 [10]. As the industry continues to grow, advancement in research and development for SLM processes of different material and metal matrix composites (MMCs) will also be developed. The idea of selective laser melting (SLM) came between the late 1980s and 1990s [11, 12]. It is a powder-based additive manufacturing technique which fabricates components layer by layer with the use of computer-aided design (CAD) modelling while a laser scans the cross-section of the respective layer. After fabrication, unused powders were then removed and recycled while the component is removed from the platform. One difficult challenge in the process is the uniform dispersion of reinforcements particles in the metal matrix [13]. During SLM, the metal powders were fully melted by the scanning laser and solidify immediately after the laser passes. The high temperature gradient and cooling rate in the SLM process often result in distortion, crack or delamination and inaccuracy in the parts built due to high residue stress, hence, limiting the size of the built parts using SLM [14, 15].

MMCs are reported to have superior strength and mechanical properties. However their application becomes limited if there is no way of joining them together. In general, the welding of aluminium requires careful preparation. Loss of strength and defect formation were the main concerns in traditional fusion welding processes. The formation of porosity defect could result from the dissolution of shielding gases (oxygen, nitrogen and hydrogen) or moisture from electrode and flux in molten metal. Moreover, the significant difference in the melting temperature of aluminium (660°C) and its oxide (2060°C) at the surface could contribute to the lack of fusion in the welded parts. The high thermal conductivity of aluminium resulted in the large temperature difference between the liquid and solidification process. This results in the formation of residual stress in the weld leading to centre-line or hot cracking. The thermal cycle of fusion welding also results in significant reduction of strength in the heat affected zones for heat treatable aluminium alloys [16, 17].

Lakshminarayanan et al. [18] did a comparative study between gas tungsten arc welding, gas metal arc welding and friction stir welding (FSW) of AA6061-T6. In their study, it was concluded that FSW AA6061 achieved superior mechanical properties. In addition to the challenges mentioned above, the welding of AMCs is more challenging with the addition of reinforcement particles. Such challenges include:

- Non-homogenous mixing of filler and base material
- Excessive formation of eutectic phase
- Formation of porosity > 100 µm
- Formation of undesirable brittle intermetallic phases such as Al_4C_3 [19].

Storjohann et al. [20] investigated the welding of AA6061 reinforced with 20 weight percent of Al_2O_3 and AA6061 reinforced with 20 weight percent whiskers SiC using gas tungsten arc (GTA), electron beam (EM), Nd-YAG continuous wave laser beam welding (LBW) and FSW. Al_2O_3 reinforcements were observed to have completely dissolved in the molten aluminium during fusion welding leading to the reduction of its strength. On the other hand, SiC was observed to form Al_4C_3 with Si-rich phase being precipitated due to the reaction between the reinforcement and the aluminium. For the case of FSW, good joint was achieved with no change in concentration of reinforcement due to its solid-state process without melting. Therefore, FSW is a suitable welding process for joining AMCs.

1.2 Motivation

As discussed in the review, it is evident that using SLM to produce large parts leads to high residue stresses, distortion and warping. This is undesirable and limits the build size. The use of conventional joining method of AMCs poses several limitations such as non-homogenous mixing of filler material, hydrogen porosity and formation of undesirable brittle intermetallic phases. In contrast, FSW is a solid-state joining technique used to join two pieces of metal materials

together without melting. Fine grain microstructure with good mechanical properties can be produced in the weld region.

As FSW does not involve the melting of the materials, the use of shielding gas is not required. It can be utilised to join materials that are challenging for fusion welding [19, 21] as it eliminates solidification and cooling thermal contractions that lead to significant shrinkage, distortions, development of pores, residue stress, brittle cast structure and hot cracking in the joint [22-24]. Therefore, it can produce high-quality welding with low production cost. The key benefits include:

- Low distortion of the workpiece
- Good dimensional stability
- Solid phase process without the formation of brittle intermetallic phases
- Fine microstructure
- Replace multiple parts join by fasteners
- No shielding gas required
- Elimination of grinding waste

Using FSW as a welding technique to join SLM printed parts possess an enormous potential in the future of manufacturing. To achieve this goal, it is essential to investigate the evolution of microstructures and mechanical properties during the various processes. Moreover, friction stir welding and processing can modify the microstructure of the material as well as provide a uniform dispersion of the reinforcements, due to its intense plastic deformation and dynamic recrystallisation [25].

Reports on joining of 3D printed AMCs via the use of FSW is limited. Hence, there is limited knowledge of the microstructural evolution as well as mechanical properties such as grain size, microstructure, micro-hardness, tensile properties, etc. Further studies and contribution to knowledge in this aspect will be of value. Therefore, the objective of this study is to use FSW to join SLM printed parts to form defect-free joints.

1.3 Objective

The main objectives of this project can be categorised into 2 major parts:

- To fabricate aluminium matrix composites (AMC) using two different processes (friction stir processing and selective laser melting).
- To join SLM parts (aluminium alloy and AMCs) using friction stir welding with good mechanical properties.

1.4 Scope

The scope of this research is listed below:

- Friction stir welding (FSW) of aluminium alloy ($AlSi_{10}Mg$) reinforced with nano-sized alumina.
- Friction stir processing (FSP) of aluminium alloy (AA6061) reinforced with nano-sized alumina and carbon nanotubes.
- To optimise the process parameters for fabrication of AMCs using FSP with varying types of reinforcement particles and number of passes.
- To optimise the process parameters for fabrication of AMCs using SLM with varying laser scanning speed and hatch spacing while keeping laser power and layer thickness constant.
- To optimise the process parameters for friction stir welding of AMCs with varying rotational speed, travel speed and tilt angle.
- Establish the mechanical properties, tensile strength and Vickers hardness.
- Characterise the resultant microstructures.

1.5 Organisation

This present thesis consists of 8 chapters.

The first chapter briefly introduces the advantages and limitations of AMCs, SLM and FSW process.

Chapter 2 covers the available literature and current developments of SLM and FSW of aluminium alloys and its composites.

Chapter 3 explains the experimental details as well as the parameters used for various characterisation methods used in this study.

Results and Discussions

Chapter 4 is a preliminary study on the friction stir processing of aluminium composites to understand the FSW process. Also, it allows us to get a better understanding of the interaction between the reinforcement particles and the aluminium matrix.

Chapter 5 studies the fabrication of SLM fabricated AMCs using $AlSi_{10}Mg$ reinforced with nano-sized alumina of various concentration and SLM parameters.

Chapter 6 studies the FSW of SLM fabricated $AlSi_{10}Mg$ to understand the butt joining properties of SLM fabricated aluminium alloy.

Chapter 7 studies the FSW of SLM fabricated AMCs ($AlSi_{10}Mg$ reinforced with nano-sized alumina) with various FSW parameters.

And finally, chapter 8 provides the conclusion of this research as well as recommendations for future work. Lastly, a list of publication during the candidature is provided.

CHAPTER 2

Literature Review

This chapter introduces the welding process available for aluminium alloy and its composites. Friction stir welding (FSW) and selective laser melting (SLM) is then presented. It provides the comprehensive literature review on the process, material as well as challenges in joining aluminium composites.

2.1 Aluminium (Al) and Al Composites

2.1.1 Aluminium

Aluminium is the most abundant metal that could be found on Earth's crust. It makes up to 8.2% mass of Earth's solid surface and is the third most abundant element following oxygen and silicon [26]. Aluminium ore, also known as bauxite, was first discovered in Les Baux, France. [26]. Bauxite can be refined to obtain pure aluminium. Pure aluminium has excellent corrosion resistance and electrical conductivity. However, its relatively low strength makes it unsuitable for structural applications (Table 2-1).

Table 2-1 Basic material properties of pure aluminium.

Atomic symbol	Al
Density	2.6989 g / cm^3
Vickers hardness	15
Elastic modulus	68 GPa
Shear modules	25 GPa
Yield strength	20.7 MPa
Ultimate strength	68.9 MPa
Melting point	660 °C
Boiling point	2519 °C
Thermal conductivity	210 W / m. k
Specific heat capacity	0.900 J / g. °C

The mechanical properties of pure aluminium could be enhanced with alloying elements such as copper (Cu), magnesium (Mg), manganese (Mn), silicon (Si) and zinc (Zn). Many of these alloys have comparable strength with carbon steel, making it a favourable weight saving solution due to this lower density. The high strength to weight ratio of aluminium alloy has resulted in its wide application in the aerospace industry. Moreover, aluminium has high machinability and workability, making it a suitable material for other industrial applications such as automobile, food preparation, energy generation, architecture as well as electrical transmission.

2.1.2 Aluminium Metal Matrix Composites (AMCs)

Particulate-reinforced metal matrix composites (MMCs) have drawn much attention in the automobile, aerospace and defence industries due to its superior high elastic modulus, stiffness and wear resistance [1-3]. Significant strengthening effects can be achieved by using small concentrations of reinforcement particles [3].

In general, MMCs is made up of two main factors: the metal matrix and the reinforcement particles used. Firstly, the monolithic material used is known as the matrix, and it provides the main support for the reinforcement. There are many metal matrix suitable for MMCs fabrication. In particular, light metals such as aluminium, cobalt, cobalt-nickel, magnesium, titanium alloys as well as superalloys were used due to the possibility to make strong and light composites. Among the light metals, aluminium alloy has been the preferred choice for research due to its wider application as well as its relatively lower cost.

Secondly, the reinforcement used to reinforce the matrix. In general, there are five main categories of reinforcements used in MMCs [3] (Table 2-2). Among the various reinforcement listed below, the most commonly used particles for AMCs are SiC and Al_2O_3 due to their low cost and a wide range of various commercially available. More recently, researchers have grown interested in the use of nano-particles as reinforcement due to their ability to further enhance strength as compared to micro-sized reinforcements [4, 5]. The use of reinforcement in AMCs contributes to improved strength, stiffness, elevated temperature mechanical performances and wear resistance [6-9].

Table 2-2 Typical reinforcement suitable for use in metal matrix composites [3].

Reinforcements category	Aspect ratio	Diameter	Examples
Particles	1-4	1-25 µm	SiC, Al_2O_3, BN, B_4C, WC
Short fibre or whisker	10-10,000	1-5 µm	C, SiC, Al_2O_3, Al_2O_3 + SiO_2
Continuous fibre	>1,000	3-150 µm	SiC, Al_2O_3. C, B, W, Nb-Ti, Nb_3Sn
Nanoparticle	1-4	<100 nm	C, Al_2O_3, SiC
Nanotube	>1,000	<100 nm	C

2.2 Strengthening Mechanism

2.2.1 Dislocation Strengthening

Cold working a material increases the dislocation density in the material. The existence of dislocations gives rise to the generation of internal stress field which requires extra effort to move a dislocation through the internal stress field of other existing dislocations. The strengthening effect could be described as a result of the flow stress being proportional to the square root of the dislocation density, ρ [3]

$$\tau = \tau_0 + \alpha G b \sqrt{\rho} \quad (1)$$

Where τ is the shear flow stress, τ_0 is the friction stress, G is the shear modulus, b is the Burgers vector, ρ is the dislocation density, and α is a constant in the order of 0.5.

2.2.2 Grain Boundary Strengthening

Grain boundary strengthening, also known as grain size control, could be explained using grain boundary theory. When a dislocation moves along the matrix and approaches a region such as the grain boundary film [27]. This region then effectively becomes a potential barrier obstructing the passage of dislocation resulting in higher yield stress than the matrix itself. Dislocations will continue to pile up along the glide plane behind the grain boundary film due to the repulsion experience at the grain boundary interface. The stress concentration at the tip of the slip band eventually become great enough to cause the film to yield causing the deformation to be transferred to the next grain. Grain boundaries strengthening is commonly referred to as the Hall-Petch equation [28]

$$\sigma = \sigma_0 + {}^{k}/_{\sqrt{d}} \quad (2)$$

Where σ is the yield strength, σ_0 is the original strength of the material/ friction stress (MPa), k is the Hall-Petch coefficient, constant for pure Al (74 MPa $\mu m^{1/2}$) while d is the average grain size (μm). However, such size strengthening approach would result in a reduction in ductility of the material. In addition, the equation is only applicable for grain sizes within a certain range (Figure 2-1).

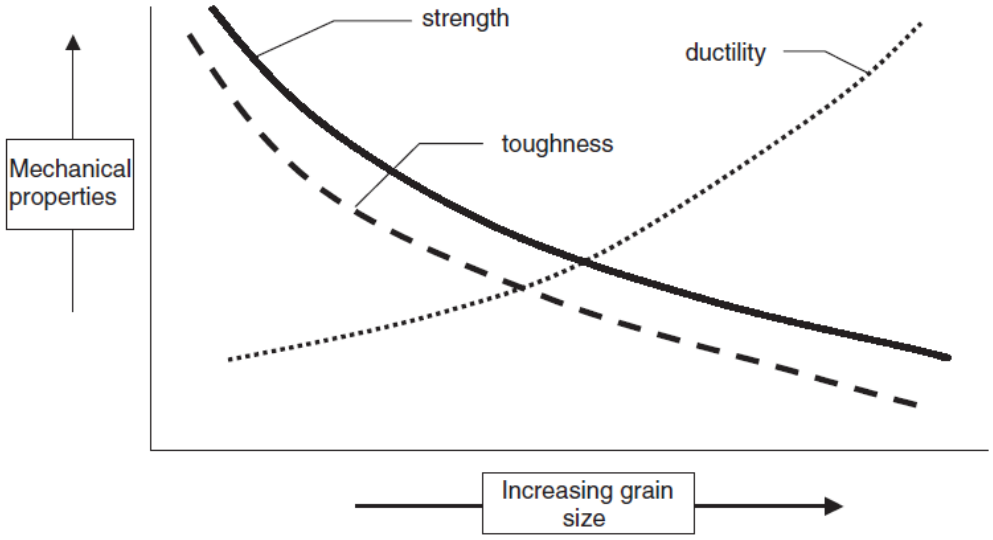

Figure 2-1 General relationship between average grain size with strength, ductility and toughness of a material [16].

The Hall-Petch equation does not hold for small grain sizes, especially of those lesser than 20 nm. Instead, the inverse Hall-Petch effect was observed when grain sizes smaller than 20 nm were achieved [29-31]. The plastic elongation experiences high tensile stress and localised necking deformation led to early failure. The necking instability could be explained by the Hart Criterion [32, 33]

$$\frac{d\sigma}{d\epsilon} + m\sigma \leq \sigma$$

Where σ is the true stress, ϵ is the true strain and m is the strain rate sensitivity. In general, the strain rate sensitivity for nanostructured metals is around 0.05 at room temperature. Therefore, a high strain hardening rate is required to achieve stability. This could result in a strength-ductility trade-off.

In the case of heterogeneous nanostructures containing both hard and soft regions, deformation incapability builds up at the grain boundaries, domain boundaries and interfaces between the hard and soft regions [34]. These accumulated dislocations, on the one hand, generate long-range stresses that prevent dislocation motion in regions away from the interfaces, hardening the material. On the other hand, it also improves strength and ductility via forest hardening and cross-slip mechanism. Therefore, the build of plastic deformation gradient between the hard and soft region could promote strength-ductility synergy as more plastic deformation occurs in the soft region.

2.2.3 Solute and Precipitation Strengthening

Strengthening of the material can also be achieved using hard particles with small particle spacing to resist the passing of dislocation. Such strengthening effect is also known as the Orowan bowing or Orowan strengthening. Particularly for aluminium, solid solution strengthening, precipitation hardening, and dispersion strengthening are commonly applied to aluminium to improve its strength via the introduction of solute atoms, precipitates and dispersoids. Precipitation hardening or ageing treatment involves the precipitation of metastable and stable precipitates from homogenous supersaturated solid solutions. Instantly after quenching, the solid solution hardening is predominant. When ageing occurs, the clusters of solute atoms start forming at the crystallographic planes. These zones are known as Guinier-Preston (GP) zones [3]. This GP zone coherent with the matrix starts to grow with increasing ageing time, giving rise to misfit strain between the matrix and precipitates. As the misfit strain increases, dislocations formed at the interface. These lead to the reduction in the elastic energy associated with reduced coherency. On the other hand, the newly formed

dislocation together with coherency strains on other planes resulted in the increase in the overall strain field around the particle. Thus, increasing the resistance to dislocation motion and increasing the strength of the alloy. Orowan bowing mechanism around the particles occurs when equilibrium precipitates with incoherent interface starts appearing. Peak ageing occurs when the critical dispersion of coherent or semi-coherent precipitates is reached where contributions from shearing and bypass of particles are equal. Beyond this point, further ageing will result in lower strength as dislocation bowing become easier from the increase in interparticle spacing.

Dislocation movement in metals occurs in the form of shear stress. When the dislocation moving along the slip plane meet a particle, the dislocation bows between the particle and the slip plane (Figure 2-2). The shear stress required to bow the dislocation to the radius can be described by the following equation.

$$\tau = \frac{Gb}{d} \quad (3)$$

Where τ is the shear stress, G is the shear modulus of the metal, b is the Burgers vector and d is the spacing between the obstacles. After the dislocation passes the particle, it forms a dislocation loop around it. Thus, the effective spacing between the particles reduces from d becomes d_1. This equation holds true when ignoring the changes in the orientation of the dislocations due to the bowing. With respect to AMCs, Orowan strengthening is only significant for nano-sized reinforcement as the reinforcement particles, and the interparticle spacing is small [35].

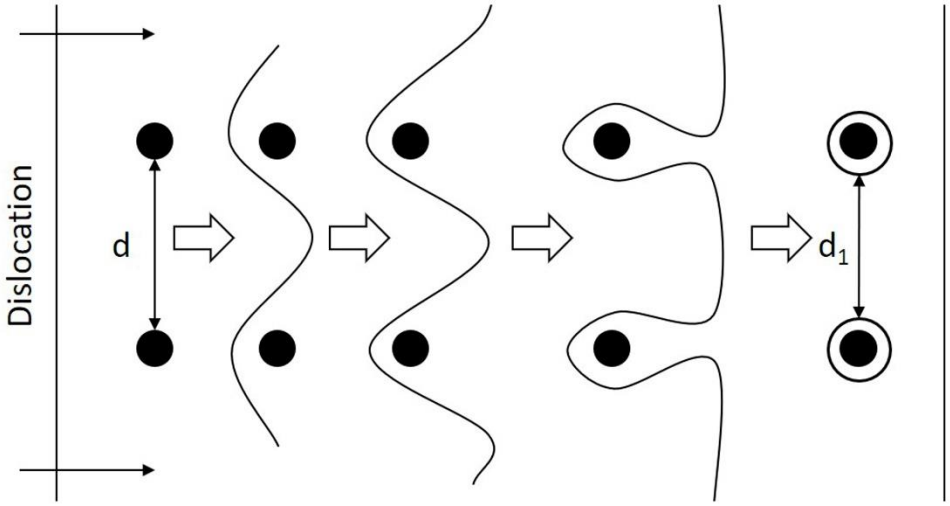

Figure 2-2 Diagram illustrating the dislocation movement passing between particles.

2.3 Additive Manufacturing of Metals

Additive manufacturing (AM) plays a crucial role in rapid prototyping, rapid tooling and manufacturing industries. The use of layerwise fabrication technique has enabled fast and relatively lower cost prototype fabrication. Recently, industries are looking at the visibility of direct fabrication of complex components via additive manufacturing, as such, commercially available machines capable of fabricating metal components were summarised in Table 2-3.

Table 2-3 Various commercially available additive manufacturing methods for metal printing.

Machine model	Company	Type of dispensing	Laser type	Reference
SLM 280 2.0	SLM Solutions	Powder-based	IPG fibre laser	[36]
M2 cusing Multilaser	Concept Laser Gmbh	Powder-based	Fibre laser	[37]
EOSINT M 280	EOS	Powder-based	Yb-fibre laser	[38]
SLM 300i	ReaLizer GmbH	Powder-based	Faserlaser	[39]
AM250	Renishaw	Powder-based	-	[40]
Electron beam melting A2X	ARCAM	Powder-based	Electron Beam	[41]
ProX DMP 300	3D Systems	Powder-based	Fiber laser	[42]
LENS MR-7 Systems	Optomec	Powder-based	IPG Fiber Laser	[43]
EBAM 68	Sciaky Inc	Wire fed	Electron Beam	[44]

From the commercially available machines for 3D printing of metal components, selective laser melting (SLM) is most commonly used due to a wide variety of materials and applications. The study and use of blended composite powders with customizable parameters could be performed on its open concept systems. Hence, the scope of this section will focus on aluminium alloys and its composites fabricated by SLM.

2.3.1 Introduction to Selective Laser Melting

The idea of selective laser melting (SLM) came between the late 1980s and 1990s [11, 12]. It is a powder-based additive manufacturing technique which fabricates components layer by layer with the use of computer-aided design (CAD) modelling. Firstly, a CAD design is modelled in the computer and sliced into many layers with specified layer thickness. The re-coater system then lays a thin layer of powder over the platform, and a laser scan is performed on the cross-section of the respective layer. The platform then lowers by a specific layer thickness before the next layer of powder is being laid over the previously melted and solidified layer (Figure 2-3). The process repeats until the component is fabricated [45-47]. The unused powders were then removed and recycled while the component is removed from the platform.

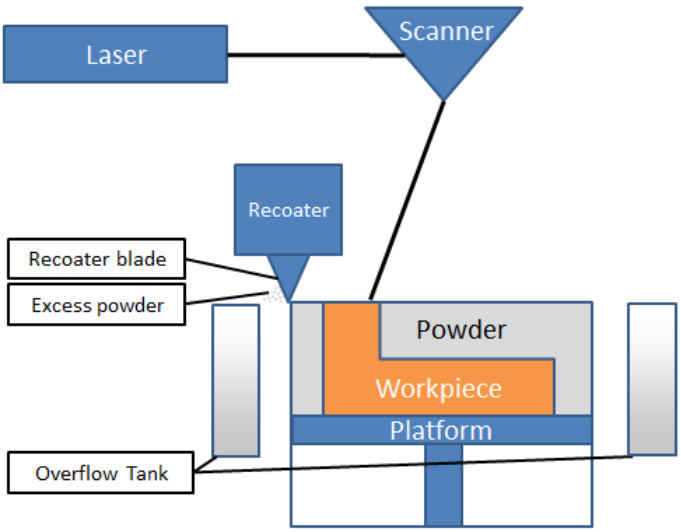

Figure 2-3 Basic schematic diagram of SLM [48].

2.3.2 The complexity of SLM for aluminium alloys

SLM is capable of fabricating components with a complex shape which are challenging to achieve with conventional manufacturing methods. The design flexibility enables functional optimisation and performance with lesser limitations. These advantages allow shorter fabrication time as no tooling and moulds were required. Another advantage of SLM technique is the reduction of waste material as the powders which were not melted could be sieved and reused for the next machine operation [49-51].

On the other hand, the cost-effectiveness and complexity of the melting and solidification process for different material have limited its application [49, 52]. Aluminium readily forms a layer of protective oxide when exposed to air. This made it challenging to work with without an inert environment. The presence of water vapour and/ or adsorbed hydrogen can also lead to the formation of hydrogen porosity during the solidification process. The high thermal diffusivity of aluminium requires the need for higher energy input to melt the powder and overcome the rapid cooling properties. Thermal contraction or solidification shrinkage could lead to hot tearing and hot cracking defects especially for aluminium alloy 6XXX series (Figure 2-4) [53].

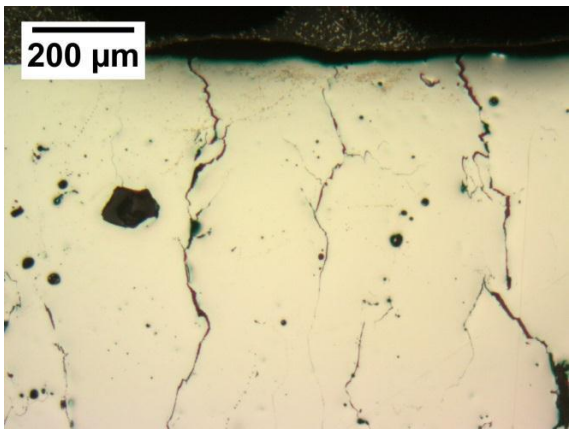

Figure 2-4 An as-built AA6061 sample using SLM showing hot cracking [53].

Currently, $AlSi_{10}Mg$ is widely used in the SLM of aluminium alloys as the high silicon content improves melt fluidity with relatively low shrinkage [54]. The optimised SLM parameters for various aluminium alloys and its composites were tabulated in Table 2-4. It is evident that the use of different processing parameter is required for different material. Therefore, the study and optimisation of process parameters for SLM to obtain optimal properties are required.

Table 2-4 SLM process parameters for various aluminium alloys.

Material	Laser power (Watts)	Scanning speed (mm/s)	Hatch spacing (µm)	Layer thickness (µm)	Reference
$AlSi_{10}Mg$	250	500	150	50	[46]
$AlSi_{10}Mg$	900	1700	50	50	[49]
$AlSi_{12}$	200	500	150	50	[55]
$AlSi_{10}Mg$/ TiC/ 5 wt. %	110	150	50	50	[56]
Al/ Al_2O_3/ 4 vol. %	200	300	70	30	[57]
Al/ Fe2O3/ 15wt%	74	200	50	75	[58]
AlMg1SiCu/ Fe2O3/ 15 wt. %	74	200	50	75	[58]
$AlSi_{10}Mg$/ Fe2O3/ 15 wt. %	74	200	50	75	[58]

2.3.3 Porosity

The formation of porosity between melt tracks could result from the use of processing parameters with insufficient energy input. During SLM laser scanning, a cylindrical shaped liquid melt track is formed. The surface energy drops as the laser moves away. The cylindrical melt track then breaks up to form several agglomerated spheres. Such phenomenon is known as the balling effect where the formation of poor inter-line bonding property or discontinuous scan tracks occurs on adjacent melt tracks. The formation of an oxide film on the previous layer could also prevent good interlayer bonding. The poor wettability between the molten metal and its oxides lead to balling effect [14, 59]. Li et al. [60] reported that keeping oxygen level of the build chamber at 0.1% while applying low scanning speed with a high laser power or rescanning of the layer with the laser could significantly reduce the balling effect.

On the other hand, when energy input exceeds the critical threshold, the surface temperature gradient between the centre and the perimeter of the melt pool becomes too great. Marangoni convection and surface tension gradient are formed. The Marangoni convection causes the melt to flow radially outwards from the centre of the melt pool [61]. The unstable melt track eventually disintegrates into agglomerated spheres.

The vaporisation of aluminium could also result in the formation of porosity. Formation of ionised metal vapour (plasma plume) was observed to exert a recoil pressure on evaporated molten metal within the cavity of the melt pool (Figure 2-5) [62]. Droplets were expelled upwards from the melt pool in the form of spatters [63]. The spattering phenomenon was further studied by Qiu et al. [64] through the use of the high-speed camera as well as simulation modelling. The melt splashing was caused by both the Marangoni effect and the recoil pressure during the metal vapour expansion. The increase in energy input causes higher melt splashing during SLM process giving rise to unstable melt flow and porosity of the material [65].

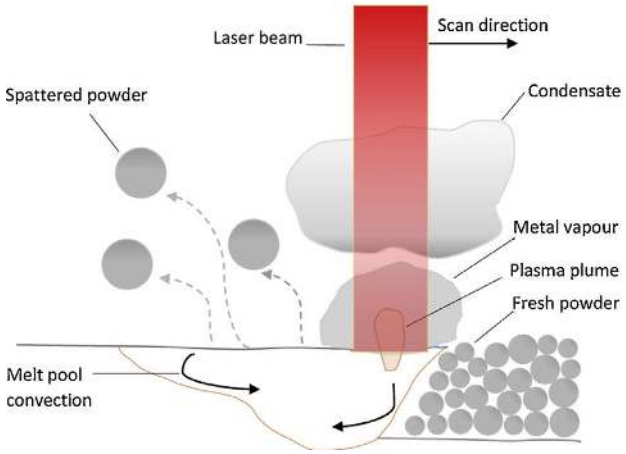

Figure 2-5 Schematic diagram showing the formation of melt pool, spatter as well as condensate during SLM process [66].

Numerous studies have reported visible porosity in SLM parts [45, 46, 50, 67, 68]. Louvis et al. [48] attributed the formation of porosity to the formation of oxides at the surface of the melt pool which led to poor fusion and wetting to the solidified surfaces. Although increasing laser density breaks up the bottom surface of the melt pool, an oxide film remains at the sides of the pool trapping powder which are not melted and air pockets when adjacent melt pools solidify (Figure 2-6a) [46]. Aboulkhair et al. [68] attributed the poor load bearing and high stress concentration along the build direction to the surface discontinuity that restricts homogeneous plastic deformation and crack initiation sites from the residual stresses (Figure 2-6b). The effect of the defects becomes more significant as bigger parts are built.

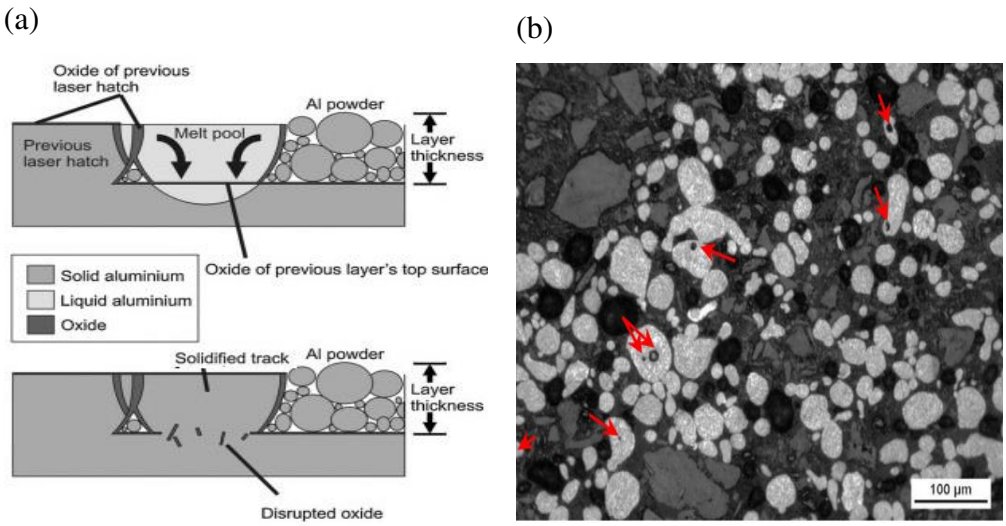

Figure 2-6 (a) Oxide interaction with the melt pool during SLM process [48]; (b) Trapped pores marked by arrows [68].

Several studies have been performed to reduce the porosity. Thijs et al. [67] reported the fabrication of SLM parts with less detrimental spherical pores via rotating scanning strategies. The use of lower laser power is associated with less oxidation and porosity formation. Alternatively, Pupo et al. [69] reported improvement in homogeneous layers could be achieved with slower cooling rates. Aboulkhair et al. [68] attempted to reduce the pores using both rotating scanning and slower cooling rate strategies. In their study, they attributed the different type of pore formation to the scanning speed and strategy. It is reported that relative density could also be improved with pre-sinter scanning, using half laser power, prior to the actual laser scan using laser power of 100W, scanning speed of 500 mm/s and hatching spacing of 50 µm (Figure 2-7). It was concluded that relative density of 99.77 % could be achieved.

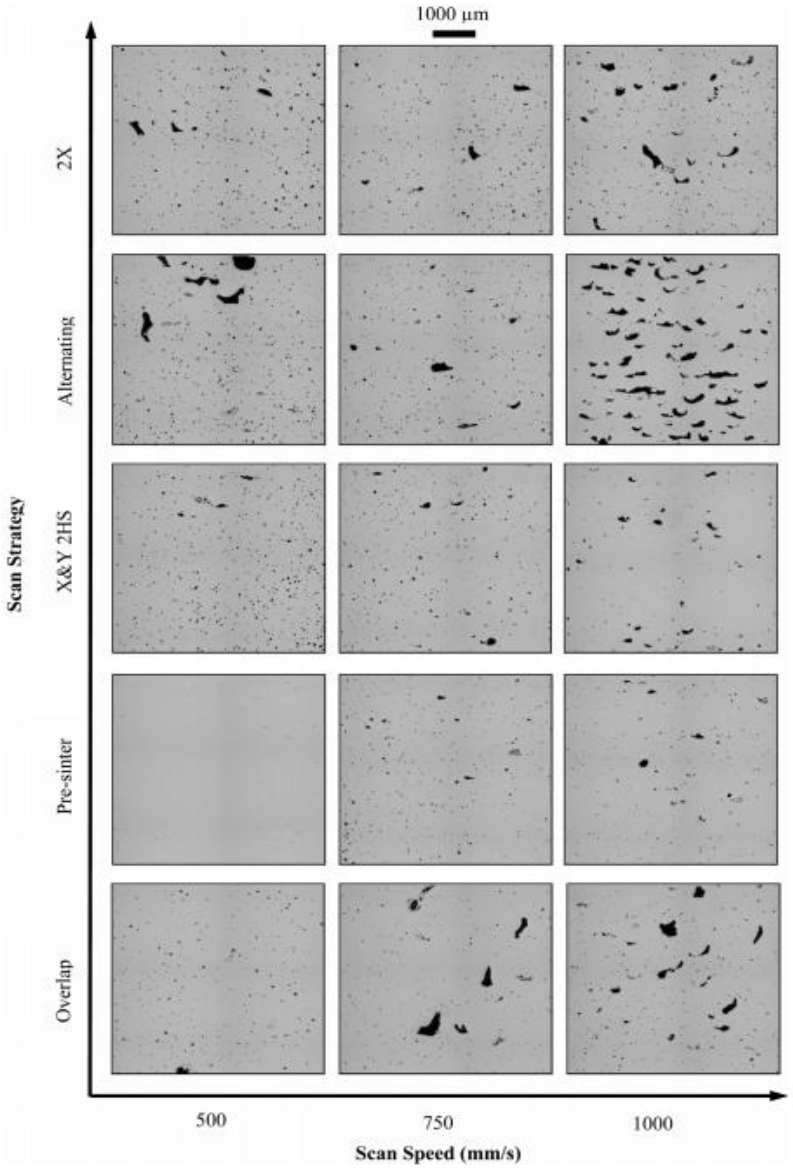

Figure 2-7 Change of porosity in $AlSi_{10}Mg$ with different scanning speed and strategy [68].

Several studies have attempted to fabricate AMCs via SLM process [56-58, 70-73]. Jue et al. [70] reported the need for higher energy input for SLM of Al-Al_2O_3 composites. The presence of Al_2O_3 resulted in the elevation of viscosity in the melt due to its high melting point. This results in the formation of microstructural

defects. Therefore, higher energy input was required to lower the dynamic viscosity of the melt track and improve the wetting characteristic.

Gu et al. [56] reported the influence of different energy input on the microstructure of $AlSi_{10}Mg$/ TiC composite. The use of sufficiently high energy input improved densification behaviour of the composite as well as increase the Marangoni convention within the molten pool. The strong convection prevents the agglomeration of the reinforcement particles allowing more uniform dispersion of the TiC particles in the matrix. However, the use of excessive energy input resulted in the disappearance of the nanostructures and coarsening of the TiC particles due to the higher melt pool temperature and slower cooling rate.

2.3.4 Thermal stresses

The high temperature gradient from the rapid melting and solidification of SLM parts often result in high thermal stresses [67]. Residual stress from various of deposition scanning pattern in layerwise manufacturing was studied (Figure 2-8a and b). It was reported that lowest deflection for fabrication of beam structure was achieved when raster pattern was used with lines oriented perpendicular to the beams long axis. Another study has reported that spiral pattern from the outer edge to the centre produces low and uniform deflections [74]. Kruth et al. [75] reported the effect of scan vector on the residual stresses. In their study, it was observed that residual stresses could be reduced with the use of shorter scanning vectors. Yasa et al. [76] divided the scanning layer into many small square sections and performed island or sectoral scanning with neighbouring grids being scanned perpendicular to one another (Figure 2-8c). It was reported that such scanning strategy regardless of its sector size resulted in significant reduction in residual stress.

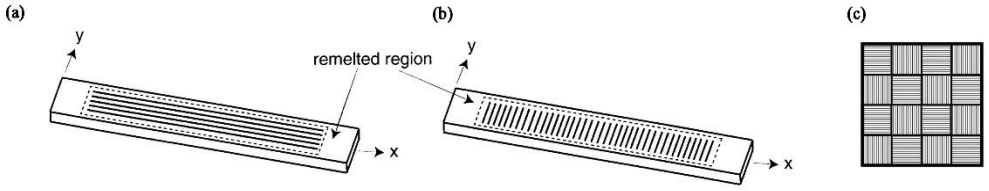

Figure 2-8 Schematic diagram showing (a) long, (b) short raster [74], (c) island [76] scanning pattern.

2.3.5 Oxidation

Another major cause of defects in the fabricated parts is the occurrence of oxidation during the process [52, 77]. This is especially true in the case of aluminium alloy as aluminium-based alloys are highly reflective, thermally conductive, lightweight and oxidise easily resulting in limited successful SLM application [48-51]. Higher laser power is required for materials with high reflectivity and conductivity. The low-density properties of aluminium have limited the flowability and compactness of its powder bed. However, the major challenge lies in the oxidation of aluminium as often observed between laser hatches (Figure 2-9) [48, 51]. These oxides significantly hindered the homogeneous diffusion of the trapped porosity between the melt pools [78].

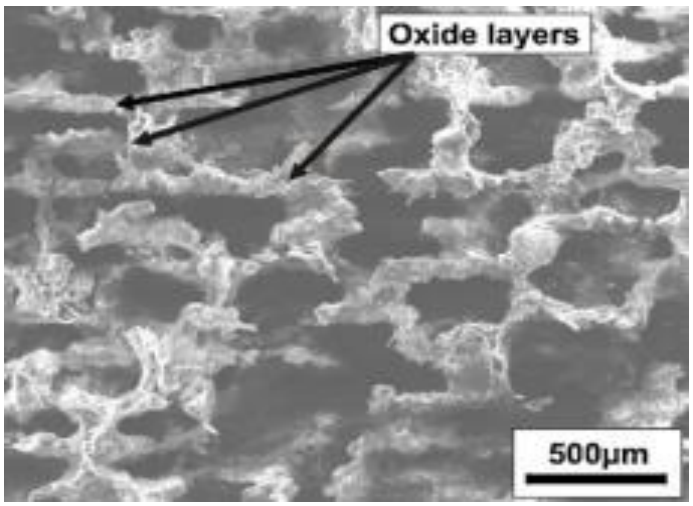

Figure 2-9 SEM image of oxide layers in AA6061 part after etching [48].

Even though oxidation issues are difficult to avoid, Louvis et al. [48] used higher laser intensity to break up the oxide layers and reported successful fabrication of highly dense parts. Thijs et al. [51] reported the fabrication of denser parts by rotating scanning directions between layers. However, higher laser power density will result in larger melt pool being created and lower melt viscosity. Thus, creating a larger heat affected zone with irregular molten vectors [49]. Laser power density and productivity are negatively correlated. The laser power density could be raised by reducing the scanning speed and hatch spacing which, in turn, lowers the production rate. On the contrary, insufficient laser power density often results in the prevalence of surface tension leading to discontinuous molten vector [47]. Therefore, much research interest was focused on optimising the various parameters to fabricate quality highly dense parts with high productivity.

2.3.6 Mechanical properties

The mechanical properties of SLM fabricated aluminium alloys and composites were tabulated in Table 2-5 and Table 2-6 respectively. As mentioned earlier, porosity defects in the fabricated part have a substantial impact on the mechanical properties. German et al. [79] reported a significant difference in the reduction in

ductility with varying shape, size, spacing as well as the location of the pores. It was also reported that porosity higher than 15% results in negligible ductility. Hence, the presence of a large amount of porosity in the material reduces the amount of load bearing material and its mechanical properties. The hardness and tensile strength of SLM fabricated aluminium alloy and composites shall be reviewed. It is noted that $AlSi_{10}Mg$ is among the most commonly used base material amongst the SLM fabrication of aluminium alloy with relative density around 99%.

Table 2-5 Mechanical properties of various SLM fabricated aluminium alloys.

Base material	Powder size (µm)	Laser type	Laser power (Watts)	Scanning speed (mm/s)	Hatch spacing (µm)	Layer thickness (µm)	Relative density (%)	Vickers hardness (Hv)	Yield strength (MPa)	Ultimate tensile strength (MPa)	Elongation (%)	Orientation	Reference
AA6061	-	Yb-fibre laser beam	100	120	200	50	89.5	-	-	-	-	-	[48]
Al-12Si	27-50	Fibre laser	200	500	150	50	97.5	108	223±11	355±8	4.2±0.6	XY	[55]
Al-20Si	-	Yb-YAG laser	320	1455	110	50	-	-	374±-4	506±5	1.6	XY	[80]
$AlSi_{10}Mg$	20-63	Nd:YAG laser	350	900	120	100	-	-	-	330	-	XY	[66]
$AlSi_{10}Mg$	-	Fibre laser	900	1700	50	50	99.5	145	-	400	-	XY	[49]
$AlSi_{10}Mg$	1-44	Yb-fibre laser	195	800	170	30	99.2	105±2	243±7	330±3	6.2±0.3	XY	[81]
$AlSi_{10}Mg$	25–45	Nd:YAG laser	250	500	150	50	99	-	-	-	-	-	[46]
$AlSi_{10}Mg$	16.3	Fibre laser	200	1400	105	30	99.8	127	-	391±6	5.55±0.4	XY	[82]
$AlSi_{10}Mg$	20-63	Nd:YAG laser	350	930	190	50	98.8	-	-	-	-	-	[83]
$AlSi_{10}Mg$	20-63	Yb-Fibre laser	175	1025	650	30	99.7	-	250	325	1.25	XY	[84]
$AlSi_{10}Mg$	20-63	Fibre laser	350	1140	170	50	-	132.55±5.3	322.17±8.1	434.25±10.7	5.3±0.22	XY	[85]
$AlSi_{10}Mg$	30	Yb-fibre laser	250	200	50	50	-	-	-	-	-	-	[86]
Recycled $AlSi_{10}Mg$	9.9	Yb-fibre laser	370	1300	190	30	-	-	210±5	386±10	8.8±0.3	XY	[87]
Mg–9Al	17-42	Nd:YAG laser	15	20	80	50	82	75	-	-	-	XY	[88]

Table 2-6 Mechanical properties of various SLM fabricated AMCs, where Cp is the concentration percentage, HV is the Vickers hardness, YS is the Yield strength, UTS is the ultimate tensile strength, EL is the elongation.

Base material	Powder size (µm)	Particle size (µm)	Cp (%)	Laser type	Laser power (Watts)	Scanning speed (mm/s)	Hatch spacing (µm)	Layer thickness (µm)	Relative density (%)	HV (Hv)	YS (MPa)	UTS (MPa)	EL (%)	Orientation	Reference
Al-Al_2O_3	2.41	9.04	20 wt.	Yb-fibre laser	130	500	-	70	97.5	175	-	-	-	-	[70]
Al-Al_2O_3	17.1	0.05	4 vol.	Yb-fibre laser	200	300	70	30	99.49	48.5	109	160	5	XY	[57]
Al/Fe_2O_3	50	53	5 wt.	laser	91	140	50	50	-	-	-	-	-	XY	[71]
Al/ Fe2O3	40	53	15 wt.	Fibre laser	74	200	50	75	70	80	-	-	-	-	[58]
AlMg1SiCu/ Fe_2O_3	40	53	15 wt.	Fibre laser	74	200	50	75	70	110	-	-	-	-	[58]
$AlSi_{10}Mg$/ CNT	30.7	0.05	1 wt.	Fibre laser	360	550	80	30	97	105	-	-	-	-	[72]
$AlSi_{10}Mg$/ Fe_2O_3	40	53	15 wt.	Fibre laser	74	200	50	75	80	165	-	-	-	-	[58]
$AlSi_{10}Mg$/ TiC	30	0.05	5 wt.	Yb-fibre laser	100	150	50	50	98	181.2	-	-	-	-	[89]
$AlSi_{10}Mg$/ TiC	30	0.05	5 wt.	Yb-fibre laser	100	150	50	50	98	185	-	482	10.7	XY	[73]

2.3.7 Micro-hardness

The micro-hardness test is a non-destructive test with a good indication of the material's mechanical properties. From Table 2-5 and Table 2-6, the optimal hardness for SLM fabricated $AlSi_{10}Mg$ is 135 HV using the laser power of 350 W, scanning speed of 1140 mm/s, hatch spacing of 170 µm and layer thickness of 50µm. It was observed that the improvement in the micro-hardness could be achieved with the addition of nano-composites. Wang et al. [73] reported a micro-hardness of 185 HV for $AlSi_{10}Mg$ reinforced with 5% wt. nano-TiC particles. The increase in hardness was mainly due to the uniform distribution of hard TiC reinforcement particles in the aluminium matrix.

2.3.8 Tensile properties

The tensile properties of SLM fabricated parts exhibit anisotropic properties. Buchbinder et al. [49] reported the highest tensile strength of 420 MPa when parts are built horizontally while vertical parts exhibit the least tensile strength of 360 MPa. The slight decrease in tensile strength was attributed to the bonding strength between the different layer of the build part. It was then further concluded that the tensile strength is superior to die-cast $AlSi_{10}Mg$ (240 MPa). The improvement in strength is mainly attributed to the fine eutectic Al-Si microstructure from the rapid melting and solidification process [85].

For the SLM of AMCs, the addition of nano-sized Al_2O_3 to pure aluminium resulted in significant improvement in the tensile properties [57]. Wang et al. [73] also reported significant improvement in the tensile result while maintaining good ductility after the addition of nano-sized TiC reinforcement. It was attributed to the piling up of dislocation at the TiC particles which prevented dislocation movement. During plastic deformation, cracks initiated at the interface while TiC delayed the crack propagation.

Much studies have been done on the possibility of fabrication of AMCs via SLM. However, there has been limited literature reporting on the tensile strength. The tensile strength is greatly affected by the presence of porosity and agglomeration of reinforcement particles which are challenging issues to overcome.

2.4 Welding Techniques

Welding is a joining process to join two or more parts together using the application of heat and/ or pressure at the contact surfaces. The joining of two components by melting the parts together is known as fusion welding. Solid phase joining process could also be achieved via the use of pressure and some heat to achieve metallic bonding across the interface. Brazing and soldering could also be done to join aluminium components together by melting the braze or solder material between the components. The principle processes are listed in Figure 2-10. Due to the limited application of some of the processes, the focus will be made on friction stir welding, a novel solid state joining technique.

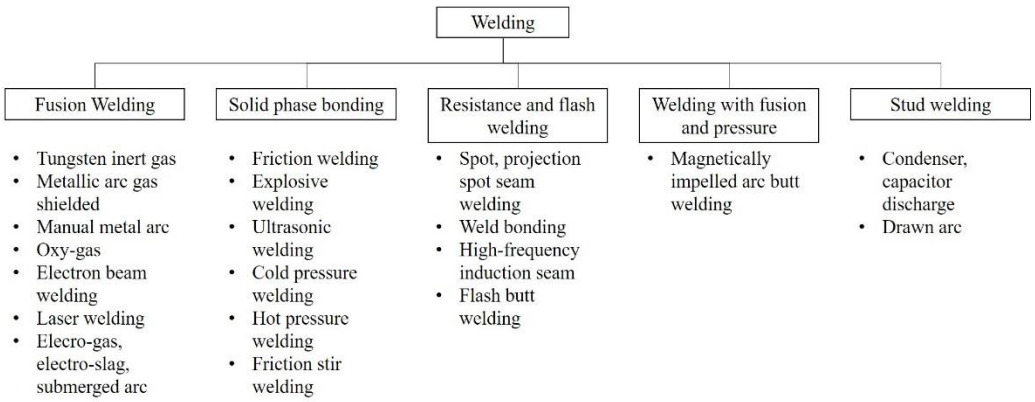

Figure 2-10 Principle processes for welding of aluminium components [16].

2.5 Weldability of Aluminium Alloys and AMCs

In general, traditional fusion welding processes for aluminium requires careful preparation as defect formation often results in loss of strength. The formation of porosity defect could result from the dissolution of shielding gases (oxygen, nitrogen and hydrogen) or moisture from electrode and flux in molten metal (Figure 2-11). Moreover, the significant difference in the melting temperature of aluminium (660°C) and its oxide (2060°C) at the surface could contribute to the lack of fusion in the welded parts. The high thermal conductivity of aluminium resulted in a large temperature difference between the liquid and solidification process. These results in the formation of residual stress in the weld which led to centre-line or hot cracking during fusion welding. The thermal cycle of fusion welding could also significantly reduce the strength in the heat affected zones at heat treatable aluminium alloys [16, 17].

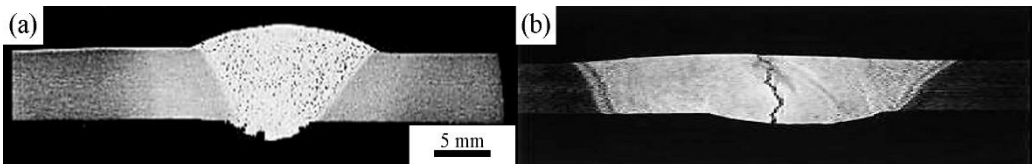

Figure 2-11 Tungsten inert gas (TIG) butt welding of 6mm plate showing trapped porosity in the weld region, and hot cracking in AA6082 with 4043 filler metal [16].

Lakshminarayanan et al. [18] did a comparative study between gas tungsten arc welding, gas metal arc welding and friction stir welding of AA6061-T6. In their study, it was concluded that FSW AA6061 achieved superior mechanical properties (Table 2-7).

Table 2-7 Mechanical properties of various welding techniques on AA6061-T6 [18], GTAW is gas tungsten arc welding, GMAW is gas metal arc welding, and FSW is friction stir welding.

Type of Material	Yield Strength (MPa)	Ultimate Tensile Strength (MPa)	Elongation (%)	Reduction in cross sectional area (%)	Hardness (VHN)
Base Metal (AA 6061)	302	334	18	12.24	105
Weld Metal (GTAW)	160	230	8	5.45	65
Weld Metal (GMAW)	150	220	6	4.5	60
Weld metal (FSW)	245	295	14	10.2	85

In addition to the challenges mentioned above, the welding of AMCs is more challenging. Such challenges include:

- Non-homogenous mixing of filler and base material
- Excessive formation of eutectic phase
- Formation of porosity > 100 µm
- Formation of undesirable brittle intermetallic phases such as Al_4C_3 [19]

MMCs are reported to have superior strength and mechanical properties. However, their application becomes limited if there is no way of joining them together. Storjohann et al. [20] investigated the welding of AA6061 reinforced with 20 weight percent of Al_2O_3 and AA6061 reinforced with 20 weight percent whiskers SiC using gas tungsten arc (GTA), electron beam (EM), Nd-YAG continuous wave laser beam (LB) and friction stir welding (FSW). Al_2O_3 reinforcements were observed to have completely dissolved in the molten aluminium during fusion welding leading to the reduction of its strength. On the other hand, SiC was observed to form Al_4C_3 with Si-rich phase being precipitated due to the reaction between the reinforcement and the aluminium [20]. For the case of FSW, defect-free joint was achieved with no change in the concentration of reinforcement due to its solid-state process without melting. Therefore, FSW is a suitable welding process for joining AMCs.

2.6 Friction Stir Welding of AMCs

Friction stir welding (FSW) was invented by The Welding Institute (TWI) of UK in 1991 [90]. It is a solid-state joining technique used to join two pieces of metal together without melting. Much research has been done on the welding of aluminium due to its relatively low melting pointing as well as its low weldability with traditional welding techniques [91-95].

The basic working principle of FSW involves a non-consumable tool with a threaded pin and shoulder being plunged into the abutting edge of two sheets before travelling along the direction of the weld (Figure 2-12). The friction between the tool and the plate generates heat which softens the workpiece. The rotation of the tool moves the material from the front to the back [96]. During FSW, the material experiences intense plastic deformation coupled with elevated temperature resulting in dynamic recrystallisation of the material [97-100]. This produces fine grain microstructure with good mechanical properties.

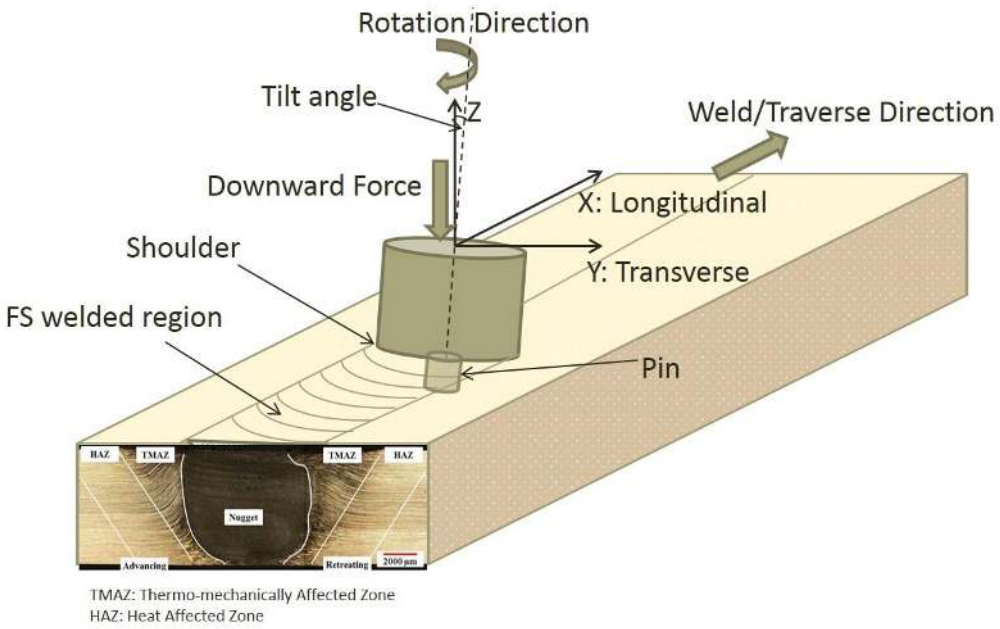

Figure 2-12 Schematic diagram of FSW [25].

As FSW does not involve the melting of the materials, the use of shielding gas is not required. It can be utilized to join materials that are challenging for fusion welding as it eliminates solidification and cooling thermal contractions that lead to significant shrinkage, distortion, development of pores, residue stress, brittle cast structure and hot cracking in the joint [19, 21-24]. It can also produce a high quality weld with low production cost. The key benefits could be summarised as shown below (Table 2-8).

Table 2-8 Key benefits of FSW [19].

Metallurgical benefits	Environmental benefits	Energy benefits
Solid phase process Low distortion of workpiece Good dimensional stability and repeatability No loss of alloying elements Excellent metallurgical properties in the joint area Fine microstructure Absence of cracking Replace multiple parts joined by fasteners	No shielding gas required No surface cleaning required Eliminate grinding wastes Eliminate solvents required for degreasing Consumable materials saving, such as rugs, wire or any other gases	Improved materials use (e.g., joining different thickness) allows reduction in weight Only 2.5% of the energy needed for a laser weld Decreased fuel consumption in light weight aircraft, automotive and ship applications

2.6.1 Process parameters

FSW involves both plastic deformation and movement of the material in the stir zone. The tool geometry, welding parameters and joint design have a significant effect on the welding temperature as well as the material flow. This section addresses the few major factors that affect the FSW process.

2.6.2 Tool geometry

The tool geometry has a significant effect on the material flow and limits the travel speed of the FSW process. The tool used in FSW can be characterized into 2 major components, mainly the tool shoulder and the pin. Generally, a concaved

shoulder and threaded cylindrical pin are used. Several studies have been conducted on the design on the tool pin and observed that increasing the dynamic volume to static volume ratio results in better mixing of weld material as well as oxide fragmentation and dispersal at weld interface (Figure 2-13) [101, 102].

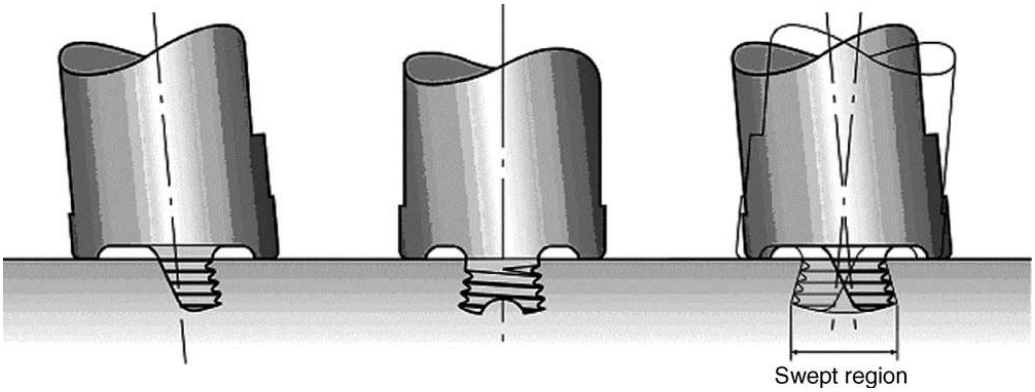

Figure 2-13 A-Skew tool illustration a tool with different static and dynamic volume [101].

2.6.3 Welding parameters

In FSW, the three main parameters that affect the weld are the tool rotation speed (RS), tool travel speed (TS) and the tilt angle (TA). The rotational speed of the tool directly affects the stirring and mixing of the material in the stir zone while the travel speed is related to the cooling rate of FSW. Higher rotational speed results in higher welding temperature due to higher friction and more intense stirring which will be discussed in a later section.

The tilt angle of the spindle with respect to the material is also an important parameter in FSW. A suitable tilt angle of the spindle ensures efficient movement of the material from the front to the back of the pin. The depth in which the pin is inserted into the workpiece is also essential for fabrication of sound weld. If the insertion of the pin is too shallow, the tool shoulder does not get in contact with the surface of the workpiece, resulting in inefficient movement of the material. This will result in the formation of an inner channel or surface groove.

However, if the pin is inserted too deep into the workpiece, excessive flashing and a concave weld will occur causing local thinning of the weld plates.

2.6.4 Joint design

The most commonly used joint configuration for FSW is butt and lap joint. A butt joint configuration (Figure 2-14a) consist of two plates with the same thickness being clamped together to prevent the abutting joint faces from being forced apart especially during the initial plunge of the tool. The rotating tool then transverses along the abutting joint to form the weld. Alternatively, lap joint configuration requires the clamping of two sheets with overlapping layer. The pin of FSW tool is being plunged through the upper layer into the next layer before traversing along the weld direction (Figure 2-14d). Various joint configuration can be fabricated through the combination of butt and lap joint. Moreover, fillet joint configuration can also be achieved (Figure 2-14g).

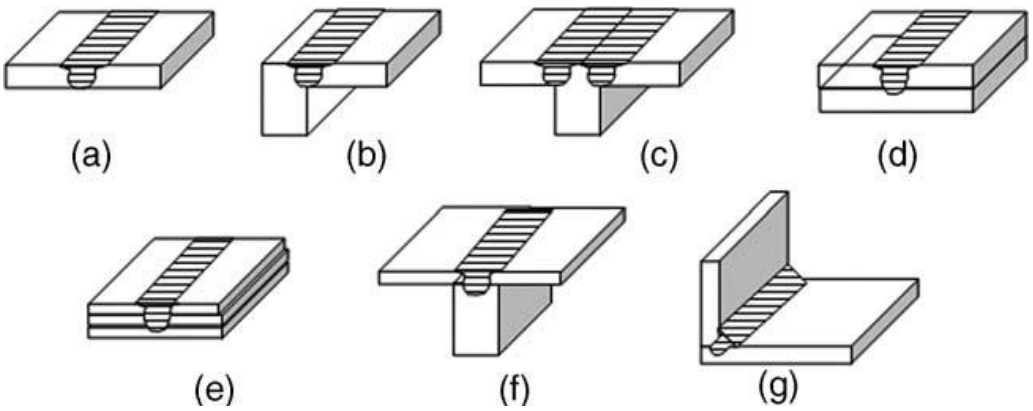

Figure 2-14 Various joint configurations suitable for FSW: (a) square butt, (b) edge butt, (c) T butt, (d) lap, (e) multiple lap, (f) T lap, and (g) fillet joint [19].

2.6.5 Material flow

The material flow during FSW is very complex and dependent on the tool geometry, processing parameter as well as the weld material. Various technique has been used to study the material flow behaviour such as the use of tracer techniques by markers, welding of dissimilar alloys or material as well as FEA simulations.

Reynold et al. [96, 103] investigated the material flow of FSW Al2195-T8 using the marker insert technique. In their study, it was suggested that the in-situ extrusion process where the tool shoulder, pin, weld backing plate as well as the cold base material outside the weld zone created an "extrusion chamber" moving relative to the workpiece. Guerra et al. [104] studied the material flow of FSW AA6061 by placing a 0.1 mm thin high-purity copper foil at the faying surface of the butt weld. At the end of the FSW process, the translation was manually stopped to produce a frozen pin in the workpiece. In their study, the material on the advancing side entered a region and rotated with the pin showing highly deformed and sloughed off feature behind the pin. The retreating side of the pin exhibited extrusion of material between the stir zone and the parent material in the form of weld fills. Schneider et al. [105] studied the FSW of AA2195-T81 with a continuous led wire aligned along a scribe mark on one of the faying surface. In their study, it was observed that the radial distribution of the rotational field around the tool oscillates due to the sporadic seizure and release of the metal contact (stick-slip) occurring at the edge of the weld tool shoulder. Xu et al. [106] studied the material flow pattern using finite element modelling and concluded that the material particles tend to pass and move behind the pin from the retreating side.

In summary, the material flow of FSW is complicated, and understanding of the deformation mechanism is limited. The material flow properties are affected by many factors such as tool geometry, welding parameters, material type as well as

workpiece temperature. Thus, it is possible that the material flow consists of several independent deformation mechanisms.

2.6.6 Temperature distribution

During FSW, frictional heat from the tool and the material together with the plastic deformation led to the elevated temperature of the material. The temperature distribution within and around the stirred zone has a significant impact on the microstructure of the weld. Therefore, it is important to understand the temperature distribution during the welding process. The maximum temperature during FSW could be estimated by examining the microstructure [97, 98, 107] or by embedding thermocouples in a region adjacent to the rotation pin [108-110].

Shojaeefard et al. [111] studied the effect of tool parameters using FEM and neural network. The maximum FSW temperature was observed to increase with increasing shoulder diameter due to higher heat generation. Less significant increase in the welding temperature was observed from the increase in the pin diameter. In recent studies, the recrystallisation grain size can be increased by increasing the rotational speed [110, 112-114] or by reducing the travel speed [115]. Therefore, from the comparison of the grain sizes and the rotational speed to travel speed ratio (RS/TS), relative welding temperature conditions could be concluded.

According to Frigaard et al. [116], the ideal heat generation during FSW considering that all the shearing work is done on the material is converted into frictional heat could be expressed by the following equation:

$$q_0 = \frac{4}{3}\pi^2 \mu P N R^3 \quad (2\text{-}1)$$

Where q_0 is the net power from the shaft (in Watts), μ is the coefficient of friction, P is the pressure from the tool and material interface, N is the rotational speed,

and R is the radius of the tool shoulder. Therefore, the heat input per unit length in a moving weld, Q, could be obtained [117]:

$$Q = \frac{\alpha q}{V} = \alpha \frac{4}{3} \pi^2 \frac{\mu P N R^3}{V} \quad (2\text{-}2)$$

Where α is the heat input efficiency and V is the travel speed.

In summary, the thermal profile could be affected by many factors. From numerous experimental and process modelling investigation, several key conclusions could be highlighted.

- Increasing rotational speed results in increasing welding temperature.
- Increasing travel speed results in an increased cooling rate of the weld.
- Temperature generation from frictional heating increases from centre to the edge of the tool shoulder while the pin provides some frictional heating.
- The coefficient of friction at interface changes with increase tool rotation.
- Frictional condition changes from ‘stick’ to ‘stick/slip’ at higher tool rotation.

2.6.7 Welding defects

The welding temperature is governed by the welding parameters such as rotational speed, travel speed and tilt angle. Excess heat or insufficient welding temperature often causes the formation of welding defects such as tunnelling, wormhole and kissing bonds.

The weld region can be classified into basin shape and elliptical shape [19]. The formation of onion-shaped weld region was reported in FSW of AA2009/SiC/15 weight percent with the rotational speed of 600 rpm and travel speed of 50 mm / min (Figure 2-15a) [118]. It was also reported that post weld heat treatment did not change the shape of the weld nugget (Figure 2-15b) [118]. The formation of basin-shaped weld region was reported with the rotational speed of 1000 rpm

(Figure 2-15c) [119]. The shape of the weld region is believed to be related to the welding temperature and the material flow during FSW. Higher welding temperature could have softened more material under the tool shoulder resulting in a basin shape weld region.

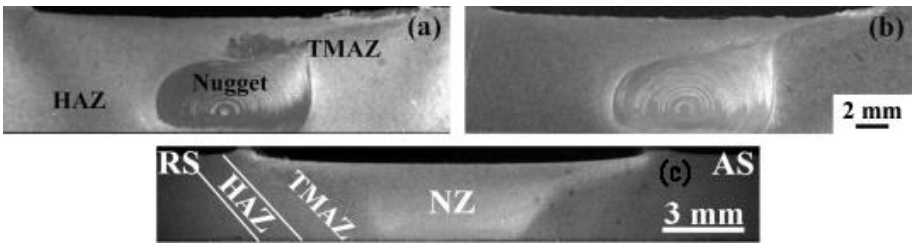

Figure 2-15 FSW of AA2009/SiC/15 weight percent with rotational speed of 600 rpm with travel speed of 50mm / min (a) as welded, (b) T4 condition showing onion ring weld zone [118]; (c) FSW with rotational speed of 1000 rpm [119]; where the nugget zone (NZ), thermomechanical zone (TMAZ), heat affected zone (HAZ), advancing side (AS) and retreating side (RS) are indicated.

FSW welding defects of aluminium have been widely studied [23, 117, 120-125]. The defects can generally be categorised into three major groups.

1. A large mass of flashing due to excessive heat input
2. Cavity, tunnelling, wormhole, or groove-like defect as well as lazy-S kiss bonding due to insufficient heat input.
3. Cavity produced by abnormal stirring.

Flashing occurs when the material experience excessive heat input during FSW. This is commonly formed with higher rotational speed or lower travel speed. The excessive heat input resulted in excessive softening of the material thus expelling large mass of material from the tool. This could result in excessing thinning of the weld region and increase the probability of the pin getting in contact with the backing plate.

The formation of wormhole or tunnelling defect could be created when there is insufficient heat input during FSW. Such defects are usually caused by inadequate material mixing from FSW with high travel speed [121, 123]. During FSW, the plasticised material around the tool pin is transferred from the retreating side to the advancing side. When heat input is insufficient, lesser volume of material is plasticized, the cavity is created behind the pin due to the unconsumed volume of the tool pin. This defect can be eliminated through the increase in shoulder diameter, rotational speed as well as reducing the travel speed to achieve higher heat input during FSW.

Kiss bond or zigzag defect could also be observed in the FSW with insufficient heat input. It is characterised by the formation of dark wavy zigzag line in the weld region [124, 125]. The defect consists of mainly partially broken Al_2O_3, located at the surface of the abutting joint surfaces, from the insufficient stirring during FSW. This defect can be eliminated by increasing the heat input via increasing the rotational tool speed. Increasing the rotational tool speed also improves the stirring and dispersion of the oxide particles.

The formation of crack-like root defect can also be observed at the bottom of the weld if the pin length used was too short for the plate thickness [126]. During FSW, the pin plays a crucial role in stirring and mixing the softened material in the weld zone. The plasticised zone is dependent on the heat input during FSW. With insufficient heat input, the relatively small plasticised zone together with the used of a pin that is too short results in inadequate or no stirring of the material at the bottom of the weld. The backing plate at the bottom acts as the heat sink, drawing heat away from the weld. Therefore, there is lesser softening of the material at the bottom.

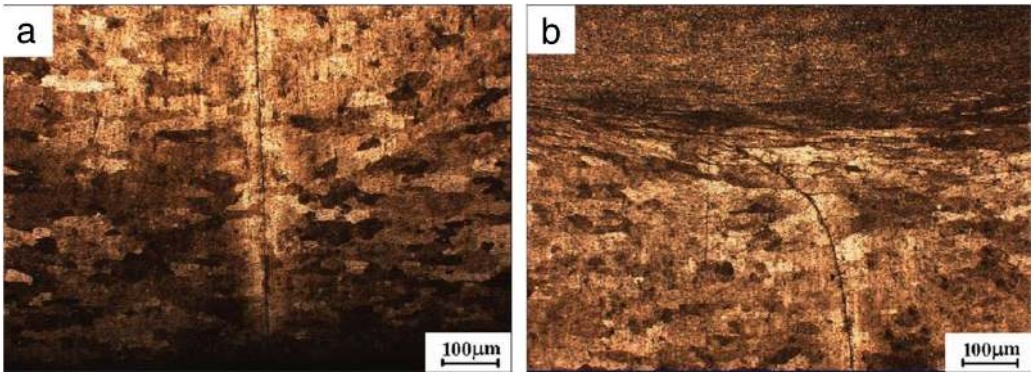

Figure 2-16 FSW of AA2219-T6 showing (a) straight partial bonding root defect (b) crack like root defect curving together with the TMAZ [126].

Abnormal stirring was observed at higher rotation speed and higher welding speeds [117]. This is mainly attributed to the significant difference in temperature between the top surface and bottom surface. It is reported that the top surface of the advancing side of the weld region has a unique shape. The different shape indicated the discontinuous flow of the stirred material (Figure 2-17). It was also reported that the defect reduces in size with increasing downward force.

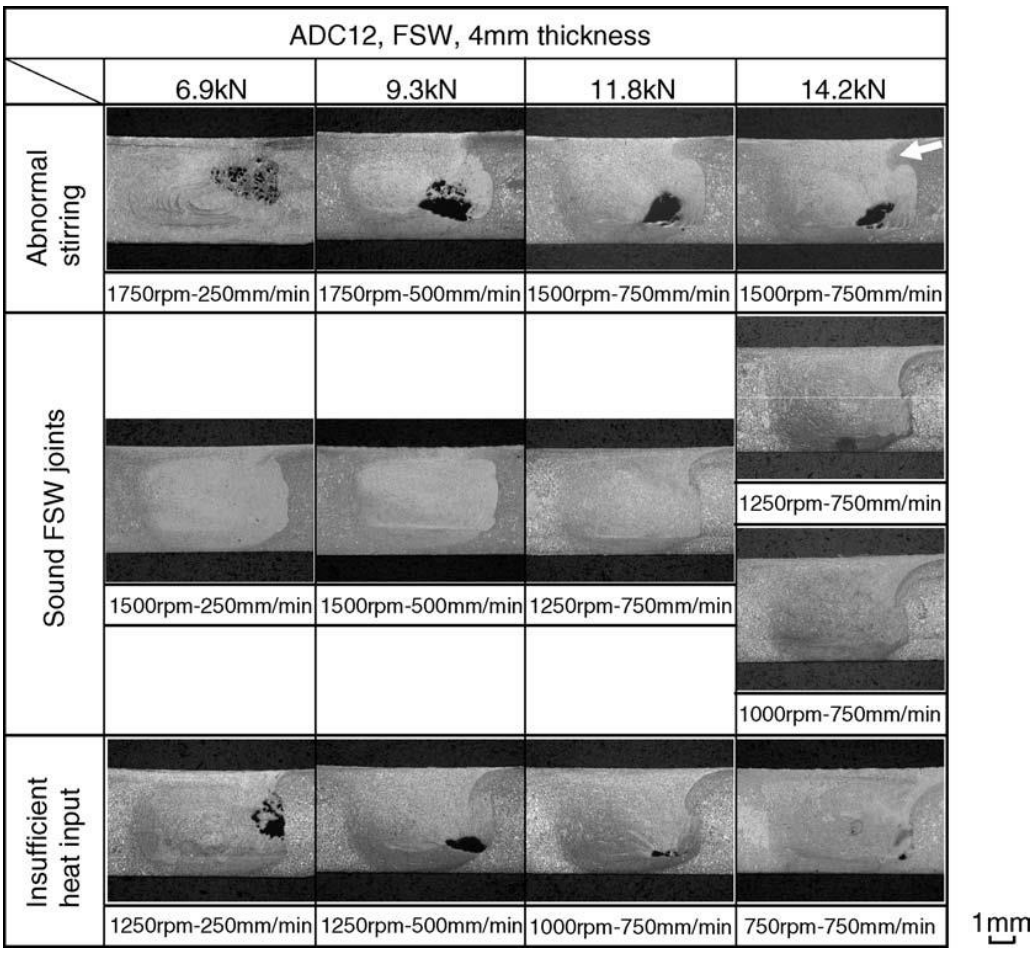

Figure 2-17 FSW of ADC12 showing various weld cross-sections with various weld qualities [117].

2.6.8 Microstructural evolution

During FSW, the weld region experiences dynamic recrystallisation, increase in temperature as well as redistribution of reinforcement particles. The grain sizes of the weld region of FSW of aluminium alloys have been well studied [110, 112-115]. It is concluded that the grain size is affected by the heat input of the welding process. For FSW, the reduction in the rotational speed to travel speed ratio will result in lower welding temperature and finer grains.

Powder and casting fabrication of AMCs often have agglomerated reinforcement particles in their microstructures resulting in isotropy mechanical properties. It was well reported that FSW could separate the clusters and disperse them evenly in the aluminium matrix [119, 127-130]. Reinforcement particles were reported to have broken up into smaller pieces with blunt edges [20, 119, 127, 131-135]. Also, finer particles were reported nearer to the shoulder than the pin of the tool [132]. During FSW, the continuous stirring motion could have caused the particles to break up when in contact with the tool or abrasion with other reinforcement particles. However, a significant reduction in the reinforcement particles was not applicable to fine particles. Storjohann et al. [20] reported reorientation of fine SiC whiskers measuring 5-7 μm in length and 1-2 μm in diameter with no significant refinement. Guo et al. [5] reported micro-bands of clustered nano-sized Al_2O_3 in the weld region with a single pass of FSW and homogenous distribution was achieved with three passes.

The grain structure of the weld region is often described to be fine equiaxed grain from the continuous dynamic recrystallisation process occurring during FSW. The continuous dynamic recrystallisation is a complex phenomenon which occurs during the continuous introduction of deformation at elevated temperature. Thermal cycle of FSW results in the constant rapid recovery and migration of the grain/subgrain boundaries. Studies have reported the addition of reinforcements has resulted in further reduction of the grain size as summarised in Table 2-9. In summary, fine grain was achieved with the use of FSW on AMCs.

Table 2-9 Grain size of various FSW of AMCs.

Material	Reinforcement type	Concentration (%)	Plate thickness (mm)	Particle size (µm)	Tool geometry	Rotational speed (rpm)	Travel speed (mm/min)	Grain size (µm)	Reference
AA6061-T6	Al_2O_3	10 wt. %	6	5	Cylindrical threaded	300	10.16	5.7	[136]
AA6061-T6	Al_2O_3	20 vol. %	7	16	Cylindrical threaded	-	-	25	[132]
AA6061	Al_2O_3	22 wt. %	4	9-10	Cylindrical threaded	880	260	40	[133]
AA6063	B_4C	10.5 wt. %	4.5	17	Cylindrical smooth	1500	600	13	[134]
AA2009-T4	SiC	15 wt.%	8	5.4	Cylindrical threaded	600	50	5	[118]

2.6.9 Micro-hardness

The hardness profile of FSW of AMCs along the cross-section of the weld could show the changes in the various phases and distribution of reinforcement in the weld. Generally, two types of profile have been reported with regards to the FSW of AMCs.

The first type of profile is the typical "W" shaped hardness profile commonly reported in FSW of aluminium alloys (Figure 2-18). This reduction of hardness in the FSW weld region is generally observed in precipitation hardening aluminium alloys and attributed to the coarsening and dissolution of hardening precipitates from the thermal cycle [98, 100, 109, 128].

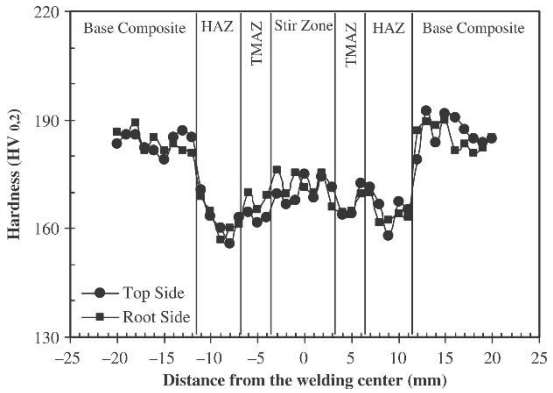

Figure 2-18 Hardness profile of FSW of AA2124 reinforced with 25 wt. % of SiC [128].

On the other hand, FSW does not result in softening of the weld region for solid -solution hardening aluminium alloys (Figure 2-19) [137, 138] and FSW of as-cast AMCs [118, 127, 129, 139, 140]. It is suggested that the hardness profile is considerably related to the dislocation density and particle distribution. The addition of reinforcement was reported to have highest hardness values located at the centre of the weld region with a gradual decrease in the hardness across the

TMAZ and HAZ. It was reported that smaller grain sizes and better distribution of particles resulted in better hardness through Hall-Petch relationship and Orowan strengthening.

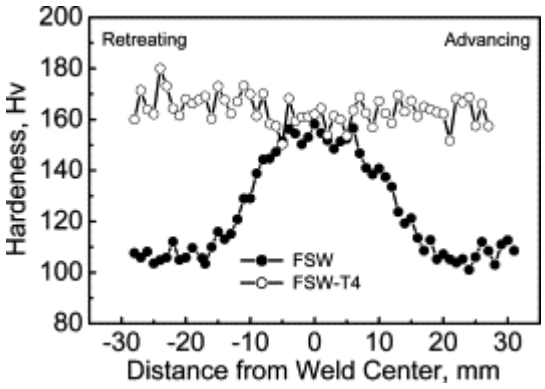

Figure 2-19 Hardness profile of FSW of AA2009 reinforced with SiC particles showing no significant changes in hardness after FSW [118].

2.6.10 Tensile properties

The tensile properties of FSW are superior in comparison to conventional arc welding techniques. Lakshminarayanan et al. [18] reported higher tensile strength, ductility and hardness in FSW samples in comparison to welding of AA6061-T6 with GMAW and GTAW. The tensile properties of FSWed AMCs butt welds were tabulated in Table 2-10. From the summarised table, it was observed that FSW is suitable for welding AMCs with a joint efficiency ranging from 62% to 108 % in comparison to its base material. It has been widely reported that the rotational speed greatly influences the tensile strength of the weld [128-130, 140-143]. Depending on the type of AMCs, the optimal rotation speed used for FSW ranges from 800 rpm to 1200 rpm. As mentioned in the earlier section, the use of lower rotational speed could result in insufficient heat input and welding defects. In contrast, the use of higher rotational speed might result in excessive heat input leading to excessive flash being generated and thinning of the weld region.

In addition to the rotational speed of the tool, one other important weld parameter is the travel speed of the tool. The travel speed during FSW determines the cooling rate. Having higher travel speed can be regarded as higher cooling rate. This would affect the microstructure, grain growth of the weld region and tensile properties. Increasing travel speed may give rise to an increase in the tensile properties from having finer grains. However, tunnelling defect occurs when travel speed becomes high enough leading to insufficient heat input during FSW as discussed in earlier section.

In conclusion, the weld parameters have a significant impact on the tensile properties of AMCs. The effect of rotation speed has considerably more impact on the tensile strength in comparison to travel speed. However, due to the complex interaction between the various welding parameters, each material will require their study to achieve optimal tensile properties for the joints.

Table 2-10 Mechanical properties of FSW of various AMCs with different welding parameters.

Base material	Particle size (µm)	Base material condition	Plate thickness (mm)	Rotational speed (rpm)	Travel speed (mm/min)	Pin geometry	Vickers' hardness (Hv)	Yield strength (MPa)	Ultimate tensile strength (MPa)	Elongation (%)	Joint efficiency (%)	Reference
AA6061-T6/Al_2O_3/10	-	Extruded	7	800	56	-	104	280	329	1.3	-	[139]
AA6061-T6/Al_2O_3/20	16	Extruded	7			Cylindrical threaded	50	193	262	2.8	71.98	[132]
AA6061-T6/Al_2O_3/20	-	-	5	1000	360	Cylindrical threaded	85	-	-	-	-	[144]
AA6061-T6/Al_2O_3/20	10-20	Extruded	7	450-700	150-300	Cylindrical	-	234	251	-	70.7	[135]
AA6061-T6/Al_2O_3/22	9-10	As-cast	4	880	260	Cylindrical threaded	90	-	227	-	99	[133]
AA7005-T6/Al_2O_3/20	-	Extruded	7	800	56	-	127	245	260	0.58	-	[139]
AA6061-T6/AIN/20	3-4	Extruded	6	1217	51.81	Square smooth	-	-	227.02	0.7	94.28	[145]
AA6063/B_4C/10.5	17	Extruded	4.5	1500	600	Cylindrical smooth	60	125	176	2.5	62	[134]
AA6063/B_4C/12	20	As-cast	6	1000	78	Square smooth	105	-	201	2.5	93.4	[127]
AA2124-T6/SiC/25	2	-	15	-	-	Cylindrical threaded	-	435.4	442.8	0.3	-	[130]
AA2009-T4/ SiC/15	5.4	Extruded	8	600	50	Cylindrical threaded	155	250	325	2	108.33	[118]
AA2009-T4/ SiC/17	7	Rolled	3	1000	800	Cylindrical threaded	160	341	501	3.5	97	[146]
AA2009-T351/ SiC/18	8	Rolled	3	1000	50	Cylindrical	160	274	443	4.7	77	[119]
AA6061/ SiC/10	-	As-cast	6	1100	45	Cylindrical threaded	95	126	206	6.5	74	[140]
AA6061/ SiC/20	-	Rolled	6	1370	88.9	Cylindrical threaded	114	201	265	-	-	[141]
Al4.5%Cu/ TiC/10	-	Rolled	5	400	20	Cylindrical threaded	-	-	178.83	2.95	-	[147]
AA6061/ ZrB_2/10	-	As-cast	6	1155	48.8	square smooth			242.56		90	[142]

2.7 Summary

From the literature review, SLM has potential capability to fabricate AMCs with superior mechanical properties. The use of nano-sized reinforcement particles contributed to the piling up of dislocation at the reinforcement particles preventing dislocation movement. However, during plastic deformation, cracks initiated at the interface while delaying the crack propagation. It is evident that the use of different processing parameter is required for different material and different concentration of reinforcement particles. Therefore, optimisation of the SLM process parameters is required to obtain parts with optimal properties.

FSW is a viable solution to join AMCs together as it does not melt the material, thus, eliminating the possibility for the formation of brittle intermetallic phases. Moreover, the dynamic recrystallisation and grain refinement give rise to a potential improvement in the mechanical properties. The welding parameters have a significant impact on the tensile properties of AMCs. The effect of rotation speed has considerably more impact on the tensile strength in comparison to travel speed. However, due to the complex interaction between the various welding parameters, each material will require their study to achieve optimal tensile properties for the joints.

CHAPTER 3

Experimental Methodology

This chapter describes the operating procedures and experimental methodology used in the studies. The equipment and details are then recorded.

3.1 Materials

This section discusses the materials and reinforcement particles used for friction stir welding, friction stir processing and selective laser melting.

3.1.1 Aluminium Alloy AA6061

Rolled sheets of aluminium alloy (AA6061-T6) was used as the base material for friction stir processing. The nominal material composition of AA6061-T6 is shown in Table 3-1.

Table 3-1 The nominal material composition for AA6061-T6.

Element	Al	Mg	Si	Cr	Mn	Ti	Cu	Zn	Fe
Weight %	Balance	1.00	0.60	0.20	0.07	0.07	0.28	0.13	0.40

3.1.2 Aluminium Alloy $AlSi_{10}Mg$

Gas atomised aluminium powders, $AlSi_{10}Mg$, with a normally distributed size between 20 µm to 63 µm by TLS Technik GmbH & Co., Germany, was used to fabricate rectangular blocks for friction stir welding. It is also the base material for fabricating aluminium composites via selective laser melting. The material composition is shown in Table 3-2 while the field scanning electron microscopy (FESEM) image of the powder is shown in Figure 3-1.

Table 3-2 The nominal material composition for $AlSi_{10}Mg$.

Element	Al	Mg	Si	Ni	Mn	Ti	Cu	Zn	Fe
Weight %	Balance	0.30	10.00	0.02	0.20	0.08	0.03	0.05	0.30

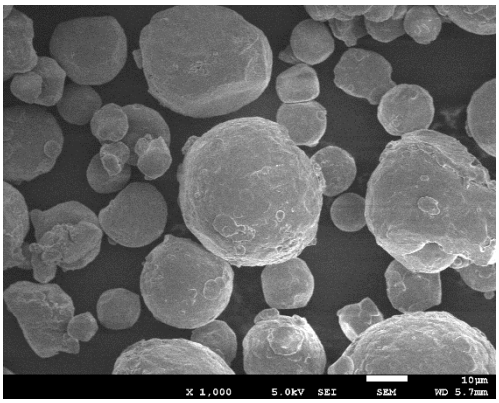

Figure 3-1 FESEM image of as received $AlSi_{10}Mg$ powder.

3.1.3 Alumina Powders

Aluminium alkoxide hydrolysis fabricated nano-sized alumina powder, APK-30, with a nominal size of 320 nm by Sumitomo, Japan, was used as reinforcement particles in this study. The alumina powder has an alpha phase crystal structure with 99.99% purity. The SEM image of the alumina powder is shown in Figure 3-2.

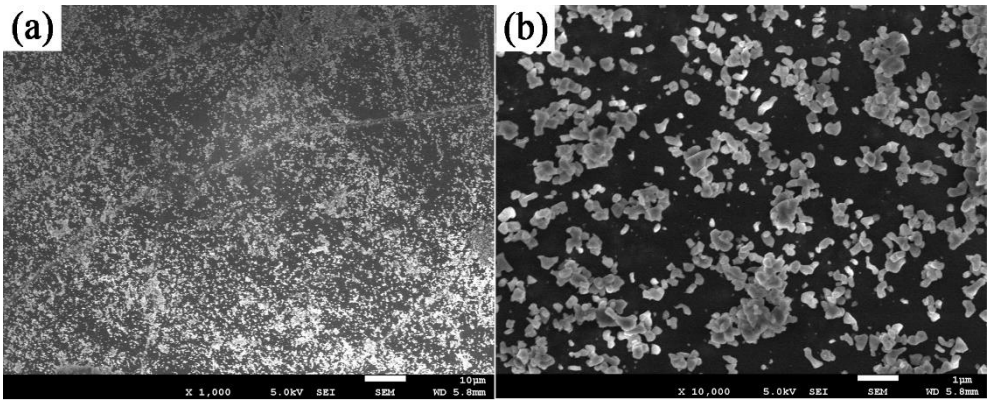

Figure 3-2 FESEM images of as-received alumina powders in (a) low magnification and (b) high magnification.

3.1.4 Carbon Nanotubes

Multi-walled carbon nanotubes (MWCNTs), Sunking International Trading, Singapore, manufactured using chemical vapour deposition process were used in this study (Figure 3-3). The detailed specifications of the as-received MWCNTs were shown in Table 3-3.

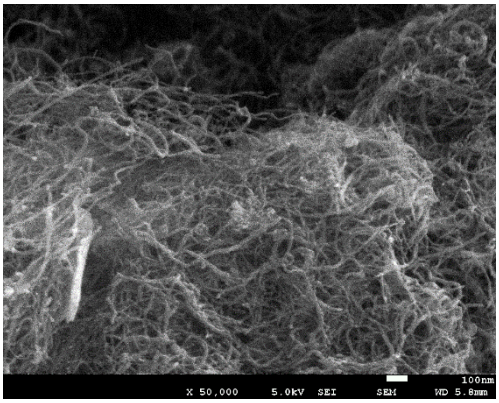

Figure 3-3 FESEM image of as-received MWCNTs.

Table 3-3 Specifications of as-received MWCNTs.

Material	MWCNTs
Production method	Chemical vapour deposition
Density (g/cm^3)	2.2
Purity (%)	95
Inner diameter (nm)	5-10
Outer diameter (nm)	10-20
Length (μm)	10-30
Specific surface area (m^3/g)	180

3.2 Material Characterisation

The effect of the reinforcement particles on the physical and mechanical properties of the composites and weld were investigated. Specimen samples were machined from the master samples and tested with the uniaxial tensile test, micro-hardness test and micro CT scan. Metallurgy characterisation was also performed.

3.2.1 Tensile Test

Tensile coupon with a gauge length of 25 mm, the width of 6 mm based on ASTM E-08 (Standard Test Method for Tension Testing of Metallic Materials) were produced using electrical discharge machining (EDM) as shown in Figure 3-4. Tensile test was conducted using Instron static tester series 5569. The experiment was conducted with a 50 kN load cell using strain rate of 1 mm min^{-1} at room temperature. Detailed tensile results were plotted in Appendix C.

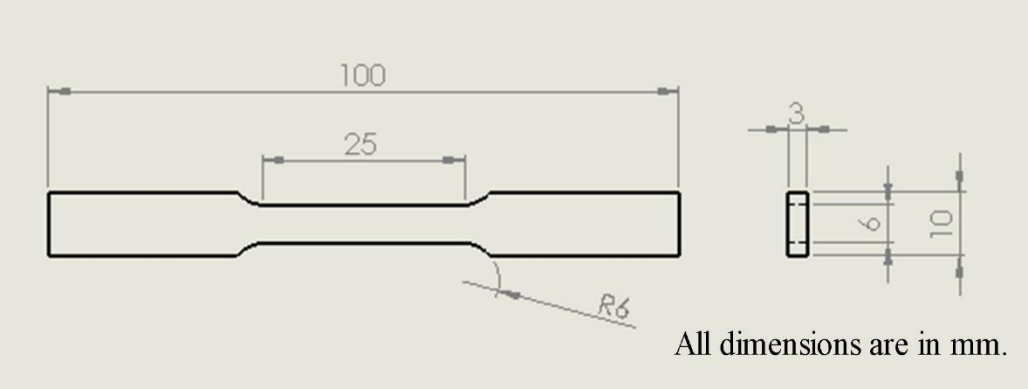

Figure 3-4 Typical dimension of tensile testing coupon.

3.2.2 Vickers Hardness Test

The micro-hardness test of the material was conducted using FM-300e, Future-tech, with 50 grams force loading and duration of 15 s over a minimum of five points.

3.2.3 Micro-Computerized Tomography (Micro CT) Scan

Micro CT scan was performed using the Skyscan 1173 X-ray Microtomography, Brunker Co., Belgium. The scan was conducted with 93 kV and 77 µA. A full rotation scan was conducted with image averaging of five frames, rotational step size of 0.40 degrees and resolution of 6 µm. The images were processed using NRecon software to calculate the relative density of the samples.

3.2.4 Optical Microscopy

The microstructure of samples was characterised using an optical microscope, Olympus SZX7-TR30, Japan, mounted with an imaging camera, Olympus SC30, Germany. Samples were sectioned and mounted before being mechanically polished using Struers Tegramin-25, Denmark, together with the steps listed in Table 3-4. Samples were etched with Keller's reagent to review the grain of polished samples before observation by an optical microscope.

Table 3-4 Polished steps used to polish aluminium and aluminium composites.

	Cloth Type	Lubricant used	RPM of Cloth	RPM of Sample	Force (N)	Duration (min)
Step 1	SiC #2000	Water	300	100	10	3
Step 2	MD-Largo	9 µm suspension	150	150	25-35	5-7
Step 3	MD-Mol	3 µm suspension	150	150	15-25	4-6
Step 4	MD-Chem	0.04 µm suspension	300	100	5	1-3

3.2.5 Field Emission Scanning Electron Microscopy (FESEM)

Microstructural analyses were performed using field emission scanning electron microscope (FESEM), JEOL JSM-7600F, USA. The FESEM was also used to analyse the fracture site of the tested tensile samples to study the failure modes.

3.2.6 Electron Backscatter Diffraction (EBSD)

Electron backscatter diffraction (EBSD) was performed to map, plot the misorientation angle histogram, grain size and inverse pole figure using Channel 5 software by HKL Technology with a step size of 0.2 - 0.5 µm.

3.2.7 Energy Dispersive X-ray Spectroscopy (EDS)

Energy dispersive X-ray spectroscopy (EDS) was performed on the weld nugget of the samples to detect the presence of intermetallic compounds and composition is the weld region.

3.2.8 X-ray Diffraction (XRD)

X-ray diffraction (XRD) machine Philips XRD-PW-1830 diffractometer with Cu K_α radiation, was used to determine the phase composition of the test samples operating at 30 kV and 20 mA. The diffraction angle of 2θ varied from 10° to 120° with a step size of 0.02°.

3.3 Nanoparticles preparation

3.3.1 Reinforcement particle preparation for FSP

CNTs were sonicated using Branson Digital Sonifier 450D with a 400W digital tip sonifier. A disruptor horn capable of generating a horn frequency 20kHz was used. The CNT were dispersed in a volatile solution with 40% sonification amplitude input (approx. 80µm) for a total of 5 min with intervals of 1 min. The beaker was placed in an ice bath to prevent the solution from heating up.

The nAl_2O_3 powder was ball milled together in a volatile solvent with a ball to powder ratio of 1:1. Alumina balls with diameters ranging from 5 mm to 15 mm were used. Ball milling was performed using U.S. Stoneware balling milling machine at 600 rpm for 5 hours.

Sonicated CNTs solution was added to the bottle of nAl_2O_3 and ball milled for another hour to ensure a homogenously mixed slurry was obtained. The slurry was then applied onto the aluminium plate containing reservoirs and dried in a vacuum oven. Multiple application of the slurry was performed to ensure all the reservoirs were fully filled.

3.3.2 Reinforcement particle preparation for SLM

$AlSi_{10}Mg$ and nAl_2O_3 were balls milled together in a volatile solvent. Alumina balls with diameters ranging from 5 mm to 15 mm were used. Ball milling was performed using U.S. Stoneware balling milling machine at 600 rpm for 5 hours. The ball to powder ratio of 1:1 [56] was used to prevent the $AlSi_{10}Mg$ powder from deforming. Deformed powders could lead to a reduction of powder flowability and uneven powder layer thickness during dispensing. The blended slurry was then air dried. The dried powder was further dried using a vacuum oven for 8 hours.

CHAPTER 4

Friction Stir Processing (FSP) of Aluminium Composites Al-CNTS and Al-Al_2O_3-CNTS

This chapter introduces the friction stir processing (FSP) processes in fabricating Al-CNTs and Al-Al_2O_3-CNTs composites. This chapter sets a foundation for understanding the microstructure evolution and strengthening mechanism associated with the introduction of nano-sized reinforcement particles of different shapes for later chapters.

4.1 Introduction

Particulate-reinforced metal matrix composite (MMCs) have drawn much attention in the automobile, aerospace and defence industries due to its superior high elastic modulus, stiffness and wear resistance [1-3]. Significant strengthening effects can be achieved by using small concentrations of small particles [3]. However, the production of MMCs especially nano-composites is quite challenging because the uniform dispersion of nano-sized reinforcements in the metallic substrate is difficult to achieve by using conventional powder metallurgy or liquid processing methods.

The fabrication of MMCs using FSP has attracted much attention ever since it was first reported by Mishra et al. [148] FSP consist of a rotating non-consumable tool being plunged into the workpiece similar to that of friction stir welding. However, the process is done on one workpiece instead of joining two pieces together. Friction between the tool and the workpiece results in the plasticity of the material without melting. The material was being processed as the rotating tool transverse along the material. FSP is a desirable process for the fabrication of MMCs as undesirable intermetallic formations between the matrix, and the reinforcement can be avoided [149, 150].

Several methods are currently available to introduce the reinforcement particles into the matrix. The first method is the application of a thin layer of reinforcement particles on the surface of the workpiece with the assistance of a volatile solvent such as methanol prior to FSP [148]. However, the particles were not uniformly dispersed, and there were significant airborne particles during placement of the particles and FSP. The second method was to create various surface reservoirs such as dimples or holes or grooves and pre-place reinforcement particles in them prior to FSP [151-154]. A thin Al sheet cover could be used to prevent the particles from being airborne during FSP [154]. As dry nano-powders have very low density, the concentration of reinforcement in a reservoir volume is also low. In order to increase the concentration, J. Qu et al. [152] used a slurry of nano-particles and volatile solvent in his study. The third method involves mechanical alloying of the aluminium powders and the reinforcement particle using ball milling before cold compacting and sintering into billets before FSP. Alternatively, the aluminium substrate can be coated with a thin layer of mechanically alloyed powder mixture using air plasma spraying technique [155]. In the present study, an array of small holes will be drilled in the aluminium sheet to create uniformly placed reservoirs to aid in the dispersion. A volatile solvent will be used to produce a slurry of homogeneous reinforcement mixture.

In a study by Guo et al. [5] on the evolution of grain structure and mechanical properties of AA6061 alloy with nano-Al_2O_3 reinforcement particles via FSP. In their study, uniform dispersion of reinforcement particles was achieved with improved micro-hardness and tensile strength. The number of passes improved the dispersion of the reinforcement particles, and finer grain size was reported with the addition of reinforcement particles due to the Zener pinning effect. It has been suggested that the dispersion of the nanoparticles depends on both the number of passes conducted and the rotational speed of the tool. However, increasing the number of passes alone does not have any significant effect on the grain size as the final grain size is dependent on the welding temperature [113].

A similar study was conducted by Du et al. [25] using multi-walled carbon nanotubes (CNTs) as reinforcement particles. Uniform dispersion of CNTs was achieved using FSP after 3 passes. Significant improvement in the Vickers hardness and tensile yield strength were observed after the addition of CNTs. CNTs were also observed at the fracture site suggesting crack bridging which is in conjunction with studies by Liao et al. [7, 156, 157]. Esawi et al. [158] studied Al-CNT composites using powder metallurgy fabrication technique. The powders were ball-milled with CNT before being compacted and hot extruded. Significant improvement in the material strength was observed. CNT pullouts were observed at the fracture site of the tensile samples indicating poor interfacial bonding between aluminium matrix and CNT. On the other hand, there are several studies [159-163] using CNT to reinforce alumina composites. Positive results and improvement of fracture toughness were observed [164]. The adhesion of Al_2O_3 and CNT is significantly strong. Hence, the combination of both in an aluminium alloy composite may proof to be further enhancing the adhesion of the reinforcements. Moreover, both reinforcements are of different shapes forming a network of nano-reinforcement reinforcing the aluminium matrix.

To the best of the authors' knowledge, there have not been any studies on the addition of multiple nano-particle reinforcements in the MMCs. The additions of spherical and thread-like nanoparticles have a different effect on the outcome of the MMCs. Hence this study aims to investigate the effect of the nano-Al_2O_3 and CNT particles addition on the grain structure evolution and mechanical behaviour of the friction stir processed aluminium matrix composite.

This chapter aims to study the microstructure evolution and strengthening mechanism of the addition of CNTs and nAl_2O_3 reinforcements in the AA6061 via FSP. It also serves as a fundamental study on AMCs for the later chapters.

4.2 Experimental Details

In this study, tempered AA6061-T6, multi-walled CNTs and nAl_2O_3 were used. AA6061-T6 alloy rolled plates with a thickness of 3 mm were cut into a smaller sheet measuring 300 mm in length and 100 mm in width (rolling direction). An array of 720 cylindrical holes over an area of 240 mm by 50 mm was machined on the surface of the plates to act as reservoirs for the reinforcement particles (Figure 4-2a). Each cylindrical hole measures 1 mm in diameter and 2 mm in depth. The plates were carefully degreased with acetone and air dried prior to FSP. As the apparent density of the alumina powder ($0.63g/cm^3$) is significantly lower than the bulk density of alumina ($3.97g/cm^3$), large holes will be required to be made on the surface to match up to the relatively high concentration required, leading to instability in the FSP. Therefore, a volatile solvent was added to form a slurry based on optimal concentrations in previous studies [5, 25, 156, 165]. The particle concentration used in this study is 10.3 wt. % of nAl_2O_3 and 0.5 wt. % of multi-walled carbon nanotubes. During FSP, the reinforcement particles might become airborne due to the high rotational speed of the rotating tool resulting in significant particle lost. Therefore, an aluminium sheet cover with a thickness of 1 mm was placed over aluminium plate prior to FSP.

FSP was performed using a friction stir welding equipment mounted onto a 6-axis robotic arm capable of generating 12 kN of downward force. The tool used in this study is a threaded conical probe with three flats. The tool shoulder has a diameter of 12.5 mm while the probe has a base diameter of 5 mm and length of 2 mm.

The grains size of FSP of Al were reported to be independent of the number of passes [5, 166-168]. It was reported that the size of the grains was closely related to the welding temperature and not the number of passes. The FSP of Al-Al_2O_3 was performed in a previous study [5]. In that study, FSP was performed with 2 and 4 passes. It was observed that there was no significant changes in the grain

size between 2 passes and 4 passes as both the flow stress of the material and the welding temperature were similar from pass to pass.

With regards to the particle dispersion, based on previous studies [5, 25], single pass and multi passes of FSP were conducted, micro bands of nano-sized reinforcements were found in single pass FSP while 3 FSP passes were sufficient to produce a homogeneous dispersion of the reinforcement particles (Figure 4-1). However, for the FSP of Al-CNT, the shortening of Al-CNT was observed from pass to pass [25, 169].

Therefore, three FSP passes were performed on the aluminium plates with rotational tool speed of 1200 rpm, the transverse speed of 3mm/s and tilt angle of 3 ° (Figure 4-2b).

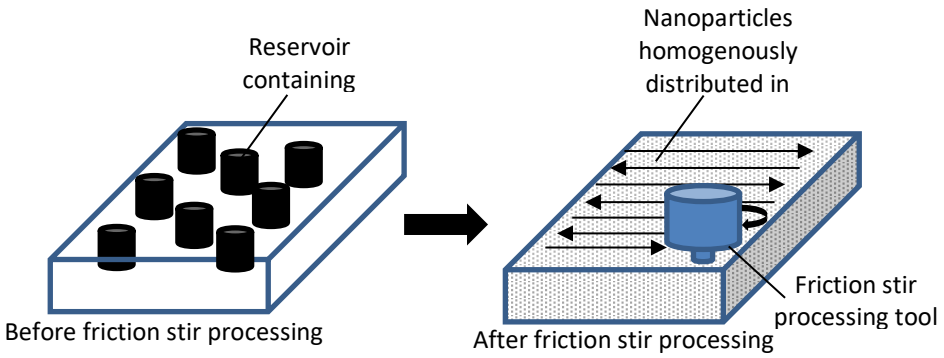

Figure 4-1 Schematic diagram showing how the FSP of the nanocomposites.

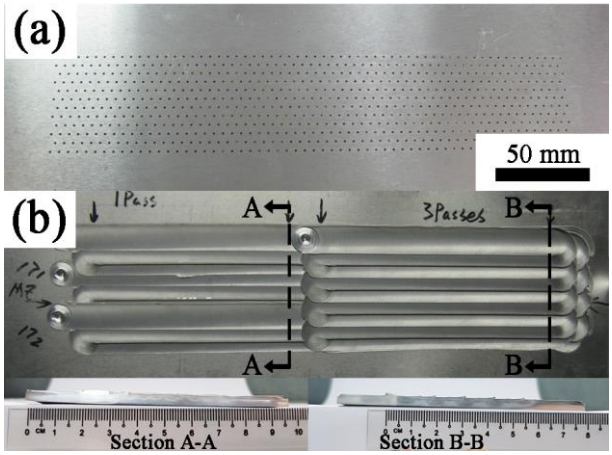

Figure 4-2 AA6061-T6 plates (a) showing array of holes and (b) after FSP.

Metallographic samples were taken from the transverse section of the FSPed plates and mechanically polished using steps mention in Chapter 3. Tensile testing coupons were machined from the plates along the longitudinal direction of the FSP. Material characterisation and mechanical properties were evaluated as mentioned in Chapter 3 and benchmarked against the FSP of Al-nAl_2O_3.

4.3 Results and Discussions

4.3.1 Particle Dispersion

During FSP, the rotating tool plunges into the workpiece before traversing along the material. The friction between the tool and the material generates heat which softens the processing material. The rotation from the tool stirs and mixes the material with the reinforcements. Uniform dispersion of the particles could be achieved with increasing passes [5, 25]. Large second phase dendrites and silicon particles were observed in the as-received AA6061-T6 samples (Figure 4-3a). The dendrites and some silicon particles were observed to have broken down and uniformly distributed in the aluminium matrix after three FSP passes (Figure 4-3b). From the FESEM images (Figure 4-3d and e), nAl_2O_3 particles were observed to have been uniformly dispersed in the matrix via FSP. Even though

CNTs were not visible in the images, it is believed that FSP had uniformly dispersed them in the matrix (Figure 4-3c). This is in conjunction with other studies on the FSP using CNTs reinforcements, where CNTs were observed to be broken down into shorter tubes in the first pass, circular after the second pass and finally, it could not be observed after the third pass [169].

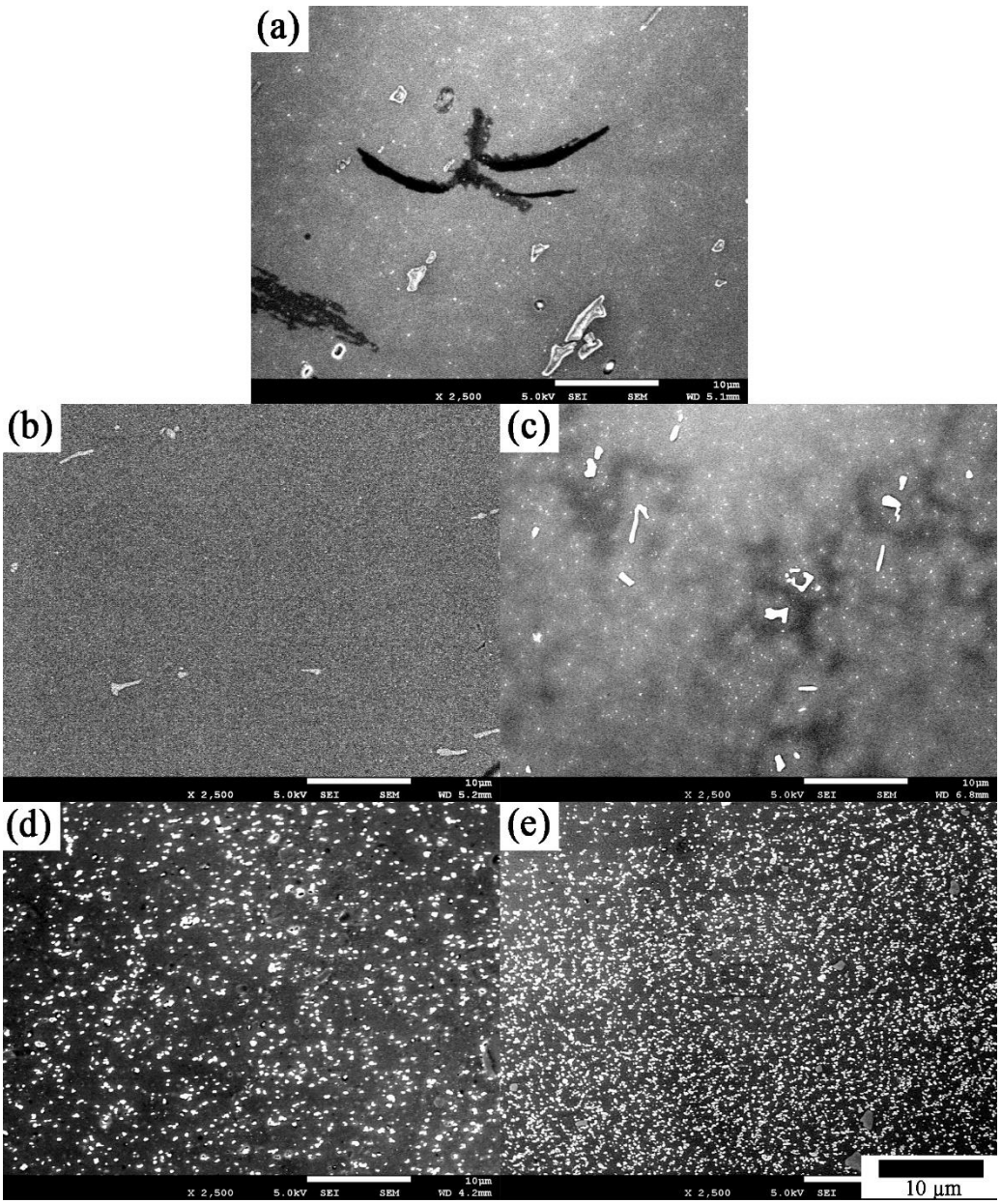

Figure 4-3 FESEM images of AA6061-T6 (a) as-received, (b) with three FSP passes; FSP Al-CNTs composite (c) with three FSP passes; FSP Al-Al_2O_3 composite with (d) four FSP passes [5]; FSP Al -Al_2O_3-CNTs composite with (e) 3 passes.

4.3.2 Grain Structure Evolution

The results from electron backscatter diffraction (EBSD) mapping were illustrated in Figure 4-4. AA6061-T6 displayed elongated grains with an average

grain size of 70 μm. Significant grain refinement was observed on AA6061-T6 samples that underwent FSP. The equiaxed grains of the samples have less than 5.04 μm. More sub-grain boundaries were observed in FSPed samples as compared to AA6061-T6. During FSP, continuous strain coupled with rapid recovery and migration of sub-grain/grain boundaries resulted in continuous dynamic recrystallisation [170-172]. The processed material undergoes severe deformations from intense dislocation, and this stored energy leads to the dynamic recovery and recrystallisation process.

The average grain size from the EBSD analysis was tabulated in Table 4-1. Humphreys et al. [173] reported that dynamic recrystallisation is a strongly related to the flow stress and not the temperature during deformation. However, several studies have observed increasing grain sizes with increasing FSP temperature showing correlations in the 2 factors [113, 168, 174]. In the previous studies [5, 174], grain sizes were observed to be independent of the number of FSP passes using the same parameters. In this study, the processing parameters were kept constant throughout and hence, the flow stress and processing temperature were kept constant.

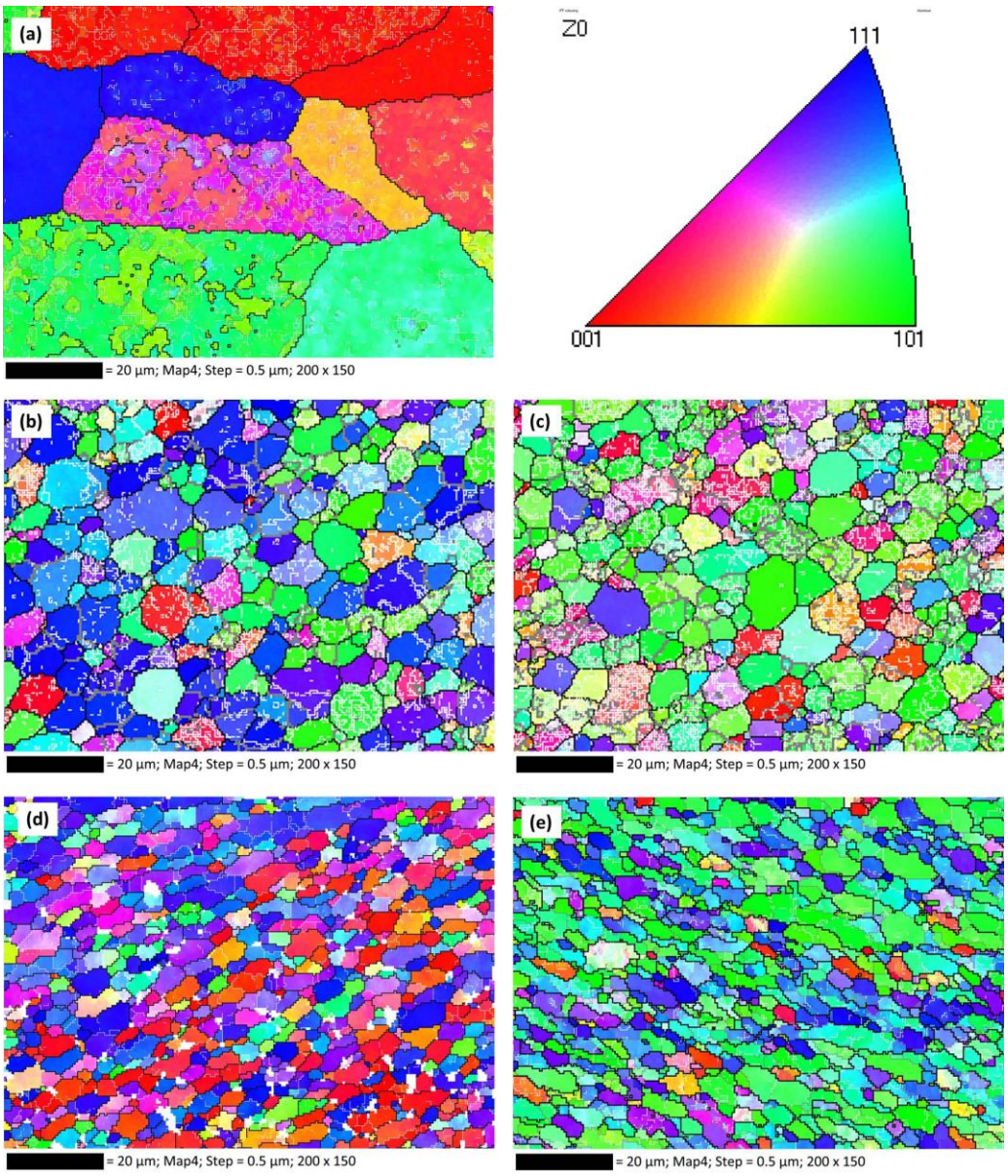

Figure 4-4 EBSD mapping showing grain structures of AA6061-T6 samples (a) as received, (b) 3 passes; (c) FSP Al-CNTs composite with 3 passes; (d) FSP Al-Al_2O_3 with 4 passes [5]; (e) FSP Al-Al_2O_3-CNTs with 3 passes. The scale bar indicates 20 µm. For the boundary misorientation: white lines: between 1° and 5°, grey lines: between 5° and 15°, black lines: >15°.

From Table 4-1, the addition of CNTs resulted in a slight decrease in the average grain size after FSP from 5.0 µm to 4.7 µm. However, significant grain refinement, from 5.0 µm to 2.5 µm, was observed with the used of nAl_2O_3. The

addition of both nAl_2O_3 and CNTs resulted in an average grain size of 3.1 μm. From the observation, less significant changes in the grain sizes were observed with the addition of CNTs. This could be due to the breaking down of CNTs during the intense deformation during FSP passes. As the welding conditions for the experimental set up were kept constant, the differences in the grain sizes for samples with and without the addition of reinforcements could only be attributed to the addition of reinforcements itself. Particle stimulated nucleation (PSN) have been reported to have occurred during FSP [2, 136, 175]. According to Humphreys et al. [173], particle stimulated dynamic recrystallisation occurs with the accumulation of dislocations at particles during deformation. In addition to that, PSN effect only happens when particles sizes are more than 1 μm with low processing temperature. In this study, the reinforcement particles are nano-sized while the processing temperature is quite high [176]. Therefore, it is unlikely for PSN to occur.

Zener pinning effect could have accounted for the finer grain sizes in the stir zone with nano-sized reinforcement particles by retarding the grain growth of the aluminium matrix. Rollett et al. [177] reported the rate of grain growth during the recrystallisation of metal with dispersed second phase particles could be described using equation (4-1).

$$\frac{dR}{dt} = M(P - P_z) = M\left(\frac{\alpha\gamma_b}{R} - \frac{3F_V\gamma_b}{2r}\right) \quad (4\text{-}1)$$

From the equation, F_v is the volume fraction, M is the boundary mobility, P is the driving pressure from the curvature of the grain boundaries, P_z is the Zener pinning pressure, R is the radius of the grain, r is the radius of the pinning particles, α is a small geometric constant and γ_b is the boundary energy.

Therefore, when $P=P_z$, grain growth stops.

$$\frac{\alpha\gamma_b}{R} = \frac{3F_V\gamma_b}{2r} \quad (4\text{-}2)$$

Thus, the Zener limiting grain size (α=1) can be obtained when the mean grain radius (D) and the radius of curvature (R) are taken to be the same.

$$D_z = \frac{4r}{3F_v} \tag{4-3}$$

At present work, $r = 0.16$ µm, $F_v = 0.11$, the theoretical $D_z = 1.9$ µm. The slightly larger grain size measured by the EBSD as due to a small amount of the reinforcement particles being extruded away as flash during FSP.

The EBSD analysis was performed to investigate the pinning effect caused by particles of the grain boundary further. The histogram of the measured boundary misorientations in the stir zone is shown in Figure 4-5. A detailed analysis of data is listed in Table 4-2 shows the mean boundary misorientation and number of high boundary angles (>15°) present. The interaction between the pinning particles and grain boundaries is very complicated. Tweed et al. [178] reported that the high-angle grain boundaries with high energy might have curved the boundary plane when in contact with a second phase inclusion resulting in the bypassing as a whole even before the boundary bent into a semi-circle. Perturbed planes are produced from low angle boundaries as it has lower energy and more flexibility. Thus, it could be the reason for the significant decrease in low-angle boundaries (<=15°) when Al_2O_3 were added.

However, with the addition of CNTs, a significant increase in the low angle boundary was observed in comparison to Al-Al_2O_3 samples. This could be because CNTs are very small in size and it causes interference and distortion in the strain during plastic deformation and dynamic recrystallisation resulting in low angle boundary grains.

Table 4-1 Average grain size values measured using EBSD technique [179].

Material and process	FSPed Al	Al-CNTs	Al-Al_2O_3	Al-Al_2O_3-CNTs
Average grain size (μm)	5.0±2	4.7±2	2.5±2	3.1±1

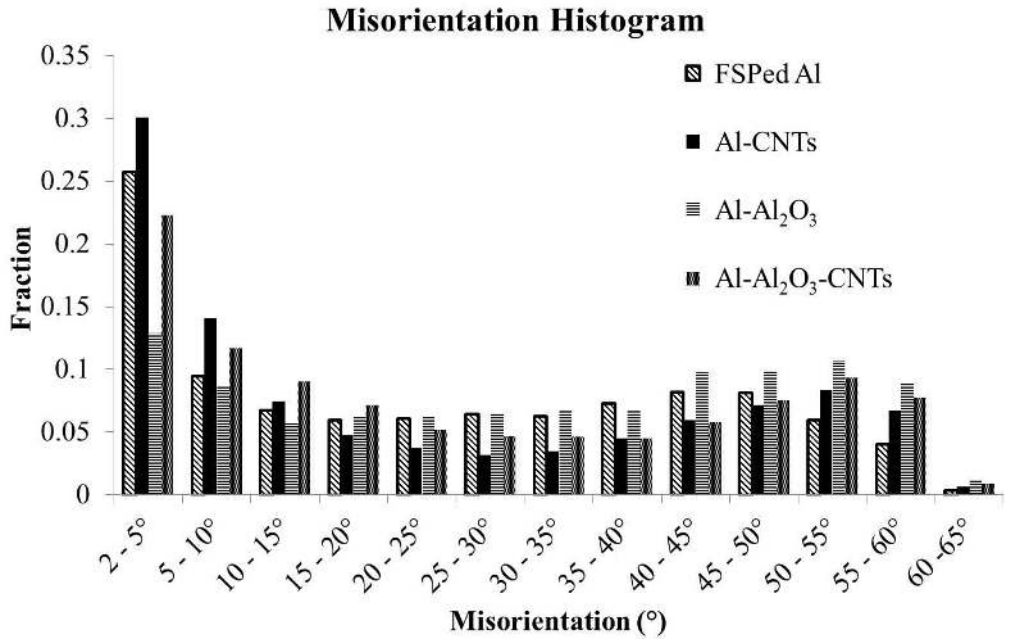

Figure 4-5 Distribution of grain/sub-grain misorientation angles for different FSPed materials.

Table 4-2 Summarized results of Grain/sub-grain boundary misorientations for various materials.

Material and process	Mean grain misorientation (°)	Fraction of high-angle grain boundaries (>15°)	Fraction of low angle grain boundaries (<=15°)		Number of grains sampled
			(1-5°)	(0-15°)	
FSPed Al	24.0	0.6	0.3	0.4	872
Al-CNTs	22.8	0.5	0.3	0.5	1002
Al-Al_2O_3	31.0	0.7	0.1	0.3	793
Al-Al_2O_3-CNTs	25.3	0.6	0.2	0.4	2079

4.3.3 Micro-hardness

The Vickers hardness values were measured on Al-Al_2O_3-CNTs and compared to the other samples from previous studies as showed in Table 4-3. The increase in hardness value of AA6061-O after FSP was believed to be mainly attributed to the grain refinement. The hardness values have increased further with the addition of reinforcement particles. There was a significant increase in the hardness values when both CNTs and Al_2O_3 were added to the matrix compared with FSP of AA6061 without reinforcement. It is believed that Orowan strengthening effect [5] is the main reason for the significant increase in values.

Table 4-3 Micro-hardness values of Al base metal and various composites produced by FSP.

Materials & process	AA6061-O	FSPed Al	Al-CNTs	Al- Al_2O_3	Al- Al_2O_3-CNTs
$HV_{0.05}$	55	66.2	90.6	103	108.4
standard deviation	2.2	0.7	0.9	0.8	0.6

4.3.4 Tensile Testing

The tensile test results were tabulated in Table 4-4. All friction stir processed materials exhibited inferior tensile properties compared to the peak aged AA6061-T6 alloy, while much better properties compared to the AA6061-O alloy. This is mainly attributed to dissolution and dissolvement of the Mg_2Si precipitates. It is assumed that all the friction stir processed materials in the study experienced very similar thermal cycles and thus have similar precipitation levels. The property difference should only be due to the addition of different particles. As shown in Table 4-4, the Al-Al_2O_3 specimens displayed a significant increase in ultimate strength and yield strength when compared to FSPed AA6061 specimens with 3 passes. The increase was believed to be mainly due to the Orowan effect [5]. For the samples with only CNTs added, there was a decrease in ultimate tensile and an increase in yield strength. It was believed that the main contributing factors were small CNTs clusters as well as the differences in the grain size, from the Hall-Petch equation [5].

$$\sigma_g = \sigma_0 + {}^{k}/_{\sqrt{d}} \tag{4-4}$$

Where σ_g is the yield strength, σ_0 is the original strength of the material/ friction stress (MPa), k is the Hall-Petch coefficient, constant for pure Al (74 MPa $\mu m^{1/2}$) while d is the average grain size (μm). The strengthening contribution from the addition of reinforcement particles could be calculated using

$$\sigma_{gd} = {}^{k}\Big/_{\sqrt{d_1}} - {}^{k}\Big/_{\sqrt{d_2}} \tag{4-5}$$

Where d_1 = 5.9 μm and d_2 = 3.1 μm are the diameters of the grain without and with reinforcement added respectively. Thus, the strengthening contribution from the refinement of grain, σ_{gd} = 13 MPa. However, this calculation assumes that the nAl_2O_3 were spherical and uniformly dispersed. The Orowan strengthening [3] could be calculated using

$$\sigma_o = \frac{Gb}{L-2r} \quad (4\text{-}6)$$

$$L = \left[\sqrt{\frac{\pi}{F_v} - 2}\right]\left(\sqrt{\frac{2}{3}}\right)r \quad (4\text{-}7)$$

Where σ is the material strength, G = 26.2 GPa is the shear modulus of the metal, b = 0.286 nm is the Burgers vector, Fv = 0.11 is the volume fraction of nanoparticles, L= 0.41μm is the spacing between the particles and r = 0.16 μm is the radius of the particles. The Orowan strengthening due to dispersed nanoparticles, σ_o = 30 MPa.

From the above calculations, the strengthening contribution is mainly attributed to the Orowan strengthening of the finely dispersed nanoparticles. However, the theoretical calculation can only be used as an indicative method to identify factor with a significant contribution as various assumption can never be true in reality.

For the samples with both Al_2O_3 and CNTs added as reinforcement, both the ultimate tensile strength and yield strength increased significantly. Comparing the results between Al-Al_2O_3 and Al-Al_2O_3-CNTs, the mean grain sizes are similar. Hence, the increase in tensile properties could only be attributed to the addition of CNTs. There is also a significant decrease in the elongation when comparing Al-Al_2O_3 and Al-Al_2O_3-CNTs. It may be because the CNTs clusters were broken down into smaller clusters and uniformly dispersed in the aluminium matrix which changed the crack propagations direction and enhancing the yield strength at a micro level as more energy will be required for yielding. It is believed that the dispersed CNTs also inhibited the occurrence of dislocation motion and deformation during tensile testing. This is observed with the significant reduction of the elongation. In the previous study, CNTs were present in the fracture sites indicating crack bridging [25]. The small clusters of CNTs might have acted as crack bridging points to prevent the sliding of grains along the boundary, holding them together [7]. However, the adhesion between aluminium and CNTs are not very good, and few studies studied Al-CNTs

composites that concluded poor adhesion and CNTs pull-outs were often observed at the fracture site [158, 180]. The adhesion between Al_2O_3 and aluminium is significantly better as compared to aluminium and CNTs. Having both Al_2O_3 and CNTs in the metal matrix composite increases the adhesion of the reinforcement and the aluminium substrate. Therefore, a significant improvement in strengths especially yield strength was observed.

As a light-weight material, Al-based composites are often used in elevated temperatures. The thermal stability of microstructure and high-temperature mechanical properties are believed to be improved significantly because of the pinning effect of particles. However, the investigation on this topic is out of the scope of the present study and will be carried out in the future work. It is to be noted that CNTs can be decomposed at temperatures higher than 530 °C [181], which should not be a problem for Al-based composites applications as their working temperatures are lower than 300 °C.

During FSP, the solutionizing and the dissolution of hardening precipitates could occur during FSP could have occurred to the AA6061 alloy. Post FSW ageing heat treatment was conducted in several studies [182-184] showing that it is possible to achieve extra strengthening with peak ageing.

In a study by Boonchouytan et al. [182], the microstructure of AA6061-T6 consists of α-Al globule with spheroidizing of Mg_2Si particles. After FSW, the stir zone contained fine structure with uniformly dispersed Mg2Si. Post weld T6 was performed with solution treatment at 530 ºC for 1 hour, quenched and artificially aged at 185 ºC for 6 hours. However, cracks were observed in the stir zone after post weld T6 heat treatment. In another study by K.N. Krishnan [183], FSW samples of AA6061 were solution heat treated at 520ºC for an hour, quenched and aged at 175ºC for 8 hours. After post weld heat ageing, grain coarsening were observed in the weld. The hardness was improved (100 HV). When bend test was conducted, as-welded and aged samples passed the 180º bend. In another study by Sato et al. [184], FSW was conducted on AA6063. The

artificial post-weld ageing was performed at 448K (175ºC) for 12 hours. It was observed that the tensile strength and hardness were recovered to that of the base material. However, recovery of the ductility was partial.

Table 4-4 Tensile Properties of Al base metal and various composites produced by FSP.

Types of tensile coupons tested	Ultimate tensile strength (MPa)	Yield strength (MPa)	Elongation (%)
As-received AA6061-O*	125	55	25
As-received AA6061-T6*	310	276	12
FSPed Al	193±3	95±4	18±2
Al-CNTs	178±28	112±2	10±5
Al-Al_2O_3 [5]	228±2	111±2	24±1
Al-Al_2O_3-CNTs	236±3	163±4	4±1

*Tensile property values for AA6061-O and AA6061-T6 base metal are from ASM Handbook [54].

4.3.5 Fractography

The fracture sites of the tensile tested samples were examined under FESEM as shown in Figure 4-6. For FSPed Al (Figure 4-6a), large dimples were observed. The failure of FSPed Al is believed to occur at the triple junctions or subgrain/ grain boundaries with void initiations and followed by rotation/ sliding, leading to either trans-granular or inter-granular cracks. These voids may then propagate along the weakest path, e.g. neighbouring grain/subgrain boundaries and started joining to form large ones [5]. For Al-CNTs composite, as shown in Figure 4-6b, the fracture surface looks like neither typical ductile nor typical brittle fracture

mode. A large number of pull-outs of CNTs threads can be observed, which made the fracture mode quite unique.

The fracture sites for samples Al-Al_2O_3 (Figure 4-6c) and Al-Al_2O_3-CNTs (Figure 4-6d) were relatively similar. It is observed that the Al_2O_3 particles can always be found at the bottom of the dimples, which is in agreement that the Al/ Al_2O_3 interfaces are the void initiation regions. It is unlikely for the small voids to join up to form a more prominent crack as there is a significant amount of finely dispersed nano-Al_2O_3 particles which will act as pinning points and change the direction of the route of crack propagation [5]. This is believed to have increased the yield strength of the composites. The significant increase in the yield strength of Al-Al_2O_3-CNTs is believed to be related to the CNTs pull-out mechanism at sub-micron scale inside/around the Al_2O_3 dominated fracture dimples. On closer observation, the dimples created in Al-Al_2O_3-CNTs (Figure 4-6d) are relatively shallower than Al-Al_2O_3 samples (Figure 4-6c) which resulted in the significant reduction of the elongation of the Al-Al_2O_3-CNTs composite. As discussed previously in the 'Tensile Testing' section, the added CNTs may have changed the crack propagations direction and enhancing yield strength. However, the CNTs may also have interrupted the dislocation movement during tensile test and led to lower elongation.

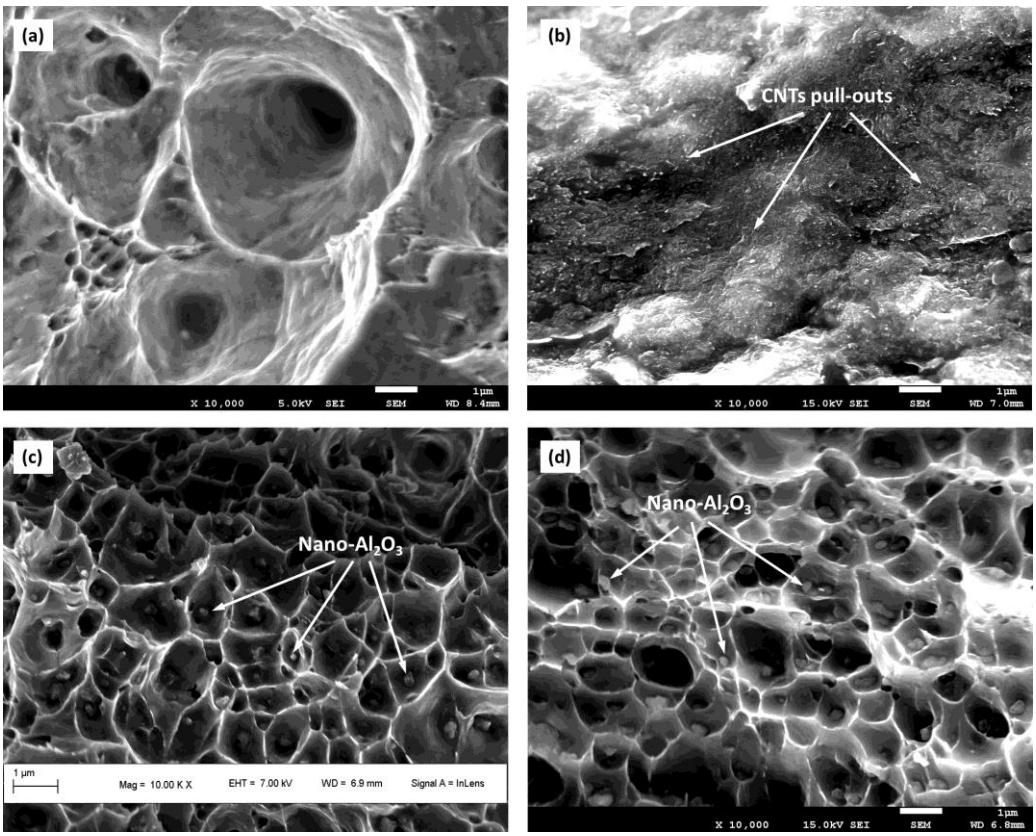

Figure 4-6 FESEM images of the fracture sites of FSPed (a) AA6061 (b) Al-CNTs (c) Al-Al_2O_3 and (d) Al-Al_2O_3-CNTs.

4.4 Conclusions

A new Al-based nano-composite reinforced with uniformly dispersed Al_2O_3 and CNTs have been successfully fabricated using FSP. The effects of having multiple types of nano-particles reinforcements on the mechanical behaviour and microstructure evolution in the friction stir processed Al matrix were studied and summarised as below.

a. Grain refinement can be observed in friction stir processing with/ without the addition of nano-sized reinforcement particles. The presence of nano-sized reinforcement led to more pronounced grain refinement as pinning effect of the nano-particles have retarded the grain growth rate in the dynamic recrystallisation process.

b. The micro-hardness and tensile strengths were increased significantly through the addition of Al_2O_3 and CNTs nanoparticles. In particular, the yield strength of the composites increased 70% compared with that of FSPed Al when both Al_2O_3 and CNTs were added in the matrix.
c. For both Al-Al_2O_3 and Al-Al_2O_3-CNTs composites, Al_2O_3 particles can always be found at the bottom of the dimples on the fracture surfaces, suggesting void initiation at the Al/ Al_2O_3 interfaces regions. The significant increase in the yield strength of Al-Al_2O_3-CNTs is believed to be related to the CNTs pull-out mechanism at sub-micron scale inside/around the Al_2O_3 dominated fracture dimples. Shallower dimples were observed on the fracture surface for composite with the addition of Al_2O_3 and CNTs, which led to significant reduction of elongation.
d. Multiple reinforcements with different shapes can be an effective method to increase the tensile strengths, especially yield strength of metal matrix composites.

CHAPTER 5

Selective Laser Melting Printed AlSi$_{10}$Mg Composites

This chapter studies the selective laser melting (SLM) of rectangular aluminium composite blocks fabricated via selective laser melting process. The microstructure and mechanical properties were examined and recorded.

5.1 Introduction

Aluminium metal matrix composites (AMCs) have attracted the attention of various industries, such as aerospace, automobile and defence, due to its superior wear resistance, stiffness and elastic modulus properties [185-187]. Significant enhancement in strength could be achieved with the addition of small concentration of reinforcement particles by preventing dislocation movements [3, 5, 179]. Al_2O_3, SiC, B_4C, TiC and TiO_2 are among the few reinforcements considered as suitable candidates for AMCs [188]. Mainly, nano-sized alumina (nAl_2O_3) is widely used in comparison to other reinforcements due to its ability to improve high-temperature properties and wear behaviour without the formation of undesirable brittle intermetallic phases [189]. Fabrication of customised components for aerospace and automotive applications have been challenging via the use of traditional manufacturing techniques.

In recent years, additive manufacturing (AM) techniques have attracted much research attention due to its ability to fabricate customised parts with complex geometry and superior mechanical properties [190-194]. Among the AM techniques, the selective laser melting (SLM) is widely used in the research and fabrication of complex metallic components. Therefore, exploration on the possibility of fabricating advanced aluminium nano-composites should be carried out.

The SLM fabricates metal components by using a laser beam to melt metal powder in a layerwise matter. The layerwise production together with the use of computer-aided design (CAD) allows the fabrication customisable components accurately with excellent mechanical properties [195]. Recently, studies have also directed their attention towards the visibility of fabricating of aluminium composites using selective laser melting [13, 56-58]. Dadbakhsh et al. [58] studied in situ fabrication of Al/ 15% wt. Fe_2O_3 using SLM and observed the improvement in hardness due to the formation of the very fine dendritic matrix. Gu et al. [56] reported densification behaviour of SLM fabricated $AlSi_{10}Mg$/ 5% wt. TiC nanocomposites with varied laser energy density. In their study, high laser energy input (200W) was used to melt the reinforcement materials fully. It was reported that uniformly distributed ring-structured nano-sized TiC reinforcements resulted in significant improvement in both tensile strength and micro-hardness. Han et al. [57] reported the addition of uniformly distributed 4% vol. of nano-sized alumina (nAl_2O_3) had resulted in the improvement in the yield strength and micro-hardness properties of SLM fabricated pure Al composites by improving dislocation density via introducing more grain boundaries. However, the poor wettability of SLM of Al-Al_2O_3 composites also contributed to porosity and microcracks defects during fabrication. Recently, $AlSi_{10}Mg$ powder has been commercially available for SLM fabrication of aluminium alloy parts [82, 196, 197]. The fluidity of the molten aluminium was improved through the addition of high Si content [54].

To the best of this authors' knowledge, the use of commercially available $AlSi_{10}Mg$ reinforced with nAl_2O_3 in SLM fabrication is limited. Therefore, this study aims to investigate the densification process, microstructure evolution, as well as mechanical properties of $AlSi_{10}Mg$, reinforced with nAl_2O_3 fabricated via SLM.

5.2 Experimental Details

In this study, gas atomised aluminium powders, $AlSi_{10}Mg$, with the normally distributed size of 20 µm to 63 µm by TLS Technik GmbH & Co., Germany, was used as the matrix material. The reinforcement particles used was nAl_2O_3 powder, Sumitomo, Japan, with a nominal diameter of 320 nm. The powder was examined under the field emission scanning electron microscope (FESEM) as shown in Figure 5-1. $AlSi_{10}Mg$ and nAl_2O_3 were ball milled together in a volatile solvent with a ball to powder ratio of 1:1 [56] to prevent the $AlSi_{10}Mg$ powder from deforming. Deformed powders lead to a reduction of powder flowability and uneven spread of powder layer during dispensing. The blended slurry was then air dried. The dried powder was further dried using a vacuum oven for 8 hours. In this study, $AlSi_{10}Mg$ – 2% wt. nAl_2O_3 and $AlSi_{10}Mg$ – 5% wt. nAl_2O_3 powders were used. The SLM 250 ^{HL}, SLM Solutions GmbH, with 80 µm laser standing spot size was used to scan the cross section and melt the powders at each layer. Dry argon gas was used to bring the oxygen level in the build chamber down to 0.2% before fabrication. Test cubes measuring 8 mm by 8 mm by 8mm [57] were fabricated using layer thickness of 0.05 mm, the laser power of 350 Watts, scanning speed ranging from 100 mm/ seconds to 1500 mm/ seconds and hatch spacing ranging from 0.1 mm to 0.2 mm [198]. Chessboard/ island laser scanning strategy with 67° rotation for every layer was used to distribute the heat across the fabricated part evenly as well as to reduce residual stresses from the process [199]. Nickel et al. [74] reported that spiral pattern scanning from the outer boundaries in an inward manner results in lesser deflection of SLM fabricated plates. Therefore, in this study, chess board laser scanning strategy was applied together with spiral inwards during fabrication.

Micro CT scan was performed on the test cubes using Skyscan 1173 X-ray Microtomography, Brunker Co., Belgium. The scan was conducted with 93 kV and 77 µA. A full rotation scan was performed with an average of five frames, resolution of 6 µm and rotation step size of 0.40 degrees. The images were processed using NRecon software to calculate the relative density of the samples.

Rectangular blocks measuring 90 mm by 60 mm by 10 mm were further fabricated for the mechanical test.

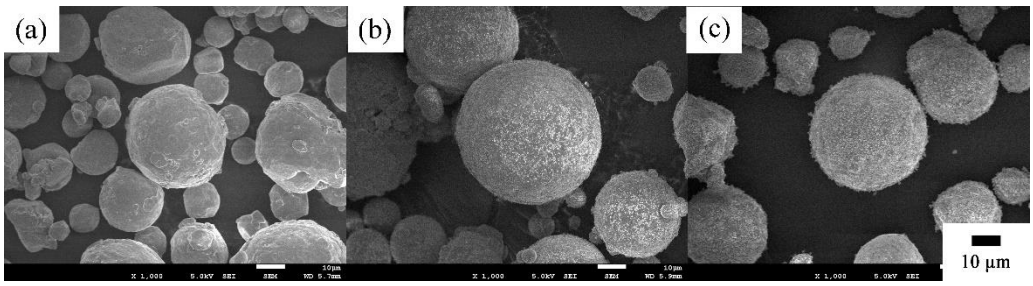

Figure 5-1 FESEM images of gas atomised $AlSi_{10}Mg$ powder (a) as-received, (b) with 2% wt. nAl_2O_3, (c) 5 % wt. nAl_2O_3.

Metallographic samples were taken from the cross-section of fabricated rectangular blocks and polished mechanically using conventional steps. Material characterisation and mechanical properties were evaluated as mentioned in Chapter 3.

5.3 Results and Discussions

5.3.1 Parameter Selection

Porosity defect is a crucial concern when it comes to SLM fabrication. The presence of defects often results in the reduction of mechanical properties. Gu et al. [56] reported densification behaviour of SLM fabricated $AlSi_{10}Mg$/ 5% wt. TiC nanocomposites with varied laser energy density. Near fully dense nanocomposite components were fabricated with increasing applied laser energy density. The volumetric energy density (VED) is defined as:

$$VED = \frac{P}{S.T.H} \tag{5-1}$$

Where VED is volumetric energy density in Joules/ mm^3, P is the laser power in Watts, S is the scanning speed in mm/s, T is the layer thickness in mm and H is the hatch spacing in mm.

Test cubes measuring 8 mm by 8 mm by 8 mm were fabricated via SLM (Figure 5-2). The relative densities of the test cubes were collected from the Micro CT scanner. From the Micro CT results, fully dense $AlSi_{10}Mg$ parts can be fabricated using SLM with VED ranging from 35 Joules/ mm^3 to 150 Joules/ mm^3. The use of VED outside this window increased porosity. The addition of 2 wt. % of nAl_2O_3 resulted in a higher VED (109 Joules/ mm^3 to 175 Joules/ mm^3) required to produce dense parts. This could be attributed to the nAl_2O_3 acting as an insulating layer surrounding the powder, absorbing part of the laser energy. Therefore, higher laser energy is required to melt the ceramic reinforcements.

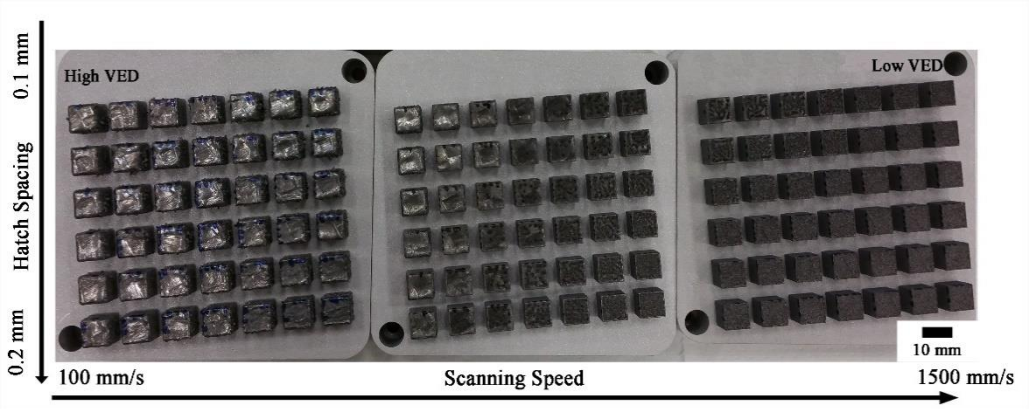

Figure 5-2 Image of test cubes fabricated using SLM of $AlSi_{10}Mg$ - 2% wt. nAl_2O_3.

The porosities were studied using the optical microscope of the etched samples (Figure 5-3). Small circular porosities (Figure 5-3a) were observed in samples with high VED while irregularly shaped porosities were observed from samples with low VED (Figure 5-3b).

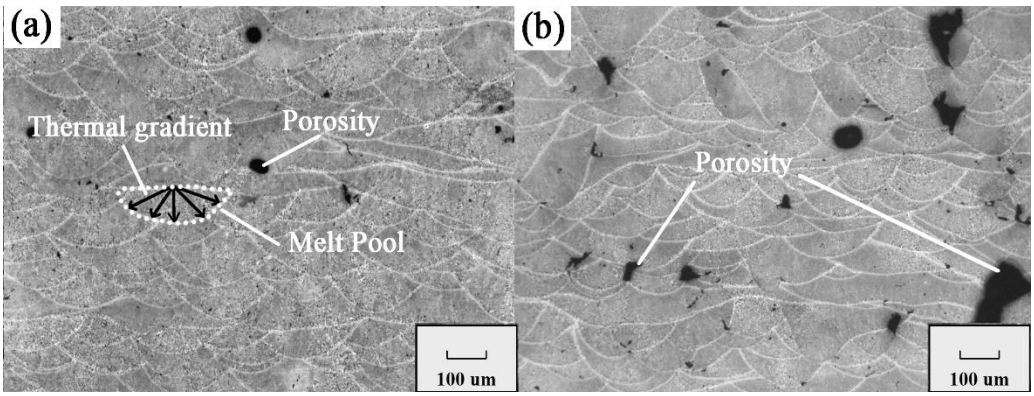

Figure 5-3 Optical microscope images showing the cross-sectional view of etched SLM of $AlSi_{10}Mg$ with (a) high VED and (b) low VED showing several porosities and thermal gradient in a melt pool (black arrow).

When the SLM laser scans the powder bed with low VED, a cylindrical shape continuous liquid melt track is formed. The surface energy of the liquid increases as the laser moves away. This resulted in the breaking up of the cylindrical melt track, forming several agglomerated spheres [56]. Such phenomenon is known as the balling effect. The formation of poor inter-line bonding property or discontinuous scan tracks occurs on adjacent melt tracks. Moreover, the addition of nAl_2O_3 reinforcement particles reduces the overall rheological and melt flow performance of the composite as the melt viscosity increases [56]. Reduction in the wettability was observed with lower VED as limited SLM temperature elevates the viscosity of the melt pool [200].

On the other hand, when VED exceeds the critical threshold, the temperature gradient across the surface between the centre and the edge of the melt pool becomes too great. Marangoni convection and surface tension gradient are formed. The Marangoni convection causes the melt to flow radially outwards from the centre of the melt pool [61, 201]. The unstable melt track eventually disintegrates into agglomerated spheres

In addition, the vaporisation of aluminium could also result in the formation of pores. The formation of ionised metal vapour (plasma plume) was observed to exert a recoil pressure on evaporated molten metal within the cavity of the melt

pool [62]. The droplet then expelled upwards from the melt pool in the form of spatters [63]. The spattering phenomenon was further studied by Qiu et al. [64] through the use of the high-speed camera as well as simulation modelling. The melt splashing was caused by both the Marangoni effect and the recoil pressure during the metal vapour expansion. The increase in VED resulted in higher melt splashing during SLM process resulting in unstable melt flow and formation of porosity of the material [65].

During the SLM process, argon gas circulation within the build chamber was designed to enter from the right and exit on the left. This resulted in the spatter being carried to the left by the argon gas. The spattered material that was ejected solidified in the atmosphere and was observed to have oxidised during flight [66]. The relatively larger spattered particles would then land on the fabricated layer. Upon dispensing the next layer of powder, some of the spatter could have been pushed away by the dispensing mechanism while remaining spatters contaminate the next layer of powder. It was observed that samples with higher porosity, exhibiting lower tensile strength, were fabricated when samples were located nearer to the argon gas outlet due to the higher amount of spatter landing and accumulating at the left region [66]. From the above preliminary experiment, the following parameters (Table 5-1) were selected for the fabrication of large blocks to examine its mechanical properties.

Table 5-1 Parameters used for fabricating rectangular block for various AMCs.

Material process and Composition	Laser scanning speed (mm/s)	Hatch spacing (mm)	VED (Joules / mm^3)	Relative porosity (%)
SLM of $AlSi_{10}Mg$ with low VED	1500	0.20	23.33	2.05 ± 0.12
SLM of $AlSi_{10}Mg$ – 2% wt. nAl_2O_3 with low VED	1500	0.20	23.33	5.90 ± 0.24
SLM of $AlSi_{10}Mg$ – 5% wt. nAl_2O_3 with low VED	1500	0.20	23.33	10.09 ± 0.37
SLM of $AlSi_{10}Mg$ with high VED	1150	0.17	35.81	0.05 ± 0.01
SLM of $AlSi_{10}Mg$ – 2% wt. nAl_2O_3 with high VED	400	0.16	109.38	0.13 ± 0.05
SLM of $AlSi_{10}Mg$ – 5% wt. nAl_2O_3 with high VED	100	0.12	583.33	0.36 ± 0.12

5.3.2 X-ray Diffraction Analysis

The X-ray diffraction (XRD) results were plotted in Figure 5-4. From the XRD patterns, it was observed that the Si peaks of samples from SLM of $AlSi_{10}Mg$ - 2% and 5% wt. nAl_2O_3 with high VED (Figure 5-4c and e) have higher intensities as compared to rest of the SLM samples. This indicated a significant decrease in the solid solubility of Si in the aluminium matrix due to higher VED used. Li et al. [85] reported an increase in Si peak intensity after heat treatment of SLM fabricated $AlSi_{10}Mg$. Also, the intensity of Mg_2Si peaks was also observed to have increased after heat treatment. The Si-rich particles being precipitated out formed Mg_2Si through the reaction with Mg present in the aluminium matrix. From the results gathered, only significant increase in Si and Mg_2Si peaks were observed in SLM of $AlSi_{10}Mg$ - 2% wt. nAl_2O_3 with high VED and SLM of $AlSi_{10}Mg$ - 5% wt. nAl_2O_3 with high VED (Figure 5-4c and e). This could be due

to the higher VED used in the process resulting in lower cooling rate and more Si being precipitated out.

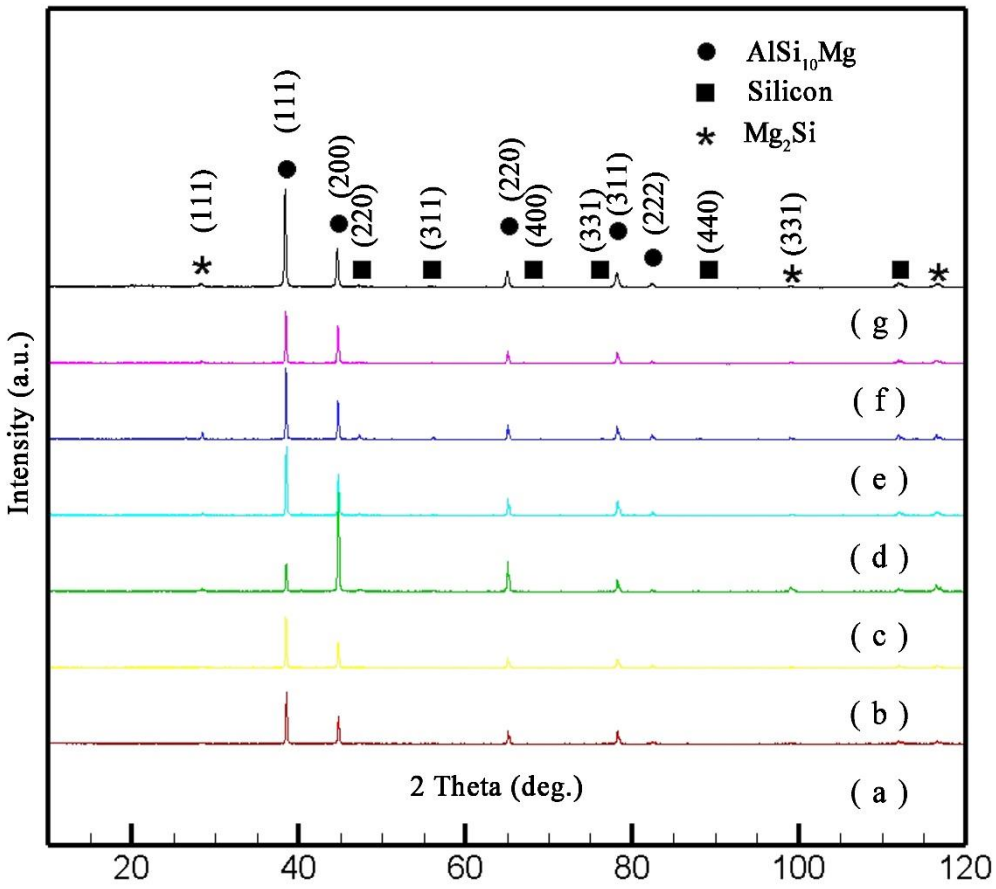

Figure 5-4 XRD pattern of (a) SLM of $AlSi_{10}Mg$ with high VED, (b) SLM of $AlSi_{10}Mg$ with low VED, (c) SLM of $AlSi_{10}Mg$ - 2% wt. nAl_2O_3 with high VED, (d) SLM of $AlSi_{10}Mg$ - 2% wt. nAl_2O_3 with low VED, (e) SLM of $AlSi_{10}Mg$ - 5% wt. nAl_2O_3 with high VED, (f) SLM of $AlSi_{10}Mg$ - 5% wt. nAl_2O_3 with low VED and (g) as-received gas atomised $AlSi_{10}Mg$ powder.

5.3.3 Energy Dispersive Spectroscopy (EDS)

From the energy dispersive spectroscopy (EDS) results with high VED, a significant increase in detection of Si was observed in SLM of $AlSi_{10}Mg$ - 2%

wt. nAl_2O_3 and SLM of $AlSi_{10}Mg$ - 5% wt. nAl_2O_3 (Figure 5-6) as compared to SLM of $AlSi_{10}Mg$ (Figure 5-5). This agrees with the XRD results mentioned earlier indicating Si being precipitated out due to higher VED used for the process. Higher oxygen levels were also detected indicating the presence of nAl_2O_3 in the matrix.

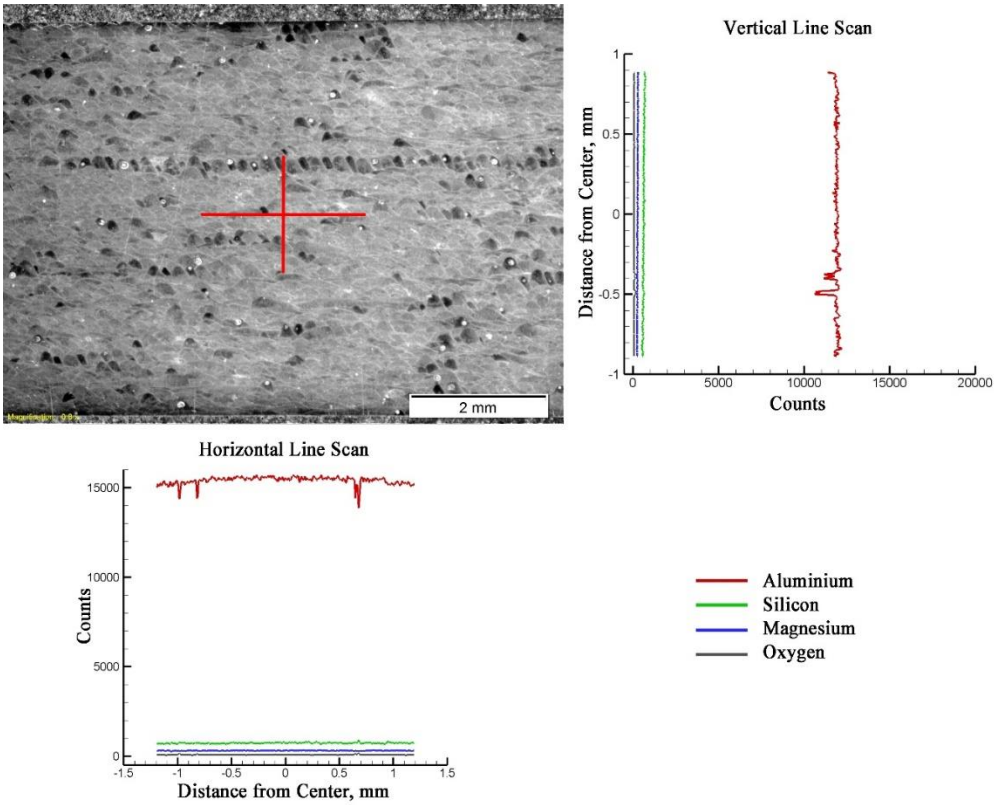

Figure 5-5 EDS scan line across SLM of $AlSi_{10}Mg$ with high VED.

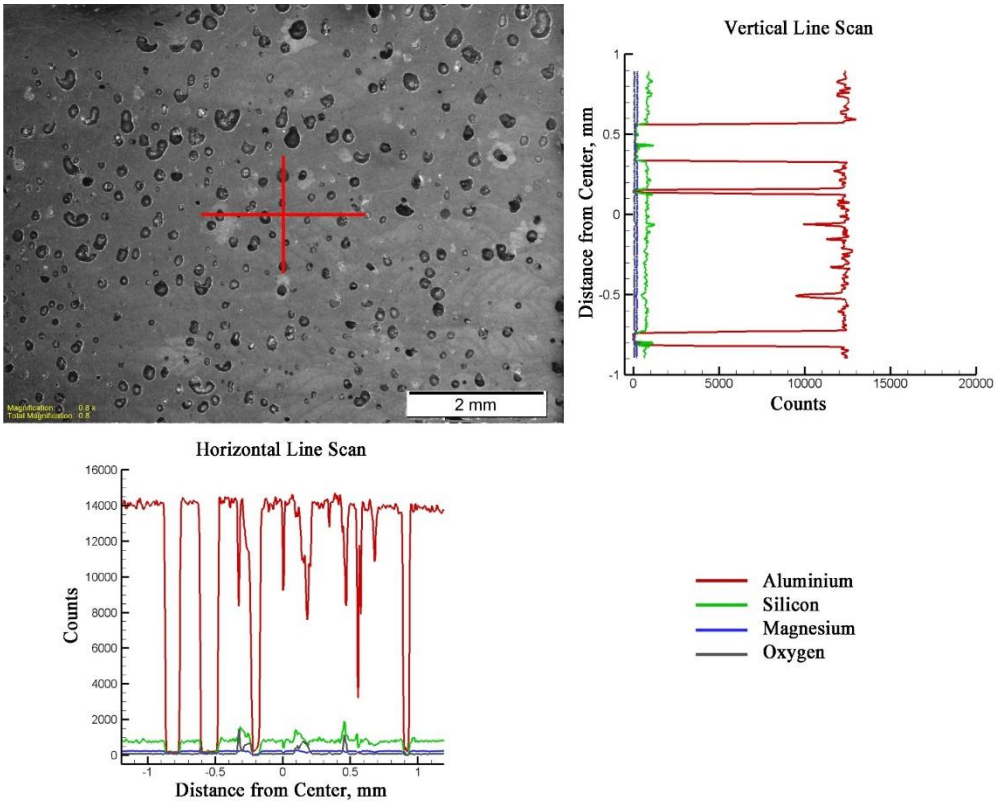

Figure 5-6 EDS scan line across SLM of AlSi$_{10}$Mg - 5% wt. nAl$_2$O$_3$ with high VED.

5.3.4 Porosity Analysis

Micro CT scan was performed on the fabricated samples (Figure 5-7) (Appendix B), and the relative porosity was tabulated as shown in (Table 5-2).

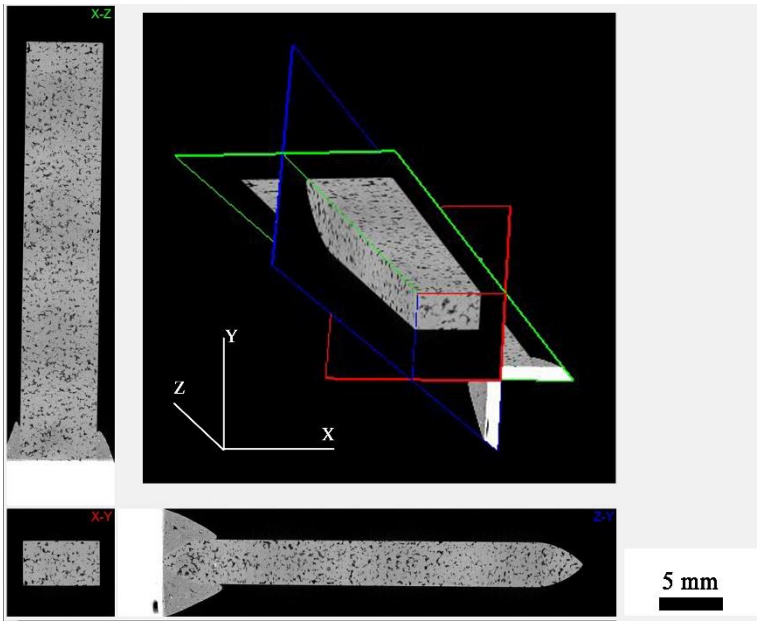

Figure 5-7 Micro CT scan of SLM of $AlSi_{10}Mg$ - 2% wt. nAl_2O_3 with low VED.

Table 5-2 Relative porosity of various $AlSi_{10}Mg$ and its composites.

Material and processes	Relative porosity (%)	
	Test cubes	Rectangular blocks
SLM of $AlSi_{10}Mg$ with low VED	2.05 ± 0.12	2.22 ± 0.12
SLM of $AlSi_{10}Mg$ - 2% wt. nAl_2O_3 with low VED	5.90 ± 0.24	9.38 ± 0.12
SLM of $AlSi_{10}Mg$ - 5% wt. nAl_2O_3 with low VED	10.09 ± 0.37	11.78 ± 0.62
SLM of $AlSi_{10}Mg$ with high VED	0.05 ± 0.01	0.16 ± 0.03
SLM of $AlSi_{10}Mg$ - 2% wt. nAl_2O_3 with high VED	0.13 ± 0.05	0.17 ± 0.06
SLM of $AlSi_{10}Mg$ - 5% wt. nAl_2O_3 with high VED	0.36 ± 0.12	18.83 ± 0.52

From Table 5-2, increase in porosity was observed in the fabrication of rectangular blocks. This could be attributed to many factors during the SLM process. A significant difference in the porosity was observed with high VED especially for SLM of $AlSi_{10}Mg$ - 5% wt. nAl_2O_3 with high VED. Firstly, the surface area to volume ratio of the test cube is significantly larger than that of the

fabricated rectangular blocks. Moreover, the presence of a significant amount of nAl_2O_3 further reduced the thermal conductivity of the part as well as the reduction of the wettability of the molten liquid as discussed earlier. Secondly, the poor thermal conductivity and higher temperature at the top surface increased spatter, fumes and ionic plasma generation during SLM process. Thus, increasing the formation of porosity via Marangoni effect and recoil pressure. Lastly, the fabrication of large parts with high VED requires much longer fabrication process time. During which, the high amount of aluminium vapour generated condenses on the laser protective glass and accumulates over time. This resulted in the degrading of the fabricated part over time. Hence, resulting in the significant difference in the porosity for high VED samples.

5.3.5 Microstructure

The FESEM image of the samples was examined in (Figure 5-8). From the images, Si enriched boundaries (approx. 0.1 µm) were observed within the melt pools which were formed when the laser melts the $AlSi_{10}Mg$ powders (Figure 5-8b). This could be due to the rapid melting and solidification process during SLM. During SLM, the powders were melted as it absorbs the energy from the laser beam. It then solidifies when the laser travels away from it. The grains then grew along the thermal gradient, as solidification takes place from the edge of the melt pool to the centre (Figure 5-3a) [13, 49, 85]. Upon closer observation, significant larger Si-rich particles were observed in samples with higher VED (approx. 0.2 µm) (Figure 5-8a). The growth in the Si-rich particles could be due to Ostwald ripening and coalescence of small neighbouring Si-rich particles when higher SLM temperature from higher VED was used [85].

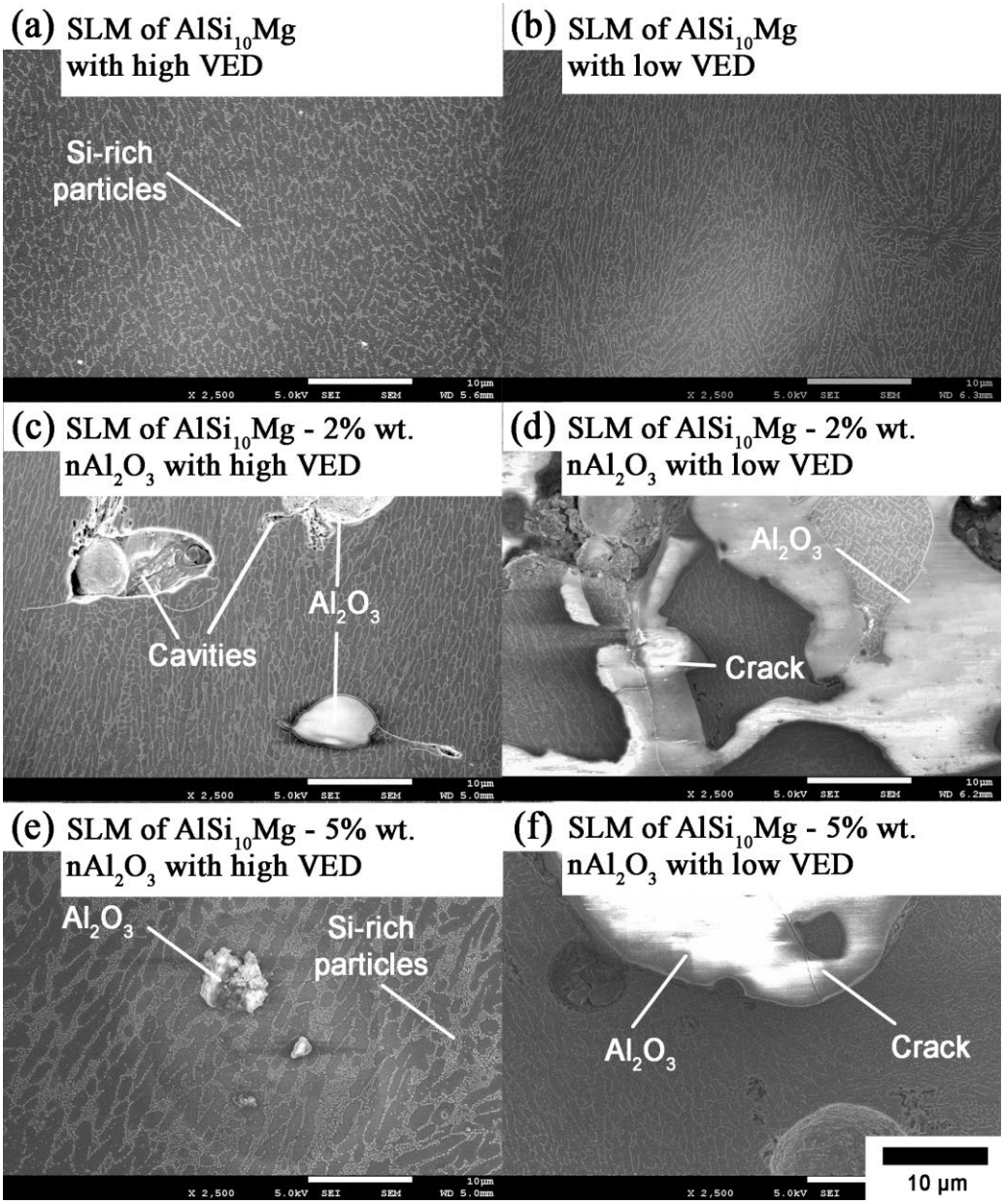

Figure 5-8 FESEM images showing the microstructure of SLM fabricated samples.

For samples with the addition of nAl_2O_3 particles (Figure 5-8c, d, e and f), some of the nAl_2O_3 appeared to have agglomerated during the SLM process. Han et al. [57] simulated the thermal performance of SLM of aluminium and observed that using laser power of 200 Watts with scanning speed of 200 mm/s was able to result in melt pool temperature reaching the melting pointing of alumina

(2040 °C). In this study, SLM was performed using laser power of 350 Watts. It is highly likely that the higher energy input resulted in the melting/ partial melting of some of nAl_2O_3 as observed in Figure 5-8 c, d, e and f. The agglomeration of nAl_2O_3 could have been aided by the migration behaviour of particles in the melt track. Depending on the interaction between the reinforcement particle and the advancing solid-liquid interface, the reinforcement particles could be either pushed or trapped [202, 203]. It was believed that particles were rejected by the interface at scanning velocities below a critical value while trapped in the solid at higher scanning velocities. At the lower scanning velocities, the low solidification process results in particles being rejected and pushed ahead into the liquid by moving along the solid-liquid interface. Therefore, particles could be pushed over long distances measuring over orders of centimetres [70]. This results in the large pile-up of reinforcement particles normal to the interface and isolated along the grain boundaries after solidification. When the solidification rate increases, the reinforcements were trapped in the incorporated solids. In this study, it is believed that pushing phenomenon took place as the laser scans across the melt track. Towards the end of the melt track, trapping occurred resulting in the relatively larger melted nAl_2O_3 being trapped (Figure 5-8d and f).

Cracks were observed in melted nAl_2O_3 in SLM of $AlSi_{10}Mg$ - 2% wt. nAl_2O_3 with low VED and SLM of $AlSi_{10}Mg$ - 5% wt. nAl_2O_3 with low VED samples. The use of high scanning speed in low VED process could have resulted in relatively lower melt pool temperature and rapid solidification. These could have resulted in shrinkage and thermal cracks in the nAl_2O_3. These led to the formation of small cavities at the edge of the nAl_2O_3 and weak interface bonding (Figure 5-8d and f). Upon increasing the VED, improvement in the particle-matrix interface was improved (Figure 5-8b). This is also confirmed in studies conducted on SLM of pure Al reinforced with Al_2O_3 [57, 70].

For SLM of $AlSi_{10}Mg$ - 2% wt. nAl_2O_3 with high VED (Figure 5-8c), small agglomeration of nAl_2O_3 was observed resulting from the higher VED used in

the process. Laurent et al. [204] suggested that an increase in the experiment temperature aided in the deoxidation process which erodes the oxide film. This resulted in the decrease in the contact angle and improved the wettability between the nAl_2O_3 and the molten Al. Moreover, at high VED, elevated melt pool temperature reduced the dynamic viscosity of the molten pool resulting in powerful Marangoni convection constantly acting on the oxides. For SLM of $AlSi_{10}Mg$ - 5% wt. nAl_2O_3 with high VED (Figure 5-8e), the use of very high VED (583.33 Joules/ mm^3) could have resulted in higher Marangoni and recoil pressure which caused some if the nAl_2O_3 to be ejected as spatters, leaving behind small agglomerated nAl_2O_3.

5.3.6 Grain Structure Evolution

EBSD was performed on the all the samples fabricated by SLM (Figure 5-9) while the average grain width was collected and tabulated in Table 5-3. From the mapping, SLM samples showed columnar grains along the thermal gradient as mentioned previously.

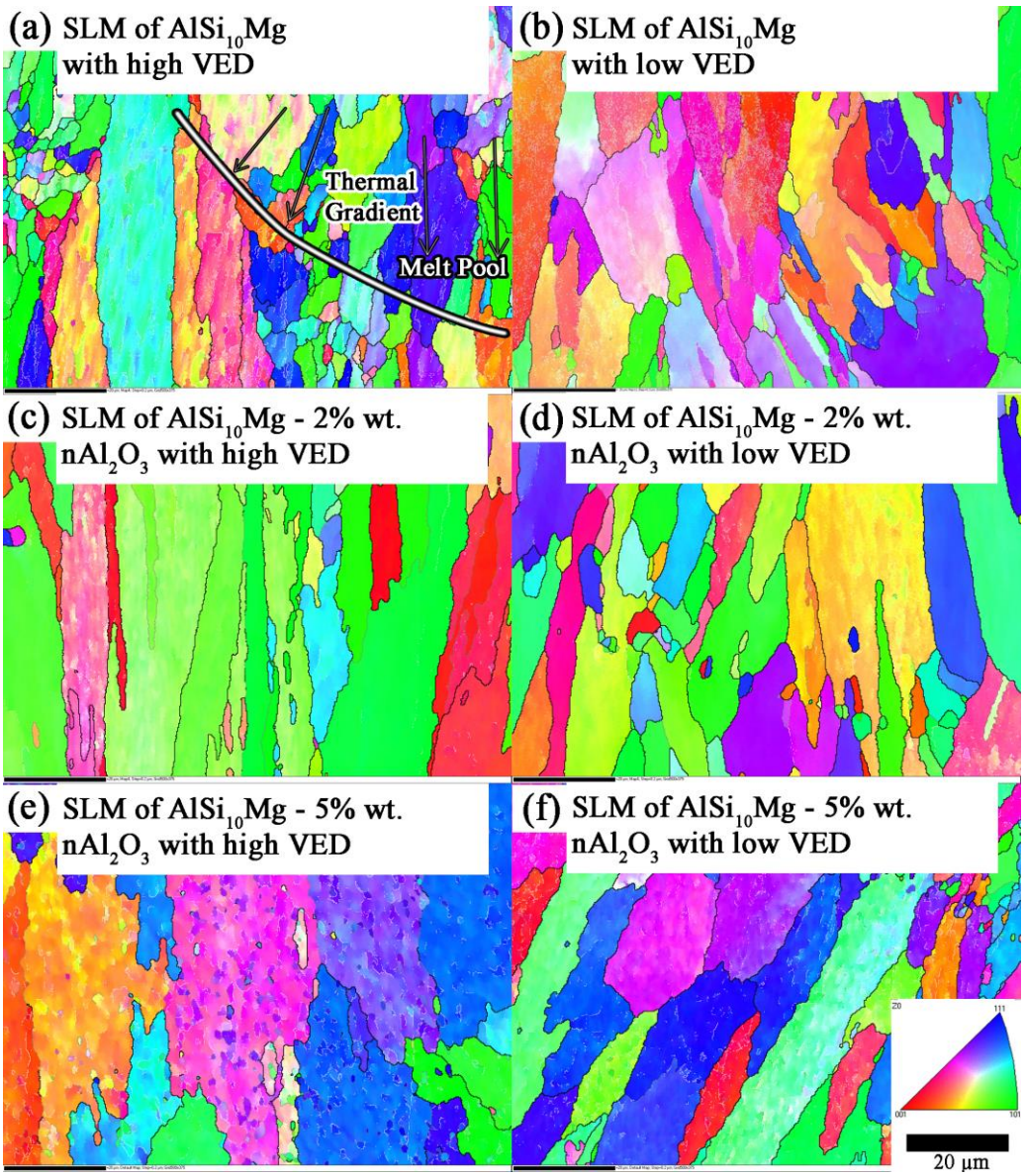

Figure 5-9 EBSD mapping of SLM of $AlSi_{10}Mg$ and its composites. The scale bar indicates 20 µm while the boundary misorientations are indicated with white lines, grey lines and black lines for angles 1° to 5°, 5° to 15° and greater than 15°.

Table 5-3 Average grain width results of various $AlSi_{10}Mg$ and its composites.

Material and processes	Average grain width (μm)
SLM of $AlSi_{10}Mg$ with low VED	7.4 ± 2
SLM of $AlSi_{10}Mg$ with high VED	8.2 ± 2
SLM of $AlSi_{10}Mg$ - 2% wt. nAl_2O_3 with low VED	6.4 ± 2
SLM of $AlSi_{10}Mg$ - 2% wt. nAl_2O_3 with high VED	7.4 ± 2
SLM of $AlSi_{10}Mg$ - 5% wt. nAl_2O_3 with low VED	5.8 ± 2
SLM of $AlSi_{10}Mg$ - 5% wt. nAl_2O_3 with high VED	6.3 ± 2

From Table 5-3, looking at samples with low VED, a significant decrease in the average grain width were observed with increasing addition of nAl_2O_3. This could be mainly attributed to the addition of nAl_2O_3 as the fabrication parameters were the same. The presence of nano-sized Si-rich and remaining nano-sized nAl_2O_3 particles in the matrix could have contributed to finer grains via Zener pinning effect [205]. For samples with high VED, relatively larger grain widths were observed in comparison with samples with low VED of the same composition. This is mainly attributed to the use of higher energy input and relatively slower solidification rate which encourages grain growth.

Thijs et al. [51] reported controllable texture in SLM fabricated $AlSi_{10}Mg$. It was reported that the texture of <001> is attributed to the radial heat dissipation and epitaxial growth. However, the texture becomes weaker with the use of island scanning strategy as well as rotating the scanning directions between layers, making it more isotropy. This agrees with the EBSD results as a strong texture in the EBSD maps were not observed.

The grain boundaries were further investigated using the misorientation profile (Figure 5-10 and Table 5-4) from the EBSD. For samples with high VED, an increase in the low angle boundaries were observed. Humphreys et al. [206] reported that the average misorientation decreased with growing subgrains due

to the low angle grain boundary migration. The boundaries of the high angle boundaries which stores higher energy were shortened or removed to lower the local energy. From the EBSD, many subgrain boundaries were observed in samples with high VED, agreeing with the misorientation profiles (Figure 5-10).

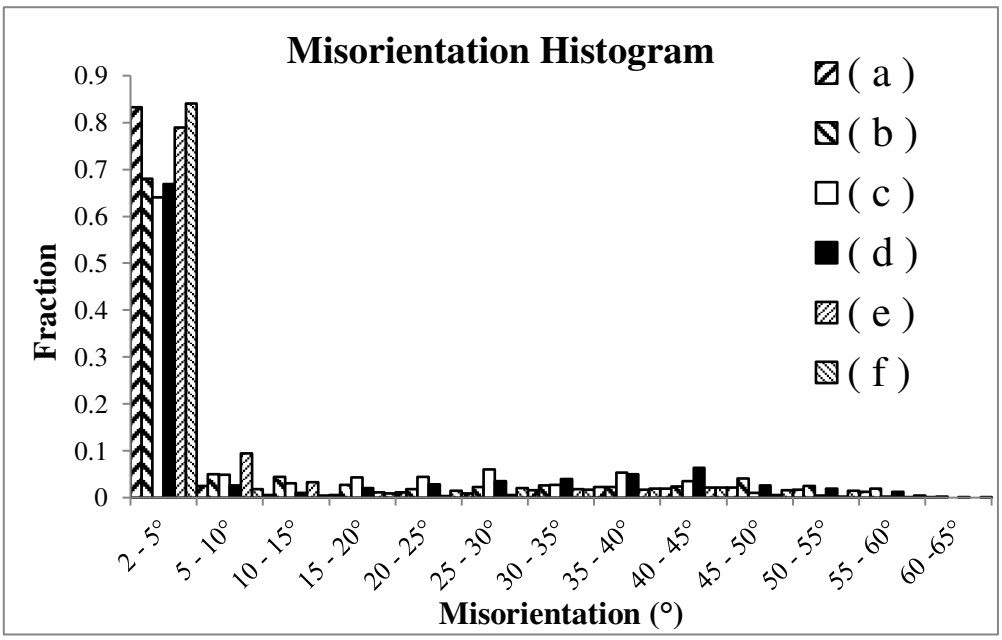

Figure 5-10 Histogram showing the distribution of grains/subgrain misorientation angles of SLM of $AlSi_{10}Mg$ with (a) high VED and (b) low VED; SLM of $AlSi_{10}Mg$ - 2% wt. nAl_2O_3 with (c) high VED and (d) low VED; SLM of $AlSi_{10}Mg$ - 5% wt. nAl_2O_3 with (e) high VED and (f) low VED.

Table 5-4 Summaries results of grain/subgrain boundary misorientations for various SLM fabricated samples.

Material and process	Concentration of Al_2O_3 (wt %)	VED (Joules / mm^3)	Average grain misorientation (°)	Fraction of high-angle grain boundaries (>15°)	Fraction of low angle grain boundaries (<=15°)		Number of samples
					(2-5°)	(2-15°)	
SLM of $AlSi_{10}Mg$ with high VED	0	35.81	7.07	0.14	0.83	0.86	99709
SLM of $AlSi_{10}Mg$ with low VED	0	23.33	10.54	0.23	0.68	0.77	38078
SLM of $AlSi_{10}Mg$ - 2% wt. nAl_2O_3 with high VED	2	109.38	10.26	0.28	0.64	0.72	30291
SLM of $AlSi_{10}Mg$ - 2% wt. nAl_2O_3 with low VED	2	23.33	12.08	0.29	0.67	0.71	34641
SLM of $AlSi_{10}Mg$ - 5% wt. nAl_2O_3 with high VED	5	583.33	5.30	0.08	0.79	0.92	62627
SLM of $AlSi_{10}Mg$ - 5% wt. nAl_2O_3 with low VED	5	23.33	6.51	0.14	0.84	0.86	73245

5.3.7 Micro-hardness

The micro-hardness results of SLM fabricated $AlSi_{10}Mg$, and its composites were collected and compared in Table 5-5. All the samples fabricated in this study have a superior hardness in comparison to AA6061-O rolled sheet, and SLM fabricated pure Al - 4% vol. nAl_2O_3. However, only SLM fabricated $AlSi_{10}Mg$, and SLM fabricated $AlSi_{10}Mg$- nAl_2O_3 with low VED displayed higher micro-hardness compared to conventional rolled AA6061-T6. The superior hardness properties could be attributed to the grain refinement (Table 5-3) and the presence of Si enriched grain boundaries (Figure 5-8). The relationship between grain size and its strengthening contribution could be explained using the Hall-Petch relationship [28]. From the Hall-Petch relationship, the presence of grain boundaries impedes dislocations propagation. As the grain size decreases, the amount of possible dislocation piles up decreases. This increased the amount of applied stress required to move a dislocation across a grain boundary. Therefore, smaller grains result in higher strength and hardness.

Table 5-5 Micro-hardness results.

Material and Processes	$HV_{0.05}$
AA6061-O [54]	55
AA6061-T6 [54]	107
SLM of pure Al - 4% vol. nAl_2O_3 [57]	48.5
SLM of $AlSi_{10}Mg$ with low VED	139 ± 6
SLM of $AlSi_{10}Mg$ - 2% wt. nAl_2O_3 with low VED	124 ± 6
SLM of $AlSi_{10}Mg$ - 5% wt. nAl_2O_3 with low VED	123 ± 3
SLM of $AlSi_{10}Mg$ with high VED	127 ± 3
SLM of $AlSi_{10}Mg$ - 2% wt. nAl_2O_3 with high VED	104 ± 5
SLM of $AlSi_{10}Mg$ - 5% wt. nAl_2O_3 with high VED	93 ± 5

For samples with low VED, the addition of nAl_2O_3 resulted in a slight reduction in the hardness. As the SLM process parameters were constant, the reduction in hardness could only be due to the addition of the reinforcements. Li et al. [85] studied the effect of heat treatment on SLM fabricated $AlSi_{10}Mg$ and observed a reduction in hardness after heat treatment was performed. It was attributed to the coalescence of the very fine Si-rich particles and Ostwald ripening [207] which resulted in the increase in Si-rich particle size and reduction in the number of particles. The introduction of alumina could have resulted in elevated processing temperature as the thermal conductivity was reduced. This resulted in the more Si-rich particles being precipitated out, encouraging the growth of the Si-rich particles, giving rise to the reduction in hardness.

For samples with high VED, further reduction in the hardness was observed in comparison with low VED samples of the same composition. This is mainly attributed to the use of higher VED, elevating the SLM processing temperature further. The use of higher VED could have resulted in more Si-rich particles being precipitated out as observed in the XRD earlier. The coarsening of the finely dispersed eutectic Si-rich in the Al matrix (Figure 5-8) via Ostwald ripening could have resulted in a reduction in hardness [85]. Also, the relatively larger grain width of high VED samples could also have contributed to lower hardness. This could be explained using the Hall-Petch relationship mentioned earlier.

5.3.8 Tensile Strength

The tensile test results of SLM samples (Appendix C) were summarised in Table 5-6. SLM of $AlSi_{10}Mg$ has superior mechanical properties which is mainly attributed to the grain refinement. As mentioned earlier, grain refinement could contribute to significant improvement in strength. Also, grain refinement could also reduce the distance between the very fine Si-rich particles (Figure 5-8). The reduction in the distance between the nano-sized eutectic network of Si-rich particles contributed to the further improvement in strength as the increase in Al-

Si interface is able to resist dislocation movement effectively, relieving the localised shear stress [85].

Table 5-6 Tensile result of various aluminium alloy and its composites. UTS is the ultimate tensile strength.

	Concentration of Al_2O_3 (wt %)	VED (Joules / mm^3)	0.2% Yield Strength (MPa)	UTS (MPa)	Elongation (%)
AA6061-O	-	-	55	125	25
AA6061-T6	-	-	276	310	12
SLM of Al - 4% vol. nAl_2O_3 [57]	-	-	110	160	5
SLM of $AlSi_{10}Mg$ with high VED	0	35.81	275 ± 6	439 ± 13	6 ± 2
SLM of $AlSi_{10}Mg$ with low VED	0	23.33	265 ± 4	355 ± 8	3 ± 1
SLM of $AlSi_{10}Mg$ - 2% wt. nAl_2O_3 with high VED	2	109.38	215 ± 3	363 ± 10	5 ± 1
SLM of $AlSi_{10}Mg$ - 2% wt. nAl_2O_3 with low VED	2	23.33	168 ± 2	175 ± 3	1 ± 1
SLM of $AlSi_{10}Mg$ - 5% wt. nAl_2O_3 with high VED	5	583.33	111 ± 5	194 ± 21	3 ± 1
SLM of $AlSi_{10}Mg$ - 5% wt. nAl_2O_3 with low VED	5	23.33	105 ± 4	105 ± 9	1 ± 1

For samples with low VED (Table 5-6e, g and i), a significant reduction in ductility was observed after the addition of nAl_2O_3. The sharp reduction in ductility is believed to be mainly attributed to higher porosity present in the material (Table 5-2). The presence of porosity could have acted as stress concentrators during the tensile test, leading to the reduction in yield stress, ultimate tensile strength and ductility. German et al. [79] reported a significant reduction in the ductility with the presence of porosity. It was also reported that porosity higher than 15% would result in negligible ductility. Therefore, the relatively high porosity of the composite samples with low VED (9.38% and 11.78%) could have attributed to the sharp reduction in the ductility. Moreover, the porosity in low VED samples was mostly irregularly shaped with several sharp edges (Figure 5-3). The sharp edges could have promoted crack propagation resulting in significant reduction in strength and ductility.

For SLM of $AlSi_{10}Mg$ and $AlSi_{10}Mg$ - 2% wt. nAl_2O_3 with high VED (Table 5-6g and h), good tensile strengths were achieved. The yield strength of $AlSi_{10}Mg$ - 2% wt. nAl_2O_3 (168±2 MPa) is significantly higher than SLM of Al - 4% vol. nAl_2O_3 (110MPa). However, comparing $AlSi_{10}Mg$ and $AlSi_{10}Mg$ - 2% wt. nAl_2O_3 with high VED, significant reduction in the yield strength was observed after the addition of nAl_2O_3. The higher VED used for fabricating $AlSi_{10}Mg$ - 2% wt. nAl_2O_3 could have resulted in more Si-rich particles being precipitated out as observed in the XRD (Figure 5-4) and FESEM (Figure 5-8). Li et al. [85] reported a decrease in the tensile strength of the $AlSi_{10}Mg$ after heat treatment. In their study, the drop in the tensile strength was mainly attributed to the coarsening of the Si-rich particles and dissolution of hardening precipitates. The decrease in localised stress or strain could be due to the increase in Si-rich particle size and the decrease in their number [208]. However, no significant increase in elongation was observed. This could be due to the presence of defects or porosity in the material. Comparing high VED and low VED samples of the same composition, samples with high VED exhibited better yield strength and ductility. The use of higher VED could have resulted in better interfacial bonding between

the aluminium matrix and the alumina. Therefore, the reduction in ductility could be mainly attributed to the presence of porosities. The porosity for SLM of $AlSi_{10}Mg$ and $AlSi_{10}Mg$ - 2% wt. nAl_2O_3 with high VED was 2.22% and 9.38% respectively. Therefore, the increase in porosity is believed to have a significant effect on the tensile properties. For SLM of $AlSi_{10}Mg$ - 5% wt. nAl_2O_3 (Table 5-6h and i), further reduction in the yield strength could be due to the presence of more porosity (18.83%) in the material.

5.3.9 Fractography

The investigation of the fracture mode at the fracture sites of the samples was performed using FESEM (Figure 5-11). Dimples were observed in all samples indicating ductile mode fracture mechanism. The shape of the dimples was elongated, corresponding to the shape of the microstructure (Figure 5-8). Unmelted spherical powders were observed in SLM of $AlSi_{10}Mg$ with low VED (Figure 5-8b) at the fracture site. Spherical pores were also observed, indicating the fracture took place in the region where there was porosity acting as defects and stress concentrators.

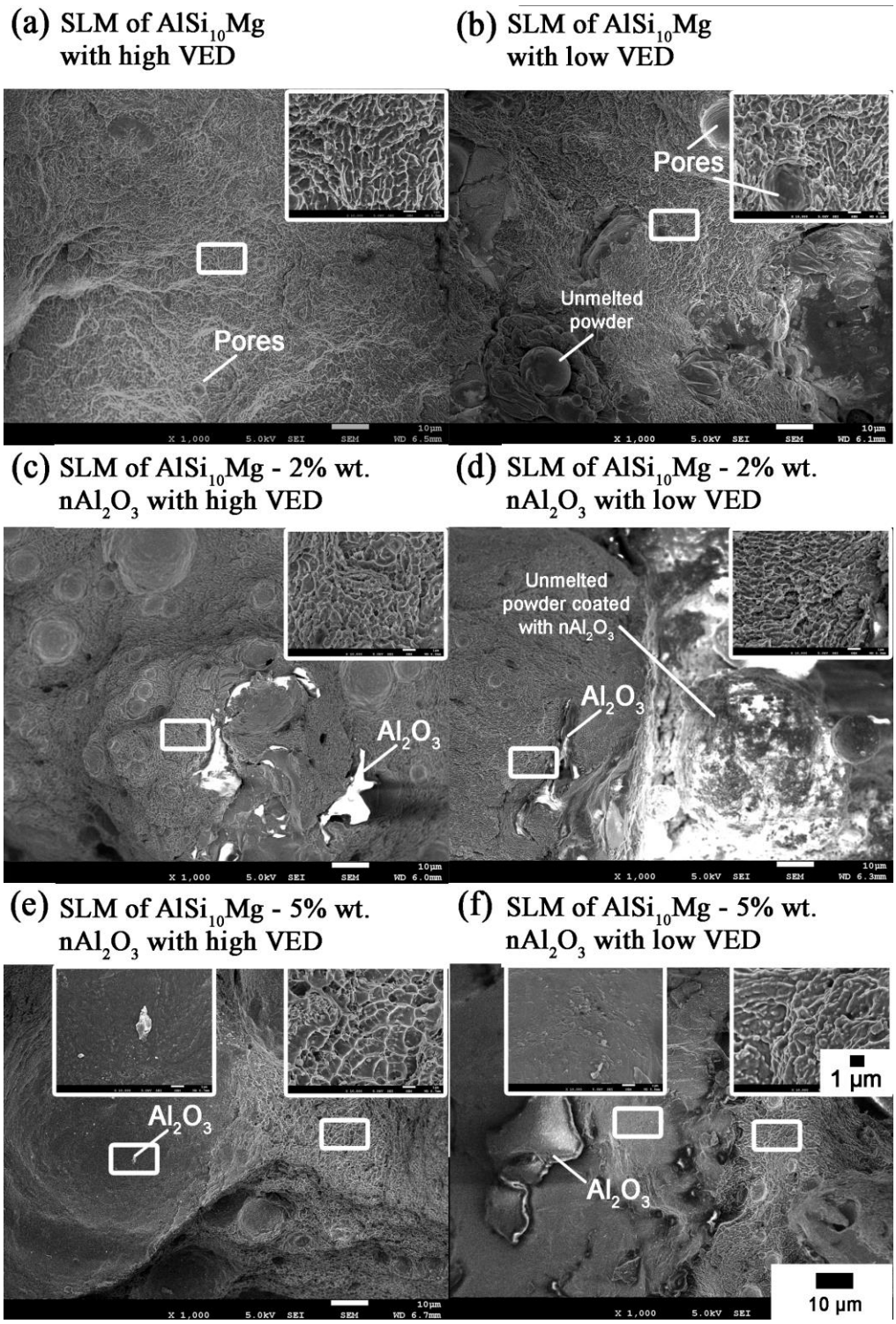

Figure 5-11 Fractography of the SLM fabricated samples.

On the fracture site of SLM of $AlSi_{10}Mg$ - 2% wt. nAl_2O_3 with high VED (Figure 5-11c), micro-pores and agglomerated nAl_2O_3 were observed. This agrees with the tensile test result where yield strength was observed to have dropped without an increase in the elongation. The presence of micropores and agglomerated nAl_2O_3 could have acted as defects resulting in the reduction in the tensile strength.

On the fracture site of SLM of $AlSi_{10}Mg$ - 2% wt. nAl_2O_3 with low VED (Figure 5-11d), relative shallower dimples were observed in the fracture site indication lower ductility. Agglomerated nAl_2O_3 and unmelted powder coated with nAl_2O_3 (Right portion of Figure 5-11d) were detected on the fracture surface. The low VED used was not sufficient to melt the powders, resulting in the formation of relatively larger porosities in the matrix. This could have given rise to the significant drop in the tensile strength and ductility.

On the fracture site of SLM of $AlSi_{10}Mg$ - 5% wt. nAl_2O_3 with high VED and low VED (Figure 5-11e and f), shallow dimples were observed. Smooth surfaces belonging to the surfaces of the porosities were also observed at the fracture sites. It is believed that a vast amount of porosity resulted in the considerable decrease in the load bearing material of the samples.

5.4 Conclusions

In this study, mechanical behaviour and microstructure evolution of SLM fabricated $AlSi_{10}Mg$, and $AlSi_{10}Mg$-nAl_2O_3 composites were studied and summarised as below.

a. Powder preparation process had successfully coated the gas-atomised spherical powder uniformly without causing any deformation.
b. Higher VED was required for the fabrication of fully dense $AlSi_{10}Mg$-nAl_2O_3 composites. Low VED resulted in the formation of porosities, microcracks and poor particle-matrix interface. The increase in VED used resulted in better wettability. The use of VED beyond the critical

threshold resulted in the formation of large circular pores and reduction of mechanical properties due to larger recoil pressure and Marangoni effect.

c. Columnar grain structure was observed via EBSD. The addition of nAl_2O_3 contributed to further reduction in the average grain width via the Zener pinning effect exerting pinning pressure during grain growth.

d. Significant reduction in the strengthening properties of $AlSi_{10}Mg$ after the introduction of nAl_2O_3 attributed to several factors such as the increase in porosity, agglomeration of nAl_2O_3, dissolution of hardening precipitates and coarsening of Si-rich particles in the matrix associated with the use of higher VED. However, the use of $AlSi_{10}Mg$ has resulted in the fabrication of $AlSi_{10}Mg$-nAl_2O_3 composites with superior mechanical properties compared to Al - 4% vol. nAl_2O_3 composites using pure aluminium.

CHAPTER 6

Joining of Selective Laser Melting Printed AlSi$_{10}$Mg by Friction Stir Welding (FSW)

This chapter introduces the friction stir butt welding process of rectangular blocks fabricated via selective laser melting process and sets the foundation to understand the butt joining properties of AlSi$_{10}$Mg via FSW. The welding properties and strength were examined and recorded.

6.1 Introduction

Aluminium alloys are widely used in the aerospace, automobile industries and high-speed ships due to its high strength to weight ratio. AA6061 aluminium alloy (Al-Si-Mg alloys) is a widely used medium strength aluminium alloy. However, conventional fusion welding process often results in softening of the weld fusion zone, heat affected zone as well as hot cracking [209].

Friction stir welding (FSW) was invented by The Welding Institute (TWI) of UK in 1991 [90]. It is a solid-state joining technique used to weld two pieces of metal together without melting. Much research has been done on the welding of aluminium due to its relatively low melting pointing and low weldability with traditional welding techniques [92, 94, 123, 210-212].

The fundamental working principle of FSW involves a non-consumable tool with a threaded pin and shoulder being plunged into the abutting edge of two sheets before travelling along the direction of the joint. The friction between the tool and the plate generates heat which softens the workpiece. The rotation of the tool moves the material from the front to the back [96]. During FSW, the material undergoes intense plastic deformation and dynamic recrystallisation forming fine equiaxed grains [213]. Studies have shown that FSW is capable of producing good mechanical properties due to the fine microstructure [25, 93, 176, 179].

In recent years, selective laser melting (SLM) has received much attention due to its ability to fabricate metal parts with complex geometry and superior mechanical properties. SLM is an additive manufacturing technique which uses a laser beam to melt powder layer by layer. With the aid of a computer-aided design (CAD) computer technique and layerwise production, high-quality parts with dimensional accuracy, superior mechanical properties and complex geometry could be produced [195]. Roberts et al. [214] studied the SLM of AA6061 and observed severe hot cracking of the fabricated part. Hence, in this study, commercially available $AlSi_{10}Mg$ was used as the higher silicon content improves fluidity during SLM. As SLM is relatively modern technology, studies on the joining of metal parts built by SLM have been limited. To the best of the authors' knowledge, there have not been any studies on the joining of SLM fabricated $AlSi_{10}Mg$. Therefore, this study aims to study the joining of SLM fabricated parts via the use of FSW. This chapter also serves as a fundamental study to understand the microstructure evolution and mechanical properties of FSWed $AlSi_{10}Mg$ for the future chapter which will investigate the FSW of SLM fabricated composites (Chapter 7).

6.2 Experimental Details

In this study, gas atomised aluminium powders, $AlSi_{10}Mg$, with the normally distributed size of 20 µm to 63 µm by TLS Technik GmbH & Co., Germany, was used. The powder was examined under the field emission scanning electron microscope (FESEM) as shown in Figure 5-1. The SLM 250 ^{HL} by SLM Solution GmbH equipped with a laser with standing spot size of 80 µm was used to scan the cross section and melt the $AlSi_{10}Mg$ powders at each layer. During the fabricating process, the build chamber was purged with argon gas until oxygen level was lower than 0.2%. The process parameters such as the laser scanning speed of 1140 mm/s, the laser power of 350 W, the layer thickness of 50 µm and hatch spacing of 0.17 mm were used based on a previous study [215].

Rectangular blocks measuring 90 mm by 60 mm by 10 mm were fabricated for friction stir welding.

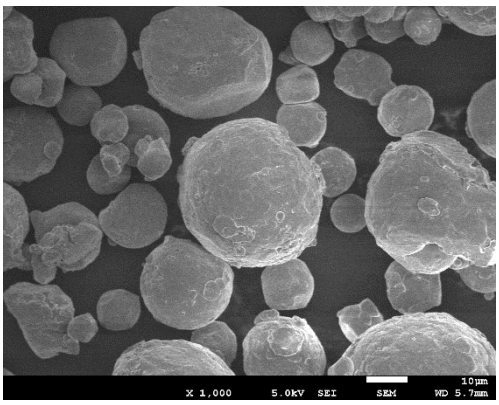

Figure 6-1 FESEM image of gas atomised AlSi$_{10}$Mg powder.

A robotic friction stir welding system with the capability of generating a maximum of 12 kN download force was used to carry out FSW. A single pass butt weld was performed to join two rectangular blocks. The surfaces were carefully degreased with acetone and brushed with wire brushed prior to FSW. The rotating tool used has a threaded conical probe with three flats. The tool probe has a length of 6.5 mm and a diameter of 7 mm at the base. The tool shoulder has a diameter of 15 mm. As the FSW of SLM is relatively new, the welding parameters were selected based on other studies. Kim et al. [117] successfully welded ADC12 using the rotational speed of 1500 rpm, the travel speed of 250 mm/min and tilt angle of 3º. Lakshminarayanan et al. [18] successfully welded AA6061-T6 using the rotational speed of 1200 rpm, travel speed of 75 mm/min. Guo et al. [5] successfully welded AA6061-T6 rolled sheet using the rotational speed of 1200 rpm, travel speed of 3 mm/s and tilt angle of 2.5°. The relative heat input could be calculated using the following formula

$$Relative\ heat\ input = \frac{RS \times DF}{TS} \quad (6\text{-}1)$$

Where RS is the rotational speed, DF is the downward force, and TS is the travel speed. From the above, the relative heat input for FSW of Al-Si alloys ranges

from approximately 26 kJ/mm to 90 kJ/mm. The detailed FSW parameters are shown Table 6-1.

Table 6-1 FSW parameters used for FSW of AA6061-T6, ADC12 and SLM fabricated samples.

Sample label	Rotational speed, RS (rpm)	Travel speed, TS (mm/s)	Tilt angle, TA (°)	Downward force, DF (kN)	RS/TS (revolutions /mm)	Relative heat input (kJ/mm)
FSW of ADC12 [117]	1500	4.17	3	7	6	42
FSW of AA6061-T6 [18]	1200	1.5	-	7	13.3	93.1
FSW of AA6061-T6 [6]	1200	3	2.5	4	6.67	26.7
Low heat input with low tilt angle	1200	3	2.5	3.75 ± 0.2	6.67	25.0
High heat input with low tilt angle	1200	1	2.5	1.57 ± 0.3	20	31.4
Low heat input with high tilt angle	600	1	4.5	3.75 ± 0.1	10	37.5
High heat input with high tilt angle	1200	1	4.5	4.0 ± 0.2	20	80

Metallographic samples were extracted from the transverse section of friction stir welding plates and polished using conventional mechanical polishing methods. Tensile coupons were machined from the plates and pulled in the direction perpendicular to the weld (Figure 6-2). Material characterisation and mechanical properties were evaluated as mentioned in Chapter 3.

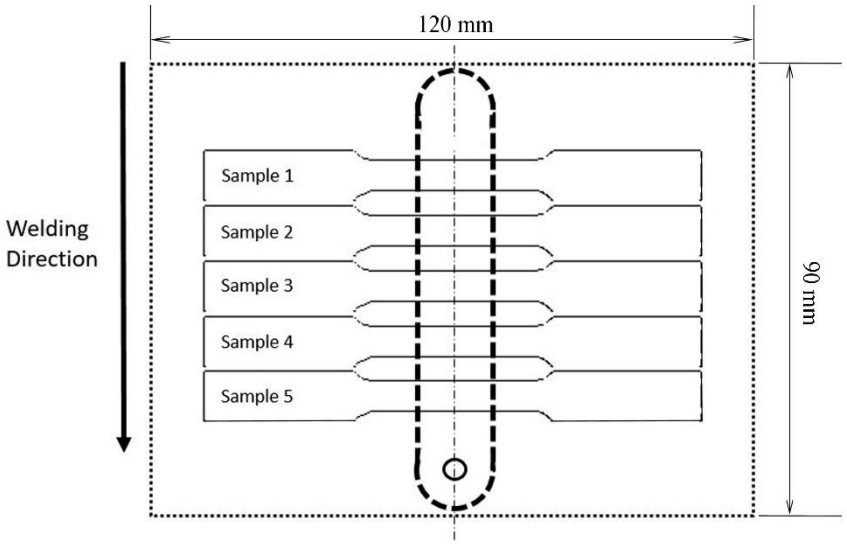

Figure 6-2 Schematic diagram showing the orientation of the tensile coupons.

6.3 Results and Discussions

6.3.1 X-ray Diffraction Analysis

The Al-Si binary phase diagram is shown in Figure 6-3 while the X-ray diffraction (XRD) results were plotted in Figure 6-4. From the Al-Si binary phase diagram, the solidification of SLM fabricated $AlSi_{10}Mg$ experiences the crystallisation reaction and the eutectic reaction. From the XRD patterns, it was observed that the Si peaks of FSWed samples have higher intensities as compared to those of SLM samples indicating a significant decrease of Si solid solubility in the aluminium matrix after FSW. Li et al. [85] studied the effect of heat treatment on $AlSi_{10}Mg$ fabricated by SLM and observed an increase in Si peak intensity after heat treatment. Also, the intensity of Mg_2Si peaks was also observed to have increased during FSW. This is mainly attributed to the Si-rich particles being precipitated out and forming Mg_2Si through the reaction with Mg present in the aluminium matrix.

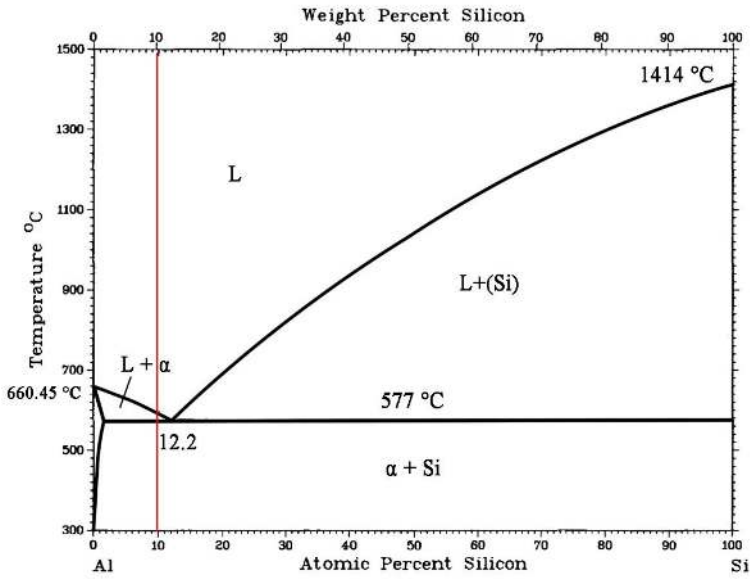

Figure 6-3 Al-Si binary phase diagram with a red line showing the solidification path and phase transition of Al-10Si.

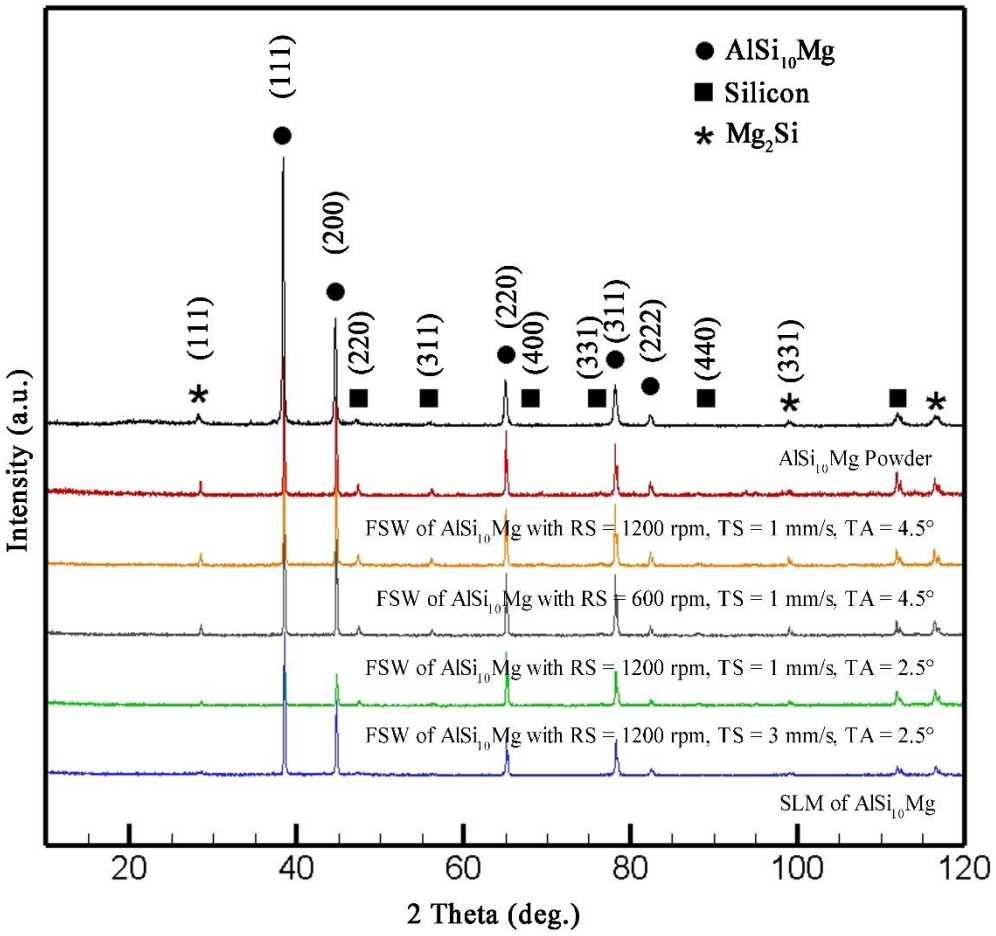

Figure 6-4 X-ray diffraction pattern of the as-received gas atomised AlSi$_{10}$Mg powders, SLM fabricated and FSWed AlSi$_{10}$Mg samples.

6.3.2 Energy Dispersive X-ray Spectroscopy (EDS)

The energy dispersive X-ray spectroscopy (EDS) was conducted on the SLM fabricated AlSi$_{10}$Mg and FSWed AlSi$_{10}$Mg samples (Appendix A). From the results, a significant increase in detection of Si was observed after FSW. The precipitation of Si-rich particles appears to take place preferably in the advancing side of the weld region. A significant increase in the number of counts for Si was observed when the line scan hits the lighter region on the advancing side of the weld (Figure 6-5). This could be attributed to the higher heat generation in the advancing side of the weld [216]. The advancing side experiences slightly higher

shear, frictional forces and heat generation as the direction of the tool and the material are moving in the opposing direction. In addition, the welding flash is larger at the retreating side, giving more surface area for radiating of heat away from the weld. Therefore, the temperature is a little higher on the advancing side of the joint, allowing more Si-rich particle to precipitate out.

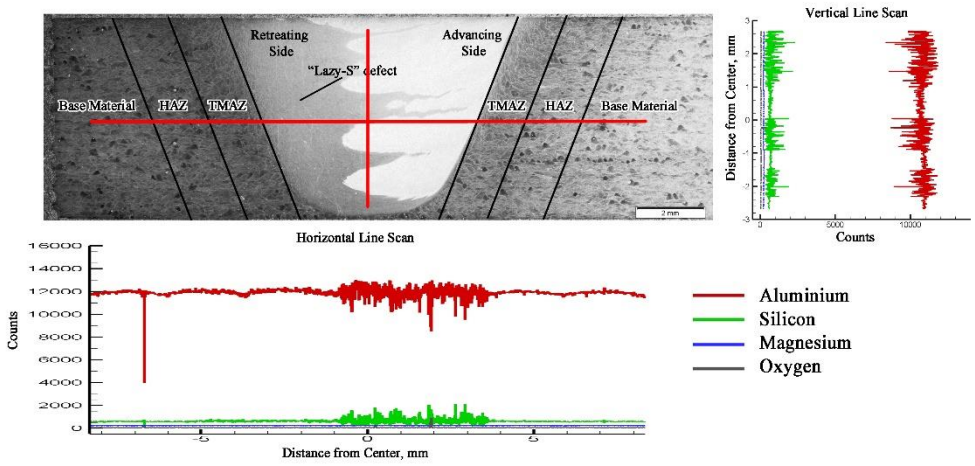

Figure 6-5 EDS line scan across the weld region of FSW of AlSi$_{10}$Mg with RS = 1200rpm, TS = 1 mm/s, TA = 2.5° showing base material, heat affected zone (HAZ), thermomechanical affected zone (TMAZ) and the stir zone.

6.3.3 Porosity Analysis

Micro CT scan (Figure 6-6) was performed on the weld region of the samples, and the relative porosity was tabulated as shown in Table 6-2 and Appendix B. From the results, no significant porosity was observed, this agrees with the FESEM observation from Figure 6-8. FSW was able to close porosity in the material due to the plastic deformation and dynamic recrystallisation properties.

Table 6-2 Relative porosity results from Micro CT scan of the weld nugget.

Material and process	Relative porosity (%)
SLM $AlSi_{10}Mg$	0.16 ± 0.03
FSW of $AlSi_{10}Mg$ with RS = 1200 rpm, TS = 3 mm/s, TA = 2.5°	0.03 ± 0.01
FSW of $AlSi_{10}Mg$ with RS = 1200 rpm, TS = 1 mm/s, TA = 2.5°	0.05 ± 0.02
FSW of $AlSi_{10}Mg$ with RS = 600 rpm, TS = 1 mm/s, TA = 4.5°	0.04 ± 0.02
FSW of $AlSi_{10}Mg$ with RS = 1200 rpm, TS = 1 mm/s, TA = 4.5°	0.03 ± 0.02

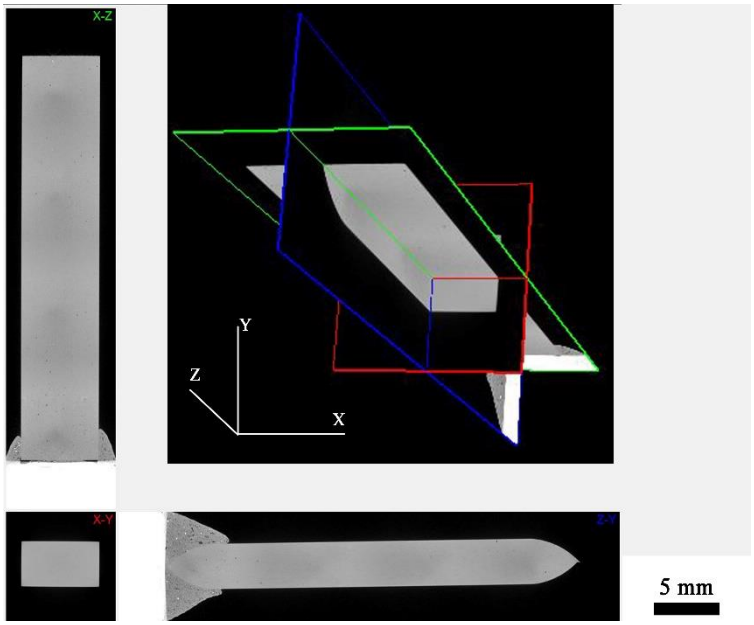

Figure 6-6 Micro CT scan of FSW $AlSi_{10}Mg$ with RS = 1200 rpm, TS = 1 mm/s, TA = 2.5°.

6.3.4 Weld Cross-section

From Figure 6-7 (b-e), different patterns were formed due to different material flow patterns. The lighter region observed resembles material from the advancing side due to their different etching response to the Keller's reagent. The increase in rotational speed led to the better mixing of the material and broadening of the weld zone. The shear layer of ranges from 0.97 mm to 1.46 mm. The periodic pattern could be explained using the Arbegast flow model [217].

During FSW, the material in the weld region experiences intense plastic deformation together with elevated temperature. An elevated temperature resulted in the softening of the material allowing the slip-stick condition to occur between the material and the tool. The material flowing from the leading side of the tool must be balanced with the material flowing to the trailing side forming periodic flow patterns. According to Arbegast et al. [217], the weld region can be divided into various deformation zones geometries as illustrated in Figure 6-7. The deformation around the pin can be divided into the retreating side (Zone I) and the advancing side (Zone II). Starting from Zone I, material flows around the pin and downwards. It then converges material in Zone II. Material from Zone I may also converge with Zone II via the region beneath the pin (Zone IV) by moving downwards into Zone IV and raising up at the advancing region into Zone II. At the top region of the weld (Zone III), the material is being dragged from the retreating side to the advancing side before being forced downwards into Zone II. On the one hand, when the excessive flow of material from Zone III enters Zone II, a collapse of the "onion ring shape occurs. On the other hand, loss of material in Zone I, III, IV from excess flashing, raised crown and sheet lifting will result in lack of material entering Zone II. This will lead to several defects such as lack of fill, wormhole or lack of consolidation volumetric defect depending on the forging force. For Zone IV, on the one hand, the excess introduction of material will result in root flow (over-penetration) defect. On the other hand, lack of material enter Zone IV will lead to the lack of penetration. Under very hot conditions, material moving downwards will be reversed upwards in a recirculation pattern which contributes to sheet thinning in lap joints.

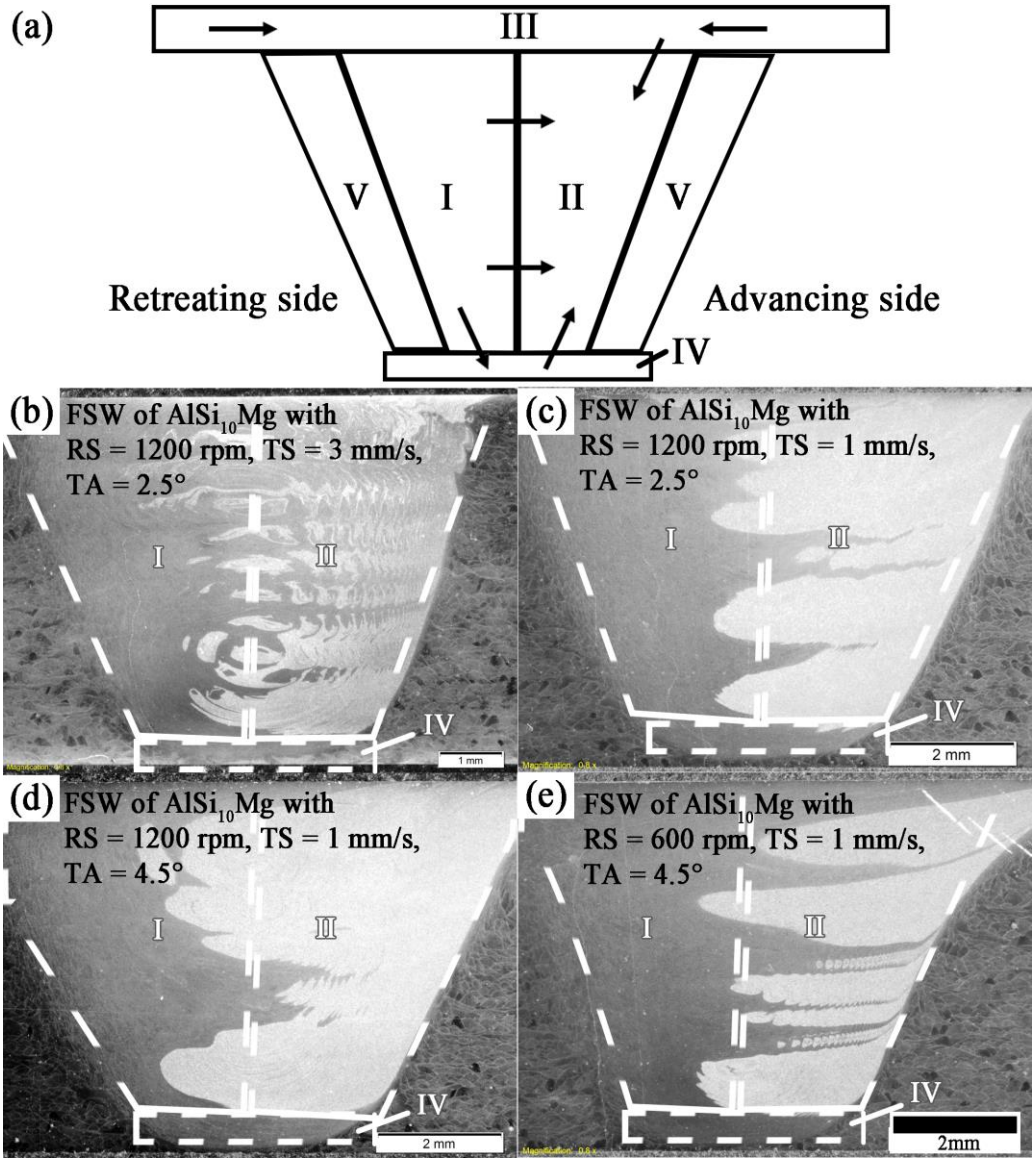

Figure 6-7 Schematic diagram (a) showing flow partition of various zones; A cross-sectional view of the weld zone from various FSW welds, with lighter region showing material from the advancing side of the weld.

6.3.5 Weld Microstructure

From the FESEM images (Figure 6-8a), melt pool was observed in SLM fabricated $AlSi_{10}Mg$ samples. Alpha phase dendrites with Si-rich eutectic constituents were also observed within the melt pools which were formed when the laser melts the $AlSi_{10}Mg$ powders. This is mainly attributed to the rapid

melting and solidification process during SLM. The powders were melted as it absorbs the energy from the laser beam. It then solidifies when the laser travels away from it. The grains then grew along the thermal gradient, as solidification takes place from the edge of the melt pool to the centre [13, 49, 85].

After FSW (Figure 6-8b to Figure 6-8e), the Si enriched boundaries were observed to have broken down into smaller particles and homogeneously distributed in the aluminium matrix. The breaking down and dispersion of reinforcement particle was observed in other studies [5, 25, 149, 179].

Upon closer observation, significant larger Si-rich particles were observed in samples with higher heat input (Figure 6-8d). Li et al. [85] studied the effect of heat treatment $AlSi_{10}Mg$ alloy fabricated by SLM and observed growth in the Si-rich particles due to coalescence of adjacent small Si-rich particles and Ostwald ripening. The thermal cycle from FSW is quite high at roughly 675K [176] therefore, the higher welding temperature resulted in the growth of the Si-rich particles.

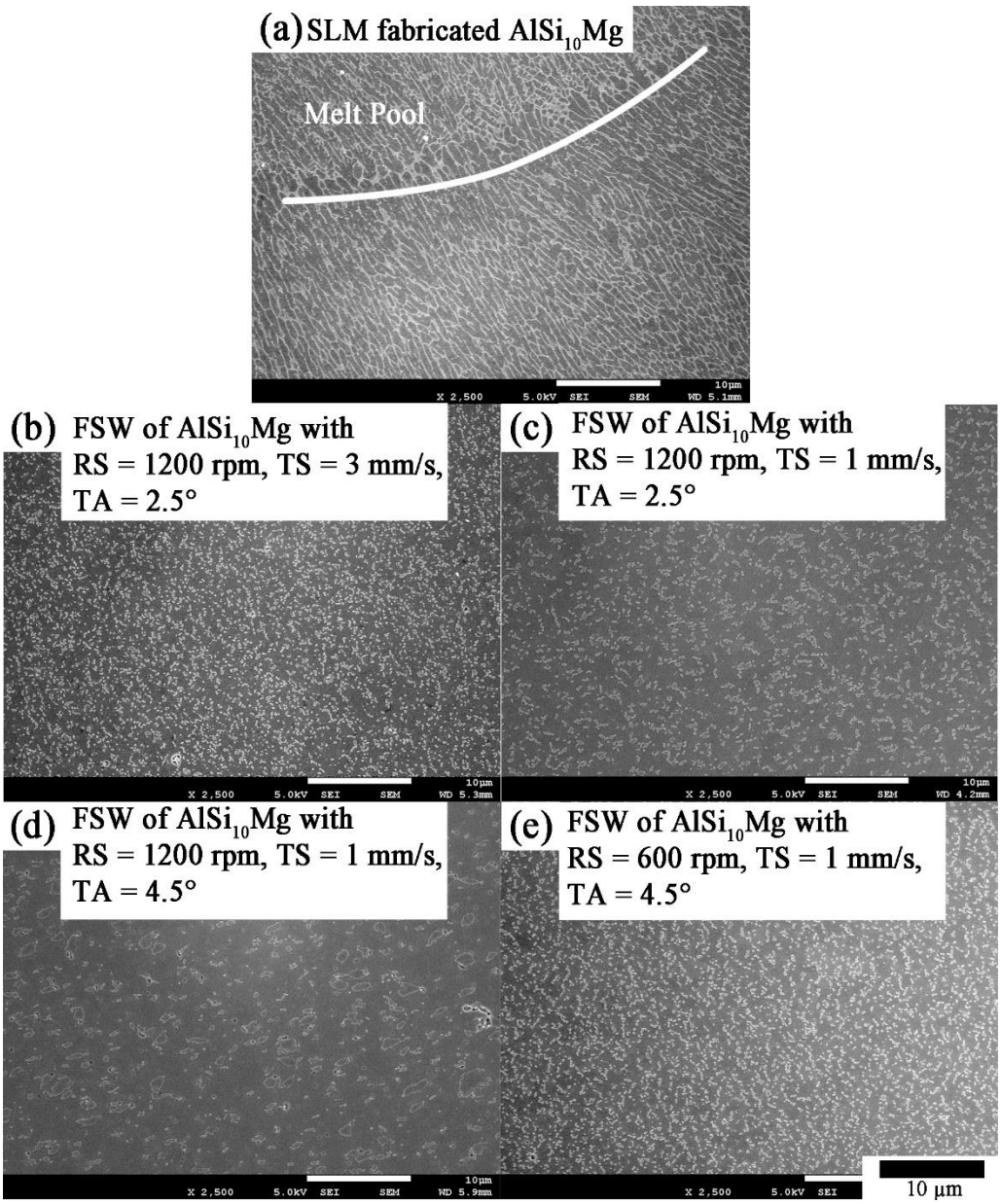

Figure 6-8 FESEM images showing the microstructure of various SLM fabricated AlSi$_{10}$Mg samples before and after FSW.

6.3.6 Grain Structure Evolution

Electron backscatter diffraction (EBSD) was performed on the samples, and mapping was obtained in Figure 6-9. From the mapping of AlSi$_{10}$Mg, grains were observed to be columnar and in the direction of the thermal gradient as mentioned earlier. For FSWed samples, significant grain refinement was observed as

tabulated in Table 6-3. During FSW, the frictional heat generated from the pin and shoulder elevated the temperature of the workpiece. The shoulder generates more heat due to its larger area as well as the higher linear velocity at the outer radius. The combination of the continuous introduction of strain, rapid recovery and migration of grain/subgrain boundaries attributes to the continuous dynamic recrystallisation [170-172]. The material in the stir zone experienced severe deformation and intense continuously induced dislocations. The stored energy in the dislocations drove the dynamic recovery recrystallisation.

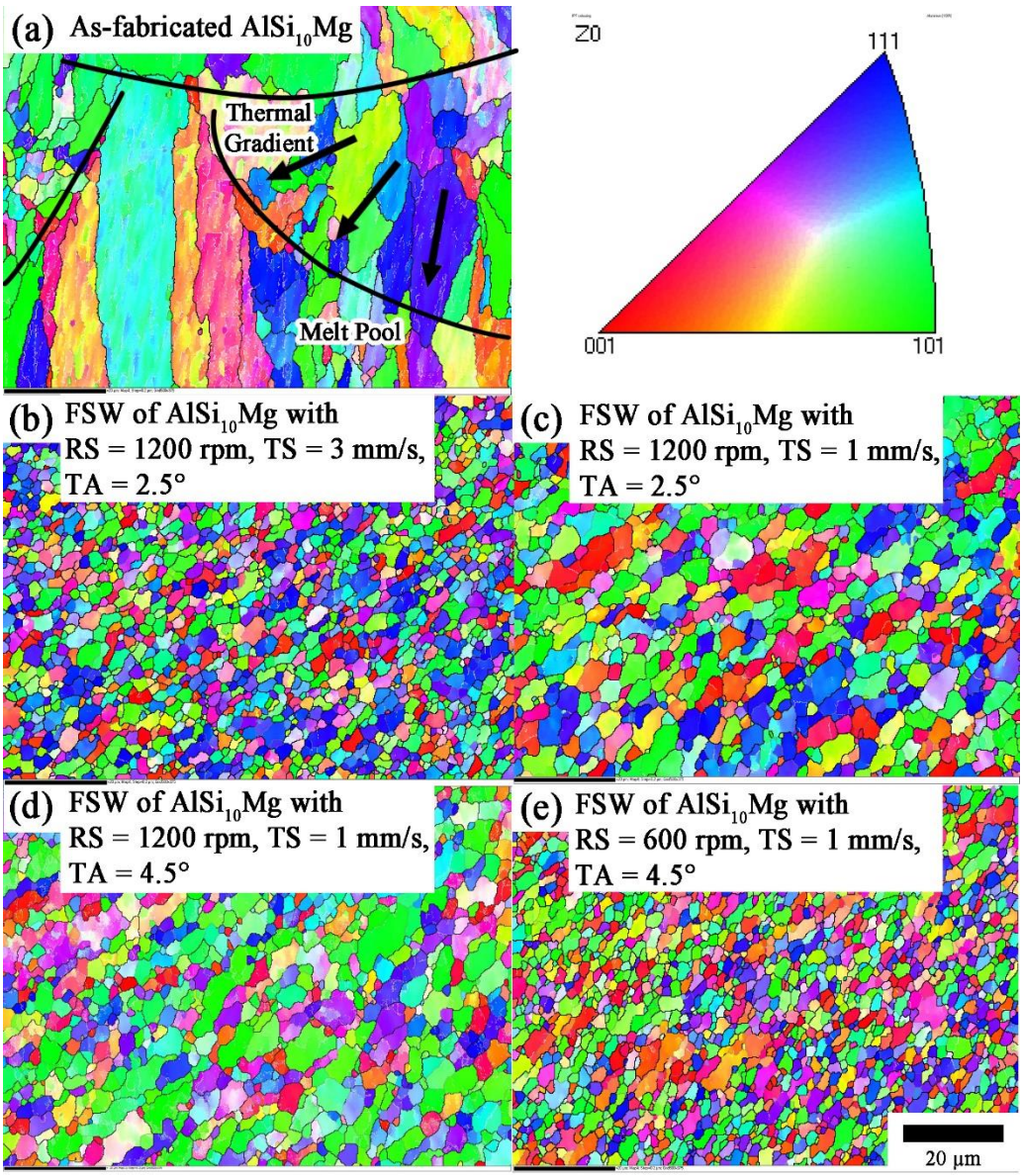

Figure 6-9 EBSD mapping showing grain structures of SLM fabricated AlSi$_{10}$Mg samples before and after FSW. The scale bar indicates 20 µm. For the boundary misorientation: white lines: between 1° and 5°, grey lines: between 5° and 15°, black lines: >15°.

Table 6-3 Average grain size values measured using EBSD technique.

Material and Process	RS/TS	Grain Size (µm)
SLM AlSi$_{10}$Mg	-	8 ± 2
FSW of AlSi$_{10}$Mg with RS = 1200 rpm, TS = 3 mm/s, TA = 2.5°	6.67	2 ± 1
FSW of AlSi$_{10}$Mg with RS = 1200 rpm, TS = 1 mm/s, TA = 2.5°	20	3 ± 2
FSW of AlSi$_{10}$Mg with RS = 600 rpm, TS = 1 mm/s, TA = 4.5°	10	2 ± 1
FSW of AlSi$_{10}$Mg with RS = 1200 rpm, TS = 1 mm/s, TA = 4.5°	20	3 ± 2

Zener pinning effect could have accounted for the finer grain sizes in the stir zone with nano-sized reinforcement particles by retarding the grain growth of the aluminium matrix. Rollett et al. [177] reported the rate of grain growth during the recrystallisation of metal with dispersed second phase particles could be described using equation (4-1).

$$\frac{dR}{dt} = M(P - P_z) = M\left(\frac{\alpha\gamma_b}{R} - \frac{3F_V\gamma_b}{2r}\right) \quad (6\text{-}1)$$

From the equation, F_v is the volume fraction, M is the boundary mobility, P is the driving pressure from the curvature of the grain boundaries, P_z is the Zener pinning pressure, R is the radius of the grain, r is the radius of the pinning Si-rich particles, α is a small geometric constant and γ_b is the boundary energy.

Therefore, when $P=P_z$, grain growth stops.

$$\frac{\alpha\gamma_b}{R} = \frac{3F_V\gamma_b}{2r} \quad (6\text{-}2)$$

Thus, the Zener limiting grain size (α=1) can be obtained when the mean grain radius (D) and the radius of curvature (R) are taken to be the same.

$$D_z = \frac{4r}{3F_v} \quad (6\text{-}3)$$

At present work, r = 0.15 µm, F_v = 0.10, the theoretical D_z = 1.9 µm. The slightly larger grain size measured by the EBSD as due to a small amount of the Si being spattered away during SLM process. The theoretical grain size can only serve as an indicative value as it is based on many assumptions that were not entirely true in reality.

From the grain sized of FSWed samples tabulated in Table 6-3, it was observed that the increase in rotational speed from 600 rpm to 1200 rpm and the decrease in travel speed from 3 mm/s to 1 mm/s resulted in significant increase in the average grain size from 2.0 µm to 2.8 µm and 2.1 µm to 2.8 µm respectively. This could be due to the increase in welding temperature with higher RS/TS.

Shojaeefard et al. [111] studied the effect of tool parameters using FEM and neural network. It was observed that the maximum welding temperature increases with increasing shoulder diameter due to higher heat generation while the pin diameter has a less significant impact on the welding temperature. In recent studies, the recrystallisation grain size can be increased by increasing the rotational speed [110, 112-114] or by reducing the travel speed [115]. Therefore, from the comparison of the grain sizes and the rotational speed to travel speed ratio (RS/TS), relative welding temperature conditions could be concluded.

According to Frigaard et al. [116], the ideal heat generation during FSW considering that all the shearing work is done on the material is converted into frictional heat could be expressed by the following equation:

$$q_0 = \frac{4}{3}\pi^2 \mu P N R^3 \quad (6\text{-}4)$$

Where q_0 is the net power from the shaft (in Watts), µ is the coefficient of friction, P is the pressure from the tool and material interface, N is the rotational speed, and R is the radius of the tool shoulder. Therefore, the heat input per unit length in a moving weld, Q, could be obtained [117]:

$$Q = \frac{\alpha q}{V} = \alpha \frac{4}{3} \pi^2 \frac{\mu P N R^3}{V} \quad (6\text{-}5)$$

Where α is the heat input efficiency and V is the travel speed.

From Table 6-1, changes in the rotation speed, travel speed and tilt angle resulted in the change in the downward force and pressure asserted from the tool. This will result in different welding temperature and grain sizes. However, for FSWed samples with the rotational speed of 1200 rpm and travel speed of 1 mm/s, there were no significant changes in the grain sizes when the tilt angle was changed. Therefore, the slight increase in tilt angle could have increased to the welding temperature, but the welding temperature was not raised enough to have a significant effect on the grain size.

The grain boundaries were further investigated using the EBSD as shown in Figure 6-10. From the misorientation profile in Table 6-4, a significant increase in the high-angle boundaries was observed on FSWed samples as compared to as-received SLM fabricated AlSi$_{10}$Mg. It was observed that the increase in rotational speed, tilt angle and the decrease in the travel speed resulted in a slight decrease in the high angle grain boundaries. It is believed that this is attributed to the heat generation and material flow during FSW. The increase in rotational speed, tilt angle and reduction in travel speed leads to the increase in heat generation. Recrystallisation and recovery of the material could have led to an increase in the number of sub-grain boundaries as observed in the EBSD images (Figure 6-9). Hence, the decrease in the fraction of the high angle boundaries.

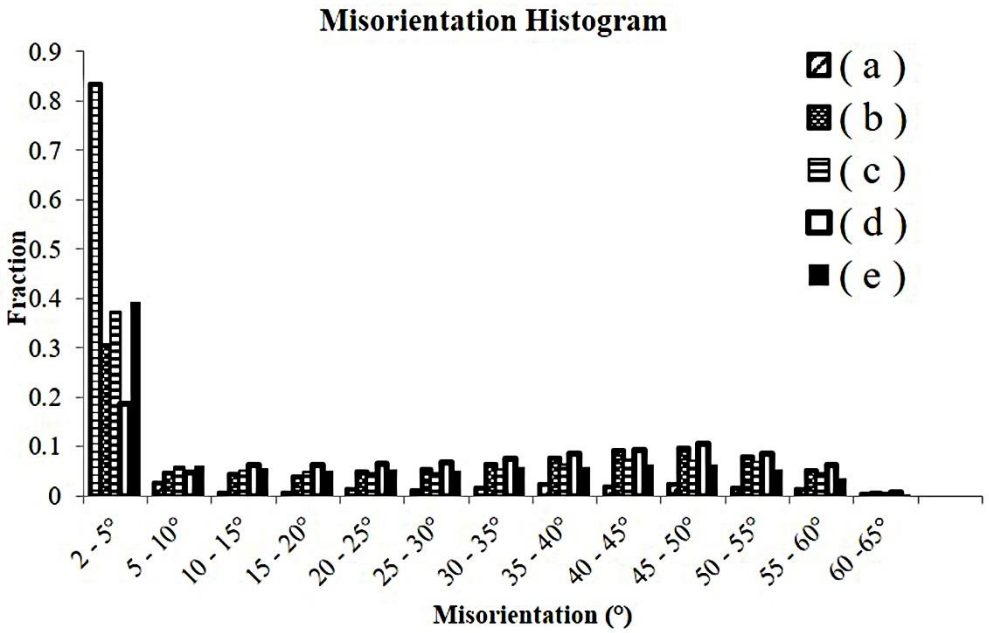

Figure 6-10 Histogram showing the distribution of grains/sub-grain misorientation angles of (a) SLM fabricated AlSi$_{10}$Mg; FSW of AlSi$_{10}$Mg with (b) RS = 1200 rpm, TS = 3 mm/s, TA = 2.5°, (c) RS = 1200 rpm, TS = 1 mm/s, TA = 2.5°, (d) RS = 600 rpm, TS = 1 mm/s, TA = 4.5°, (e) RS = 1200 rpm, TS = 1 mm/s, TA = 4.5°.

Table 6-4 Summaries results of grain/subgrain boundary misorientations.

Material and process	Mean grain misorientation (°)	Fraction of high-angle grain boundaries (>15°)	Fraction of low angle grain boundaries (<=15°)		Number of samples
			(2-5°)	(2-15°)	
SLM of $AlSi_{10}Mg$	7.07	0.14	0.83	0.86	99709
FSW $AlSi_{10}Mg$ with RS = 1200 rpm, TS = 3 mm/s, TA = 2.5°	25.43	0.61	0.30	0.39	68292
FSW $AlSi_{10}Mg$ with RS = 1200 rpm, TS = 1 mm/s, TA = 2.5°	21.80	0.52	0.37	0.48	53217
FSW $AlSi_{10}Mg$ with RS = 600 rpm, TS = 1 mm/s, TA = 4.5°	28.82	0.71	0.19	0.29	60846
FSW $AlSi_{10}Mg$ with RS = 1200 rpm, TS = 1 mm/s, TA = 4.5°	20.04	0.49	0.39	0.51	56795

6.3.7 Micro-hardness

From the micro-hardness results, it was observed that the micro-hardness of the SLM samples were significantly higher than FSWed samples and AA6061-T6 rolled sheets. This could be due to the presence of finely dispersed eutectic Si in the Al matrix as well as hardening precipitates of Mg_2Si from the rapid cooling process during the SLM process [85].

Significant reduction in the micro-hardness was observed in the FSWed samples. This could be due to the dissolution of hardening precipitates during the FSW process [25, 218]. The difference in the micro-hardness values among the FSWed samples could be explained by the difference in the strengthening contribution of the grain size difference based on the Hall-Petch equation [28].

$$\sigma = \sigma_0 + {}^{k}/_{\sqrt{d}} \tag{6-6}$$

Where σ_0 is the original strength of the material (MPa), k is the constant for pure Al (74 MPa $\mu m^{1/2}$) while d is the average grain size (μm). From the equation, smaller grains will result in significant improvement in strength and hardness.

The horizontal Vickers hardness profile of the weld was shown in Figure 6-12. Considerable softening in the weld region was observed throughout the weld zone. It was suggested that the softening is caused by the coarsening and dissolution of strengthening precipitates during the thermal cycle of FSW [98, 112, 137, 166, 176]. Sato et al. [176] reported that the hardness profile was strongly affected by the precipitate distribution rather than grain size in the weld. As mentioned earlier, the dissolution of the hardening precipitates is affected by the welding temperature of FSW process. It is evident that the FSW of AlSi$_{10}$Mg with RS = 1200 rpm, TS = 3 mm/s, TA = 2.5° has the lowest welding temperature. The decrease in travel speed resulted in an increase in the welding temperature and softening effect of the material. The increase in the tilt angle resulted in

softening of the material over a wider distance from the centre. This is mainly attributed to large and deeper contact from the tool shoulder with larger tilt angle.

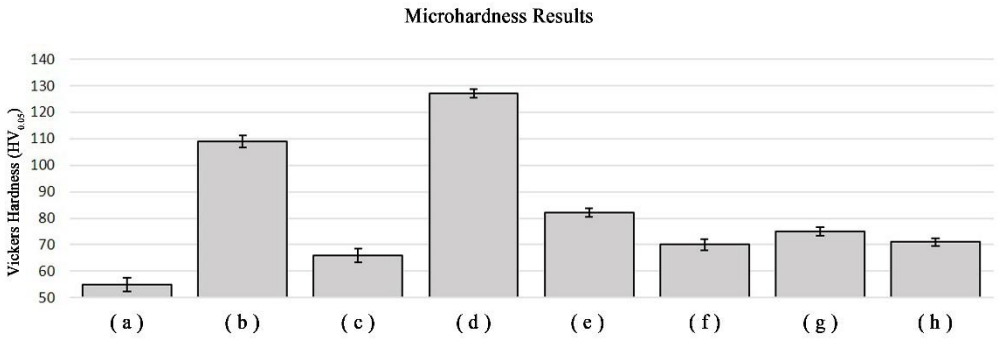

Figure 6-11 Micro-hardness results of rolled sheets (a) AA6061-O, (b) AA6061-T6, (c) FSW of AA6061-T6 [98]; (d) SLM fabricated AlSi$_{10}$Mg; FSW of AlSi$_{10}$Mg with (e) RS = 1200 rpm, TS = 3 mm/s, TA = 2.5°, (f) RS = 1200 rpm, TS = 1 mm/s, TA = 2.5°, (g) RS = 600 rpm, TS = 1 mm/s, TA = 4.5°, (h) RS = 1200 rpm, TS = 1 mm/s, TA = 4.5°.

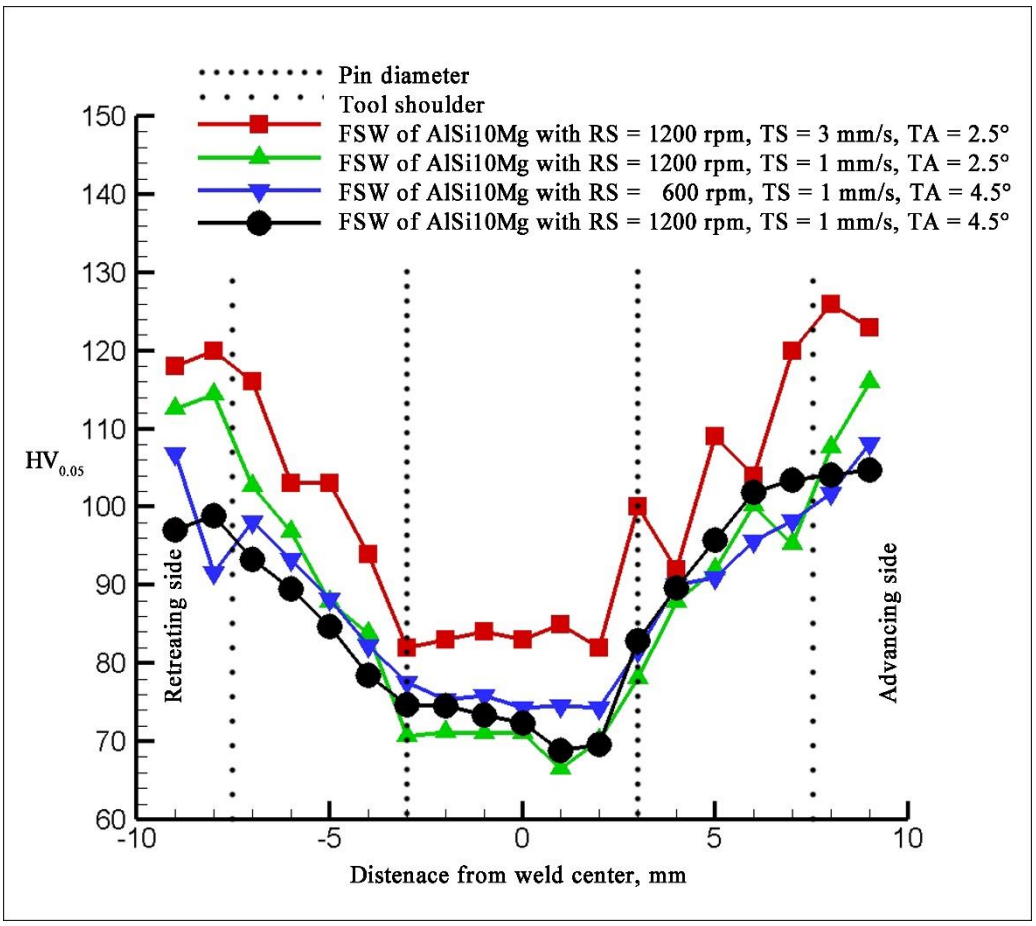

Figure 6-12 Horizontal hardness profile of various FSW parameters.

6.3.8 Tensile Strength

The tensile results were tabulated in Figure 6-13 and Appendix C. From the observation in Figure 6-13, SLM of AlSi$_{10}$Mg has superior mechanical properties. The significant improvement is mainly attributed to the very fine eutectic microstructure in the SLM part as well as the presence of very fine Si-rich particles [85] as shown in Figure 6-8a. The reduction in the distance between the Si-rich particles contributed in the increase in strength as the increased Al-Si interface can effectively reduce the movement in dislocations, moreover, localised shear stress can be relieved.

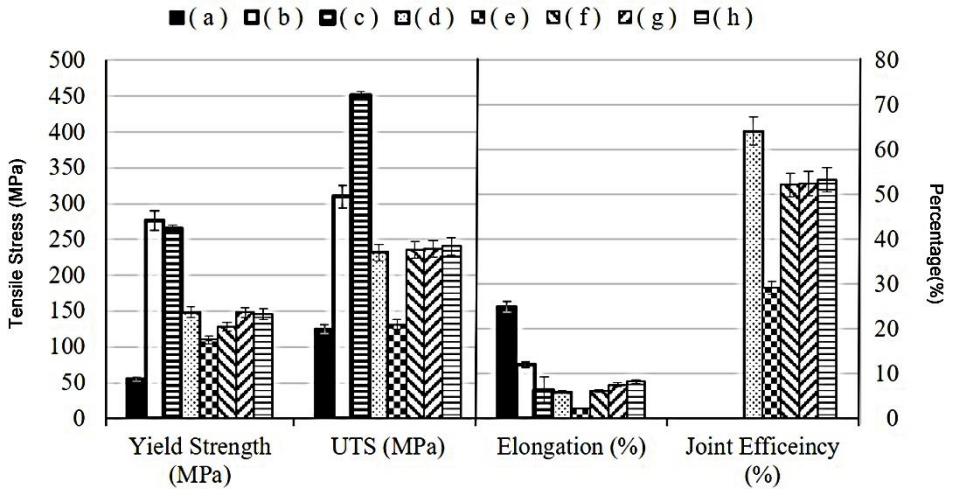

Figure 6-13 Tensile results of rolled sheets (a) AA6061-O [54], (b) AA6061-T6 [54] and (c) SLM fabricated AlSi$_{10}$Mg; FSW of rolled sheets (d) AA6061-T6 [219]; FSW of AlSi$_{10}$Mg with (e) RS = 1200 rpm, TS = 3 mm/s, TA = 2.5°, (f) RS = 1200 rpm, TS = 1 mm/s, TA = 2.5°, (g) RS = 600 rpm, TS = 1 mm/s, TA = 4.5°, (h) RS = 1200 rpm, TS = 1 mm/s, TA = 4.5°.

Comparing among FSWed samples, FSW of AlSi$_{10}$Mg with RS = 1200 rpm, TS = 3 mm/s, TA = 2.5°, ruptured at relative low tensile strength and ultimate tensile strength (Figure 6-13e). Upon closer examination at the weld region, a faint zigzag-line crack was observed near the retreating side of the stir zone (Figure 6-14c). Kiss bond or zigzag defect is characterised by the formation of dark wavy zigzag line in the weld region due to insufficient heat input [124, 125]. This defect is also known as “lazy-S” defect as reported in another study [220]. The wavy contour of the crack is mainly attributed to the low heat-input parameters and insufficient material flow. The defect consists of mainly partially broken Al_2O_3, located at the surface of the abutting joint surfaces, from the insufficient stirring during FSW. As mentioned earlier, the heat input during FSW could be increased by increasing the rotational speed or decreasing the travel speed. The RS/TS ratio generally correlates with the degree of the stirring (strain introduced per unit volume of the material). The degree of stirring is larger with the increase in RS/TS ratio [221]. The rotation of the welding tool along the pin column surface generates intense shear stresses during FSW. In this study, the shear layer

thickness, from the pin to the shear boundary, measures from 1.0 mm to 1.5 mm for various FSW heat input. These shear stresses interact with the initial oxide film on the initial butt surfaces by breaking up the Al_2O_3 oxides and creating new oxide-free surfaces around the pin. It then moves along with the material flow. The degree of collective movement is dependent on the degree of stirring and welding parameters during FSW. Hence, a higher degree of stirring would lead to a wider and diluted distribution of the oxides particles. This defect can be eliminated by increasing the heat input via increasing the rotational tool speed. Increasing the rotational tool speed also improves the stirring and dispersion of the oxide particles.

The material in the stir zone is unable to completely flow from the advancing side to the retreating side of the weld. The presence of the "lazy-S" defect creates a weak region leading to a crack during the tensile test and poor mechanical properties. Therefore, increasing the heat input for FSW would be required to eliminate the defect. Heat input for FSW could be influenced by several FSW parameters. Several studies report the increase in rotational speed increased peak temperature [110, 113].

Significant improvement in the tensile test result was observed by reducing the transverse speed from 3 mm/s to 1 mm/s (Figure 6-13e and f). This could only be mainly attributed to the increase in heat input which allows better material mixing during FSW. However, "lazy-S" defect was still visible in the weld and rupture is still observed in the defect (Figure 6-14e). During the FSW with high heat input (RS = 1200 rpm, TS = 1 mm/s, TA = 2.5°)), flashing of the material were also observed. This is an indication of having too much heat input and the material in contact with the tool shoulder has softened sufficiently to be spin out of the shoulder. Thus, increasing the heat further via increasing the RS/TS will only result in further softening of the material and more flashing defect. The tool will also sink deeper into the material due to the conservation of volume leading to excessing thinning of the weld.

Kim et al. [117] studied the formation of various FSW defects with varying RS, TS and tool downward force. In their study, it was reported that increasing the downward force could increase the boundaries for producing a sound weld. The downward force could be increased by increasing the traversing speed and tilt angle. From the earlier mentioned parameters, the increase in traversing speed result in the formation of "Lazy-S" defect. Thus, the "lazy-S" defect could be eliminated with an increase in downward force via an increase in the tilt angle was used (RS = 1200 rpm, TS = 1 mm/s, TA = 4.5°). From Table 6-1, the downward force increased from 1.57 kN to 4.0 kN when tilt angle was increased from 2.5º to 4.5º. The increase in downward force forges and increase the material flow in the stir zone, creating a sound weld. From the tensile results, significant improvement in the ductility was observed without significant improvement in the tensile strength.

Comparing FSW of $AlSi_{10}Mg$ with RS = 600 rpm, TS = 1 mm/s, TA = 4.5° and FSW of $AlSi_{10}Mg$ with RS = 1200 rpm, TS = 1 mm/s, TA = 4.5° (Figure 6-13g and h), the increase in welding temperature resulted in a slight decrease in the yield strength and ultimate tensile strength. This could be explained using the Hall-Petch equation mentioned earlier as the increase in welding temperature increased in grain size. Significant improvement in the ductility was observed with the increase in welding temperature. From the FESEM images (Figure 6-8d and e), significant coarsening of the Si-rich particles was observed. The decrease in the number of Si-rich particles and increase in the Si-rich particles sizes could have attributed to the reduction of localised stress or strain [208]. FSW is capable of welding $AlSi_{10}Mg$ with comparable welding strength and joint efficiency (>50%).

6.3.9 Fractography

Looking at the weld zone (Figure 6-14), the increase in the tilt angle resulted in an increase in the size of the stir zone at the top of weld due to the increase in surface contact and downward forces. SLM of $AlSi_{10}Mg$ fractured without visible

necking, and the fracture path is perpendicular to the direction of the applied force. FSW of $AlSi_{10}Mg$ with RS = 1200 rpm, TS = 3 mm/s, TA = 2.5° and RS = 1200 rpm, TS = 1 mm/s, TA = 2.5° fractured at the weld defect (Figure 6-14c-f). Sample with higher heat input fractured at the weld region with significant necking (Figure 6-14g-j).

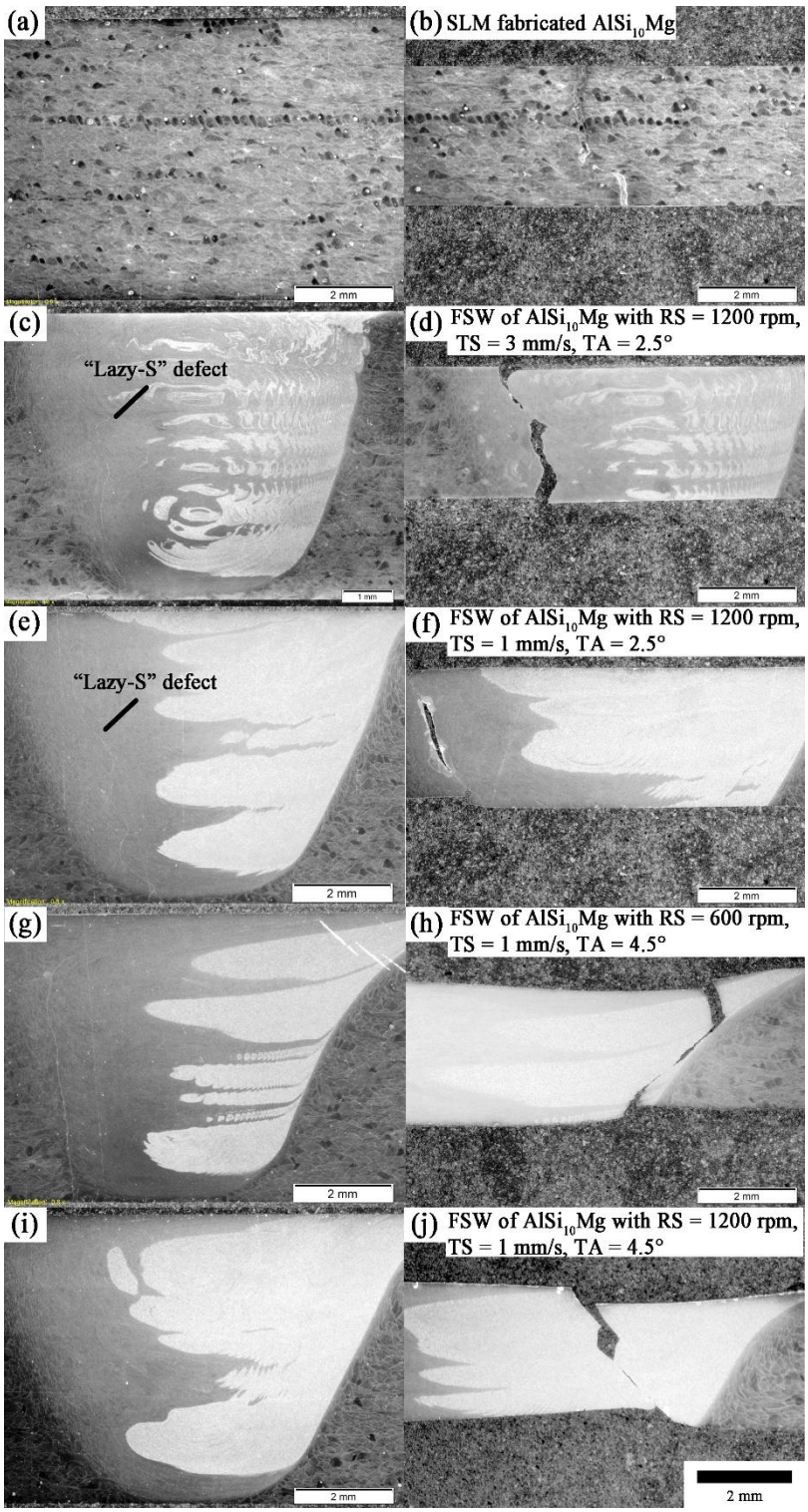

Figure 6-14 Transverse view of the samples before (left) and after the tensile test (right).

Observation of the fracture site under the FESEM reviews the fracture mechanism that took place at the fracture site. Looking at fracture surface of the SLM fabricated AlSi$_{10}$Mg (Figure 6-15a) and FSW of AlSi$_{10}$Mg (Figure 6-15b-e), dimples were observed at the fracture surfaces indicating ductile fracture mechanism. The dimples of the SLM fabricated AlSi$_{10}$Mg is relatively elongated as compared to those of the FSWed samples. These could be due to the differences in the microstructure of the different processes. The grains of the SLM fabricated AlSi$_{10}$Mg samples are columnar and grow in the direction of the thermal gradient in the melt pool. Therefore, crack propagation could be along the grain boundaries resulting in elongated dimples. Voids were also observed on the fracture site indicating the presence of small pores in the material.

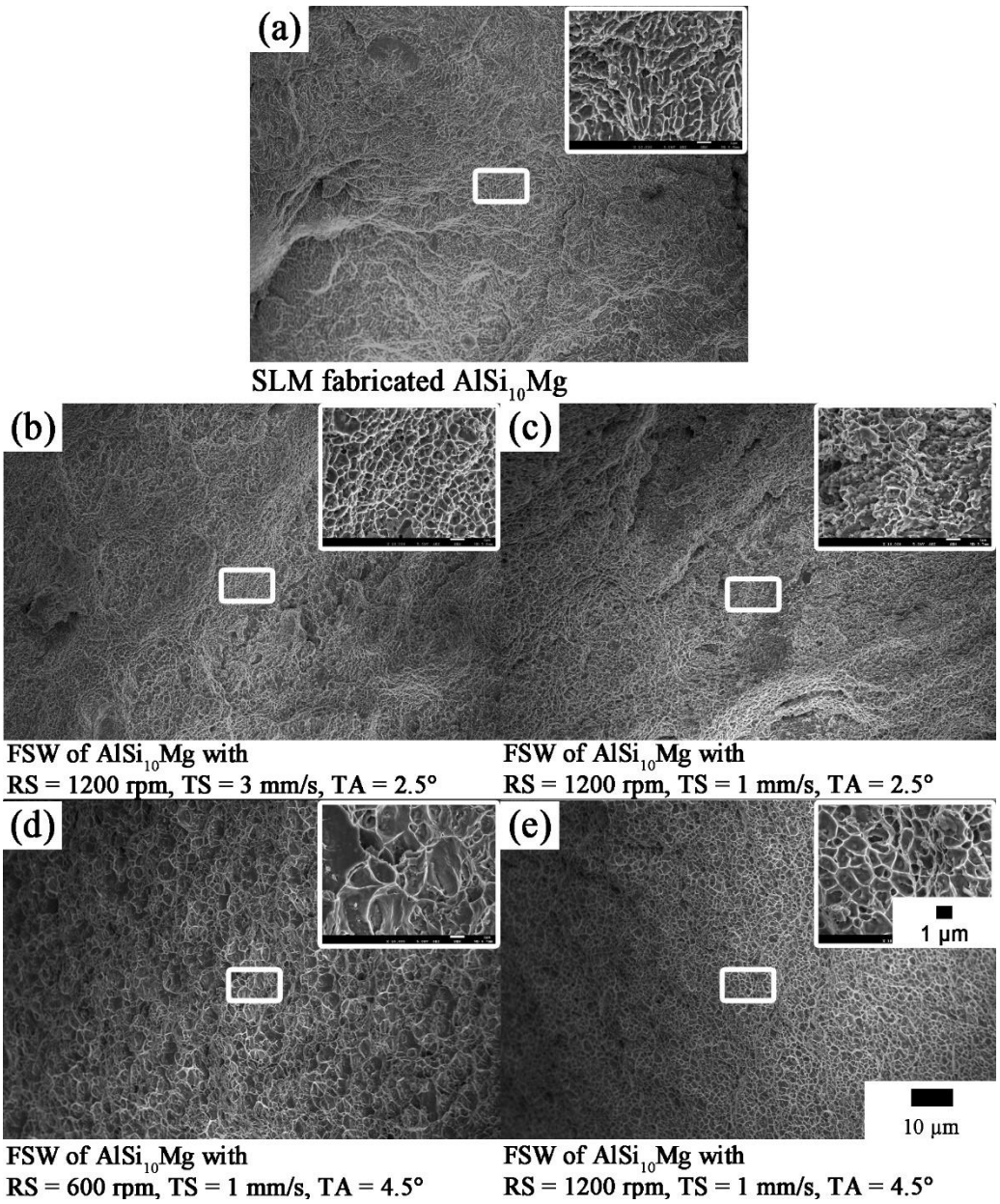

Figure 6-15 Typical fractography of SLM fabricated AlSi$_{10}$Mg samples with and without FSW.

On the other hand, the dimples of the FSW of AlSi$_{10}$Mg with RS = 1200 rpm, TS = 3 mm/s, TA = 2.5° and RS = 1200 rpm, TS = 1 mm/s, TA = 2.5° were observed to be relatively smaller and shallower (Figure 6-15b and c), assembling the crack propagation along the weld defect.

For FSW of $AlSi_{10}Mg$ with RS = 600 rpm, TS = 1 mm/s, TA = 4.5° (Figure 6-15d), deeper and larger dimples were observed. This could be due to better mixing during welding with higher heat input. Comparing this with FSW of $AlSi_{10}Mg$ with RS = 1200 rpm, TS = 1 mm/s, TA = 4.5° (Figure 6-15e), a significant increase in depth and reduction in the size of the dimple were observed indicating a very ductile fracture. The increase in the rotational speed increased the heat generation during welding and eliminated the welding defects. During the tensile test, the slight plastic deformation phase as seen in the stress-strain curve could be due to the formation of microvoids at the grain boundaries. These voids continued to grow as the stress increases. The voids eventually merged and formed cracks that lead to the failure of the material.

6.4 Conclusions

FSW was successfully used to join SLM fabricated $AlSi_{10}Mg$ parts together without the presence of welding defects with RS = 1200 rpm, TS = 1 mm/s, TA = 4.5°. The mechanical behaviour and microstructure evolution were studied and summarised as below.

a. The higher amount of Si was detected at the advancing side of the weld region. This is mainly attributed to the higher temperature generated at the advancing side resulting in more Si-rich particles being precipitated out.
b. Grain refinement was observed in the friction stir welding region due to dynamic recrystallisation process together with a significant increase in the fraction of high-angle grain boundaries during FSW.
c. A significant decrease in the hardness and tensile strength were observed in the weld region due to the precipitation of Si. The use of higher RS/TS increased the grain size and slight reduction of hardness.
d. Ductility was improved after FSW, and tensile strength is comparable to FSW of AA6061-T6 rolled sheets.

CHAPTER 7

Joining of Selective Laser Melting Fabricated AlSi$_{10}$Mg Composites by Friction Stir Welding (FSW)

This chapter focus on the friction stir butt welding of rectangular aluminium composite blocks fabricated via selective laser melting process. The welding properties and strength were examined and recorded.

7.1 Introduction

Aluminium matrix composites (AMCs) have drawn much research interest owing to their improved elastic modulus, wear resistance and stiffness [185-187]. A small concentration of reinforcement particles can provide significant strengthening effect [3]. However, joining of AMCs using conventional welding methods were challenging [222] as reaction often occurs between the reinforcement particles and matrix to form brittle secondary phases [223].

Friction stir welding (FSW) was invented in the UK in 1991 by The Welding Institute (TWI) [90]. The basic working principle of FSW involves the use of a tool shoulder with threaded pin and being forced into the edges between two clamped sheets before travelling along the weld direction. The material in the weld region is softened by frictional heat between the tool and the workpiece. The material in the weld region gets driven by the tool and moves from the front to the back [96]. Much extensive research has been done on FSW of sheet aluminium due to its relatively low melting temperature and unattractiveness with traditional fusion welding. During FSW, the material undergoes intense plastic deformation and dynamic recrystallisation forming fine equiaxed grains [213]. Studies have shown that FSW can produce good mechanical properties due to the fine microstructure [93, 176, 179, 224].

In recent years, selective laser melting (SLM) has received much attention due to its ability to fabricate metal parts with complex geometry and superior mechanical properties. The use of computer-aided design (CAD) together with SLM technique can fabricate, quality components with complex shapes accurately with excellent mechanical properties [195]. More recently, studies have also directed their attention towards the visibility of fabricating composites using selective laser melting (SLM) [13, 58, 225-227]. As SLM is a relatively modern technology, studies on the joining of metal parts built by SLM have been limited. Therefore, there is a need to study the joining of SLM printed composites. Friction stir welding comes into play as it can refine grains, promising improvement in mechanical properties with no formation of brittle intermetallic compounds.

As far as the authors' knowledge is concern, the joining of SLM fabricated aluminium composites via FSW have not been studied. Therefore, this study aims to study the weldability of SLM fabricated aluminium composites via the use of FSW with and without porosity.

7.2 Experimental Details

In this study, gas atomised aluminium powders, $AlSi_{10}Mg$, with the normally distributed size of 20 µm to 63 µm by TLS Technik GmbH & Co., Germany was used. The nano-sized alumina (nAl_2O_3) reinforcement powder used was from Sumitomo, Japan. The nominal diameter is 320 nm. $AlSi_{10}Mg$ and nAl_2O_3 were ball milled together in a volatile solvent with a ball to powder ratio of 1:1 [56] to prevent the $AlSi_{10}Mg$ powder from deforming. Deformed powders lead to a reduction of powder flowability and uneven spread of powder layer during dispensing. The blended slurry was then air dried. The dried powder was further dried using a vacuum oven for 8 hours. The blended powder was examined under the field emission scanning electron microscope (FESEM) as shown in Figure 7-1. Rectangle blocks were fabricated with SLM 250 ^{HL} from SLM Solution GmbH. The SLM laser parameters used in this study was in the based on a

previous study (Chapter 5) (Table 7-1). Rectangular blocks measuring 90 mm by 60 mm by 10 mm were fabricated for friction stir welding.

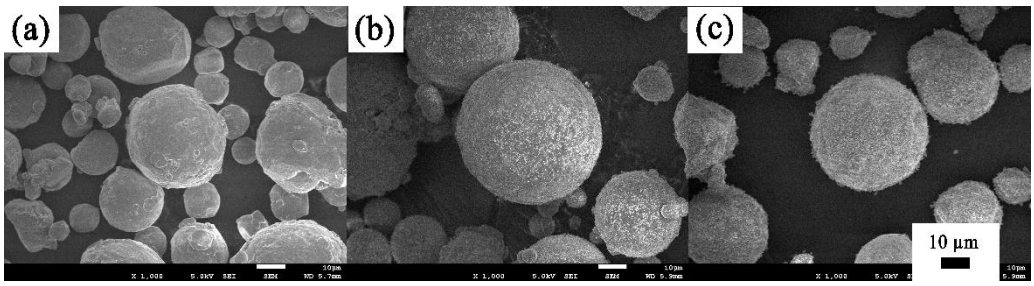

Figure 7-1 FESEM images of gas atomised $AlSi_{10}Mg$ powder (a) as-received, (b) with 2% weight nAl_2O_3, (c) 5 % weight nAl_2O_3.

Table 7-1Parameters used for as received base material with different percentage of nAl_2O_3.

Material process and composition	Volumetric energy density (VED) (Joules / mm^3)
SLM of $AlSi_{10}Mg$ with low VED	23.33
SLM of $AlSi_{10}Mg$ - 2% wt. nAl_2O_3 with low VED	23.33
SLM of $AlSi_{10}Mg$ - 5% wt. nAl_2O_3 with low VED	23.33
SLM of $AlSi_{10}Mg$ with high VED	35.81
SLM of $AlSi_{10}Mg$ - 2% wt. nAl_2O_3 with high VED	109.38
SLM of $AlSi_{10}Mg$ - 5% wt. nAl_2O_3 with high VED	291.67

A robotic FSW system with a maximum downward load of 12 kN was operated. The surfaces were carefully degreased with acetone and brushed with wire brushed before performing a single pass butt weld to join two rectangular blocks. The tool has a shoulder diameter of 15 mm and a threaded conical probe length and base diameter measuring 6.5 mm and 7 mm respectively. The welding parameters for this study were based on the optimised welding parameter used for FSW of $AlSi_{10}Mg$ (Chapter 6) (Table 7-2).

Table 7-2 Parameters used for FSW in this study.

FSW processes	Rotational speed, RS (rpm)	Travel speed, TS (mm/s)	Tilt angle, TA (°)
FSW with high heat input	1200	1	4.5
FSW with low heat input	600	1	4.5

The cross-section section of friction stir welding was polished mechanically with conventional polishing means. Tensile coupons were machined from the plates and pulled perpendicular to the weld (Figure 6-2). Material characterisation and mechanical properties were evaluated as mentioned in Chapter 3.

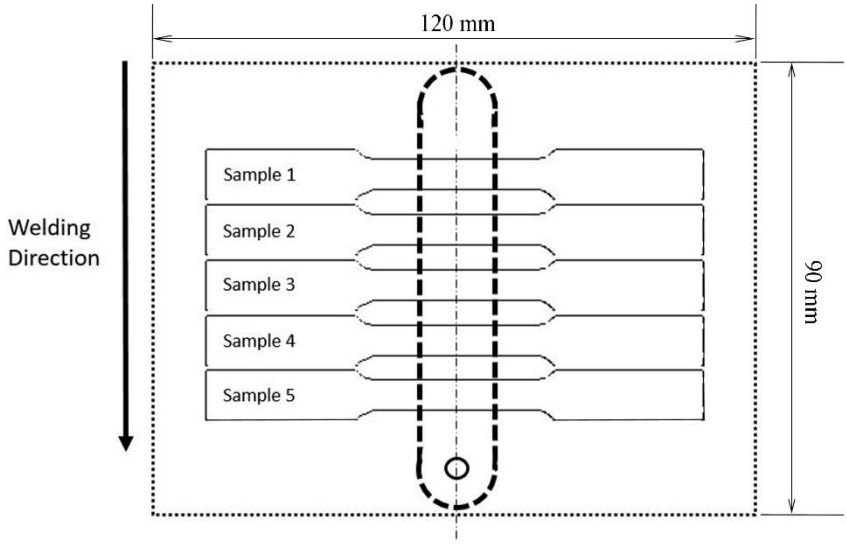

Figure 7-2 Schematic diagram of the welded plate with the orientation of the tensile coupons.

7.3 Results and Discussions

7.3.1 X-ray Diffraction (XRD) Analysis

The phase diagram of Al-Si is shown in Figure 7-3 while the X-ray diffraction (XRD) results were plotted in Figure 7-4, Figure 7-5 and Figure 7-6. From the diagram, AlSi$_{10}$Mg experiences both crystallisation reaction and eutectic reaction during SLM fabricated. From the XRD patterns, it was observed that the Si peaks of FSWed samples have higher intensities as compared to those of SLM samples indicating a considerable reduction of solid solubility of Si in the aluminium matrix after FSW. Si-rich particles could have been precipitated out and formed Mg_2Si through the reaction with Mg present in the aluminium matrix as explained in Chapter 6.

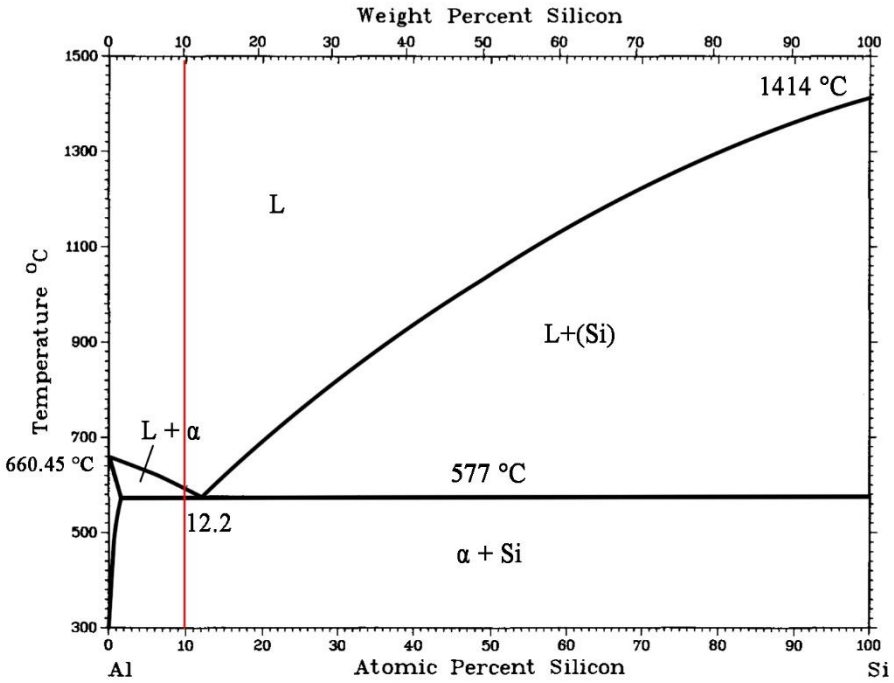

Figure 7-3 Binary phase diagram of Al-Si showing the solidification path and phase transition of Al-10Si (red line).

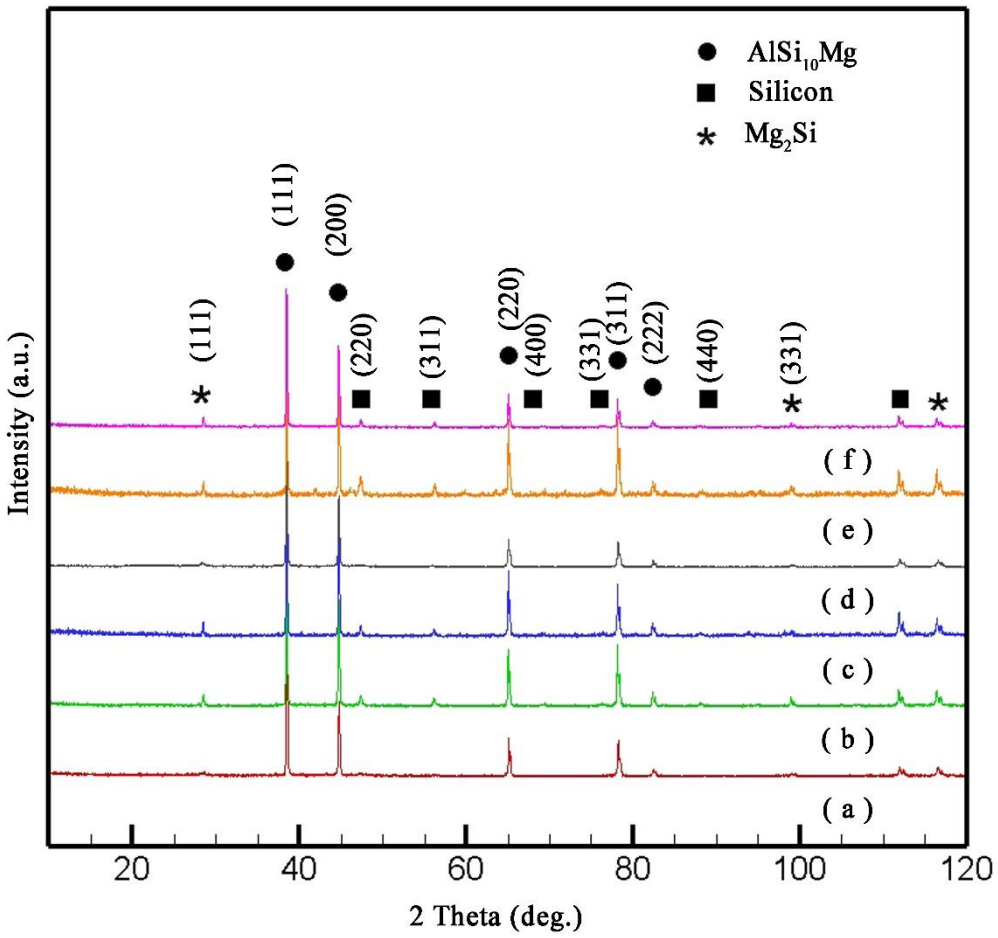

Figure 7-4 X-Ray diffraction pattern of the SLM of AlSi$_{10}$Mg with high VED (a) as-received, (b) FSW with low heat input, (c) FSW with high heat; SLM of AlSi$_{10}$Mg with low VED (d) as-received, (e) FSW with low heat input, (f) FSW with high heat input.

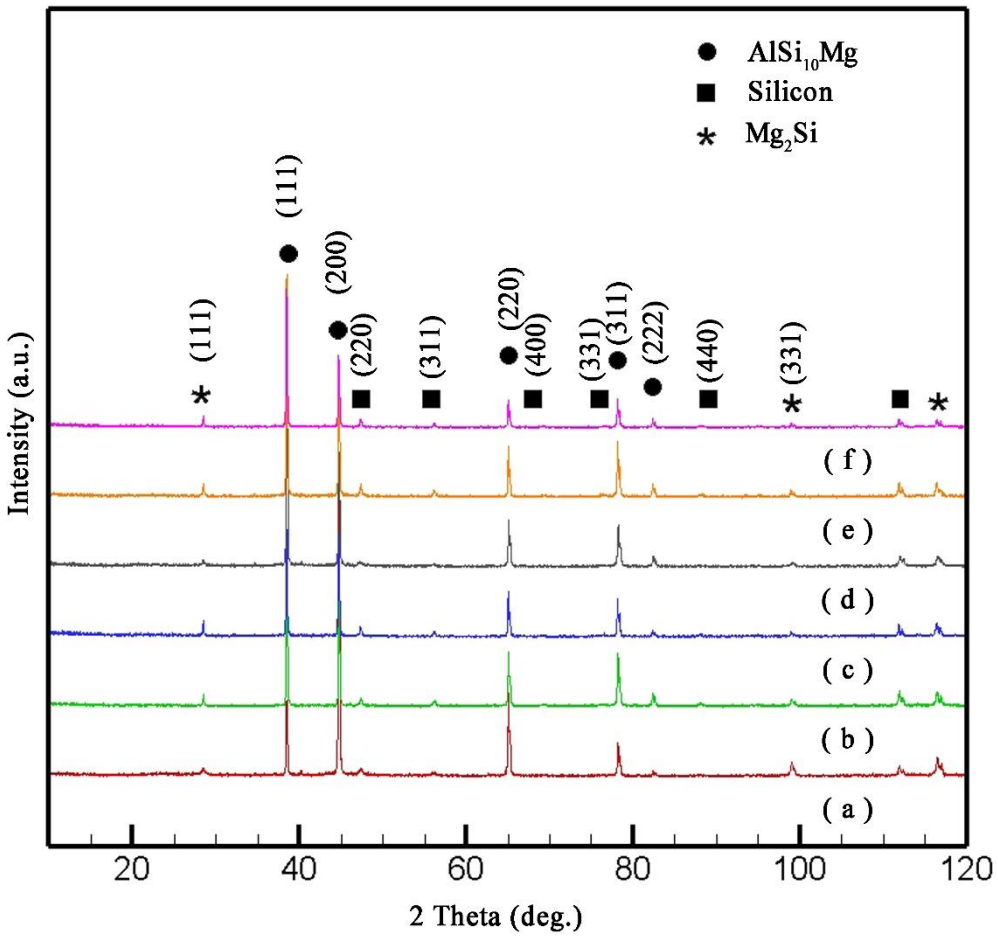

Figure 7-5 X-Ray diffraction pattern of the SLM of $AlSi_{10}Mg$ - 2% wt. nAl_2O_3 with high VED (a) as-received, (b) FSW with low heat input, (c) FSW with high heat input; SLM of $AlSi_{10}Mg$ - 2% wt. nAl_2O_3 with low VED (d) as-received, (e) FSW with low heat input, (f) FSW with high heat input.

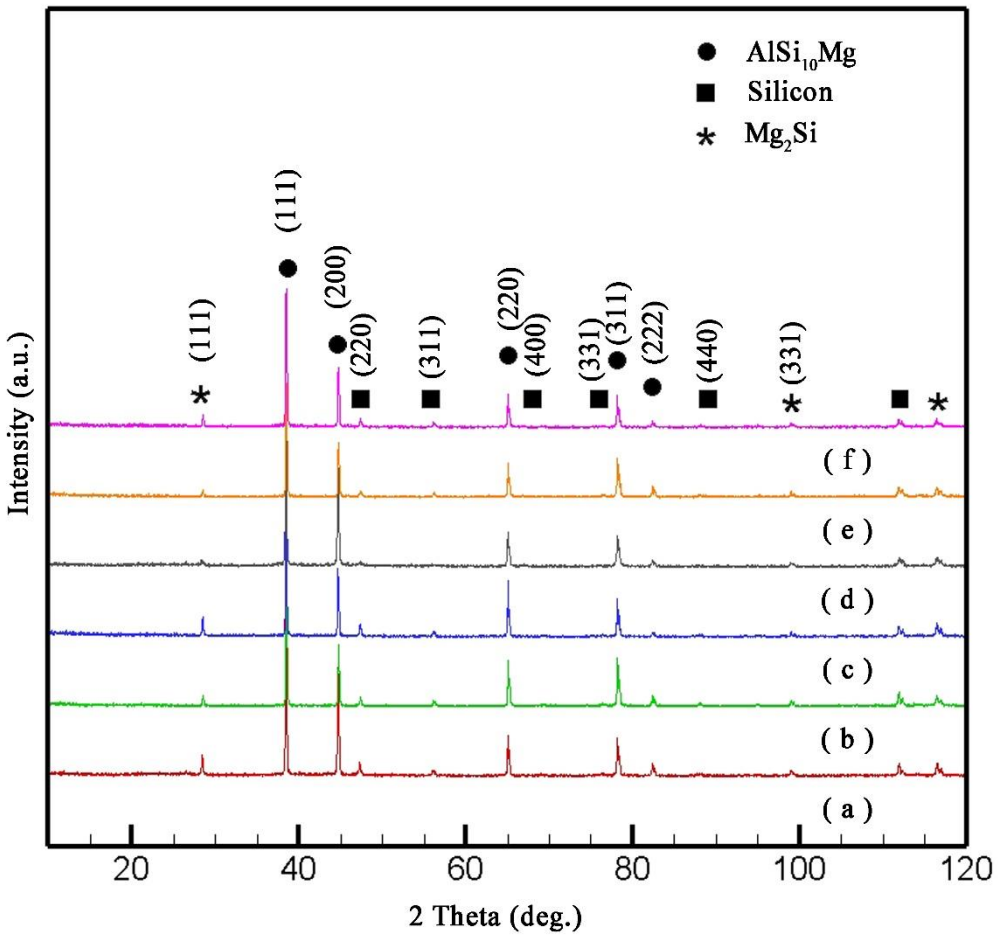

Figure 7-6 X-Ray diffraction pattern of the SLM of AlSi$_{10}$Mg - 5% wt. nAl$_2$O$_3$ with high VED (a) as-received, (b) FSW with low heat, (c) FSW with high heat input; SLM of AlSi$_{10}$Mg - 5% wt. nAl$_2$O$_3$ with low VED (d) as-received, (e) FSW with low heat input (f) FSW with high heat input.

7.3.2 Energy Dispersive Spectroscopy (EDS)

The energy dispersive spectroscopy (EDS) was conducted on the SLM fabricated samples and FSWed samples (Appendix A). From the results, a significant increase in detection of Si in the weld was observed after FSW (Figure 7-7). The precipitation of Si-rich particles appears to take place preferably in the advancing side of the weld region. An increase in the number of counts of Si was observed when the line scan hits the lighter region on the advancing side of the weld. This

could be attributed to the higher heat generation on the advancing side of the weld as explained in Chapter 6 [216].

Looking at the weld zones, different patterns were observed due to different material flow behaviour. The increase in RS resulted in higher welding temperature, better mixing of the aluminium matrix and broadening of the weld region. Broadening of the stir zone was observed in samples with porosity as well as samples with the addition of nAl_2O_3 reinforcement. It is believed that the reduction of heat conductivity of the material from the presence of porosity and nAl_2O_3 reinforcement resulted in higher welding temperature and more extended area of the softened material.

Upon closer examination at the weld region (Figure 7-7), a faint zigzag-line crack was detected near the retreating side of the weld region of FSW samples with low heat input. This defect is also known as “lazy-S” defect as reported in another study [220]. The wavy contour of the crack is mainly attributed to the low heat-input parameters and insufficient mixing of the material. The aluminium matrix in the stir zone is unable to completely flow from the advancing side to the retreating side of the weld. The presence of the “lazy-S” defect creates a weak region, leading to a crack during the tensile test and reduction in mechanical properties. Therefore, increasing the heat input for FSW would be required to eliminate the defect. Heat input for FSW could be influenced by several FSW parameters. Several studies report higher welding temperature with increasing rotational speed [110, 113].

For FSW samples with high heat input, the addition of nAl_2O_3 has resulted in the stir region beginning to show signs of abnormal stirring (Figure 7-8) [117]. This could be due to the difference in the temperature at the upper surface and the base resulting in the different plastic flow. The material at the top experienced high heat generation, resulting in material being spun out by the tool (flashing). The lower surface is in contact with the backing plate which acts as a heat sink removing heat from the weld. The difference in the temperature and plastic flow

of the material at the top and bottom of the weld led to a discontinuous flow of material at the advancing side. Abnormal stirring can be overcome with the increase of downward force during FSW as well as changing of tool geometry to improve the metal flow during FSW [117].

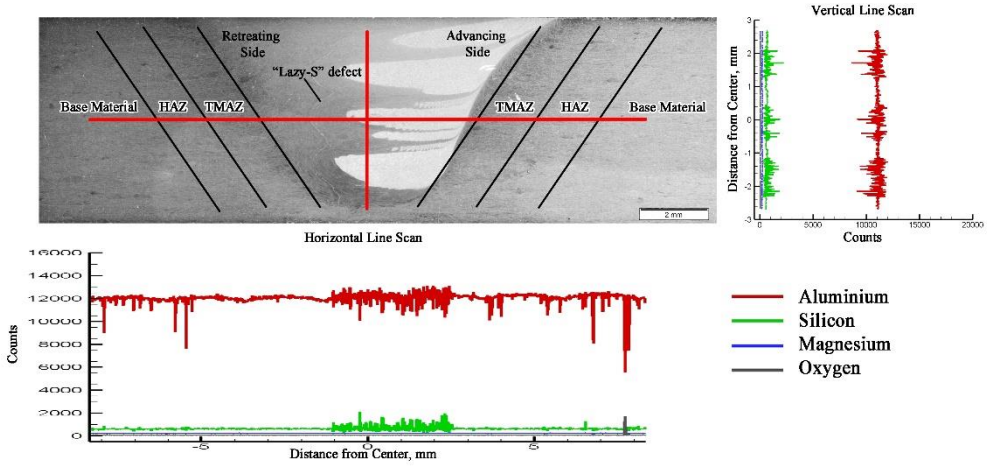

Figure 7-7 EDS scan of FSW with low heat input of SLM of AlSi$_{10}$Mg - 2% wt. nAl$_2$O$_3$ with high VED showing the stir zone, thermomechanical affected zone (TMAZ), heat affected zone (HAZ) and base material region.

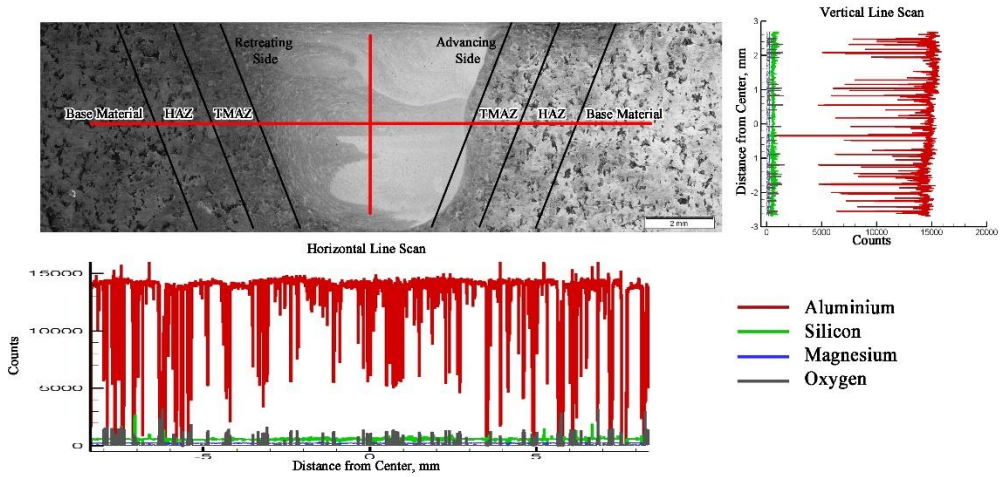

Figure 7-8 EDS scan of FSW with high heat input of SLM of AlSi$_{10}$Mg - 5% wt. nAl$_2$O$_3$ with low VED showing the stir zone, thermomechanical affected zone (TMAZ), heat affected zone (HAZ) and base material region.

7.3.3 Porosity Analysis

Micro CT scan was performed on the weld region of the samples (Figure 7-9) (Appendix B), and the relative porosity was tabulated as shown in Figure 7-10, Figure 7-11 and Figure 7-12. The Micro CT scanner was a minimum resolution of 6 µm. Pores measuring smaller than 6 µm in diameter were not detected. However, the FESEM could be used to detect smaller pores on the cross-sections. A significant amount of porosity was observed in as-received samples (Figure 7-10b, Figure 7-11b and Figure 7-12a and b). The causes of porosity in the SLM fabricated samples were explained in Chapter 5. From the results (Figure 7-10, Figure 7-11 and Figure 7-12), no significant porosity was detected in the weld region, this agrees with the FESEM observation from Figure 7-13, Figure 7-14 and Figure 7-15. The plastic deformation and dynamic recrystallisation process during FSW were able to close porosity in the weld region. From the micro CT scan results, it is evident that FSW can close up porosities in the material.

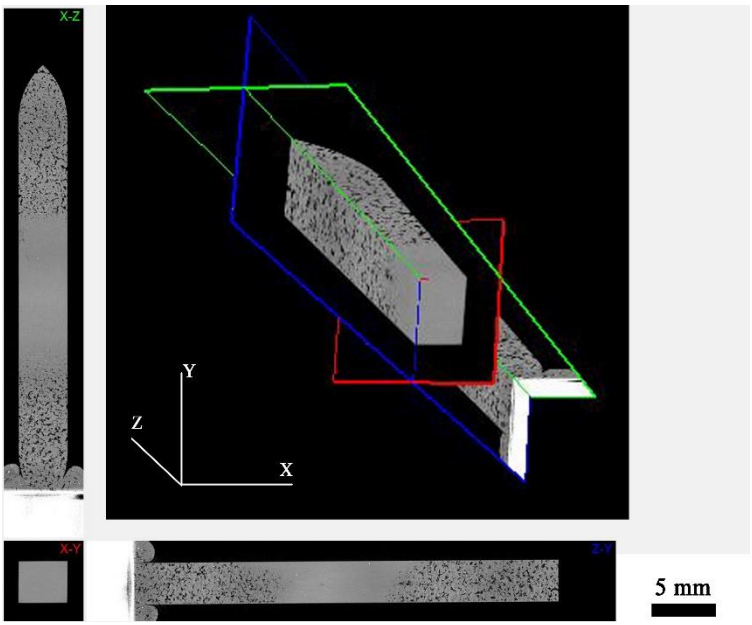

Figure 7-9 Micro CT image of FSW with high heat input of SLM of AlSi$_{10}$Mg - 5% wt. nAl_2O_3 with Low VED.

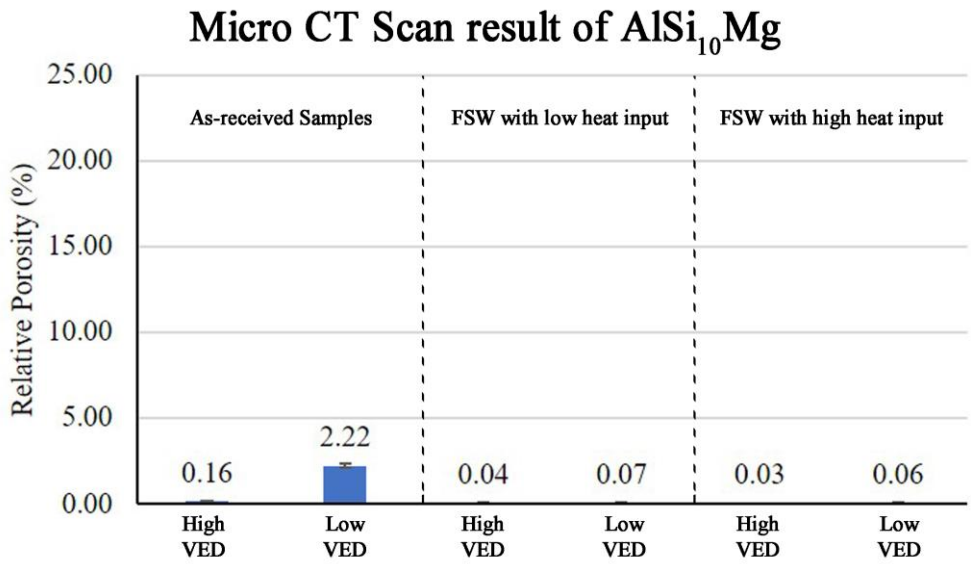

Figure 7-10 Micro CT scan result of as-received and FSWed samples of SLM fabricated $AlSi_{10}Mg$.

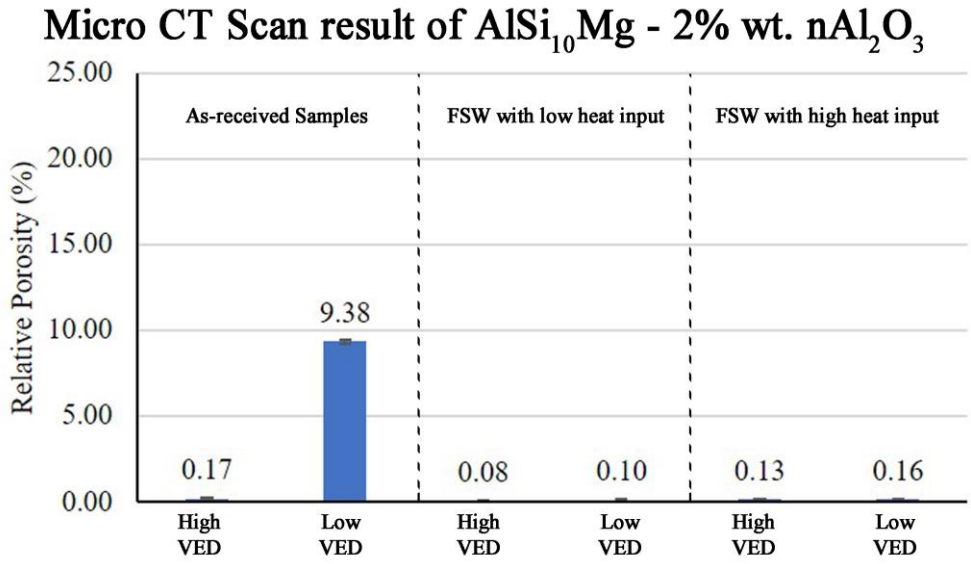

Figure 7-11 Micro CT scan result of as-received and FSWed samples of SLM fabricated $AlSi_{10}Mg$ - 2% wt. nAl_2O_3.

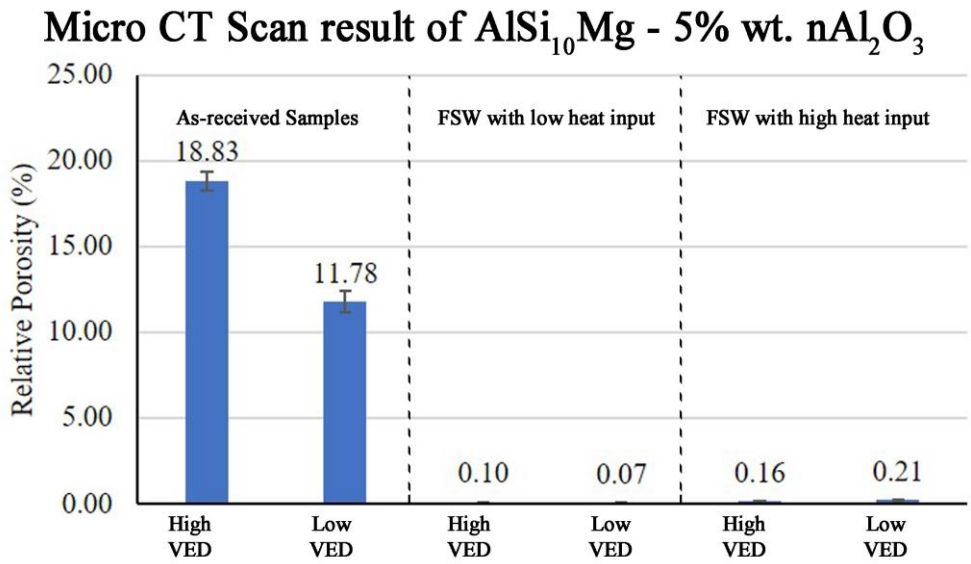

Figure 7-12 Micro CT scan result of as-received and FSWed samples of SLM fabricated AlSi$_{10}$Mg - 5% wt. nAl$_2$O$_3$.

7.3.4 Weld Microstructure

From the FESEM images (Figure 7-13), melt pool was observed in the images of as-received SLM AlSi$_{10}$Mg with high and low VED (Figure 7-13a and b). Si enriched boundaries were also observed within the melt pools which were formed when the laser melts the AlSi$_{10}$Mg powders. During SLM the powders were rapidly melted as it absorbs the energy from the laser beam. It then rapidly solidifies when the laser travels away from it. The grains then grew along the thermal gradient as solidification takes place from the edge of the melt pool to the centre [13, 49, 85].

After FSW, the Si enriched boundaries were observed to have disintegrated into smaller particles and homogeneously distributed in the aluminium matrix (Figure 7-13c-f). The breaking down and dispersion of reinforcement particle was also observed in other studies [5, 149, 179, 224].

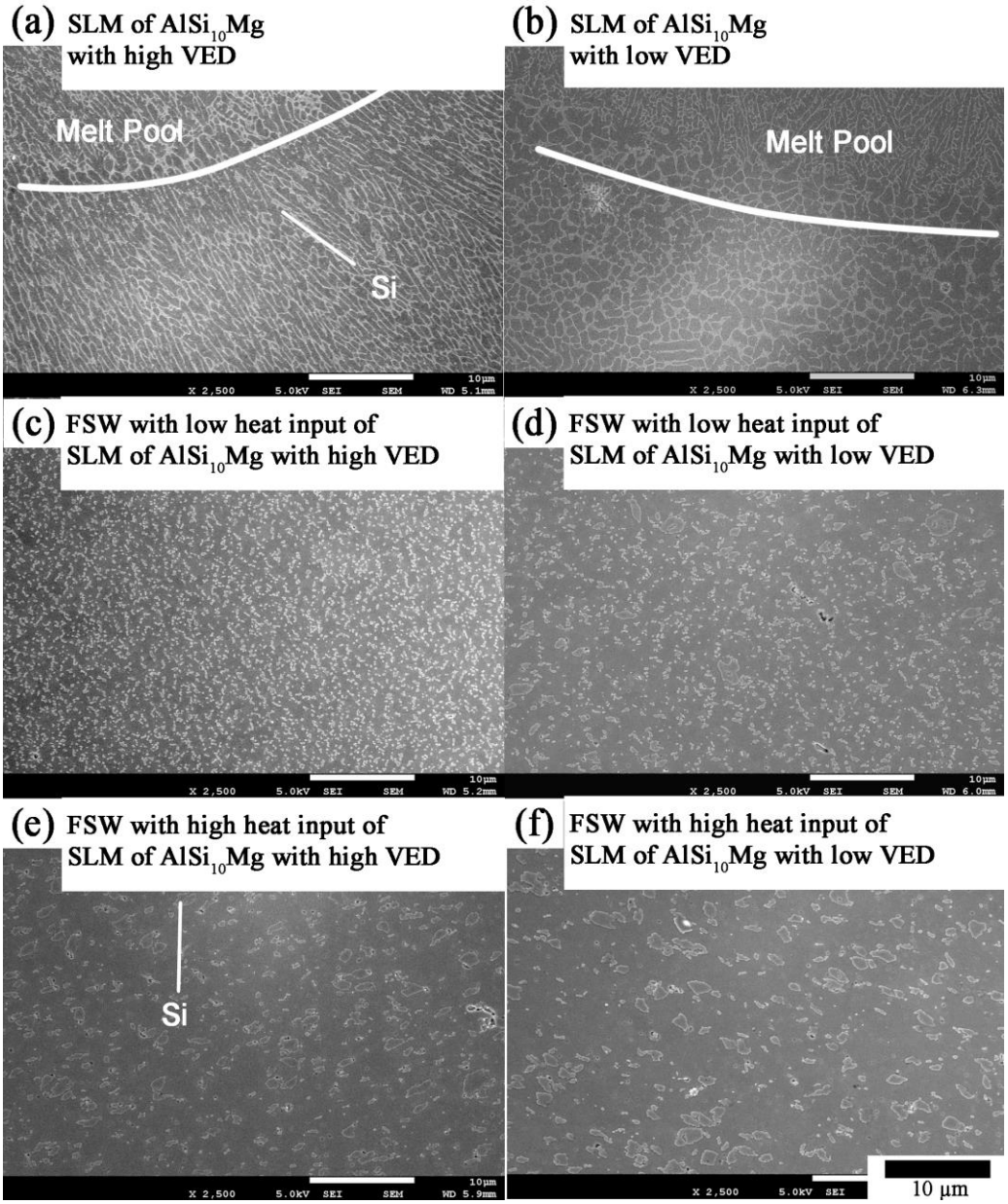

Figure 7-13 FESEM images of SLM of AlSi$_{10}$Mg with and without FSW.

Upon closer observation, significant larger Si-rich particles were observed in samples with higher heat input (Figure 7-13e and f). Li et al. [85] reported growth in the Si-rich particles due to coalescence of adjacent small Si-rich particles and Ostwald ripening. The thermal cycle from FSW is quite high at roughly 675K

[176]. Therefore, the higher welding temperature could have resulted in larger Si-rich particles.

From the FESEM images (Figure 7-14 and Figure 7-15), some of the nAl_2O_3 appeared to have agglomerated during the SLM process. The agglomeration process of the nAl_2O_3 was discussed in Chapter 5 and shall not be discussed here.

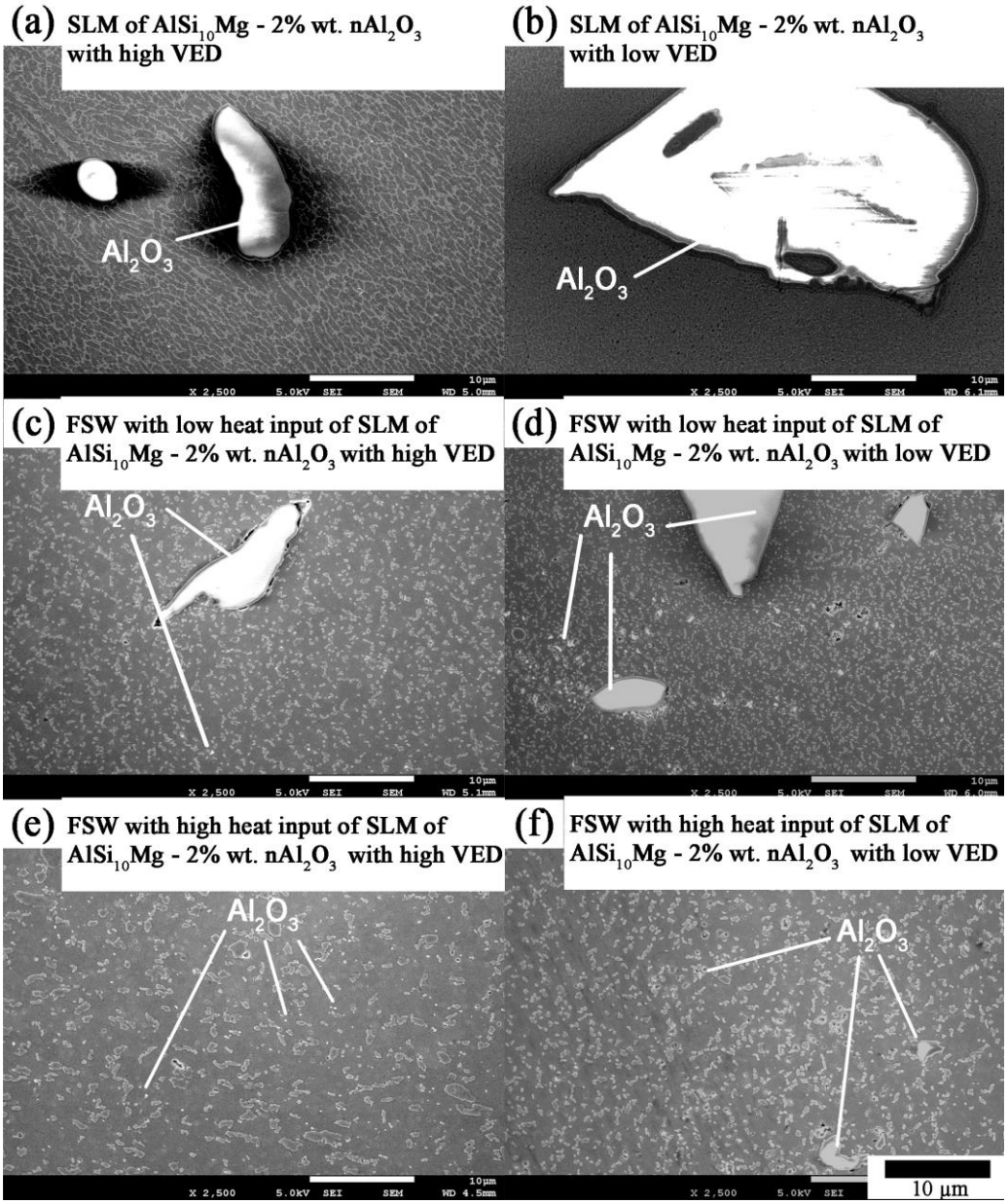

Figure 7-14 FESEM images of SLM of AlSi$_{10}$Mg - 2% wt. nAl$_2$O$_3$ with and without FSW.

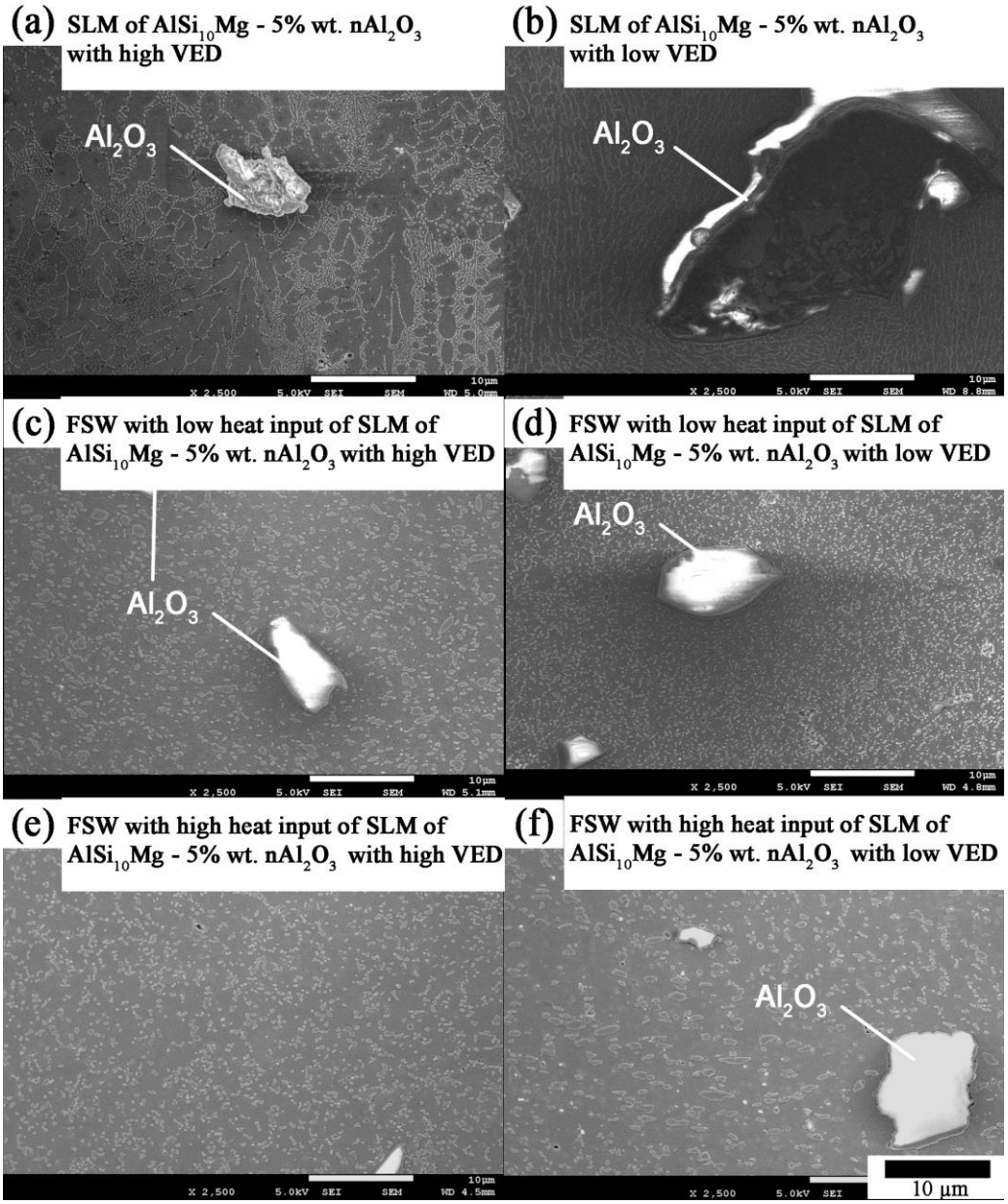

Figure 7-15 FESEM images of SLM of AlSi$_{10}$Mg - 5% wt. nAl2O3 with and without FSW.

After FSW, nAl_2O_3 particles were observed and believed to have fragmented and dispersed in the weld region (Figure 7-14c-f and Figure 7-15c-f). For FSW with low heat input of SLM of AlSi$_{10}$Mg - 2% wt. nAl_2O_3 with high VED and low VED (Figure 7-14c and d), small cavities were observed at the interface between

the nAl_2O_3 and the aluminium matrix. A similar observation was reported by Uzun [228] where cavities were observed at the Al/ SiC interface. The formation of cavities indicated lack of interfacial bonding from the lack of heat input. Higher welding temperature is required to soften the workpiece to close the cavities. Therefore, the interface and dispersion of nAl_2O_3 could be achieved with higher FSW heat input by using greater RS (Figure 7-14f).

As mentioned earlier, FSW with high heat input of SLM of $AlSi_{10}Mg$ with high VED showed larger Si-rich particles in comparison with its low FSW heat input counterpart. However, smaller Si-rich particles were observed with the addition of nAl_2O_3 reinforcements. This could be attributed to the addition of nAl_2O_3 which aided in breaking up the Si-rich particles as it moves along the matrix during FSW. For samples reinforced with nAl_2O_3, higher tool RS resulted in further breaking up of the nAl_2O_3 particles due to the increase in the plastic deformation. Root et al. [136] studied the crystallographic texture in the FSW of AA6061 with Al_2O_3 and observed that Al_2O_3 particles fractured from the contact with rotating tool during FSW.

7.3.5 Grain Structure Evolution

Electron backscatter diffraction (EBSD) was performed on the all the samples before and after FSW (Figure 7-16, Figure 7-17 and Figure 7-18). From the mapping, as-received SLM samples showed columnar grains in the direction of the thermal gradient (Figure 7-16a and b, Figure 7-17a and b and Figure 7-18a and b) as mentioned in the previous section.

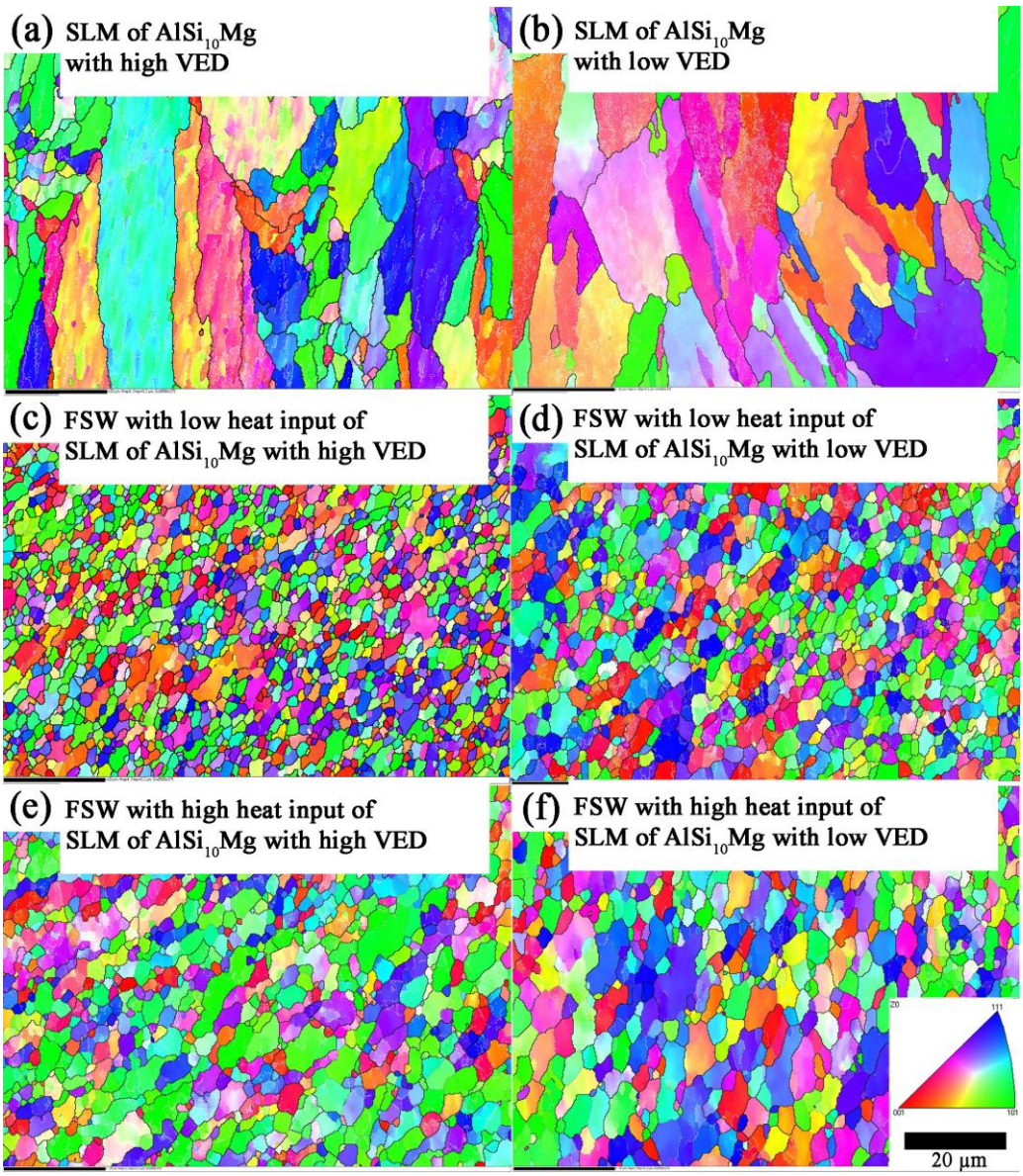

Figure 7-16 EBSD mapping of as-received and FSWed samples of SLM fabricated AlSi$_{10}$Mg. The scale bar indicates 20 µm. The boundary misorientation are indicated with white, grey and black lines for angles :1°to 5°, 5° to 15° and greater than 15° respectively.

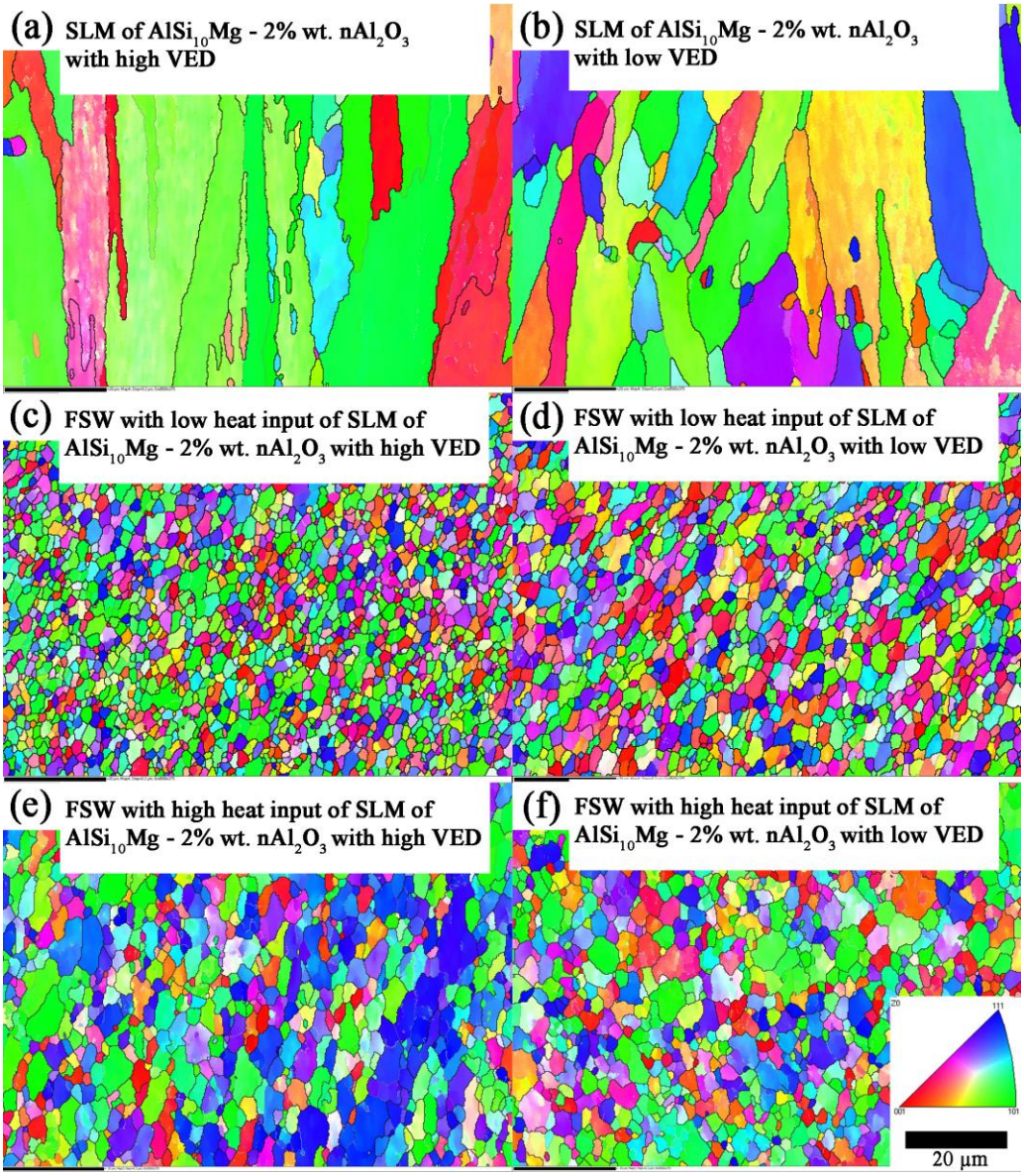

Figure 7-17 EBSD mapping of as-received and FSWed samples of SLM fabricated $AlSi_{10}Mg$ - 2% wt. nAl_2O_3. The scale bar indicates 20 µm. The boundary misorientation are indicated with white, grey and black lines for angles :1°to 5°, 5° to 15° and greater than 15° respectively.

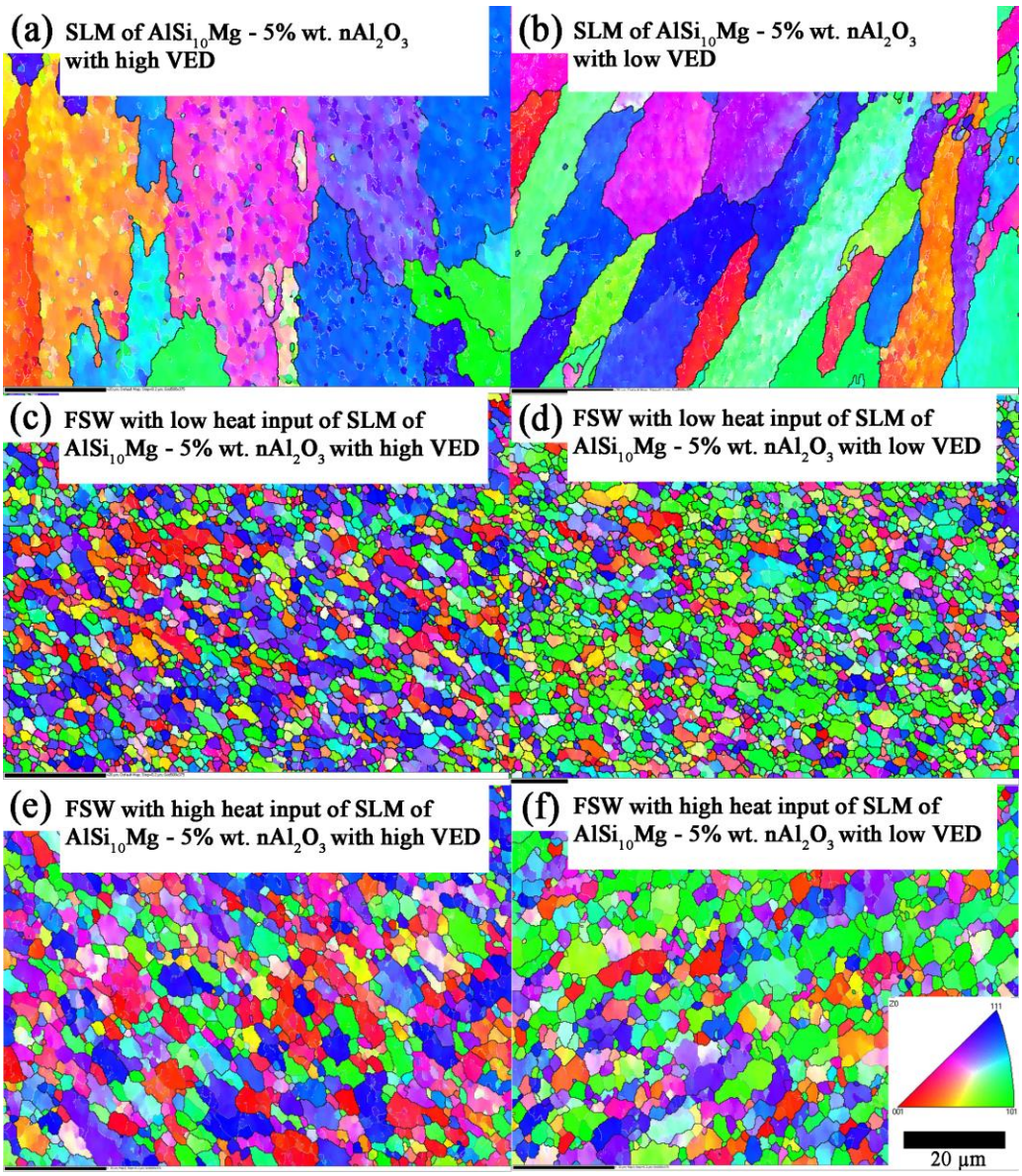

Figure 7-18 EBSD mapping of as-received and FSWed samples of SLM fabricated AlSi$_{10}$Mg - 5% wt. nAl$_2$O$_3$. The scale bar indicates 20 µm. The boundary misorientation are indicated with white, grey and black lines for angles :1°to 5°, 5° to 15° and greater than 15° respectively.

For FSWed samples, significant grain refinement with fine equiaxed grains was observed (Table 7-3) due to plastic deformation and dynamic recrystallisation occurring in the weld nugget. During FSW, the frictional heat was produced from the pin and shoulder. The shoulder generates more heat due to its larger area as well as the higher linear velocity at the outer radius. The combination of the

constant application of strain, migration of grain/subgrain boundaries and rapid recovery attributed to the continuous dynamic recrystallisation [170-172]. The weld region underwent intense deformation and intense continuously induced dislocations. The stored energy in the dislocations drove the dynamic recovery recrystallisation.

Table 7-3 Average grain size results of various $AlSi_{10}Mg$ and its composite before and after FSW.

Material and processes	Grain size (μm)		
	As-received	FSW with low heat input	FSW with high heat input
SLM of $AlSi_{10}Mg$ with low VED	7.4 ± 2	2.6 ± 1	3.5 ± 1
SLM of $AlSi_{10}Mg$ with high VED	8.2 ± 2	2.0 ± 1	2.8 ± 1
SLM of $AlSi_{10}Mg$ - 2% wt. nAl_2O_3 with low VED	6.4 ± 2	2.3 ± 1	2.6 ± 1
SLM of $AlSi_{10}Mg$ - 2% wt. nAl_2O_3 with high VED	7.4 ± 2	1.9 ± 1	2.2 ± 1
SLM of $AlSi_{10}Mg$ - 5% wt. nAl_2O_3 with low VED	5.8 ± 2	1.9 ± 1	2.2 ± 1
SLM of $AlSi_{10}Mg$ - 5% wt. nAl_2O_3 with high VED	6.3 ± 2	1.6 ± 1	1.8 ± 1

Zener pinning effect could have accounted for the finer grain sizes in the stir zone with nano-sized reinforcement particles by retarding the grain growth of the aluminium matrix. Rollett et al. [177] reported the rate of grain growth during the recrystallisation of metal with dispersed second phase particles could be described using equation (7-1).

$$\frac{dR}{dt} = M(P - P_z) = M\left(\frac{\alpha\gamma_b}{R} - \frac{3F_V\gamma_b}{2r}\right) \quad (7\text{-}1)$$

From the equation, F_v is the volume fraction, M is the boundary mobility, P is the driving pressure from the curvature of the grain boundaries, P_z is the Zener pinning pressure, R is the radius of the grain, r is the radius of the pinning Si-rich particles, α is a small geometric constant and γ_b is the boundary energy.

Therefore, when P=P_z, grain growth stops.

$$\frac{\alpha\gamma_b}{R} = \frac{3F_V\gamma_b}{2r} \quad (7\text{-}2)$$

Thus, the Zener limiting grain size (α=1) can be obtained when the mean grain radius (D) and the radius of curvature (R) are taken to be the same.

$$D_z = \frac{4r}{3F_v} \quad (7\text{-}3)$$

At present work, r = 0.15 μm, F_v = 0.10, the theoretical D_z = 1.9 μm for FSW samples without nAl_2O_3; r = 0.15 μm, F_v = 0.12, the theoretical D_z = 1.6 μm for FSW samples with 2% wt. nAl_2O_3 and r = 0.15 μm, F_v = 0.14, the theoretical D_z = 1.4 μm for FSW samples with 5% wt. nAl_2O_3. The slightly larger grain size measured by the EBSD as due to a small amount of the Si being spattered away and the agglomeration of the nAl_2O_3 during SLM process. The theoretical grain size can only serve as an indicative value as it is based on many assumptions that were not entirely true in reality.

From Table 7-3, a significant increase in grain size was identified when increasing RS from 600 rpm to 1200 rpm. Shojaeefard et al. [111] reported that maximum welding temperature increases with the use of shoulder with larger diameter due to greater heat being generated. In recent studies, the recrystallised grain size can be increased by increasing the RS [110, 112-114, 166-168] or by reducing the transverse speed [115]. Therefore, from the comparison of the grain sizes and the rotational speed to travel speed ratio (RS/TS), relative welding temperature conditions could be concluded.

From the Chapter 6, the heat input per unit length in a moving weld, Q, could be expressed as follows [117]:

$$Q = \frac{\alpha q}{V} = \frac{4}{3}\pi^2 \frac{\mu P N R^3}{V} \quad (7\text{-}4)$$

Where α is the slope is the heat input efficiency, and V is the travel speed.

All welding parameters were kept constant in this study except for tool RS while the average downward force was observed to be around 4 kN (Table 7-4). Therefore, the difference in grain size could only be due to the difference in welding temperature caused by the change in the RS.

Table 7-4 Average downward forces for FSW of AlSi$_{10}$Mg and its composites.

Downward force (kN) / Material and Processes	FSW with low heat input	FSW with high heat input
SLM of AlSi$_{10}$Mg with low VED	4.5 ± 0.1	3.8 ± 0.2
SLM of AlSi$_{10}$Mg with high VED	3.8 ± 0.1	4.0 ± 0.2
SLM of AlSi$_{10}$Mg - 2% wt. nAl_2O_3 with low VED	3.5 ± 0.2	3.5 ± 0.2
SLM of AlSi$_{10}$Mg - 2% wt. nAl_2O_3 with high VED	4.2 ± 0.2	3.8 ± 0.2
SLM of AlSi$_{10}$Mg - 5% wt. nAl_2O_3 with low VED	3.8 ± 0.2	4.4 ± 0.2
SLM of AlSi$_{10}$Mg - 5% wt. nAl_2O_3 with high VED	3.9 ± 0.2	4.1 ± 0.2

From Table 7-3, increasing addition of nAl_2O_3 caused a considerable decrease in the grain sizes. Particle simulated nucleation (PSN) is known to occur in heterogenous aluminium during recrystallisation [229]. It is believed that particle simulated nucleation (PSN) occurred during FSW. PSN is possible if dislocations accumulate at the large particles during deformation, low temperature and high strain rates [206]. From the FESEM images (Figure 7-14 and Figure 7-15), nAl_2O_3 particles larger than 1 micrometre in diameter were observed, therefore, PSN could have taken place. Another possible explanation is due to the existence

of nano-sized Si and remaining nano-sized nAl_2O_3 particles in the weld region. The Si-rich particles were significantly smaller in the FSWed samples with the addition of nAl_2O_3 particles. The finer grains could also be attributed to Zener pinning effect where the nano-particles exerted pinning pressure on the growing grains [5, 179].

The grain boundaries were further investigated using the misorientation profile from the EBSD for as-received SLM $AlSi_{10}Mg$ with high and low VED before and after FSW (Figure 7-19). From the misorientation profile (Table 7-5), a significant increase in the high angle boundaries was observed after FSW. FSW with high heat input was observed to have slightly lesser high angle grain boundaries. The increase in RS, TA and the decrease in the TS gave rise to a slight decrease in the high angle grain boundaries as previously reported in Chapter 6. The increase in RS, TA and reduction in TS leads to the increase in heat generation. It is believed that the increase in heat generation together with recrystallisation and recovery of the material led to the increase in the number of sub-grain boundaries (Figure 7-16) and a higher fraction of the low angle boundaries.

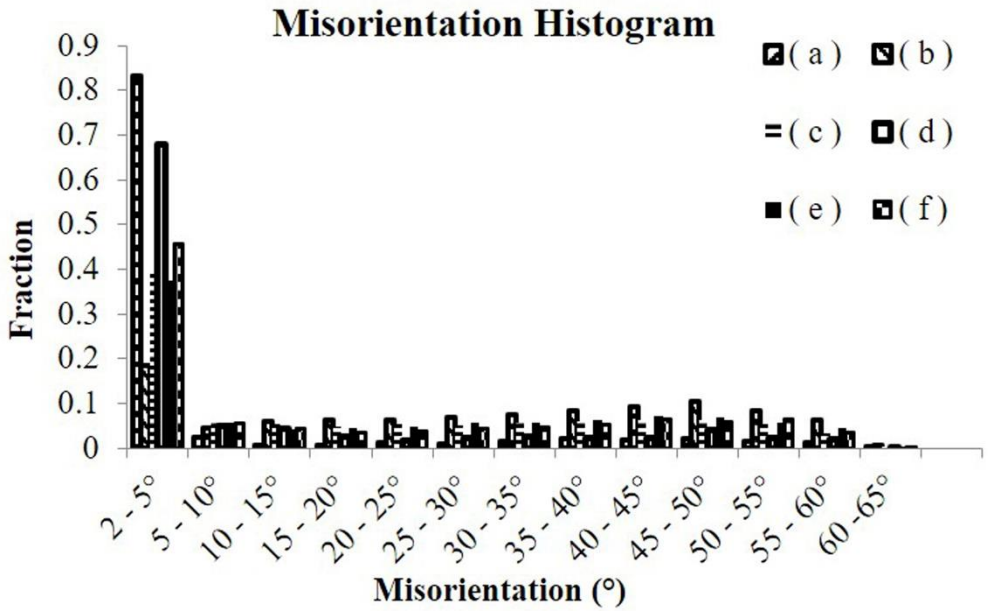

Figure 7-19 Histogram showing the distribution of grains/subgrain misorientation angles of as-received SLM of AlSi$_{10}$Mg with (a) high VED (b) low VED; FSW with low heat input of SLM of AlSi$_{10}$Mg with (c) high VED, (d) low VED; FSW with high heat input of SLM of AlSi$_{10}$Mg with (e) high VED, (f) low VED.

Table 7-5 Summaries results of grain/subgrain boundary misorientations for as-received SLM AlSi$_{10}$Mg before and after FSW.

Material and process	Mean grain misorientation (°)	Fraction of high-angle grain boundaries (>15°)	Fraction of low angle grain boundaries (<=15°)		Number of samples
			(2-5°)	(2-15°)	
As-received SLM AlSi$_{10}$Mg with high VED	7.07	0.14	0.83	0.86	99709
FSW with low heat input of SLM AlSi$_{10}$Mg with high VED	28.82	0.71	0.19	0.29	60846
FSW with high heat input of SLM AlSi$_{10}$Mg with high VED	20.04	0.49	0.39	0.51	56795
As-received SLM AlSi$_{10}$Mg with low VED	10.54	0.23	0.68	0.77	38078
FSW with low heat input of SLM AlSi$_{10}$Mg with low VED	21.68	0.53	0.37	0.47	59835
FSW with high heat input of SLM AlSi$_{10}$Mg with low VED	18.99	0.44	0.46	0.56	51157

The misorientation histogram for samples with the addition of nAl_2O_3 was plotted in Figure 7-20 and Figure 7-21 while the misorientation profile for high and low angle grain boundaries was tabulated in (Table 7-6 and Table 7-7). A significant increase in the fraction of high angle grain boundaries was observed when comparing samples before and after FSW. This agrees with the results mentioned earlier. The effect of nAl_2O_3 on the grain boundaries was further examined. Guo et al. [5] reported a reduction in the high angle boundaries in the FSP of AA6061 with the addition of nano-Al_2O_3. Tweed et al. [178] reported that high angle boundary might curve the boundary plane when it touches a second phase inclusion due to its high energy. This allows the boundary plane to bypass the particle before bending into a semi-circle. On the other hand, low angle grain boundaries are higher in flexibility and lower in energy, leading to more perturbed boundary plane. The cooperative process of migrating low angle grain boundaries requires the sequential movement of the constituent dislocation. Therefore, it was observed that all low angle boundaries were detected to display pinning effect while the relatively higher amount of high angle boundaries were unpinned. However, in this study, it was observed that the addition of nAl_2O_3 resulted in slight increase in the high angle grain boundaries. The agglomerated Al_2O_3 could have resulted in PSN allowing more grains to nucleate at the interface and increasing the amount of high angle grain boundaries. The nAl_2O_3 could also have caused more dislocations during FSW. The dislocations may turn into high angle boundaries via rotation assisted by dislocation glide [230].

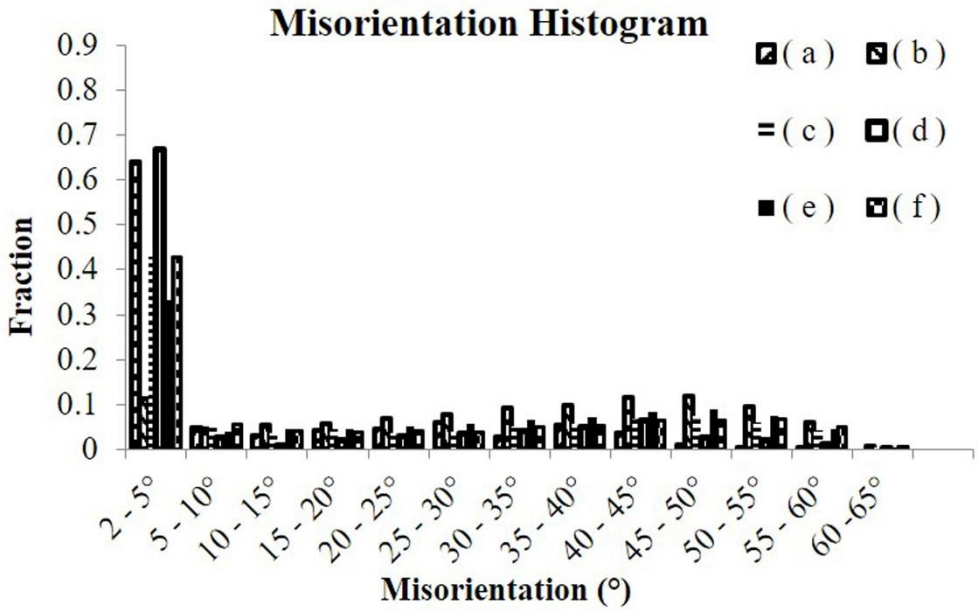

Figure 7-20 Histogram showing the distribution of grains/subgrain misorientation angles of as-received SLM $AlSi_{10}Mg$ - 2% wt. nAl_2O_3 with (a) high VED (b) low VED; FSW with low heat input of SLM of $AlSi_{10}Mg$ - 2% wt. nAl_2O_3 with (c) high VED, (d) low VED; FSW with high heat input of SLM of $AlSi_{10}Mg$ - 2% wt. nAl_2O_3 with (e) high VED, (f) low VED.

Table 7-6 Summaries results of grain/subgrain boundary misorientations for as-received SLM $AlSi_{10}Mg$ - 2% wt. nAl_2O_3 before and after FSW.

Material and process	Mean grain misorientation (°)	Fraction of high-angle grain boundaries (>15°)	Fraction of low angle grain boundaries (<=15°)		Number of samples
			(2-5°)	(2-15°)	
As-received SLM $AlSi_{10}Mg$ - 2% wt. nAl_2O_3 with high VED	10.26	0.28	0.64	0.72	30291
FSW with low heat input of SLM $AlSi_{10}Mg$ - 2% wt. nAl_2O_3 with high VED	32.01	0.79	0.11	0.21	58112
FSW with high heat input of SLM $AlSi_{10}Mg$ - 2% wt. nAl_2O_3 with high VED	20.46	0.48	0.43	0.52	56998
As-received SLM $AlSi_{10}Mg$ - 2% wt. nAl_2O_3 with low VED	12.08	0.29	0.67	0.71	34641
FSW with low heat input of SLM $AlSi_{10}Mg$ - 2% wt. nAl_2O_3 with low VED	24.16	0.59	0.33	0.41	63792
FSW with high heat input of SLM $AlSi_{10}Mg$ - 2% wt. nAl_2O_3 with low VED	20.59	0.48	0.43	0.52	63133

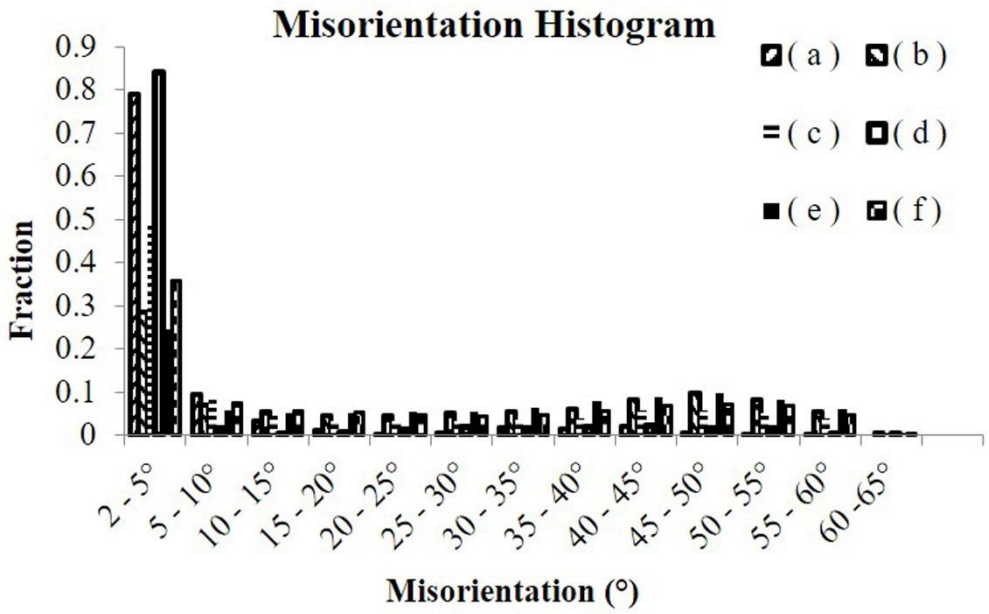

Figure 7-21 Histogram showing the distribution of grains/subgrain misorientation angles of as-received SLM $AlSi_{10}Mg$ - 5% wt. nAl_2O_3 with (a) high VED (b) low VED; FSW with low heat input of SLM of $AlSi_{10}Mg$ - 5% wt. nAl_2O_3 with (c) high VED, (d) low VED; FSW with high heat input of SLM of $AlSi_{10}Mg$ - 5% wt. nAl_2O_3 with (e) high VED, (f) low VED.

Table 7-7 Summaries results of grain/subgrain boundary misorientations for as-received SLM $AlSi_{10}Mg$ - 5% wt. nAl_2O_3 before and after FSW.

Material and process	Mean grain misorientation (°)	Fraction of high-angle grain boundaries (>15°)	Fraction of low angle grain boundaries (<=15°)		Number of samples
			(2-5°)	(2-15°)	
As-received SLM $AlSi_{10}Mg$ - 5% wt. nAl_2O_3 with high VED	5.30	0.08	0.79	0.92	62627
FSW with low heat input of SLM $AlSi_{10}Mg$ - 5% wt. nAl_2O_3 with high VED	25.32	0.59	0.29	0.41	71846
FSW with high heat input of SLM $AlSi_{10}Mg$ - 5% wt. nAl_2O_3 with high VED	17.35	0.39	0.49	0.61	71480
As-received SLM $AlSi_{10}Mg$ - 5% wt. nAl_2O_3 with low VED	6.51	0.14	0.84	0.86	73245
FSW with low heat input of SLM $AlSi_{10}Mg$ - 5% wt. nAl_2O_3 with low VED	26.94	0.64	0.25	0.36	74188
FSW with high heat input of SLM $AlSi_{10}Mg$ - 5% wt. nAl_2O_3 with low VED	21.56	0.51	0.36	0.49	56412

7.3.6 Micro-hardness

The micro-hardness results of as-received SLM of $AlSi_{10}Mg$ and its composites before and after FSW were collected and tabulated in Table 7-8. Comparing all the as-received SLM of $AlSi_{10}Mg$ and its composites, it was observed that only as-received SLM of $AlSi_{10}Mg$ - 2% wt. nAl_2O_3 with high VED and as-received SLM of $AlSi_{10}Mg$ - 5% wt. nAl_2O_3 with high VED have lower micro-hardness compared to conventional rolled AA6061-T6. This could be due to the use of relatively high VED (Table 7-1) resulting in the coarsening of the finely dispersed eutectic Si phase together with the dissolution of hardening precipitates of Mg_2Si as mention earlier in the weld microstructure section [85].

After FSW, hardness was observed to have dropped even though grain refinement was achieved. Liu et al. [98] conducted a study on FSW butt weld of AA6061-T6 and observed a similar decrease in hardness in the weld nugget with Vickers hardness of 66 HV. Other studies have also observed similar trends and concluded that dissolution of hardening precipitates in the weld region gave rise to the reduction of the hardness in comparison to the parent material [218, 224]. Further reduction of the hardness was observed in samples with higher heat input could be explained by the larger grain sizes via the Hall-Petch equation [28, 231]. The difference in the micro-hardness values among the FSWed samples could be explained by the difference in the strengthening contribution of the grain size difference based on the Hall-Petch equation as explained in Chapter 6 [28].

Comparing among FSW samples with low heat input and low VED, a significant increase in the hardness results were observed with increase addition of nAl_2O_3. A similar observation was identified from samples with FSW with low heat input and high VED, FSW with high heat input and low VED as well as FSW with high heat input and high VED. This could be due to the finer grains resulting from the addition of nAl_2O_3 and Zener pinning effect explained earlier.

The horizontal Vickers hardness profile of the welds are shown in Figure 7-22, Figure 7-23 and Figure 7-24. Considerable softening in the weld region was observed throughout the weld zone. It was suggested that the thermal cycle of FSW caused the coarsening and dissolution of strengthening precipitates resulting in the softening of the weld region [98, 112, 137, 166, 176]. Sato et al. [176] reported that precipitate distribution has a stronger influence on the hardness profile than the grain size in the weld. The increase in the welding RS should have improved the precipitation distribution and increased the hardness. However, higher RS also resulted in greater welding temperature and more Si being precipitated out from the aluminium composite substrates, leading to a drop in the hardness.

Table 7-8 Micro-hardness results.

Material and Processes	Micro-hardness (HV)		
	As-received	FSW with low heat input	FSW with high heat input
SLM of $AlSi_{10}Mg$ with low VED	139 ± 5	68 ± 4	67 ± 3
SLM of $AlSi_{10}Mg$ - 2% wt. nAl_2O_3 with low VED	124 ± 6	75 ± 3	74 ± 2
SLM of $AlSi_{10}Mg$ - 5% wt. nAl_2O_3 with low VED	123 ± 3	80 ± 1	77 ± 2
SLM of $AlSi_{10}Mg$ with high VED	127 ± 3	75 ± 1	71 ± 2
SLM of $AlSi_{10}Mg$ - 2% wt. nAl_2O_3 with high VED	104 ± 4	81 ± 2	77 ± 4
SLM of $AlSi_{10}Mg$ - 5% wt. nAl_2O_3 with high VED	93 ± 4	84 ± 3	81 ± 5
AA6061-O		55 ± 3	
AA6061-T6		107 ± 4	
FSW AA6061-T6 [98]		66 ± 3	

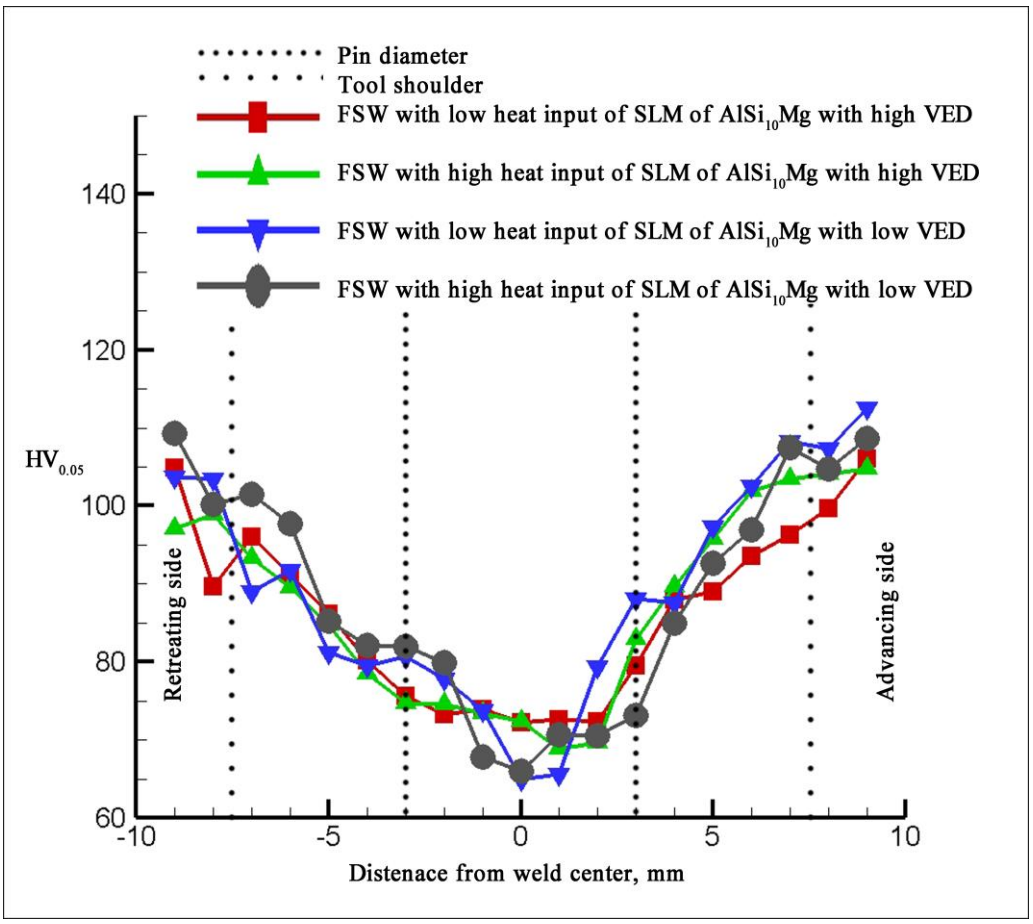

Figure 7-22 Hardness profile of FSWed samples of SLM fabricated AlSi$_{10}$Mg.

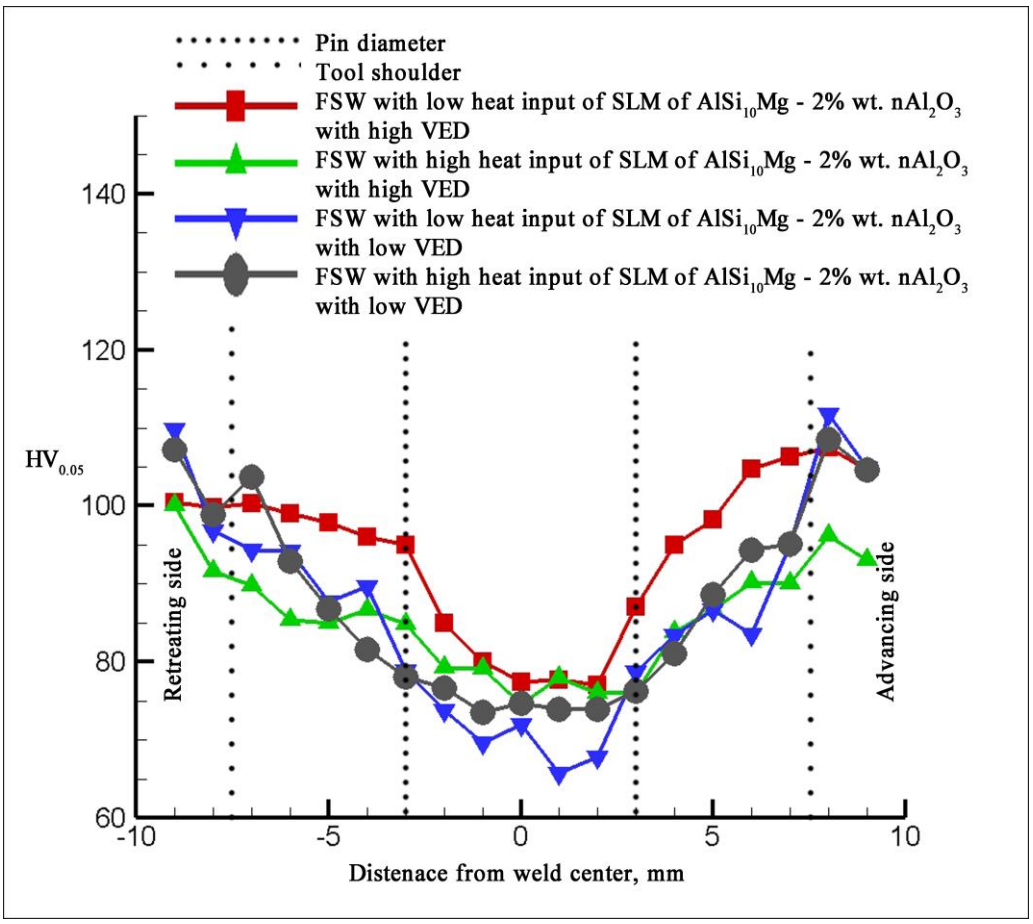

Figure 7-23 Hardness profile of FSWed samples of SLM fabricated AlSi$_{10}$Mg - 2% wt. nAl$_2$O$_3$ composites.

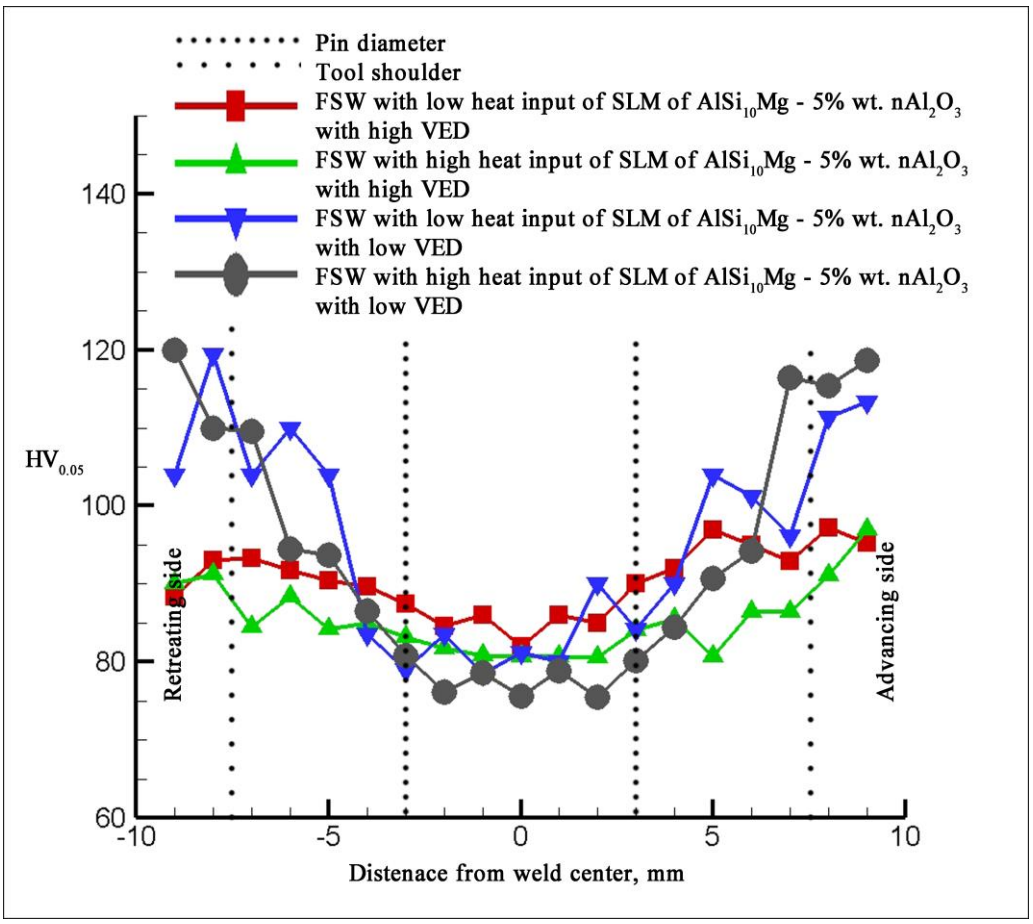

Figure 7-24 Hardness profile of FSWed samples of SLM fabricated AlSi$_{10}$Mg - 5% wt. nAl_2O_3 composites.

7.3.7 Tensile Strength

The tensile results of as-received samples were plotted (Figure 7-25) (Appendix C), SLM of AlSi$_{10}$Mg has superior mechanical properties. The significant improvement is mainly attributed to the very fine eutectic microstructure in the SLM part as well as the presence of very fine Si-rich particles (Figure 7-13a) [85]. The reduction in the distance between the Si-rich particles contributed to the improvement in strength as dislocations movements were reduced and localised shear stress can be relieved with increasing Al-Si interface. The addition of nAl_2O_3 resulted in an increase in porosity which led to the reduction of yield strength and ultimate tensile strength.

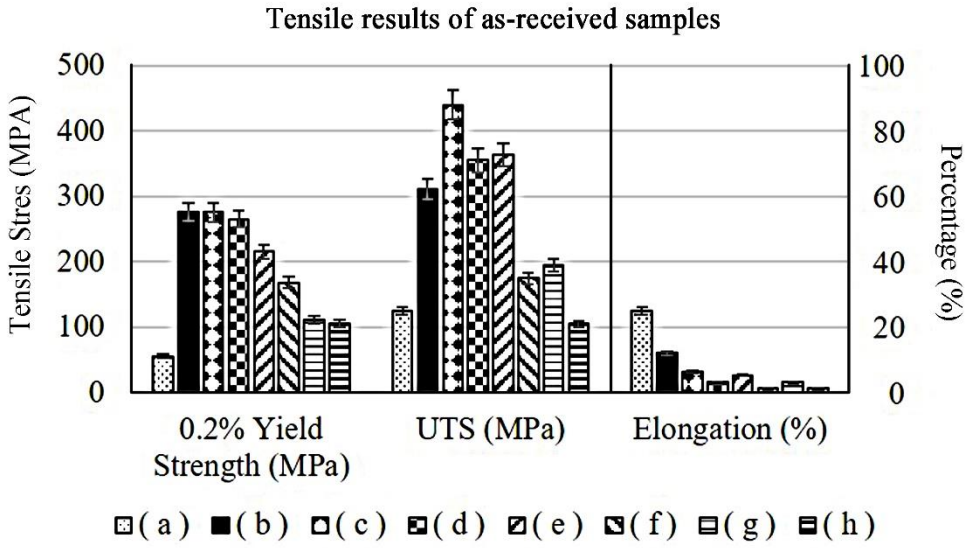

Figure 7-25 Tensile results of as rolled sheets (a) AA6061-O, (b) AA6061-T6; As-received SLM of AlSi$_{10}$Mg with (c) high VED, (d) low VED; As-received SLM of AlSi$_{10}$Mg - 2% wt. nAl_2O_3 with (e) high VED, (f) low VED; As-received SLM of AlSi$_{10}$Mg - 5% wt. nAl_2O_3 with (g) high VED, (h) low VED.

Looking at tensile samples of FSW of SLM of AlSi$_{10}$Mg (Figure 7-26d, e, g and h), a significant reduction in the yield strength was observed. This agrees with the observation in lower hardness in the weld region. Li et al. [85] reported a significant decrease in the tensile strength of the AlSi$_{10}$Mg after heat treatment. In their study, the drop in the tensile strength was mainly attributed to the coarsening of the Si-rich particles and dissolution of hardening precipitates. This agrees with the FESEM image (Figure 7-13c-f) showing coarsening of Si-rich particles after FSW. Ductility was observed to have improved after FSW due to the reduction of residual stresses from the thermal cycle of FSW [85].

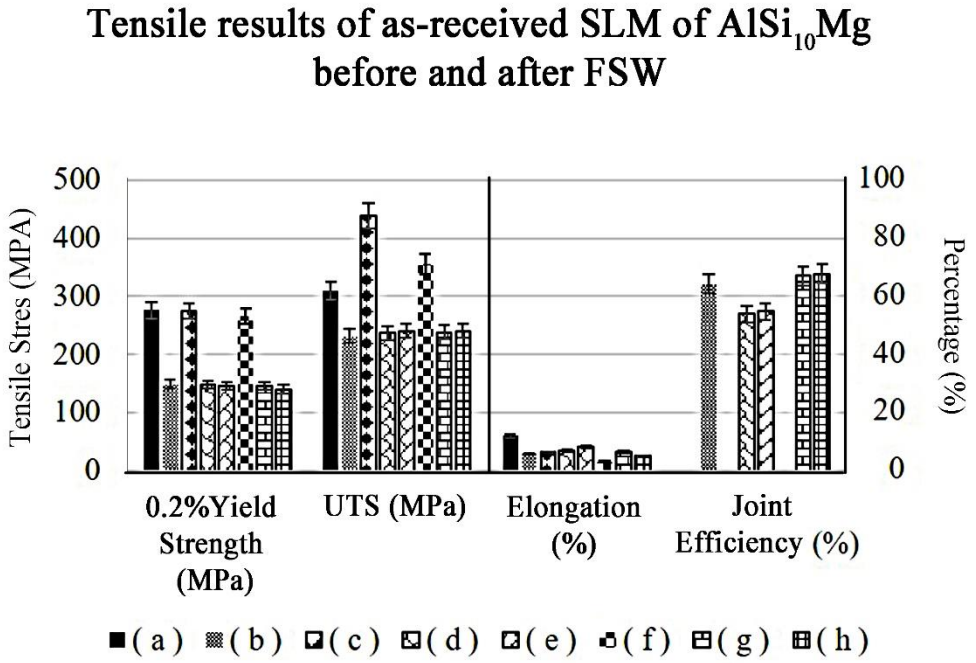

Figure 7-26 Tensile results of rolled sheets AA6061-T6 (a) as-received, (b) FSWed [219]; SLM of AlSi$_{10}$Mg with high VED (c) as-received, (d) FSW with low heat input, (e) FSW with high heat input; SLM of AlSi$_{10}$Mg with low VED (f) as-received, (g) FSW with low heat input, (h) FSW with high heat input.

Comparing between FSW of AlSi$_{10}$Mg with high and low heat input (Figure 7-26d, e, g and h), the increase in welding temperature resulted in a slight reduction in the yield strength and ultimate tensile strength. The increase in welding temperature increased in grain size. The relationship between the increase in grain size and the reduction in tensile strength could be explained using the Hall-Petch equation mentioned earlier. Considerable better ductility was observed with increase in welding temperature. The increase in Si-rich particles size together with its decrease in numbers (Figure 7-13d and e) could have attributed to the reduction of localised stress or strain and better ductility [208].

Comparing between FSWed SLM of $AlSi_{10}Mg$ with low VED (Figure 7-26g and h) and FSWed SLM of $AlSi_{10}Mg$ with high VED (Figure 7-26d and e), no significant difference in the tensile strength was observed. However, the reduction in porosity of the weld region during dynamic recrystallisation of the FSW process was observed. FSW is capable of welding $AlSi_{10}Mg$ with comparable weld strength and joint efficiency (>50%).

Looking at SLM samples with 2% wt. nAl_2O_3 added (Figure 7-27), a significant reduction in the tensile strength was observed. However, grain refinement and increase in hardness mentioned earlier should have resulted in higher yield strength. From the FESEM images (Figure 7-14), it was observed that some of the nAl_2O_3 have agglomerated and sintered to form micro-sized particles during the SLM process. This could have acted as stress concentrator during tensile test leading to the reduction in the tensile properties for SLM of $AlSi_{10}Mg$ - 2% wt. nAl_2O_3 with high VED samples. Higher porosity was observed in SLM of $AlSi_{10}Mg$ - 2% wt. nAl_2O_3 with low VED samples, which led to further reduction in the tensile properties. After FSW, the dissolution of hardening precipitates could have further lowered the tensile strength as mention earlier.

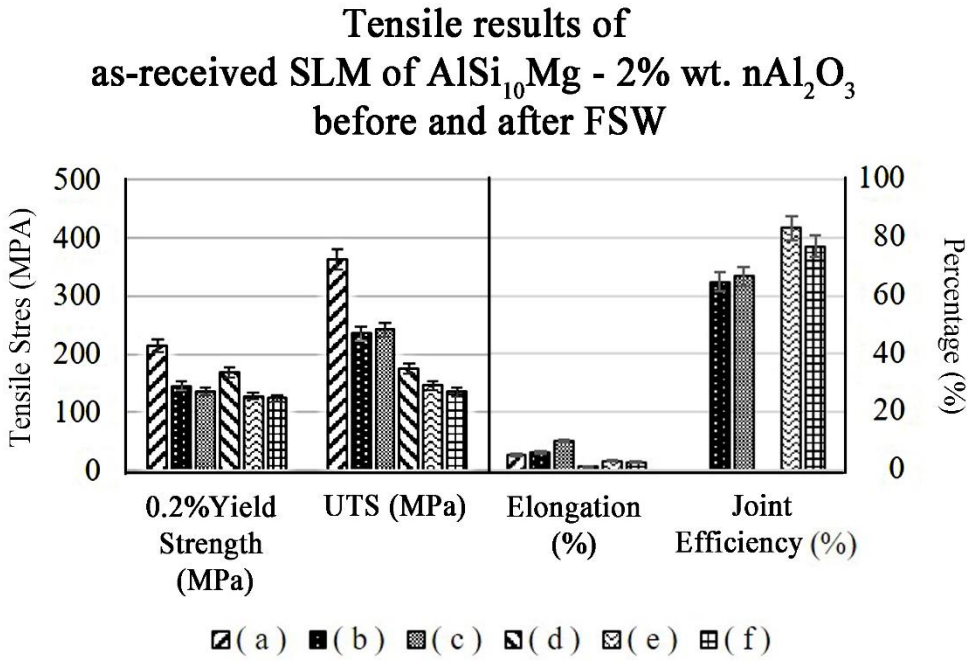

Figure 7-27 Tensile results of SLM of $AlSi_{10}Mg$ - 2% wt. nAl_2O_3 with high VED (a) as-received, (b) FSW with low heat input, (c) FSW with high heat input; SLM of $AlSi_{10}Mg$ - 2% wt. nAl_2O_3 with low VED (d) as-received, (e) FSW with low heat input, (f) FSW with high heat input.

Looking at the SLM samples with 5% wt. nAl_2O_3, significant reduction in the tensile strength was observed. From the FESEM images (Figure 7-15), it was observed that some of the nAl_2O_3 have agglomerated and sintered to form micro-sized particles. The fracture mechanism is similar to that of SLM samples with 2% wt. nAl_2O_3. A larger amount of porosity in the SLM samples with 5% wt. nAl_2O_3 further reduction in the tensile properties. For SLM of $AlSi_{10}Mg$ - 5% wt. nAl_2O_3 with high VED samples, porosity observed were spherical shape attributed by high VED resulting in trapped gas in the matrix while SLM of $AlSi_{10}Mg$ - 5% wt. nAl_2O_3 with low VED samples showed porosity with sharp edges (Figure 5-3). The presence of porosity with sharp edges acted as stress concentrators during tensile testing and resulted in further reduction in tensile strength.

The post weld heat treatment of FSWed samples of AA6601 were able to provide strengthening effect on the welded material. However, several studies have been done on the heat treatment on SLM fabricated parts. Li et at. [85] conducted post-SLM ageing of $AlSi_{10}Mg$ and observed a reduction of strength in the parts. The yield strength is approximately 126 MPa. In another study by Zhang et al. [232], ageing was performed on Al-7 wt. % Si-0.3 wt. % Mg parts. The yield strength reported was approximately 150 MPa. In this study, the yield strength of FSWed samples was approximately 146 MPa. Therefore, post-weld ageing may not recover the loss of strength. In addition, post-weld ageing will result in a significant loss of strength in the base material.

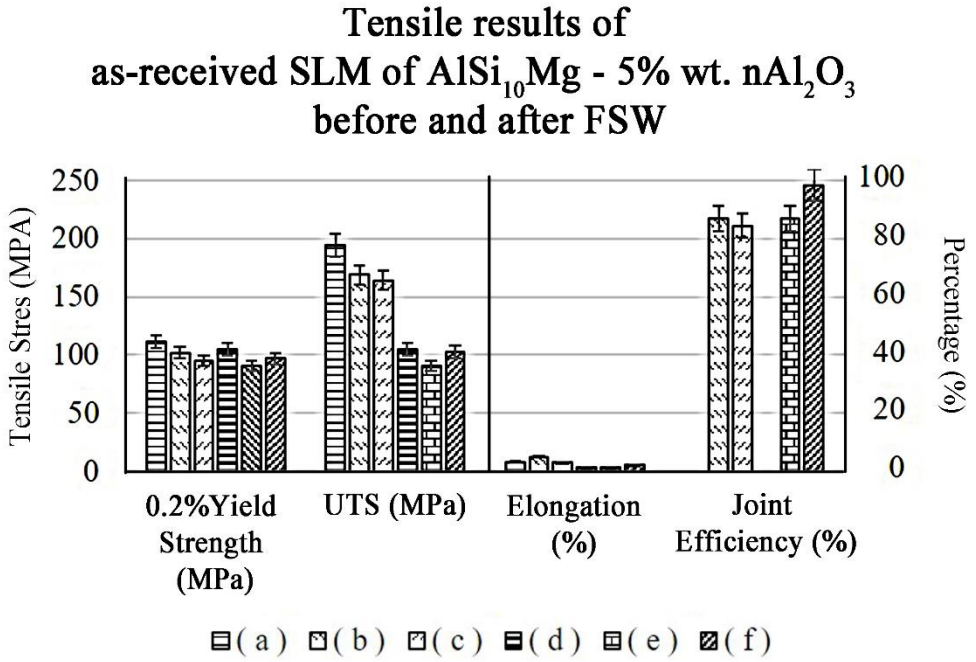

Figure 7-28 Tensile results of SLM of $AlSi_{10}Mg$ - 5% wt. nAl_2O_3 with high VED (a) as-received, (b) FSW with low heat input, (c) FSW with high heat input; SLM of $AlSi_{10}Mg$ - 5% wt. nAl_2O_3 with low VED (d) as-received, (e) FSW with low heat input, (f) FSW with high heat input.

7.3.8 Fractography

The cross-sectional view of the fracture site of $AlSi_{10}Mg$ with high VED and low VED (Figure 7-29 and Figure 7-30) were studied. SLM of $AlSi_{10}Mg$ with high and low VED fractured without visible necking, and fracture path is perpendicular to the direction of the applied force. FSW with low heat input of SLM of $AlSi_{10}Mg$ with high VED (Figure 7-29d) as well as FSW with low and high heat input of SLM of $AlSi_{10}Mg$ with low VED (Figure 7-30d and e) samples fractured at the TMAZ region of the advancing side while FSW with high heat input of SLM of $AlSi_{10}Mg$ with high VED fracture in the stir zone. Significant necking at the weld regions was observed for all FSW samples of SLM fabricated $AlSi_{10}Mg$. Moreira et al. [219] studied the FSW of AA6061 with RS/TS of 5 revolutions/mm and observed fracture occurring near the weld edge line, conforming to the region between the TMAZ and HAZ. This is believed that the dissolution of hardening precipitates gave rise to the reduction in strength. For FSW with high heat input of SLM fabricated $AlSi_{10}Mg$ with high VED, fracture occurred in the stir zone due to the higher heat input leading to the considerable amount of dissolution of hardening precipitates and coarsening of Si-rich particles from as identified in FESEM (Figure 7-13e and f) and XRD (Figure 7-4c).

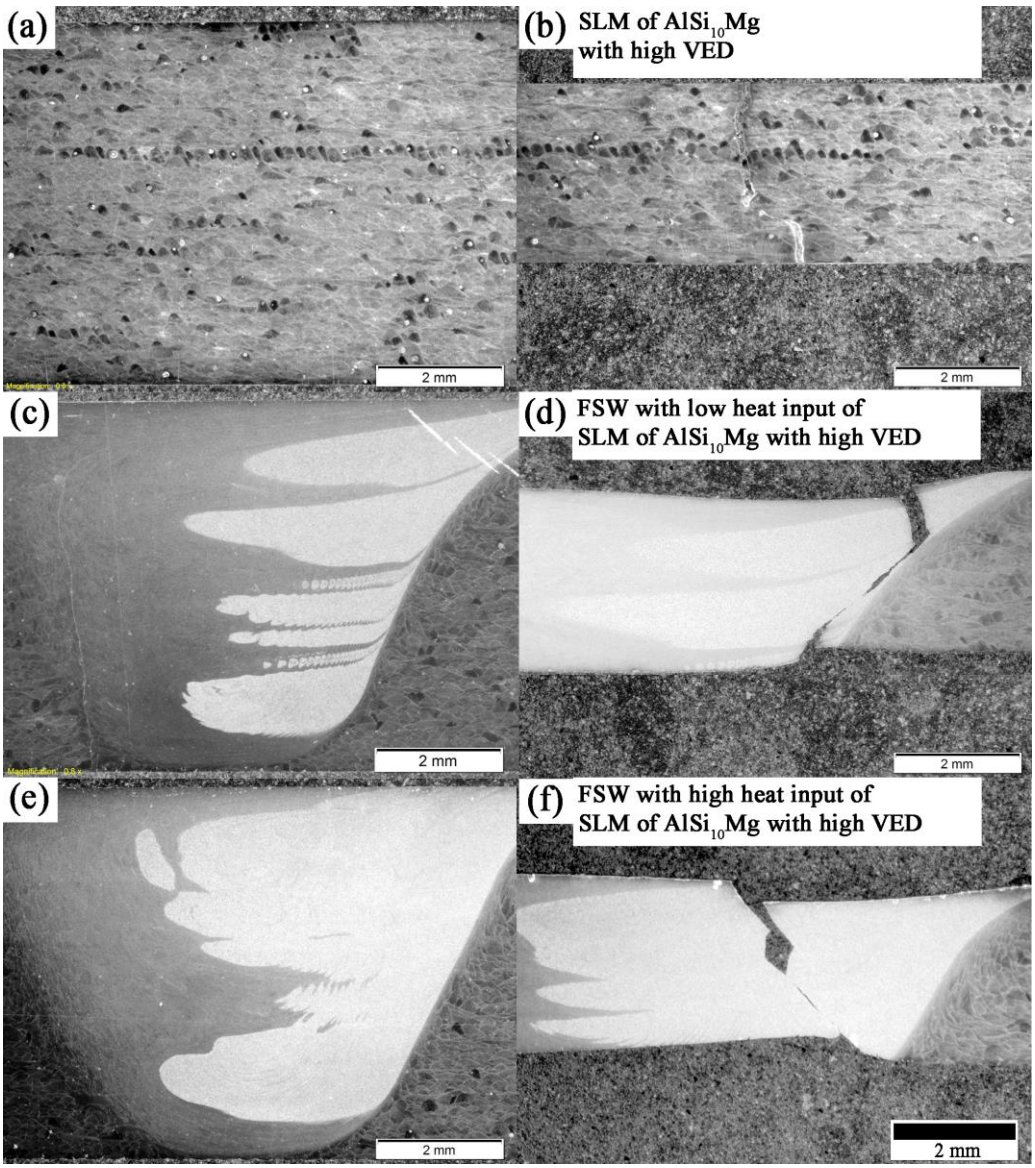

Figure 7-29 Cross-sectional view of the samples before (left) and after the tensile test (right).

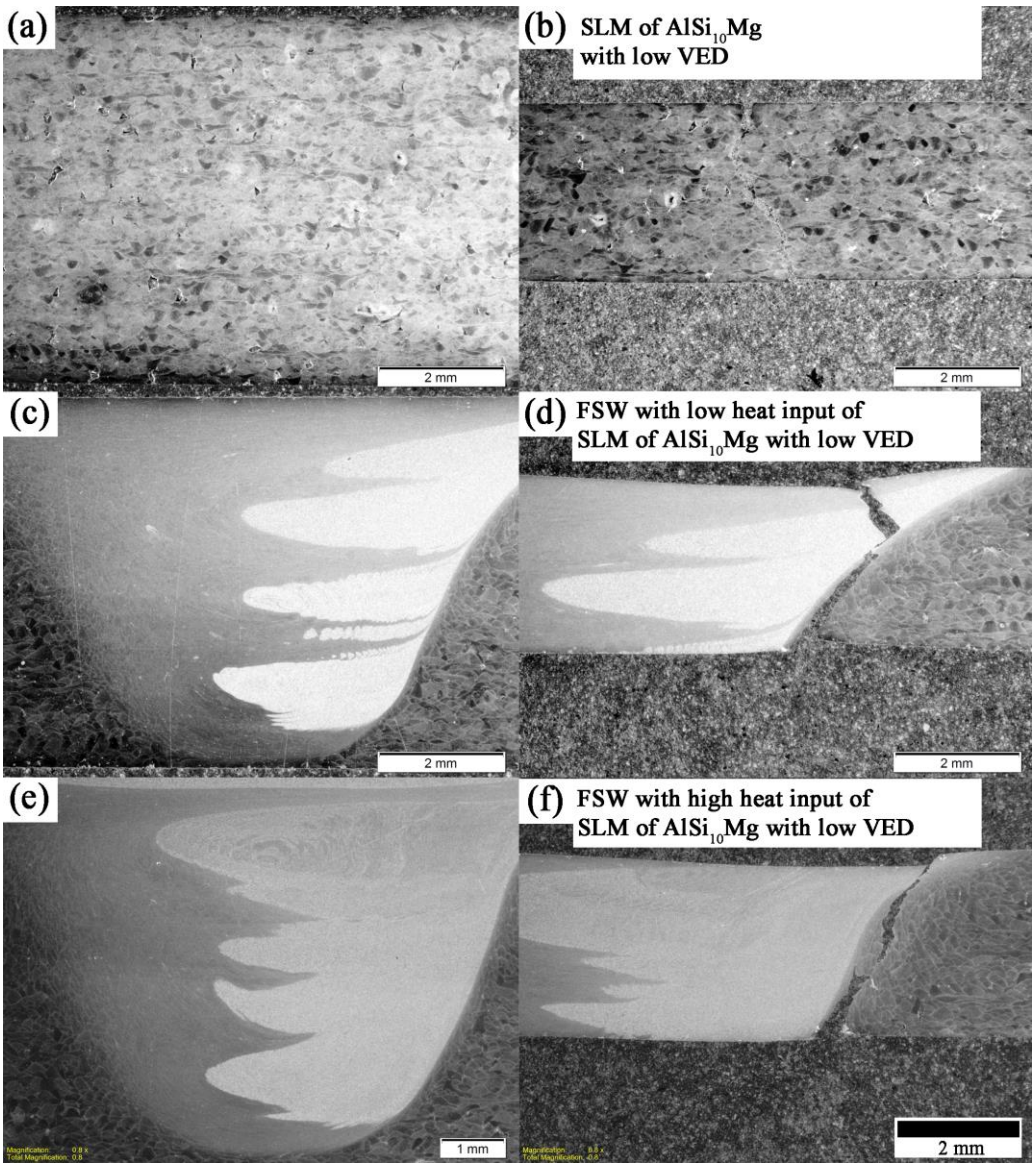

Figure 7-30 Cross-sectional view of the samples before (left) and after the tensile test (right).

Observation of the fracture site under the FESEM (Figure 7-31) reviews the fracture mechanism that took place at the fracture site. Looking at fracture surface of the as-received SLM of $AlSi_{10}Mg$ with high VED (Figure 7-31a) and low VED (Figure 7-31b), elongated dimples were observed at the fracture surfaces indicating ductile mode fracture mechanism. The grains of the SLM of $AlSi_{10}Mg$

samples are columnar and grows along the thermal gradient in the melt pool. Therefore, crack propagation could be along the grain boundaries resulting in elongated dimples. Voids were also detected on the fracture surfaces indicating the presence of small pores in the material.

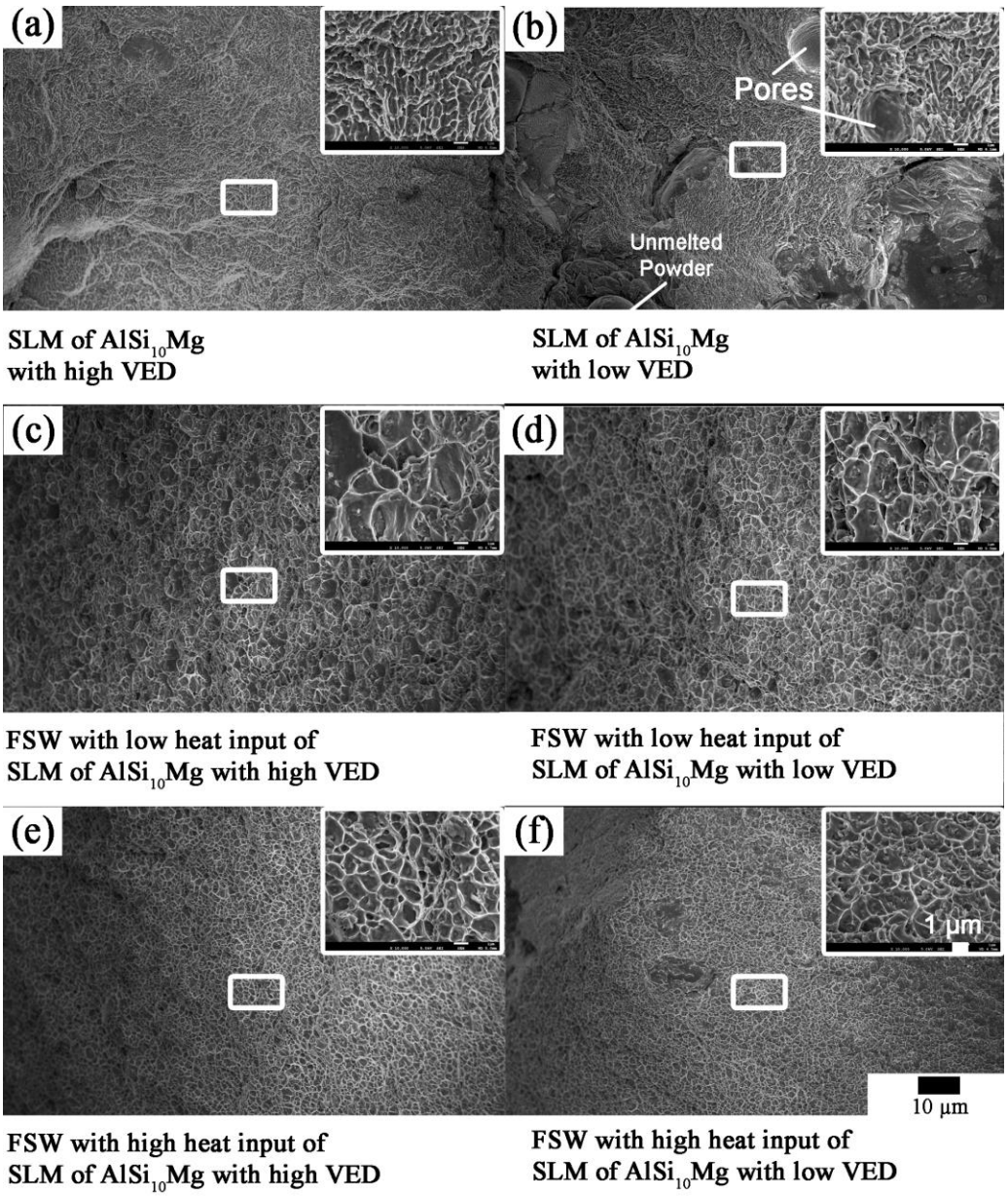

Figure 7-31 Fractography of SLM of AlSi$_{10}$Mg with and without FSW.

Looking at the fracture site of the FSWed samples (Figure 7-31c-f), equiaxed dimples were observed indicating ductile mode fracture mechanism. Similar dimple structure was observed in samples with same FSW parameters. Smaller dimples were observed in samples with high heat input indicating higher ductility of the material which is consistent with the tensile results mentioned earlier. During the tensile test, the slight plastic deformation phase as seen in the stress-strain curve could be due to the development of microvoids at the grain boundaries. These voids continued to grow as the stress increases. The voids eventually merged and formed cracks that lead to the failure of the material.

The cross-sectional view (Figure 7-32 and Figure 7-33) and the FESEM image of the fracture site (Figure 7-34) of as-received SLM of $AlSi_{10}Mg$ - 2% wt. nAl_2O_3 with high VED and low VED were studied. SLM of $AlSi_{10}Mg$ - 2% wt. nAl_2O_3 with high and low VED fractured without visible necking, and the fracture path is perpendicular to the applied force similar to as-received SLM of $AlSi_{10}Mg$ with high VED and low VED. SLM of $AlSi_{10}Mg$ - 2% wt. nAl_2O_3 with low VED appeared to have fracture along the path connecting the porosity. The sharp edges of the porosity could have acted as stress concentrators during tensile testing, resulting in a reduction in the tensile strength.

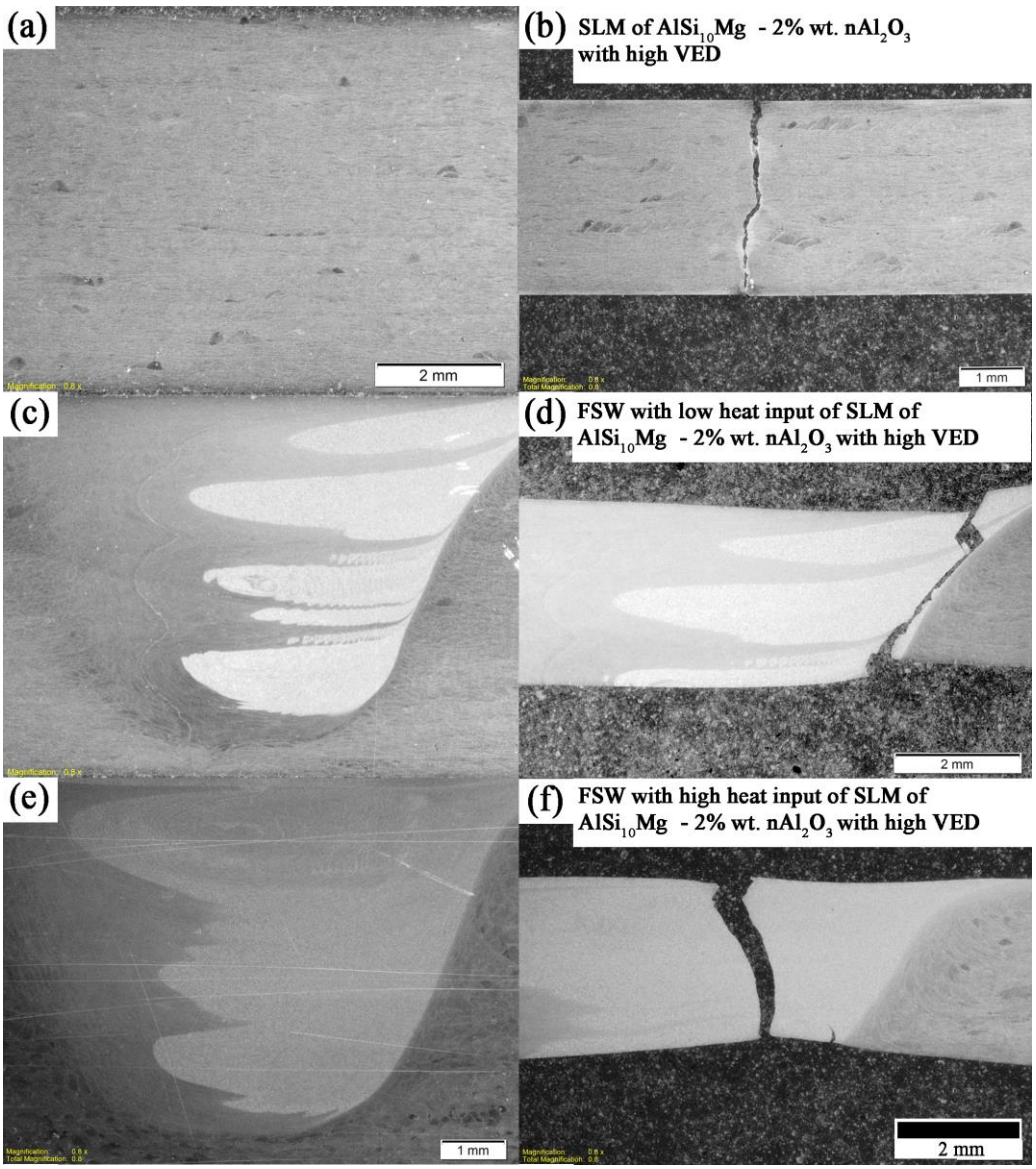

Figure 7-32 Cross-sectional view of the samples before (left) and after the tensile test (right).

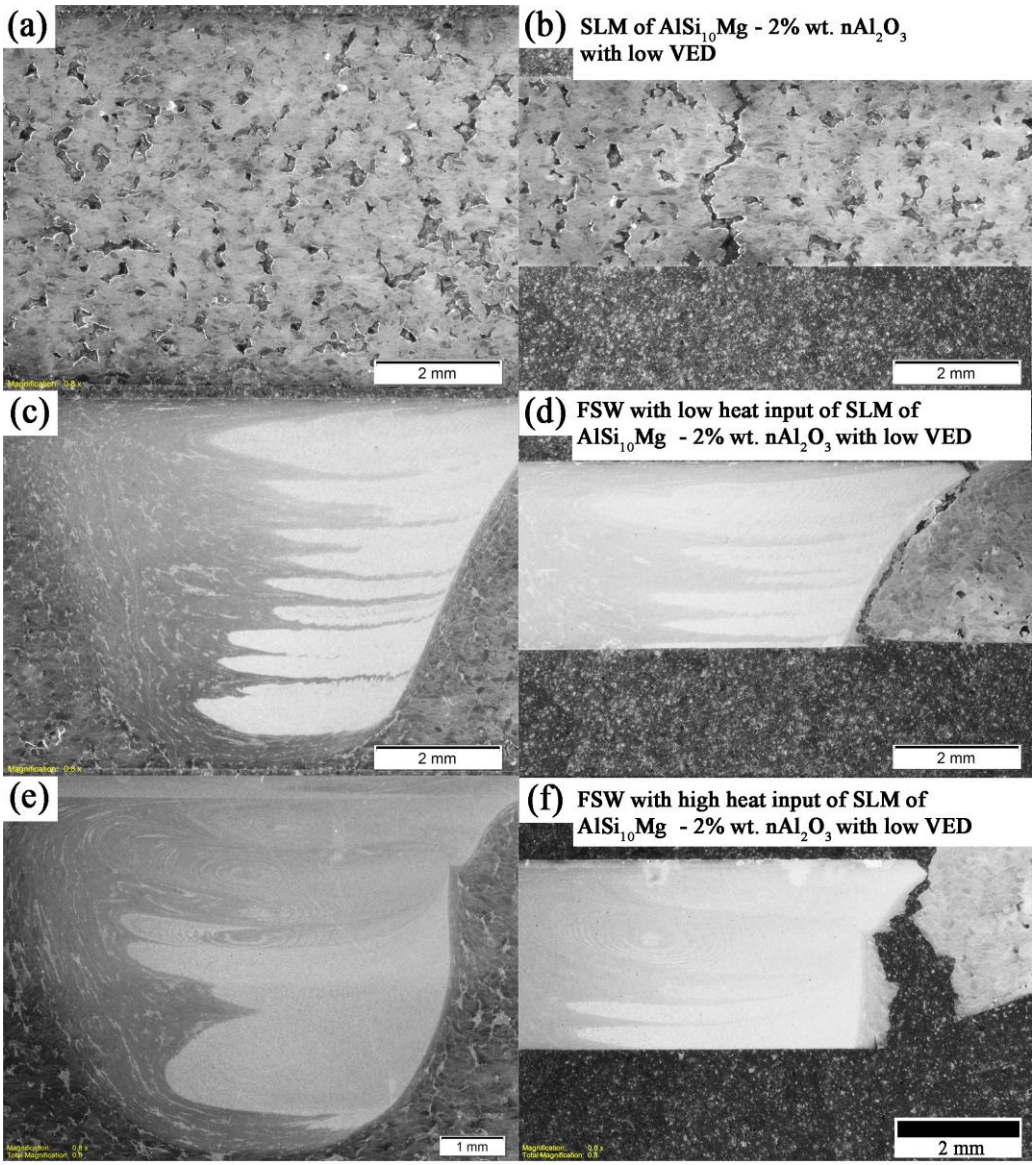

Figure 7-33 Cross-sectional view of the samples before (left) and after the tensile test (right).

FSW with low heat input of SLM of $AlSi_{10}Mg$ - 2% wt. nAl_2O_3 with high VED (Figure 7-32d) as well as FSW with low and high heat input of SLM of $AlSi_{10}Mg$ - 2% wt. nAl_2O_3 with low VED (Figure 7-33d and e) samples fractured at the TMAZ region of the advancing side while FSW with high heat input of SLM of

$AlSi_{10}Mg$ - 2% wt. nAl_2O_3 with high VED (Figure 7-32f) fracture in the stir zone. This observation is similar to FSW of SLM of $AlSi_{10}Mg$ mentioned earlier.

Observation from the fracture site under the FESEM (Figure 7-34) reviews the fracture mechanism that took place at the fracture site. Looking at fracture surface of the as-received SLM of $AlSi_{10}Mg$ - 2% wt. nAl_2O_3 with high VED (Figure 7-34a) and low VED (Figure 7-34b), elongated dimples were observed at the fracture surfaces indicating ductile mode fracture mechanism similar to that of as-received SLM of $AlSi_{10}Mg$ with high VED and low VED. Agglomerated and sintered nAl_2O_3 was observed at the fracture site corresponding to the observation on the microstructure mentioned earlier (Figure 7-13a and b). The presence of agglomerated nAl_2O_3 could have acted as defects in the matrix resulting in stress concentration in the region. For as-received SLM of $AlSi_{10}Mg$ - 2% wt. nAl_2O_3 with low VED (Figure 7-34b), clusters of unmelted powders with nAl_2O_3 was observed, this could be the site of the porosity. The presence of porosity could have acted as stress concentration sites during tensile testing, giving rise to lower tensile strength as observed earlier.

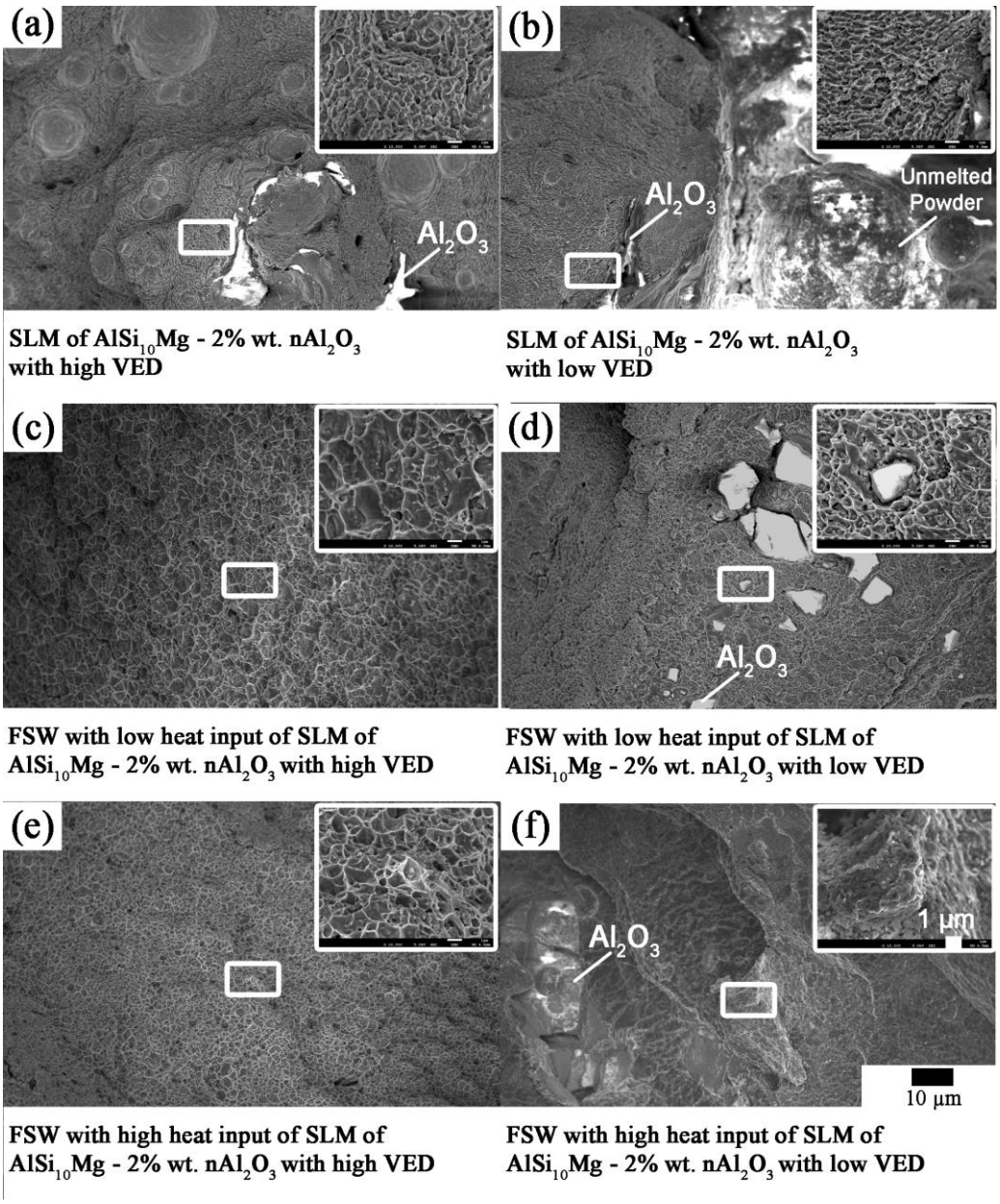

Figure 7-34 Fractography of SLM of $AlSi_{10}Mg$ - 2% wt. nAl_2O_3 with and without FSW.

Looking at FSWed samples, FSW with low and high heat input of SLM of $AlSi_{10}Mg$ - 2% wt. nAl_2O_3 with high VED (Figure 7-34c and e) showed similar dimples to those of FSW with low and high heat input of SLM of $AlSi_{10}Mg$ with high VED (Figure 7-31c and e). FSW with low heat input of SLM of $AlSi_{10}Mg$ - 2% wt. nAl_2O_3 with low VED showed shallower dimples at the fracture sites

(Figure 7-34d) corresponding to lesser elongation in the tensile results. FSW with high heat input of SLM of $AlSi_{10}Mg$ - 2% wt. nAl_2O_3 with low VED showed cleavage fracture with a break along smooth planes indicating lack of bonding. The fracture occurred in the TMAZ region of the weld identified by its highly deformed structure. During FSW, the TMAZ experiences both elevated temperature and deformation resulting in the deformation of the material. The TMAZ underwent plastic deformation and not recrystallisation due to the insufficient deformation strain. During increased deformation from the higher tool rotation speed, the porosity in the TMAZ of SLM of $AlSi_{10}Mg$ - 2% wt. nAl_2O_3 with low VED could have connected or elongated, hence, the phenomenon only occurred for FSW with high heat input of SLM of $AlSi_{10}Mg$ - 2% wt. nAl_2O_3 with low VED.

The cross-sectional view (Figure 7-35and Figure 7-36) and the FESEM image of the fracture site (Figure 7-37) of as-received SLM of $AlSi_{10}Mg$ - 5% wt. nAl_2O_3 with high VED and low VED were studied. SLM of $AlSi_{10}Mg$ - 5% wt. nAl_2O_3 with high and low VED fractured without visible necking. The fracture path is perpendicular to the direction of the applied force and connecting with the porosity along the path. As-received SLM of $AlSi_{10}Mg$ - 5% wt. nAl_2O_3 with low VED fractured in a similar way to as-received SLM of $AlSi_{10}Mg$ with low VED. SLM of $AlSi_{10}Mg$ - 5% wt. nAl_2O_3 with low VED appeared to have fracture along the path connecting the porosity. The sharp edges of the porosity could have acted as stress concentrators during the tensile test, resulting in a significant drop in tensile strength. For samples after FSW, the fracture occurred at the parent material. During FSW, the intense plastic deformation and dynamic recrystallisation resulted in the evolution of the microstructure and eliminated the porosity in the material. This resulted in the weld region being stronger than the parent material, corresponding to the tensile results.

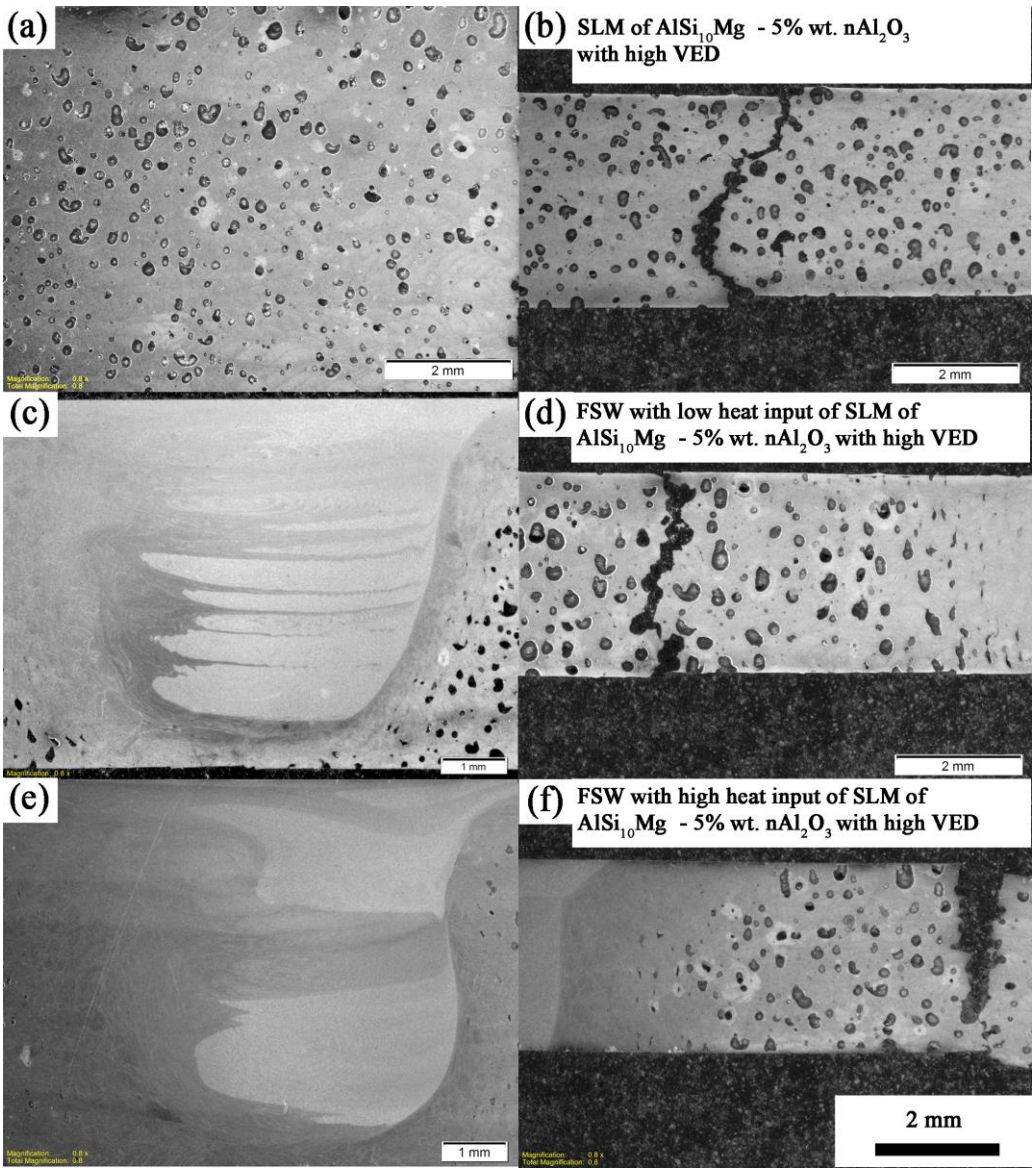

Figure 7-35 Cross-sectional view of the samples before (left) and after the tensile test (right).

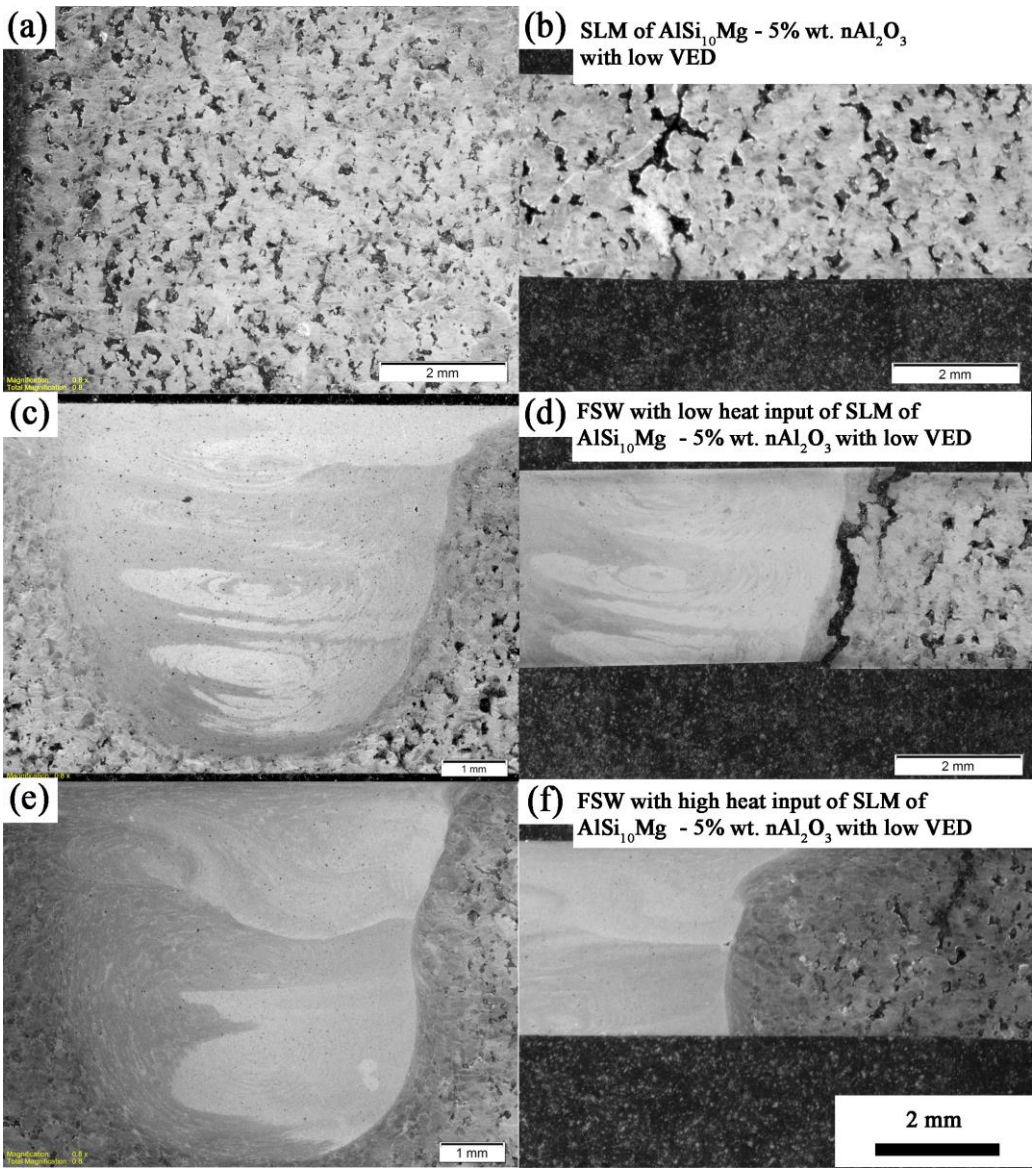

Figure 7-36 Cross-sectional view of the samples before (left) and after the tensile test (right).

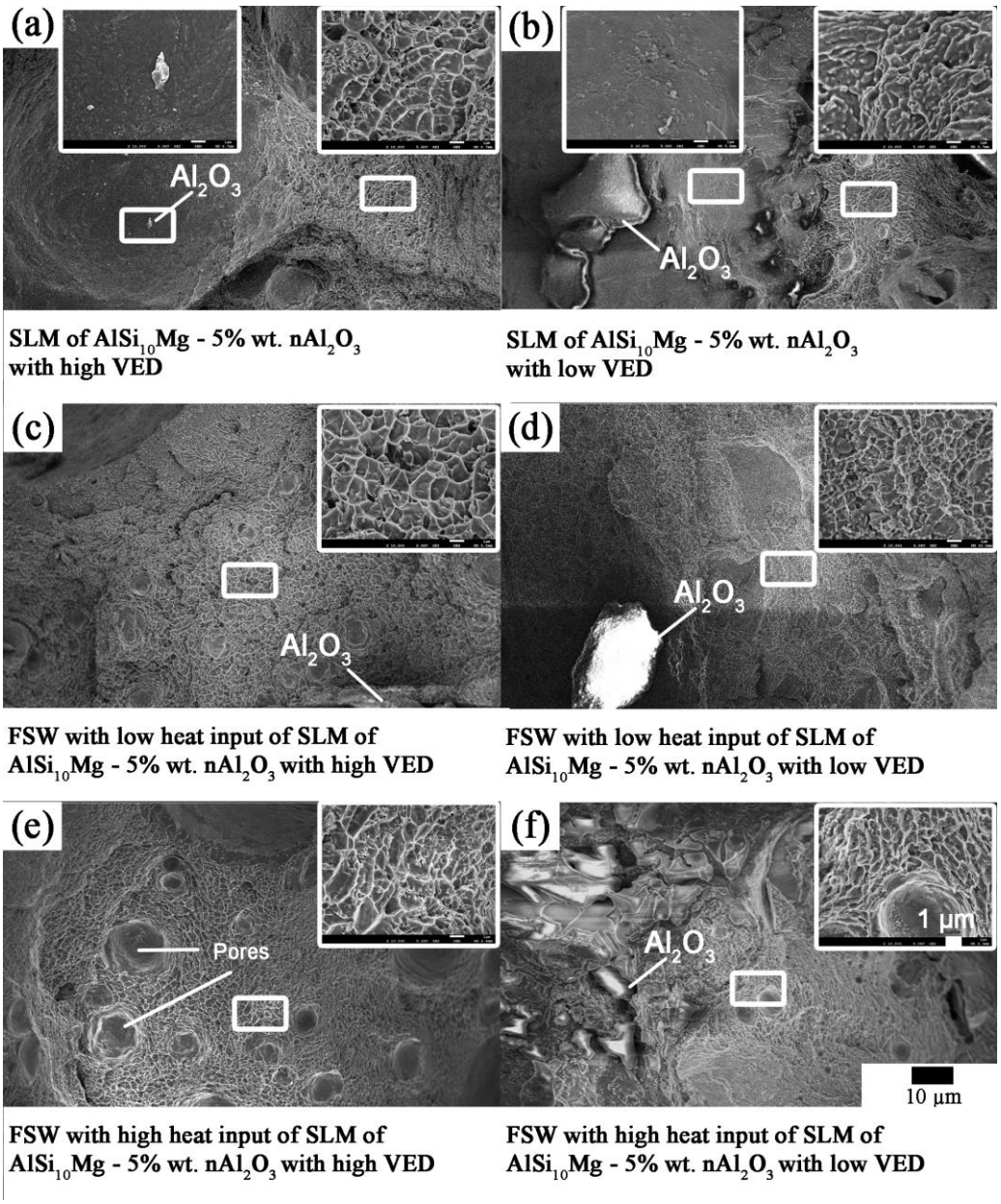

Figure 7-37 Fractography of SLM of $AlSi_{10}Mg$ - 5% wt. nAl_2O_3 with and without FSW.

7.3.9 Conclusions

FSW was successfully used to join SLM fabricated AlSi$_{10}$Mg and its composites together. The weldability, mechanical behaviour and microstructure evolution were investigated and summarised as below.

a. Finer grains were achieved in the FSW region due to dynamic recrystallisation process together with a considerably higher fraction of high-angle grain boundaries during FSW.
b. Agglomerated and sintered nAl_2O_3 were observed to have broken down and dispersed in the matrix after FSW. Larger grains were detected with the use of higher tool rotational speed.
c. The higher amount of Si was detected at the advancing side of the weld region. This is mainly attributed to the higher temperature generated at the advancing side resulting in more Si-rich particles being precipitated out.
d. Considerable reduction in hardness and tensile strength were observed in the weld region due to the precipitation of Si. Higher RS/TS gave rise to larger grain sizes and lower hardness.
e. The addition of nAl_2O_3 contributed to finer grains and higher hardness due to Zener pinner effect.
f. FSW can generate porosity-free welds while 18% porosity density was received from as-printed substrates.

CHAPTER 8

Conclusions and Future Work

These chapter summaries all major findings of this thesis; as well as proposes for future work. Lastly, published works by the author are listed.

8.1 Conclusions

The fabrication of new Al-nAl_2O_3-CNTs composite, as well as the joining of SLM fabricated $AlSi_{10}Mg$, as well as $AlSi_{10}Mg$-nAl_2O_3 composite was explored for the first time were presented.

8.1.1 Fabrication of Al-nAl_2O_3-CNTs Composites via Friction Stir Processing. (Chapter 4)

A new Al-based nano-composite reinforced with uniformly dispersed Al_2O_3 and CNTs have been successfully fabricated using FSP. The effects multiple of nano-particles reinforcement on the mechanical behaviour and microstructure evolution in the friction stir processed Al matrix were studied and are summarised as below.

a. Grain refinement can be observed in friction stir processing with/ without the addition of nano-sized reinforcement particles. The presence of nano-sized reinforcement led to more pronounced grain refinement as pinning effect of the nano-particles have retarded the grain growth rate in the dynamic recrystallisation process.
b. The micro-hardness and tensile strengths were increased significantly through the addition of Al_2O_3 and CNTs nanoparticles. In particular, the yield strength of the composites increased 70% compared with that of FSPed Al when both Al_2O_3 and CNTs were added in the matrix.

c. For both Al-Al_2O_3 and Al-Al_2O_3-CNTs composites, Al_2O_3 particles can always be found at the bottom of the dimples on the fracture surfaces, suggesting void initiation at the Al/ Al_2O_3 interfaces regions. The significant increase in the yield strength of Al-Al_2O_3-CNTs is believed to be related to the CNTs pull-out mechanism at sub-micron scale inside/around the Al_2O_3 dominated fracture dimples. Shallower dimples were observed on the fracture surface for composite with the addition of Al_2O_3 and CNTs, which led to significant reduction of elongation.
d. Multiple reinforcements with different shapes can be an effective method to increase the tensile strengths, especially yield strength of metal matrix composites.

8.1.2 Fabrication and Optimisation of SLM Process Parameters for The Fabrication of $AlSi_{10}Mg$-nAl_2O_3 Composites. (Chapter 5)

The fabrication and optimisation of SLM process parameters for $AlSi_{10}Mg$-nAl_2O_3 were studied and summarised as follows:

a. Powder preparation process has successfully coated the gas-atomised spherical powder uniformly without causing any deformation. The densification behaviour of the composites has been investigated, and dense parts were fabricated with the use of high energy density input within a threshold. The results have shown that SLM is indeed capable in fabrication AMCs.

b. The mechanical behaviour and microstructure evolution of SLM fabricated $AlSi_{10}Mg$, and $AlSi_{10}Mg$-nAl_2O_3 composites were studied. Columnar grain structure along the thermal gradient was observed via EBSD. The addition of nAl_2O_3 contributed to further reduction in the average grain sizes via the Zener pinning effect exerting pinning pressure during grain growth.

c. Significant reduction in the strengthening properties of $AlSi_{10}Mg$ after the introduction of nAl_2O_3 attributed to several factors such as the increase in porosity, agglomeration of nAl_2O_3, dissolution of hardening precipitates and coarsening of Si-rich particles in the matrix at high energy density input. However, in this study, the use of $AlSi_{10}Mg$ have resulted in the fabrication of $AlSi_{10}Mg$-nAl_2O_3 composites with superior mechanical properties compared to Al-nAl_2O_3 composites using pure aluminium.

8.1.3 The Joining of SLM Fabricated $AlSi_{10}Mg$ (Chapter 6)

FSW was successfully used to join SLM fabricated $AlSi_{10}Mg$ parts together without the presence of welding defects with rotational speed (RS) = 1200 rpm, travel speed (TS) = 1 mm/s, the tilt angle (TA) = 4.5°. The mechanical behaviour and microstructure evolution were studied and summarised as below.

a. Higher amount of Si was detected at the advancing side of the weld region. This is mainly attributed to the higher temperature generated at the advancing side resulting in more Si-rich particles being precipitated out.

b. Grain refinement was observed in the friction stir welding region due to dynamic recrystallisation process together with a significant increase in the fraction of high-angle grain boundaries during FSW.

c. A significant decrease in the hardness and tensile strength were observed in the weld region due to the precipitation of Si. The use of higher RS/TS increased the grain size and slight reduction of hardness.

8.1.4 The joining of SLM Fabricated $AlSi_{10}Mg$-nAl_2O_3 Composites via FSW (Chapter 7)

FSW was successfully used to join SLM fabricated $AlSi_{10}Mg$-nAl_2O_3 composites. The weldability, mechanical behaviour and microstructure evolution were investigated and summarised as below.

a. Finer grains were achieved in the FSW region due to dynamic recrystallisation process together with a considerably higher fraction of high-angle grain boundaries during FSW.

b. Agglomerated and sintered nAl_2O_3 were observed to have broken down and dispersed in the matrix after FSW. Larger grains were detected with the use of higher tool rotational speed.

c. Higher amount of Si was detected at the advancing side of the weld region. This is mainly attributed to the higher temperature generated at the advancing side resulting in more Si-rich particles being precipitated out.

d. Considerable lower hardness and tensile strength were observed in the weld region due to the precipitation of Si. Higher rotational speed to travel speed ratio gave rise to larger grain sizes and lower hardness.

e. The addition of nAl_2O_3 contributed to finer grains and higher hardness due to Zener pinner effect

f. FSW can generate porosity-free welds while 18% porosity density was received from the as-printed substrates.

The above favourable results have shown that FSW has good potential as a suitable joining technique for additive manufacturing (AM) fabricated aluminium matrix composites (AMCs).

8.2 Suggestions for Future Work

8.2.1 Elevated Temperature Tensile Test

Al-based composites are often used in elevated temperature applications. The addition of reinforcement is believed to improve the thermal stability of the microstructure and high-temperature mechanical properties due to the pinning effect of the particles. Therefore, future work could be done to evaluate the mechanical properties and performances at various elevated temperature.

8.2.2 Performing FSW Using Different Weld Configurations

Square butt weld configuration was tested in this research. However, there are also many different types of welding configurations for different applications. Therefore, building on the success of the current work, further work can be carried out on other welding configuration like double sided butt joint, T-joint and lap joint to increase its range of applications.

8.2.3 Residual Stress Analysis

The residual stress of FSW of aluminium alloy has been reported to be very low in comparison to fusion welding [233]. However, the rapid melting and solidification process of SLM has resulted in very large thermal and residual stress in the build component [194]. Therefore, the study on the residual stress of FSW joining of SLM fabricated component might be of value.

8.2.4 Corrosion Test

Al-Si aluminium alloy has good corrosion resistant properties. Studies have reported that FSW can join aluminium alloys AA6061 together without compromising the corrosion resistance properties. However, poorer corrosion resistance was reported with conventional arc welding methods [234, 235]. On the other hand, studies have shown that corrosion resistance has reduced at the

melt pool due to the formation of preferential dissolution path in the HAZ of the pool where silicon particles form idiomorphic crystals giving rise to galvanic couples [236]. Thus, the study of corrosion behaviour could be of value.

8.2.5 Fatigue Analysis

Fatigue and durability are major concerns when it comes to structural material especially in the aerospace or conductor applications as AMCs experiences vibrations and other fluctuating loads which potentially leads to material degradation [237]. Hence, the FSW joints must be able to have sustainable fatigue crack growth resistance for it to be used.

8.2.6 Optimization of SLM fabricated composites

The fabrication of Al-Al_2O_3 using SLM is relatively new. Hence, the use of different concentration of reinforcement was to explore the effect of different composition on a preliminary study. However, the optimised concentration of reinforcements for SLM fabricated Al-Al_2O_3, Al-CNT and Al-Al_2O_3-CNT could be of interest as future work.

8.2.7 Youngs modulus determination

The Youngs modulus of the aluminium alloy and its composites is difficult to establish as the maximum stress ramping rate required for accurate measurement is 12 MPa/min. The ramping rate used in the current thesis appears to be much higher than the allowed to support the accurate determination of the Youngs modulus. Therefore, the determination of the Youngs modulus could be conducted using ASTM B556 instead of ASTM E8.

8.2.8 Nanoparticle yield of SLM fabricated composites

The nanoparticles could have been lost during the fabrication process of SLM. The nanoparticles could have been expelled together with the recoil pressure

together with the spatters. It could also have been caught in the fume filters. The nanoparticle yield and management of the process could have added valuable insights to the future fabrication of composites via SLM.

8.2.9 Investigation of material flow, shear layer thickness and dispersion of oxide film from the faying surface using different tool geometry

The tool geometry also played a significant role in the flow of the material in the stir zone. Thomas et al. [238] suggested that the ratio of the dynamic volume to the static volume of the pin could increase the material flow properties. This could allow FSW to be conducted with lower welding force accompanied with easier plasticized flow and downward augering effect of the material. In this study, a threaded pin with three flats was used has a ratio around 1.3:1. The use of a Whorl™ tool with a ratio of 1.8:1 and MX Triflute™ pin with a ratio of 2.6:1 could improve the material flow in the weld.

8.3 List of Publications

The author has produced several publications during this research. The publications include five international peer-reviewed journal paper and three international conference papers.

8.3.1 Journal Papers

1) **Zhenglin Du**, Ming-Jen Tan, Jun-Feng Guo, Guijun Bi, Jun Wei. (2016). "Fabrication of a new Al-Al_2O_3-CNTs composite using friction stir processing (FSP)", Journal of Materials Science and Engineering: A: Structural Materials: Properties, Microstructure and Processing, Volume 667, 125–131. [Q1]

2) **Zhenglin Du**, Ming-Jen Tan, Jun-Feng Guo and Jun Wei. (2016). "Aluminium-carbon nanotubes composites produced from friction stir processing and selective laser melting", Materialwissenschaft und Werkstofftechnik, Volume 47, 539-548. [Q3].

3) **Zhenglin Du**, Ming-Jen Tan, Jun-Feng Guo and Jun Wei. (2016). "Friction stir processing of Al–CNT composites", Proceedings of the Institution of Mechanical Engineers, Part L: Journal of Materials: Design and Applications. Volume 230, Issue 3, 825-833. [Q3].

4) **Zhenglin Du**, Ming-Jen Tan, Hui-Chi Chen, Guijun Bi, and Chee Kai Chua. (2018). "Joining of 3D-printed AlSi10Mg by friction stir welding", Welding in the World. Volume 62, Issue 3, 675-682. [Q2].

5) Junfeng Guo, Bing Yang Lee, **Zhenglin Du**, Guijun Bi, Ming Jen Tan and Jun Wei (2016) "Effect of Nano-Particle Addition on Grain Structure Evolution of Friction Stir Processed Al 6061 During Postweld Annealing", The Journal of The Minerals, Metals & Materials Society (TMS) [JOM], Volume 68, Issue 8, 2268-2273. [Q1]

6) Chor Yen Yap, Hongyi Kenneth Tan, **Zhenglin Du**, Chee Kai Chua, and Zhili Dong (2017) "Selective laser melting of nickel powder", Rapid Prototyping Journal, Volume 23, Issue 4, 750-757. [Q1].

8.3.2 Conference Papers

1) **Zhenglin Du**, Ming-Jen Tan, Jun-Feng Guo, Jun Wei and Chee Kai Chua. (2016). "Dispersion of CNTs in Selective Laser Melting printed $AlSi_{10}Mg$ composites via Friction Stir Processing", Material Science Forum, Volume 879, 1915-1920. DOI: 10.4028/www.scientific.net/MSF.879.1915

2) **Zhenglin Du**, Ming-Jen Tan, Jun-Feng Guo, Jun Wei. Dispersion of Al_2O_3 Reinforcements in Al Composites via Friction Stir Processing. Material Science Forum, 2016, 861, pp.236-240. DOI: 10.4028/www.scientific.net/MSF.861.236

3) **Zhenglin Du**, Ming-Jen Tan, Jun-Feng Guo, Chee Kai Chua and Lim Jun Jie Dalton. "The effect of Laser Power and scanning speed on the density of selective laser melting fabricated AL-CNT Composites", In Proceedings of the 2nd International Conference on Progress in Addition Manufacturing, Singapore, 16-19 May, 2016, pp.488-493. http://hdl.handle.net/10220/41859

8.3.3 Journal Papers Under Review or In Preparation

1) **Zhenglin Du**, Hui-Chi Chen, Ming Jen Tan, Guijun Bi, Chee Kai Chua. "Selective laser melting of advanced nano-composite material $AlSi_{10}Mg$-nAl_2O_3: Densification behaviour, microstructure and mechanical properties"

2) **Zhenglin Du**, Hui-Chi Chen, Ming Jen Tan, Guijun Bi, Chee Kai Chua. "Joining of selective laser melting fabricated advanced $AlSi_{10}Mg$-nAl_2O_3 nano-composites by friction stir welding (FSW): Mechanical and metallurgy properties"

References

1. Miracle D.B., Metal matrix composites – From science to technological significance. Composites Science and Technology, 2005. 65(15–16): p. 2526-2540.
2. Guo J., Gougeon P., and Chen X.G., Study on laser welding of AA1100-16 vol.% B_4C metal–matrix composites. Composites Part B: Engineering, 2012. 43(5): p. 2400-2408.
3. Chawla N. and Chawla K.K., Metal Matrix Composites. 2006: Springer, New York.
4. Du Z., Tan M.J., Guo J.F., and Wei J., Dispersion of Al_2O_3 reinforcements in Al composites via friction stir processing. Materials Science Forum, 2016. 861: p. 236-240.
5. Guo J.F., Liu J., Sun C.N., Maleksaeedi S., Bi G., Tan M.J., and Wei J., Effects of nano-Al_2O_3 particle addition on grain structure evolution and mechanical behaviour of friction-stir-processed Al. Materials Science and Engineering: A, 2014. 602(0): p. 143-149.
6. Guo J., Lee B.Y., Du Z., Bi G., Tan M.J., and Wei J., Effect of nano-particle addition on grain structure evolution of friction stir-processed Al 6061 during postweld annealing. JOM, 2016. 68(8): p. 2268-2273.
7. Liao J.Z. and Tan M.J., Improved tensile strength of carbon nanotube reinforced aluminum composites processed by powder metallurgy. Advanced Materials Research, 2012. 500: p. 651-656.
8. Yajima S., Okamura K., Tanaka J., and Hayase T., High-temperature strengths of aluminium composite reinforced with continuous SiC fibre. Journal of Materials Science, 1981. 16(11): p. 3033-3038.
9. Atïk E., Mechanical properties and wear strengths in aluminium-alumina composites. Materials and Structures. 31(6): p. 418-422.
10. wohlers T., Wohlers report 2015: Wholers Associates. 2015.
11. Kruth J.P., Material Incress Manufacturing by Rapid Prototyping Techniques. CIRP Annals, 1991. 40(2): p. 603-614.
12. Kruth J.P., Leu M.C., and Nakagawa T., Progress in Additive Manufacturing and Rapid Prototyping. CIRP Annals, 1998. 47(2): p. 525-540.
13. Du Z., Tan M.J., Guo J.F., Wei J., Chua C.K., and Lim J.J.D. The effect of laser power and scanning speed on the density of selective laser melting fabricated Al-CNT composites. in Proceedings of the 2nd International Conference on Progress in Additive Manufacturing (ProAM 2016). 2016. Singapore.
14. Kruth J.P., Froyen L., Van Vaerenbergh J., Mercelis P., Rombouts M., and Lauwers B., Selective laser melting of iron-based powder. Journal of Materials Processing Technology, 2004. 149(1–3): p. 616-622.
15. Dai K. and Shaw L., Distortion minimization of laser - processed components through control of laser scanning patterns. Rapid Prototyping Journal, 2002. 8(5): p. 270-276.

16. Mathers G., The welding of aluminium and its alloys. [electronic resource]. 2002: Boca Raton, Fla. : CRC Press ; Cambridge, England : Woodhead Pub., 2002.
17. Kou S., Welding metallurgy. [electronic resource]. 2nd ed. ed. 2003: Hoboken, N.J. : Wiley-Interscience.
18. Lakshminarayanan A.K., Balasubramanian V., and Elangovan K., Effect of welding processes on tensile properties of AA6061 aluminium alloy joints. The International Journal of Advanced Manufacturing Technology, 2009. 40(3): p. 286-296.
19. Mishra R.S. and Ma Z.Y., Friction stir welding and processing. Materials Science and Engineering: R: Reports, 2005. 50(1–2): p. 1-78.
20. Storjohann D., Barabash O.M., David S.A., Sklad P.S., Bloom E.E., and Babu S.S., Fusion and friction stir welding of aluminum-metal-matrix composites. Metallurgical and Materials Transactions A, 2005. 36(11): p. 3237-3247.
21. Lee W.B., Yeon Y.M., and Jung S.B., The improvement of mechanical properties of friction-stir-welded A356 Al alloy. Materials Science and Engineering: A, 2003. 355(1–2): p. 154-159.
22. Price D.A., Williams S.W., Wescott A., Harrison C.J.C., Rezai A., Steuwer A., Peel M., Staron P., and Koçak M., Distortion control in welding by mechanical tensioning. Science and Technology of Welding and Joining, 2007. 12(7): p. 620-633.
23. Li W., Yang Q., Zhang Z., and Gao D., Effect of weld curvature radius and tool rotation direction on joint microstructure in friction stir welding casting alloys. Materials & Design, 2014. 53(0): p. 124-128.
24. Li B., Zhang Z., Shen Y., Hu W., and Luo L., Dissimilar friction stir welding of Ti–6Al–4V alloy and aluminum alloy employing a modified butt joint configuration: Influences of process variables on the weld interfaces and tensile properties. Materials & Design, 2014. 53(0): p. 838-848.
25. Du Z., Tan M.J., Guo J.F., and Wei J., Friction stir processing of Al–CNT composites. Proceedings of the Institution of Mechanical Engineers, Part L: Journal of Materials: Design and Applications, 2016. 230(3): p. 825-833.
26. Anderston T., Welding aluminum. [electronic resource] : questions and answers : a practical guide for troubleshooting aluminum welding-related problems. 2010: Miami, FL : Americal Welding Society, c2010. 2nd ed.
27. Arzt E., Size effects in materials due to microstructural and dimensional constraints: a comparative review. Acta Materialia, 1998. 46(16): p. 5611-5626.
28. Hall E.O., The Deformation and Ageing of Mild Steel: III Discussion of Results. Proceedings of the Physical Society. Section B, 1951. 64(9): p. 747.
29. Schiøtz J., Di Tolla F.D., and Jacobsen K.W., Softening of nanocrystalline metals at very small grain sizes. Nature, 1998. 391: p. 561.

30. Yip S., The strongest size. Nature, 1998. 391: p. 532.
31. Argon A.S. and Yip S., The strongest size. Philosophical Magazine Letters, 2006. 86(11): p. 713-720.
32. Hart E.W., Theory of the tensile test. Acta Metallurgica, 1967. 15(2): p. 351-355.
33. Hutchinson J.W. and Neale K.W., Influence of strain-rate sensitivity on necking under uniaxial tension. Acta Metallurgica, 1977. 25(8): p. 839-846.
34. Ma E. and Zhu T., Towards strength–ductility synergy through the design of heterogeneous nanostructures in metals. Materials Today, 2017. 20(6): p. 323-331.
35. Zhang Z. and Chen D.L., Consideration of Orowan strengthening effect in particulate-reinforced metal matrix nanocomposites: A model for predicting their yield strength. Scripta Materialia, 2006. 54(7): p. 1321-1326.
36. SLM S.S.G. SELECTIVE LASER MELTING MACHINE SLM 280 2.0. 2017 [cited 2017 16/11/2017]; Available from: https://slm-solutions.com/products/machines/selective-laser-melting-machine-slm-280-20.
37. Laser G.C. Metal 3D Printing - Concept Laser. 2017 [cited 2017 16/11/2017]; Available from: https://www.concept-laser.de/en/products/machines.html.
38. EOS E.O.S.G. EOSINT M 280. 2017 [cited 2017 16/11/2017]; Available from: https://www.eos.info/systems_solutions/metal/systems_equipment/eosint_m280.
39. ReaLizer. SLM 300I. 2017 [cited 2017 16/11/2017]; Available from: http://www.realizer.com/en/?page_id=1210.
40. Renishaw. Am 250. 2017 [cited 2017 16/11/2017]; Available from: http://www.renishaw.com/en/am250--15253.
41. Arcam. Arcam A2X – for aerospace production and materials R&D. 2017 [cited 2017 16/11/2017]; Available from: http://www.arcam.com/technology/products/arcam-a2x-3/.
42. Systems D. ProX DMP 300. 2017 [cited 2017 16/11/2017]; Available from: https://www.3dsystems.com/3d-printers/prox-dmp-300/specifications.
43. Optomec. LENS MR-7 Systems. 2017 [cited 2017 16/11/2017]; Available from: https://www.optomec.com/3d-printed-metals/lens-printers/metal-research-and-development-3d-printer/.
44. Sciaky I. The EBAM® 68 System. 2017 [cited 2017 16/11/2017]; Available from: http://www.sciaky.com/additive-manufacturing/metal-additive-manufacturing-systems.
45. Bremen S., Meiners W., and Diatlov A., Selective Laser Melting. Laser Technik Journal, 2012. 9(2): p. 33-38.

46. Brandl E., Heckenberger U., Holzinger V., and Buchbinder D., Additive manufactured $AlSi_{10}Mg$ samples using Selective Laser Melting (SLM): Microstructure, high cycle fatigue, and fracture behavior. Materials & Design, 2012. 34: p. 159-169.
47. Yadroitsev I., Bertrand P., and Smurov I., Parametric analysis of the selective laser melting process. Applied Surface Science, 2007. 253(19): p. 8064-8069.
48. Louvis E., Fox P., and Sutcliffe C.J., Selective laser melting of aluminium components. Journal of Materials Processing Technology, 2011. 211(2): p. 275-284.
49. Buchbinder D., Schleifenbaum H., Heidrich S., Meiners W., and Bültmann J., High Power Selective Laser Melting (HP SLM) of Aluminum Parts. Physics Procedia, 2011. 12, Part A(0): p. 271-278.
50. Wong M., Tsopanos S., Sutcliffe C.J., and Owen I., Selective laser melting of heat transfer devices. Rapid Prototyping Journal, 2007. 13(5): p. 291-297.
51. Thijs L., Kempen K., Kruth J.-P., and Van Humbeeck J., Fine-structured aluminium products with controllable texture by selective laser melting of pre-alloyed $AlSi_{10}Mg$ powder. Acta Materialia, 2013. 61(5): p. 1809-1819.
52. Rombouts M., Kruth J.P., Froyen L., and Mercelis P., Fundamentals of Selective Laser Melting of alloyed steel powders. CIRP Annals - Manufacturing Technology, 2006. 55(1): p. 187-192.
53. Fulcher B.A., Leigh D.K., and Watt T.J. Comparison of $AlSi_{10}Mg$ and Al 6061 Processed through DMLS. in Proceedings of International Solid Freeform Fabrication Symposium. 2014. Texas, Austin, USA.
54. Committee A.h., Properties and selection: nonferros alloys and special-purpose materials. 1991, Materials Park, OH: ASM International.
55. Wang X.J., Zhang L.C., Fang M.H., and Sercombe T.B., The effect of atmosphere on the structure and properties of a selective laser melted Al–12Si alloy. Materials Science and Engineering: A, 2014. 597(Supplement C): p. 370-375.
56. Gu D., Wang H., Chang F., Dai D., Yuan P., Hagedorn Y.-C., and Meiners W., Selective Laser Melting Additive Manufacturing of $TiC/AlSi_{10}Mg$ Bulk-form Nanocomposites with Tailored Microstructures and Properties. Physics Procedia, 2014. 56(0): p. 108-116.
57. Han Q., Setchi R., Lacan F., Gu D., and Evans S.L., Selective laser melting of advanced $Al\text{-}Al_2O_3$ nanocomposites: Simulation, microstructure and mechanical properties. Materials Science and Engineering: A, 2017. 698(Supplement C): p. 162-173.
58. Dadbakhsh S. and Hao L., Effect of Al alloys on selective laser melting behaviour and microstructure of in situ formed particle reinforced composites. Journal of Alloys and Compounds, 2012. 541(0): p. 328-334.

59. Das H., Chakraborty D., and Kumar Pal T., High-cycle fatigue behavior of friction stir butt welded 6061 aluminium alloy. Transactions of Nonferrous Metals Society of China, 2014. 24(3): p. 648-656.
60. Li R., Liu J., Shi Y., Wang L., and Jiang W., Balling behavior of stainless steel and nickel powder during selective laser melting process. The International Journal of Advanced Manufacturing Technology, 2012. 59(9): p. 1025-1035.
61. Niu H. and Chang I., Instability of scan tracks of selective laser sintering of high speed steel powder. Vol. 41. 1999. 1229–1234.
62. Mumtaz K.A. and Hopkinson N., Selective Laser Melting of thin wall parts using pulse shaping. Journal of Materials Processing Technology, 2010. 210(2): p. 279-287.
63. Verhaeghe F., Craeghs T., Heulens J., and Pandelaers L., A pragmatic model for selective laser melting with evaporation. Acta Materialia, 2009. 57(20): p. 6006-6012.
64. Qiu C., Panwisawas C., Ward M., Basoalto H.C., Brooks J.W., and Attallah M.M., On the role of melt flow into the surface structure and porosity development during selective laser melting. Acta Materialia, 2015. 96(Supplement C): p. 72-79.
65. Liu Y., Yang Y., Mai S., Wang D., and Song C., Investigation into spatter behavior during selective laser melting of AISI 316L stainless steel powder. Materials & Design, 2015. 87(Supplement C): p. 797-806.
66. Anwar A.B. and Pham Q.-C., Selective laser melting of $AlSi_{10}Mg$: Effects of scan direction, part placement and inert gas flow velocity on tensile strength. Journal of Materials Processing Technology, 2017. 240: p. 388-396.
67. Thijs L., Verhaeghe F., Craeghs T., Humbeeck J.V., and Kruth J.-P., A study of the microstructural evolution during selective laser melting of Ti–6Al–4V. Acta Materialia, 2010. 58(9): p. 3303-3312.
68. Aboulkhair N.T., Everitt N.M., Ashcroft I., and Tuck C., Reducing porosity in $AlSi_{10}Mg$ parts processed by selective laser melting. Additive Manufacturing, 2014. 1-4(Supplement C): p. 77-86.
69. Pupo Y., Delgado J., Serenó L., and Ciurana J., Scanning Space Analysis in Selective Laser Melting for CoCrMo Powder. Procedia Engineering, 2013. 63(0): p. 370-378.
70. Jue J., Gu D., Chang K., and Dai D., Microstructure evolution and mechanical properties of Al-Al_2O_3 composites fabricated by selective laser melting. Powder Technology, 2017. 310(Supplement C): p. 80-91.
71. Dadbakhsh S. and Hao L., In Situ Formation of Particle Reinforced Al Matrix Composite by Selective Laser Melting of Al/Fe_2O_3 Powder Mixture. Advanced Engineering Materials, 2012. 14(1-2): p. 45-48.
72. Zhao X., Song B., Fan W., Zhang Y., and Shi Y., Selective laser melting of carbon/$AlSi_{10}Mg$ composites: Microstructure, mechanical and electronical properties. Journal of Alloys and Compounds, 2016. 665(Supplement C): p. 271-281.

73. Wang H. and Gu D., Nanometric TiC reinforced $AlSi_{10}Mg$ nanocomposites: Powder preparation by high-energy ball milling and consolidation by selective laser melting. Journal of Composite Materials, 2015. 49(13): p. 1639-1651.
74. Nickel A.H., Barnett D.M., and Prinz F.B., Thermal stresses and deposition patterns in layered manufacturing. Materials Science and Engineering: A, 2001. 317(1–2): p. 59-64.
75. Kruth J.P., Deckers J., Yasa E., and Wauthle R. Assessing and comparing influencing factors of residual stresses in selective laser melting using a novel analysis method. in Proceedings of the Institution of Mechanical Engineers, Part B: Journal of Engineering Manufacture. 2012.
76. Yasa E., Deckers J., Kruth J.-P., Rombouts M., and Luyten J., Investigation of Sectoral Scanning in Selective Laser Melting. 2010(49187): p. 695-703.
77. Campbell J., Castings. 2003: Butterworth-Heinemann.
78. Munir Z.A., Analytical treatment of the role of surface oxide layers in the sintering of metals. Journal of Materials Science, 1979. 14(11): p. 2733-2740.
79. German R.M., Powder metallurgy of iron and steel. 1998: New York : Wiley, c1998.
80. Ma P., K G P., Scudino S., Jia Y., Wang H., Zou C., Wei Z., and Eckert J., Influence of Annealing on Mechanical Properties of Al-20Si Processed by Selective Laser Melting. Vol. 4. 2014. 28-36.
81. Manfredi D., Calignano F., Krishnan M., Canali R., Ambrosio E., and Atzeni E., From Powders to Dense Metal Parts: Characterization of a Commercial AlSiMg Alloy Processed through Direct Metal Laser Sintering. Materials, 2013. 6(3): p. 856.
82. Kempen K., Thijs L., Van Humbeeck J., and Kruth J.P., Mechanical Properties of $AlSi_{10}Mg$ Produced by Selective Laser Melting. Physics Procedia, 2012. 39(0): p. 439-446.
83. Lam L.P., Zhang D.Q., Liu Z.H., and Chua C.K., Phase analysis and microstructure characterisation of $AlSi_{10}Mg$ parts produced by Selective Laser Melting. Virtual and Physical Prototyping, 2015. 10(4): p. 207-215.
84. Read N., Wang W., Essa K., and Attallah M.M., Selective laser melting of $AlSi_{10}Mg$ alloy: Process optimisation and mechanical properties development. Materials & Design (1980-2015), 2015. 65: p. 417-424.
85. Li W., Li S., Liu J., Zhang A., Zhou Y., Wei Q., Yan C., and Shi Y., Effect of heat treatment on $AlSi_{10}Mg$ alloy fabricated by selective laser melting: Microstructure evolution, mechanical properties and fracture mechanism. Materials Science and Engineering: A, 2016. 663: p. 116-125.
86. Li Y. and Gu D., Parametric analysis of thermal behavior during selective laser melting additive manufacturing of aluminum alloy powder. Materials & Design, 2014. 63: p. 856-867.

87. Asgari H., Baxter C., Hosseinkhani K., and Mohammadi M., On microstructure and mechanical properties of additively manufactured $AlSi_{10}Mg$_200C using recycled powder. Materials Science and Engineering: A, 2017. 707(Supplement C): p. 148-158.
88. Zhang B., Liao H., and Coddet C., Effects of processing parameters on properties of selective laser melting Mg–9%Al powder mixture. Materials & Design, 2012. 34(Supplement C): p. 753-758.
89. Gu D., Wang H., Dai D., Chang F., Meiners W., Hagedorn Y.-C., Wissenbach K., Kelbassa I., Poprawe R., D. B., W. M., N. P., K. W., and J. S., Densification behavior, microstructure evolution, and wear property of TiC nanoparticle reinforced $AlSi_{10}Mg$ bulk-form nanocomposites prepared by selective laser melting. Journal of Laser Applications, 2015. 27(S1): p. S17003.
90. Thomas W.M., Nicholas E.D., Needham J.C., Murch M.G., Templesmith P., and Dawes C.J., G.B.P.A.N. 9125978.8, Editor. December 1991.
91. Ahmed M.M.Z., Ataya S., El-Sayed Seleman M.M., Ammar H.R., and Ahmed E., Friction stir welding of similar and dissimilar AA7075 and AA5083. Journal of Materials Processing Technology, 2017. 242(Supplement C): p. 77-91.
92. Boz M. and Kurt A., The influence of stirrer geometry on bonding and mechanical properties in friction stir welding process. Materials & Design, 2004. 25(4): p. 343-347.
93. El-Danaf E.A. and El-Rayes M.M., Microstructure and mechanical properties of friction stir welded 6082 AA in as welded and post weld heat treated conditions. Materials & Design, 2013. 46(0): p. 561-572.
94. Koilraj M., Sundareswaran V., Vijayan S., and Koteswara Rao S.R., Friction stir welding of dissimilar aluminum alloys AA2219 to AA5083 – Optimization of process parameters using Taguchi technique. Materials & Design, 2012. 42(Supplement C): p. 1-7.
95. Threadgill P.L., Leonard A.J., Shercliff H.R., and Withers P.J., Friction stir welding of aluminium alloys. International Materials Reviews, 2009. 54(2): p. 49-93.
96. Reynolds A.P., Visualisation of material flow in autogenous friction stir welds. Science and Technology of Welding and Joining, 2000. 5(2): p. 120-124.
97. Rhodes C.G., Mahoney M.W., Bingel W.H., Spurling R.A., and Bampton C.C., Effects of friction stir welding on microstructure of 7075 aluminum. Scripta Materialia, 1997. 36(1): p. 69-75.
98. Liu G., Murr L.E., Niou C.S., McClure J.C., and Vega F.R., Microstructural aspects of the friction-stir welding of 6061-T6 aluminum. Scripta Materialia, 1997. 37(3): p. 355-361.
99. Jata K.V., Sankaran K.K., and Ruschau J.J., Friction-stir welding effects on microstructure and fatigue of aluminum alloy 7050-T7451. Metallurgical and Materials Transactions A, 2000. 31(9): p. 2181-2192.

100. Benavides S., Li Y., Murr L.E., Brown D., and McClure J.C., Low-temperature friction-stir welding of 2024 aluminum. Scripta Materialia, 1999. 41(8): p. 809-815.
101. Thomas W.M., Johnson K.I., and Wiesner C.S., Friction Stir Welding – Recent Developments in Tool and Process Technologies. Advanced Engineering Materials, 2003. 5(7): p. 485-490.
102. Thomas W., Norris I., Staines D., and Watts E., Friction stir welding—process developments and variant techniques. The SME Summit, 2005: p. 3-4.
103. Seidel T.U. and Reynolds A.P., Two-dimensional friction stir welding process model based on fluid mechanics. Science and Technology of Welding and Joining, 2003. 8(3): p. 175-183.
104. Guerra M., Schmidt C., McClure J.C., Murr L.E., and Nunes A.C., Flow patterns during friction stir welding. Materials Characterization, 2002. 49(2): p. 95-101.
105. Schneider J., Beshears R., and Nunes A.C., Interfacial sticking and slipping in the friction stir welding process. Materials Science and Engineering: A, 2006. 435(Supplement C): p. 297-304.
106. Xu S., deng X., Reynolds A.P., and Seidel T.U., Finite element simulation of material flow in friction stir welding. Science and Technology of Welding and Joining, 2001. 6(3): p. 191-193.
107. Murr L.E., Liu G., and McClure J.C., A TEM study of precipitation and related microstructures in friction-stir-welded 6061 aluminium. Journal of Materials Science, 1998. 33(5): p. 1243-1251.
108. Mahoney M.W., Rhodes C.G., Flintoff J.G., Bingel W.H., and Spurling R.A., Properties of friction-stir-welded 7075 T651 aluminum. Metallurgical and Materials Transactions A, 1998. 29(7): p. 1955-1964.
109. Sato Y.S., Kokawa H., Enmoto M., and Jogan S., Microstructural evolution of 6063 aluminum during friction-stir welding. Metallurgical and Materials Transactions A, 1999. 30(9): p. 2429-2437.
110. Kwon Y., Saito N., and Shigematsu I., Friction stir process as a new manufacturing technique of ultrafine grained aluminum alloy. Journal of Materials Science Letters, 2002. 21(19): p. 1473-1476.
111. Shojaeefard M.H., Khalkhali A., Akbari M., and Asadi P., Investigation of friction stir welding tool parameters using FEM and neural network. Proceedings of the Institution of Mechanical Engineers, Part L: Journal of Materials: Design and Applications, 2015. 229(3): p. 209-217.
112. Li Y., Murr L.E., and McClure J.C., Flow visualization and residual microstructures associated with the friction-stir welding of 2024 aluminum to 6061 aluminum. Materials Science and Engineering: A, 1999. 271(1): p. 213-223.
113. Sato Y., Urata M., and Kokawa H., Parameters controlling microstructure and hardness during friction-stir welding of precipitation-hardenable aluminum alloy 6063. Metallurgical and Materials Transactions A, 2002. 33(3): p. 625-635.

114. Kwon Y.J., Shigematsu I., and Saito N., Mechanical properties of fine-grained aluminum alloy produced by friction stir process. Scripta Materialia, 2003. 49(8): p. 785-789.
115. Ma Z.Y., Mishra R.S., and Mahoney M.W., Superplastic deformation behaviour of friction stir processed 7075Al alloy. Acta Materialia, 2002. 50(17): p. 4419-4430.
116. Frigaard Ø., Grong Ø., and Midling O.T., A process model for friction stir welding of age hardening aluminum alloys. Metallurgical and Materials Transactions A, 2001. 32(5): p. 1189-1200.
117. Kim Y.G., Fujii H., Tsumura T., Komazaki T., and Nakata K., Three defect types in friction stir welding of aluminum die casting alloy. Materials Science and Engineering: A, 2006. 415(1): p. 250-254.
118. Feng A.H., Xiao B.L., and Ma Z.Y., Effect of microstructural evolution on mechanical properties of friction stir welded AA2009/SiCp composite. Composites Science and Technology, 2008. 68(9): p. 2141-2148.
119. Ni D.R., Chen D.L., Wang D., Xiao B.L., and Ma Z.Y., Influence of microstructural evolution on tensile properties of friction stir welded joint of rolled SiCp/AA2009-T351 sheet. Materials & Design, 2013. 51(Supplement C): p. 199-205.
120. Liu H.J., Fujii H., Maeda M., and Nogi K., Tensile properties and fracture locations of friction-stir-welded joints of 2017-T351 aluminum alloy. Journal of Materials Processing Technology, 2003. 142(3): p. 692-696.
121. Chen H.-B., Yan K., Lin T., Chen S.-B., Jiang C.-Y., and Zhao Y., The investigation of typical welding defects for 5456 aluminum alloy friction stir welds. Materials Science and Engineering: A, 2006. 433(1): p. 64-69.
122. Kah P., Rajan R., Martikainen J., and Suoranta R., Investigation of weld defects in friction-stir welding and fusion welding of aluminium alloys. International Journal of Mechanical and Materials Engineering, 2015. 10(1): p. 26.
123. Elangovan K. and Balasubramanian V., Influences of tool pin profile and tool shoulder diameter on the formation of friction stir processing zone in AA6061 aluminium alloy. Materials & Design, 2008. 29(2): p. 362-373.
124. Hou X., Yang X., Cui L., and Zhou G., Influences of joint geometry on defects and mechanical properties of friction stir welded AA6061-T4 T-joints. Materials & Design, 2014. 53: p. 106-117.
125. Zhao Y., Zhou L., Wang Q., Yan K., and Zou J., Defects and tensile properties of 6013 aluminum alloy T-joints by friction stir welding. Materials & Design, 2014. 57: p. 146-155.
126. Li B., Shen Y., and Hu W., The study on defects in aluminum 2219-T6 thick butt friction stir welds with the application of multiple non-destructive testing methods. Materials & Design, 2011. 32(4): p. 2073-2084.
127. Kalaiselvan K., Dinaharan I., and Murugan N., Characterization of friction stir welded boron carbide particulate reinforced AA6061

aluminum alloy stir cast composite. Materials & Design, 2014. 55(Supplement C): p. 176-182.
128. Bozkurt Y., Uzun H., and Salman S., Microstructure and mechanical properties of friction stir welded particulate reinforced AA2124/SiC/25p–T4 composite. Journal of Composite Materials, 2011. 45(21): p. 2237-2245.
129. Nami H., Adgi H., Sharifitabar M., and Shamabadi H., Microstructure and mechanical properties of friction stir welded Al/Mg2Si metal matrix cast composite. Materials & Design, 2011. 32(2): p. 976-983.
130. Cioffi F., Fernández R., Gesto D., Rey P., Verdera D., and González-Doncel G., Friction stir welding of thick plates of aluminum alloy matrix composite with a high volume fraction of ceramic reinforcement. Composites Part A: Applied Science and Manufacturing, 2013. 54(Supplement C): p. 117-123.
131. Pirondi A. and Collini L., Analysis of crack propagation resistance of Al–Al_2O_3 particulate-reinforced composite friction stir welded butt joints. International Journal of Fatigue, 2009. 31(1): p. 111-121.
132. Ceschini L., Boromei I., Minak G., Morri A., and Tarterini F., Microstructure, tensile and fatigue properties of AA6061/20 vol.% Al_2O_3p friction stir welded joints. Composites Part A: Applied Science and Manufacturing, 2007. 38(4): p. 1200-1210.
133. Minak G., Ceschini L., Boromei I., and Ponte M., Fatigue properties of friction stir welded particulate reinforced aluminium matrix composites. International Journal of Fatigue, 2010. 32(1): p. 218-226.
134. Chen X.G., da Silva M., Gougeon P., and St-Georges L., Microstructure and mechanical properties of friction stir welded AA6063–B_4C metal matrix composites. Materials Science and Engineering: A, 2009. 518(1): p. 174-184.
135. Marzoli L.M., Strombeck A.v., Dos Santos J.F., Gambaro C., and Volpone L.M., Friction stir welding of an AA6061/Al_2O_3/20p reinforced alloy. Composites Science and Technology, 2006. 66(2): p. 363-371.
136. Root J.M., Field D.P., and Nelson T.W., Crystallographic Texture in the Friction-Stir-Welded Metal Matrix Composite Al6061 with 10 Vol Pct Al2O3. Metallurgical and Materials Transactions A, 2009. 40(9): p. 2109-2114.
137. Sato Y., Park S., and Kokawa H., Microstructural factors governing hardness in friction-stir welds of solid-solution-hardened Al alloys. Metallurgical and Materials Transactions A, 2001. 32(12): p. 3033-3042.
138. Svensson L.E., Karlsson L., Larsson H., Karlsson B., Fazzini M., and Karlsson J., Microstructure and mechanical properties of friction stir welded aluminium alloys with special reference to AA 5083 and AA 6082. Science and Technology of Welding and Joining, 2000. 5(5): p. 285-296.
139. Cavaliere P., Cerri E., Marzoli L., and Dos Santos J., Friction Stir Welding of Ceramic Particle Reinforced Aluminium Based Metal Matrix Composites. Applied Composite Materials, 2004. 11(4): p. 247-258.

140. Periyasamy P., Mohan B., and Balasubramanian V., Effect of Heat Input on Mechanical and Metallurgical Properties of Friction Stir Welded AA6061-10% SiCp MMCs. Journal of Materials Engineering and Performance, 2012. 21(11): p. 2417-2428.
141. Periyasamy P., Mohan B., Balasubramanian V., Rajakumar S., and Venugopal S., Multi-objective optimization of friction stir welding parameters using desirability approach to join Al/SiCp metal matrix composites. Transactions of Nonferrous Metals Society of China, 2013. 23(4): p. 942-955.
142. Dinaharan I. and Murugan N., Optimization of friction stir welding process to maximize tensile strength of AA6061/ZrB_2 in-situ composite butt joints. Metals and Materials International, 2012. 18(1): p. 135-142.
143. Kalaiselvan K. and Murugan N., Role of friction stir welding parameters on tensile strength of AA6061–B_4C composite joints. Transactions of Nonferrous Metals Society of China, 2013. 23(3): p. 616-624.
144. Prado R.A., Murr L.E., Soto K.F., and McClure J.C., Self-optimization in tool wear for friction-stir welding of Al 6061+20% Al_2O_3 MMC. Materials Science and Engineering: A, 2003. 349(1): p. 156-165.
145. Ashok Kumar B. and Murugan N., Optimization of friction stir welding process parameters to maximize tensile strength of stir cast AA6061-T6/AlNp composite. Materials & Design, 2014. 57(Supplement C): p. 383-393.
146. Wang D., Xiao B.L., Wang Q.Z., and Ma Z.Y., Evolution of the Microstructure and Strength in the Nugget Zone of Friction Stir Welded SiCp/Al–Cu–Mg Composite. Journal of Materials Science & Technology, 2014. 30(1): p. 54-60.
147. Kumar A., Mahapatra M.M., Jha P.K., Mandal N.R., and Devuri V., Influence of tool geometries and process variables on friction stir butt welding of Al–4.5%Cu/TiC in situ metal matrix composites. Materials & Design, 2014. 59(0): p. 406-414.
148. Mishra R.S., Ma Z.Y., and Charit I., Friction stir processing: a novel technique for fabrication of surface composite. Materials Science and Engineering: A, 2003. 341(1–2): p. 307-310.
149. Guo J., Gougeon P., and Chen X.G., Microstructure evolution and mechanical properties of dissimilar friction stir welded joints between AA1100-B4C MMC and AA6063 alloy. Materials Science and Engineering: A, 2012. 553(0): p. 149-156.
150. Mahmoud E.R.I., Takahashi M., Shibayanagi T., and Ikeuchi K., Wear characteristics of surface-hybrid-MMCs layer fabricated on aluminum plate by friction stir processing. Wear, 2010. 268(9–10): p. 1111-1121.
151. Morisada Y., Fujii H., Nagaoka T., and Fukusumi M., Effect of friction stir processing with SiC particles on microstructure and hardness of AZ31. Materials Science and Engineering: A, 2006. 433(1–2): p. 50-54.
152. Qu J., Xu H., Feng Z., Frederick D.A., An L., and Heinrich H., Improving the tribological characteristics of aluminum 6061 alloy by surface

compositing with sub-micro-size ceramic particles via friction stir processing. Wear, 2011. 271(9–10): p. 1940-1945.
153. Lee C.J., Huang J.C., and Hsieh P.J., Mg based nano-composites fabricated by friction stir processing. Scripta Materialia, 2006. 54(7): p. 1415-1420.
154. Lim D.K., Shibayanagi T., and Gerlich A.P., Synthesis of multi-walled CNT reinforced aluminium alloy composite via friction stir processing. Materials Science and Engineering: A, 2009. 507(1–2): p. 194-199.
155. Zahmatkesh B. and Enayati M.H., A novel approach for development of surface nanocomposite by friction stir processing. Materials Science and Engineering: A, 2010. 527(24–25): p. 6734-6740.
156. Liao J., Processing and mechanical properties of carbon nanotube reinforced aluminium composites. 2012: Nanyang Technological University, Singapore.
157. Liao J.Z., Tan M.J., and Santoso A., High strength aluminum nanocomposites reinforced with multi-walled carbon nanotubes. Advanced Materials Research, 2011. 311-313: p. 80-83.
158. Esawi A.M.K., Morsi K., Sayed A., Gawad A.A., and Borah P., Fabrication and properties of dispersed carbon nanotube–aluminum composites. Materials Science and Engineering: A, 2009. 508(1–2): p. 167-173.
159. Lu D., Jiang Y., and Zhou R., Wear performance of nano-Al_2O_3 particles and CNTs reinforced magnesium matrix composites by friction stir processing. Wear, 2013. 305(1–2): p. 286-290.
160. Liu S., Hu N., Yamamoto G., Cai Y., Zhang Y., Liu Y., Li Y., Hashida T., and Fukunaga H., Investigation on CNT/alumina interface properties using molecular mechanics simulations. Carbon, 2011. 49(11): p. 3701-3704.
161. Yamamoto G., Omori M., Hashida T., and Kimura H., A novel structure for carbon nanotube reinforced alumina composites with improved mechanical properties. Nanotechnology, 2008. 19(31): p. 315708.
162. Yamamoto G., Omori M., Yokomizo K., Hashida T., and Adachi K., Structural characterization and frictional properties of carbon nanotube/alumina composites prepared by precursor method. Materials Science and Engineering: B, 2008. 148(1–3): p. 265-269.
163. Sun J., Gao L., and Li W., Colloidal Processing of Carbon Nanotube/Alumina Composites. Chemistry of Materials, 2002. 14(12): p. 5169-5172.
164. Zhan G.-D., Kuntz J.D., Wan J., and Mukherjee A.K., Single-wall carbon nanotubes as attractive toughening agents in alumina-based nanocomposites. Nat Mater, 2003. 2(1): p. 38-42.
165. Du Z., Tan M.J., Guo J.F., Wei J., and Chua C.K., Dispersion of CNTs in selective laser melting printed $AlSi_{10}Mg$ composites via friction stir processing. Materials Science Forum, 2017. 879: p. 1915-1920.

166. Sato Y.S., Urata M., and Kokawa H., Parameters controlling microstructure and hardness during friction-stir welding of precipitation-hardenable aluminum alloy 6063. Metallurgical and Materials Transactions A, 2002. 33(3): p. 625-635.
167. Brown R., Tang W., and Reynolds A.P., Multi-pass friction stir welding in alloy 7050-T7451: Effects on weld response variables and on weld properties. Materials Science and Engineering: A, 2009. 513–514(0): p. 115-121.
168. Hassan K.A.A., Norman A.F., Price D.A., and Prangnell P.B., Stability of nugget zone grain structures in high strength Al-alloy friction stir welds during solution treatment. Acta Materialia, 2003. 51(7): p. 1923-1936.
169. Izadi H. and Gerlich A.P., Distribution and stability of carbon nanotubes during multi-pass friction stir processing of carbon nanotube/aluminum composites. Carbon, 2012. 50(12): p. 4744-4749.
170. Su J.-Q., Nelson T.W., and Sterling C.J., Microstructure evolution during FSW/FSP of high strength aluminum alloys. Materials Science and Engineering: A, 2005. 405(1–2): p. 277-286.
171. Guo J., Amira S., Gougeon P., and Chen X.G., Effect of the surface preparation techniques on the EBSD analysis of a friction stir welded AA1100-B4C metal matrix composite. Materials Characterization, 2011. 62(9): p. 865-877.
172. Fonda R.W., Knipling K.E., and Bingert J.F., Microstructural evolution ahead of the tool in aluminum friction stir welds. Scripta Materialia, 2008. 58(5): p. 343-348.
173. Humphreys F.J. and Hatherly M., Chapter 13 - Hot deformation and dynamic restoration, in *Recrystallization and Related Annealing Phenomena (Second Edition)*, F.J. Humphreys and M. Hatherly, Editors. 2004, Elsevier Ltd.: Oxford. p. 415-450.
174. Brown R., Tang W., and Reynolds A., Multi-pass friction stir welding in alloy 7050-T7451: Effects on weld response variables and on weld properties. Materials Science and Engineering: A, 2009. 513: p. 115-121.
175. Shahani R.A. and Clyne T.W., Recrystallization in fibrous and particulate metal matrix composites. Materials Science and Engineering: A, 1991. 135(Supplement C): p. 281-285.
176. Sato Y.S., Kokawa H., Enomoto M., and Jogan S., Microstructural evolution of 6063 aluminum during friction-stir welding. Metallurgical and Materials Transactions A, 1999. 30(9): p. 2429-2437.
177. Rollett A., Humphreys F., Rohrer G.S., and Hatherly M., Recrystallization and related annealing phenomena. 2004: Elsevier.
178. Tweed C.J., Ralph B., and Hansen N., The pinning by particles of low and high angle grain boundaries during grain growth. Acta Metallurgica, 1984. 32(9): p. 1407-1414.
179. Du Z., Tan M.J., Guo J.F., Bi G., and Wei J., Fabrication of a new Al-Al_2O_3-CNTs composite using friction stir processing (FSP). Materials Science and Engineering: A, 2016. 667: p. 125-131.

180. Wu Y., Kim G.-Y., and Russell A.M., Effects of mechanical alloying on an Al6061–CNT composite fabricated by semi-solid powder processing. Materials Science and Engineering: A, 2012. 538(0): p. 164-172.
181. Yu H., Lu C., Xi T., Luo L., Ning J., and Xiang C., Thermal decomposition of the carbon nanotube/SiO_2 precursor powders. Journal of Thermal Analysis and Calorimetry, 2005. 82(1): p. 97-101.
182. Boonchouytan W., Chatthong J., Rawangwong S., and Burapa R., Effect of Heat Treatment T6 on the Friction Stir Welded SSM 6061 Aluminum Alloys. Energy Procedia, 2014. 56: p. 172-180.
183. Krishnan K.N., The effect of post weld heat treatment on the properties of 6061 friction stir welded joints. Journal of Materials Science, 2002. 37(3): p. 473-480.
184. Sato Y.S. and Kokawa H., Distribution of tensile property and microstructure in friction stir weld of 6063 aluminum. Metallurgical and Materials Transactions A, 2001. 32(12): p. 3023-3031.
185. Rajesh S., Krishna A.G., Raju P.R.M., and Duraiselvam M., Multi-response optimization of tribological characteristics of aluminum MMCs using PCA. Multidiscipline Modeling in Materials and Structures, 2014. 10(2): p. 276-287.
186. Kathiresan M. and Sornakumar T., Friction and wear studies of die cast aluminum alloy - aluminum oxide - reinforced composites. Industrial Lubrication and Tribology, 2010. 62(6): p. 361-371.
187. Anna K., Audi moves forward with all - aluminium cars. Assembly Automation, 2000. 20(2): p. 132-135.
188. Mazahery A., Abdizadeh H., and Baharvandi H.R., Development of high-performance A356/nano-Al_2O_3 composites. Materials Science and Engineering: A, 2009. 518(1): p. 61-64.
189. Durai T.G., Das K., and Das S., Synthesis and characterization of Al matrix composites reinforced by in situ alumina particulates. Materials Science and Engineering: A, 2007. 445–446: p. 100-105.
190. Yap C.Y., Tan H.K., Du Z., Chua C.K., and Dong Z., Selective laser melting of nickel powder. Rapid Prototyping Journal, 2017. 23(4): p. 750-757.
191. Chi Chung N., Monica S., and Hau Chung M., Fabrication of magnesium using selective laser melting technique. Rapid Prototyping Journal, 2011. 17(6): p. 479-490.
192. Il Hyuk A., Seung Ki M., Jihong H., and Guijun B., Characteristic length of the solidified melt pool in selective laser melting process. Rapid Prototyping Journal, 2017. 23(2): p. 370-381.
193. Matthew W., Sozon T., Chris J.S., and Ieuan O., Selective laser melting of heat transfer devices. Rapid Prototyping Journal, 2007. 13(5): p. 291-297.
194. Peter M. and Jean - Pierre K., Residual stresses in selective laser sintering and selective laser melting. Rapid Prototyping Journal, 2006. 12(5): p. 254-265.

195. Chua C.K. and Leong K.F., 3D Printing and Additive Manufacturing: principles and applications. 5th ed. 2017: Singapore ; New Jersey : World Scientific.
196. Wong K.K., Ho J.Y., Leong K.C., and Wong T.N., Fabrication of heat sinks by Selective Laser Melting for convective heat transfer applications. Virtual and Physical Prototyping, 2016. 11(3): p. 159-165.
197. Salmi A. and Atzeni E., History of residual stresses during the production phases of $AlSi_{10}Mg$ parts processed by powder bed additive manufacturing technology. Virtual and Physical Prototyping, 2017. 12(2): p. 153-160.
198. Yap C.Y., Chua C.K., and Dong Z.L., An effective analytical model of selective laser melting. Virtual and Physical Prototyping, 2016. 11(1): p. 21-26.
199. Jhabvala J., Boillat E., Antignac T., and Glardon R., On the effect of scanning strategies in the selective laser melting process. Virtual and Physical Prototyping, 2010. 5(2): p. 99-109.
200. Simchi A. and Pohl H., Direct laser sintering of iron–graphite powder mixture. Materials Science and Engineering: A, 2004. 383(2): p. 191-200.
201. Olakanmi E.O., Selective laser sintering/melting (SLS/SLM) of pure Al, Al–Mg, and Al–Si powders: Effect of processing conditions and powder properties. Journal of Materials Processing Technology, 2013. 213(8): p. 1387-1405.
202. Youssef Y.M., Dashwood R.J., and Lee P.D., Effect of clustering on particle pushing and solidification behaviour in TiB2 reinforced aluminium PMMCs. Composites Part A: Applied Science and Manufacturing, 2005. 36(6): p. 747-763.
203. Neumann A.W., Szekely J., and Rabenda E.J., Thermodynamics of particle engulfment by solidifying melts. Journal of Colloid and Interface Science, 1973. 43(3): p. 727-732.
204. Laurent V., Chatain D., Chatillon C., and Eustathopoulos N., Wettability of monocrystalline alumina by aluminium between its melting point and 1273 K. Acta Metallurgica, 1988. 36(7): p. 1797-1803.
205. Humphreys J., Rohrer G.S., and Rollett A., Chapter 6 - Recovery After Deformation, in *Recrystallization and Related Annealing Phenomena (Third Edition)*. 2017, Elsevier: Oxford. p. 199-244.
206. Rollett A., Humphreys F.J., Rohrer G.S., and Hatherly M., Recrystallization and Related Annealing Phenomena. 2nd ed. 2004: Elsevier Science.
207. Jarfors A.E.W., Keife H., and Antonsson T., Deformation enhanced liquid phase sintering (DELPS): a study on the use of partial adiabatic melting during powder consolidation. Journal of Materials Processing Technology, 2002. 127(2): p. 159-164.
208. Li X., J Wang X., Saunders M., Suvorova A., Zhang L., J Liu Y., Fang M., H Huang Z., and Sercombe T., A selective laser melting and solution heat treatment refined Al–12Si alloy with a controllable ultrafine eutectic

microstructure and 25% tensile ductility. Acta Materialia, 2015. 95: p. 74-82.
209. Mandal N.R., Aluminum welding. 2002: New Delhi, India : Narosa Publishing House : ASM International (North American distributor), c2002.
210. Thomas W.M. and Nicholas E.D., Friction stir welding for the transportation industries. Materials & Design, 1997. 18(4–6): p. 269-273.
211. Scialpi A., De Filippis L.A.C., and Cavaliere P., Influence of shoulder geometry on microstructure and mechanical properties of friction stir welded 6082 aluminium alloy. Materials & Design, 2007. 28(4): p. 1124-1129.
212. Cavaliere P., De Santis A., Panella F., and Squillace A., Effect of welding parameters on mechanical and microstructural properties of dissimilar AA6082–AA2024 joints produced by friction stir welding. Materials & Design, 2009. 30(3): p. 609-616.
213. Murr L.E., Liu G., and McClure J.C., Dynamic recrystallization in friction-stir welding of aluminium alloy 1100. Journal of Materials Science Letters, 1997. 16(22): p. 1801-1803.
214. Roberts C.E., Bourell D., Watt T., and Cohen J., A Novel Processing Approach for Additive Manufacturing of Commercial Aluminum Alloys. Physics Procedia, 2016. 83(Supplement C): p. 909-917.
215. Loh L.E., Selective laser melting of aluminium alloys : numerical modelling and material properties characterisation. in School of Mechanical and Aerospace Engineering, 2014(Nanyang Technological University: Singapore).
216. Xu W., Liu J., Luan G., and Dong C., Temperature evolution, microstructure and mechanical properties of friction stir welded thick 2219-O aluminum alloy joints. Materials & Design, 2009. 30(6): p. 1886-1893.
217. Arbegast W.J., A flow-partitioned deformation zone model for defect formation during friction stir welding. Scripta Materialia, 2008. 58(5): p. 372-376.
218. Al-Fadhalah K.J., Almazrouee A.I., and Aloraier A.S., Microstructure and mechanical properties of multi-pass friction stir processed aluminum alloy 6063. Materials & Design, 2014. 53(0): p. 550-560.
219. Moreira P.M.G.P., Santos T., Tavares S.M.O., Richter-Trummer V., Vilaça P., and de Castro P.M.S.T., Mechanical and metallurgical characterization of friction stir welding joints of AA6061-T6 with AA6082-T6. Materials & Design, 2009. 30(1): p. 180-187.
220. Takahara H., Tsujikawa M., Chung S.W., Okawa Y., Higashi K., and Oki S., Optimization of welding condition for nonlinear friction stir welding. Materials Transactions, 2008. 49(6): p. 1359-1364.
221. Seidel T.U. and Reynolds A.P., Visualization of the material flow in AA2195 friction-stir welds using a marker insert technique. Metallurgical and Materials Transactions A, 2001. 32(11): p. 2879-2884.

222. Hassan A.M., Almomani M., Qasim T., and Ghaithan A., Effect of Processing Parameters on Friction Stir Welded Aluminum Matrix Composites Wear Behavior. Materials and Manufacturing Processes, 2012. 27(12): p. 1419-1423.
223. Huang R.Y., Huang J.C., and Chen S.C., Electron and laser beam welding of high strain rate superplastic Al-6061/SiC composites. Metallurgical and Materials Transactions A, 2001. 32(10): p. 2575-2584.
224. Du Z., Tan M.-J., Guo J.-F., and Wei J., Friction stir processing of Al–CNT composites. Proceedings of the Institution of Mechanical Engineers, Part L: Journal of Materials: Design and Applications, 2016. 230(3): p. 825-833.
225. Sing S.L., Yeong W.Y., and Wiria F.E., Selective laser melting of titanium alloy with 50 wt% tantalum: Microstructure and mechanical properties. Journal of Alloys and Compounds, 2016. 660(Supplement C): p. 461-470.
226. Hao L., Dadbakhsh S., Seaman O., and Felstead M., Selective laser melting of a stainless steel and hydroxyapatite composite for load-bearing implant development. Journal of Materials Processing Technology, 2009. 209(17): p. 5793-5801.
227. Vrancken B., Thijs L., Kruth J.P., and Van Humbeeck J., Microstructure and mechanical properties of a novel β titanium metallic composite by selective laser melting. Acta Materialia, 2014. 68(Supplement C): p. 150-158.
228. Uzun H., Friction stir welding of SiC particulate reinforced AA2124 aluminium alloy matrix composite. Materials & Design, 2007. 28(5): p. 1440-1446.
229. Humphreys F.J., The nucleation of recrystallization at second phase particles in deformed aluminium. Acta Metallurgica, 1977. 25(11): p. 1323-1344.
230. Yadav D. and Bauri R., Nickel particle embedded aluminium matrix composite with high ductility. Materials Letters, 2010. 64(6): p. 664-667.
231. Petch N.J., The Cleavage Strength of Polycrystals. Journal of the Iron and Steel Institute, 1953. 174: p. 25-28.
232. Zhang D.L., Zheng L.H., and StJohn D.H., Effect of a short solution treatment time on microstructure and mechanical properties of modified Al–7wt.%Si–0.3wt.%Mg alloy. Journal of Light Metals, 2002. 2(1): p. 27-36.
233. Prime M.B., Gnäupel-Herold T., Baumann J.A., Lederich R.J., Bowden D.M., and Sebring R.J., Residual stress measurements in a thick, dissimilar aluminum alloy friction stir weld. Acta Materialia, 2006. 54(15): p. 4013-4021.
234. Maggiolino S. and Schmid C., Corrosion resistance in FSW and in MIG welding techniques of AA6XXX. Journal of Materials Processing Technology, 2008. 197(1): p. 237-240.

235. Fahimpour V., Sadrnezhaad S.K., and Karimzadeh F., Corrosion behavior of aluminum 6061 alloy joined by friction stir welding and gas tungsten arc welding methods. Materials & Design, 2012. 39(Supplement C): p. 329-333.
236. Cabrini M., Lorenzi S., Pastore T., Pellegrini S., Manfredi D., Fino P., Biamino S., and Badini C., Evaluation of corrosion resistance of Al–10Si–Mg alloy obtained by means of Direct Metal Laser Sintering. Journal of Materials Processing Technology, 2016. 231(Supplement C): p. 326-335.
237. Zhang W., Gu M., Chen J., Wu Z., Zhang F., and Deve H.E., Tensile and fatigue response of alumina-fiber-reinforced aluminum matrix composite. Materials Science and Engineering: A, 2003. 341(1): p. 9-17.
238. Thomas W.M., Nicholas E.D., and Smith S.D. Aluminum 2001-Proceedings of the TMS 2001 Aluminum Automotive and Joining Sessions, TMS. 2001.

Appendix A

Energy Dispersive Spectroscopy (EDS) Results

This appendix contains the energy dispersive spectroscopy results of all the samples in this study.

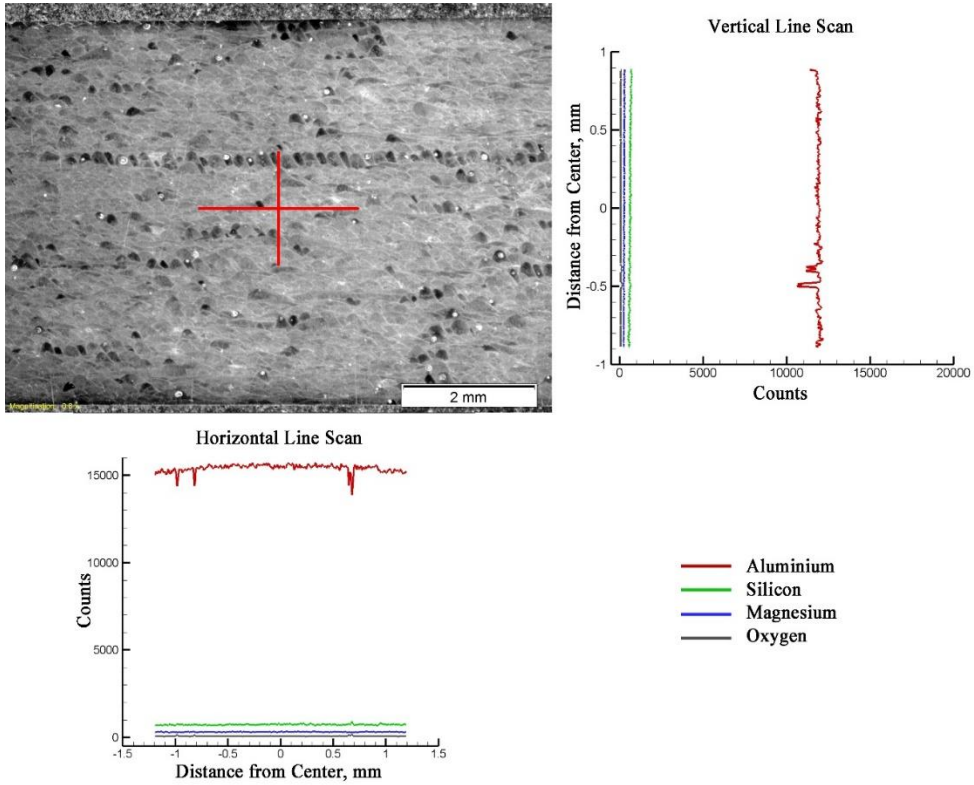

As-received SLM of $AlSi_{10}Mg$ with high VED.

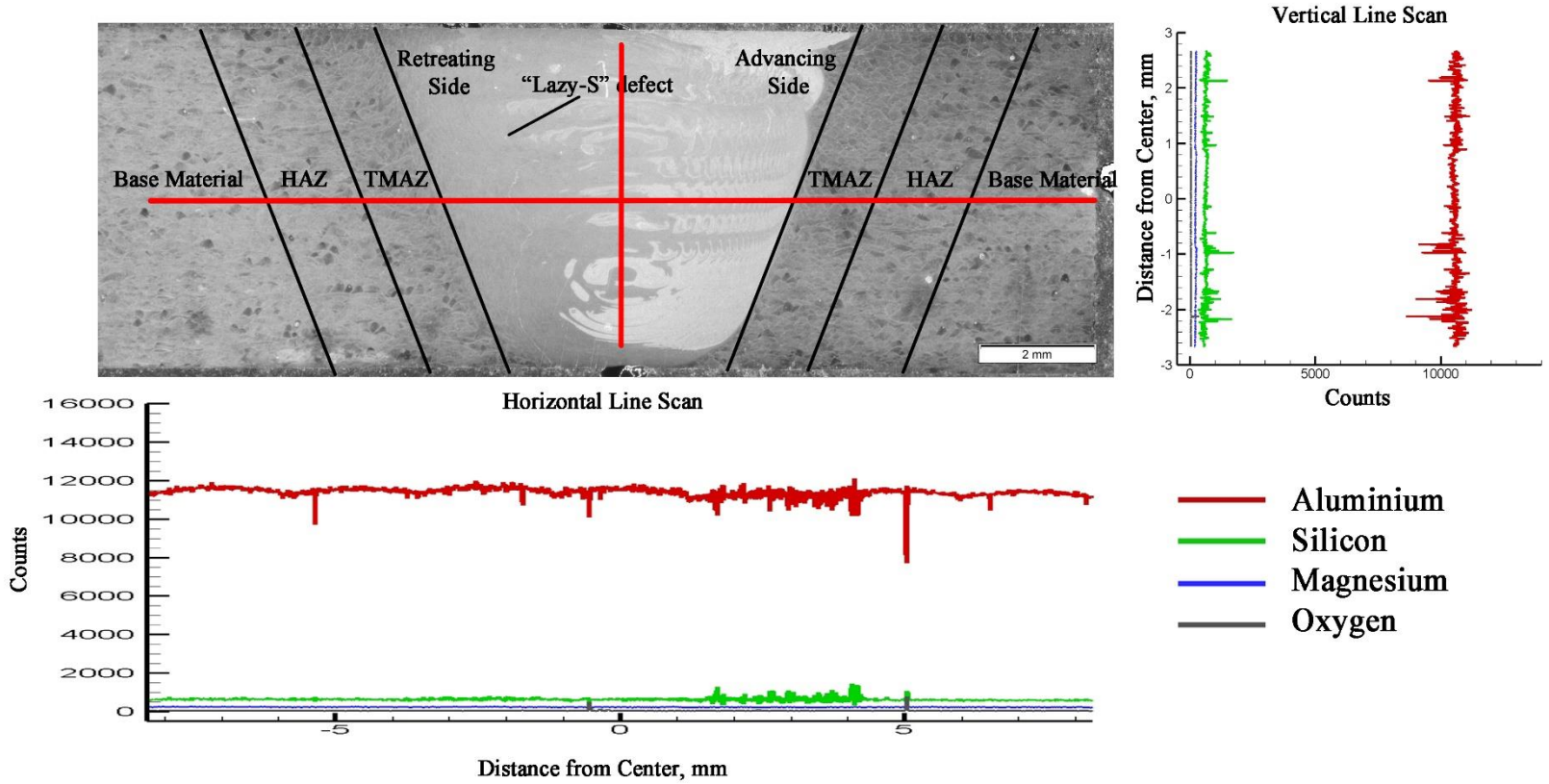

FSW with low heat input with low tilt angle of SLM of $AlSi_{10}Mg$ with high VED.

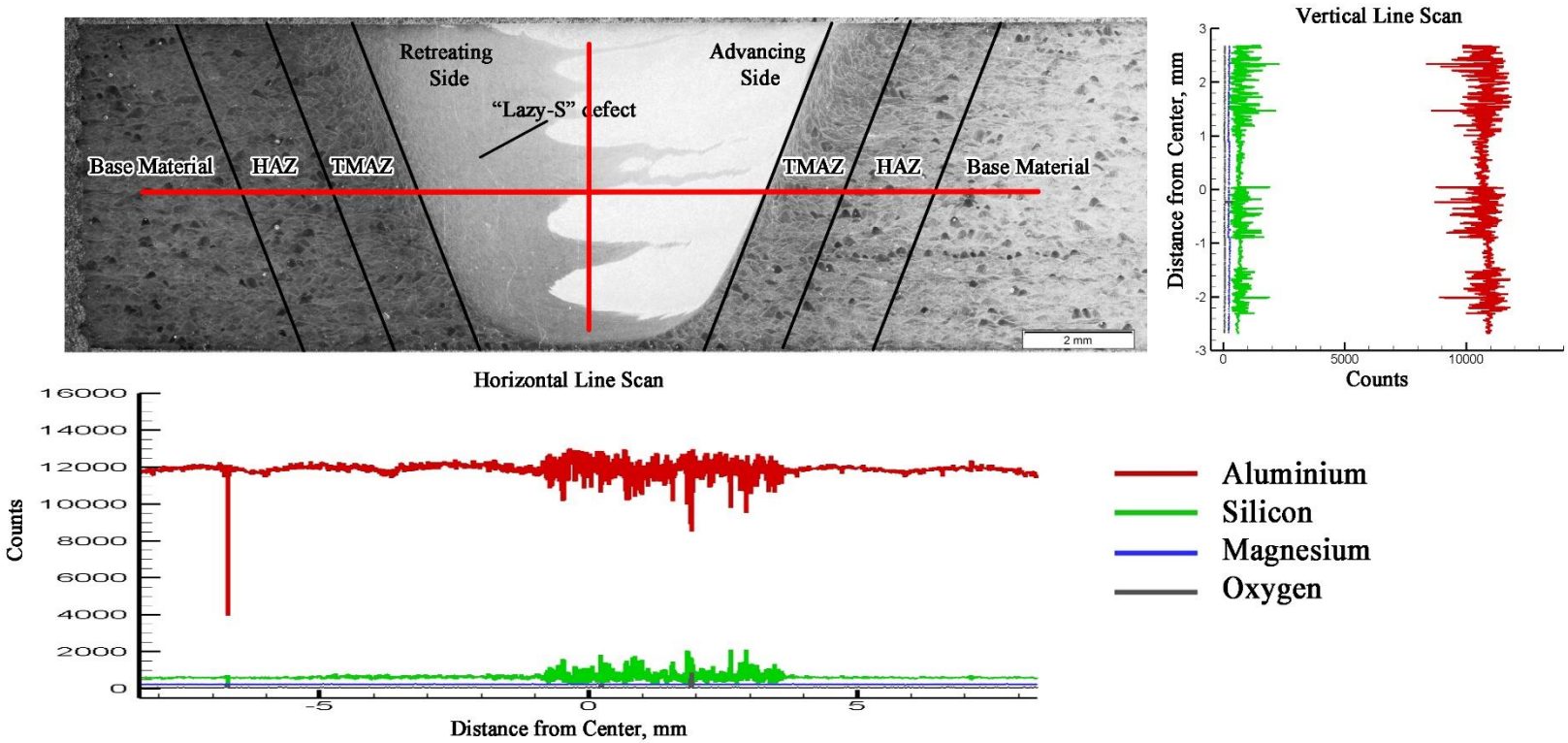

FSW with high heat input with low tilt angle SLM of $AlSi_{10}Mg$ with high VED.

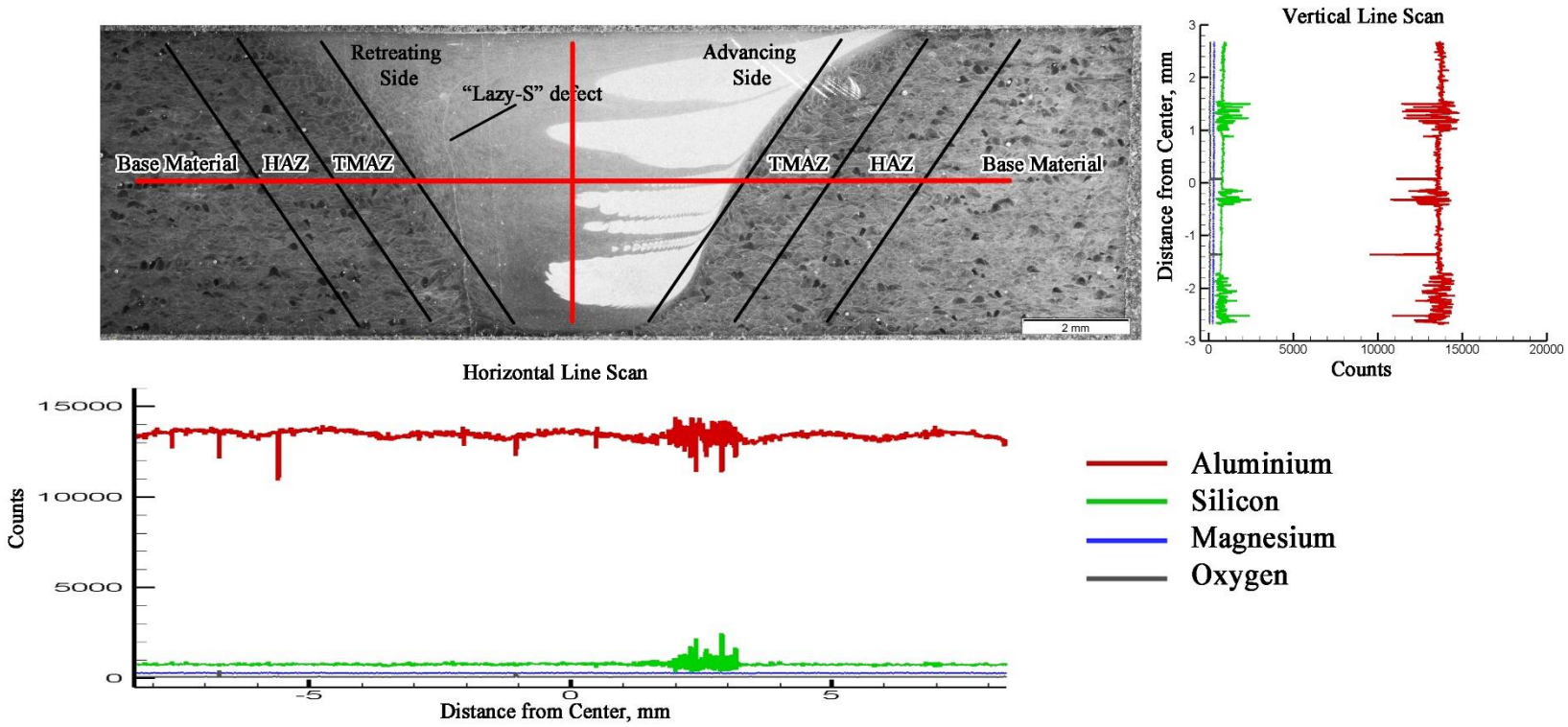

FSW with low heat input with high tilt angle of SLM of $AlSi_{10}Mg$ with high VED.

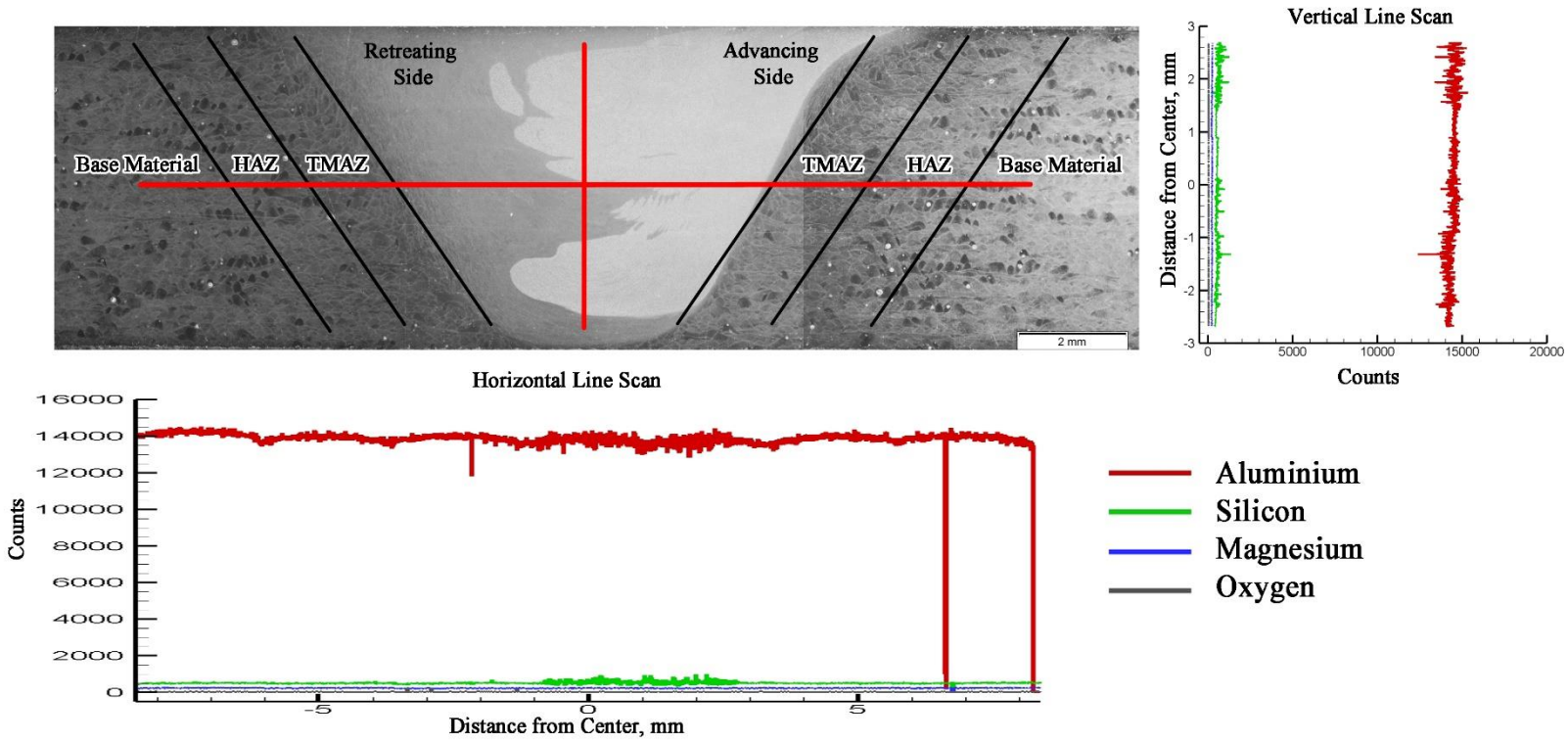

FSW with high heat input with high tilt angle of SLM of $AlSi_{10}Mg$ with high VED.

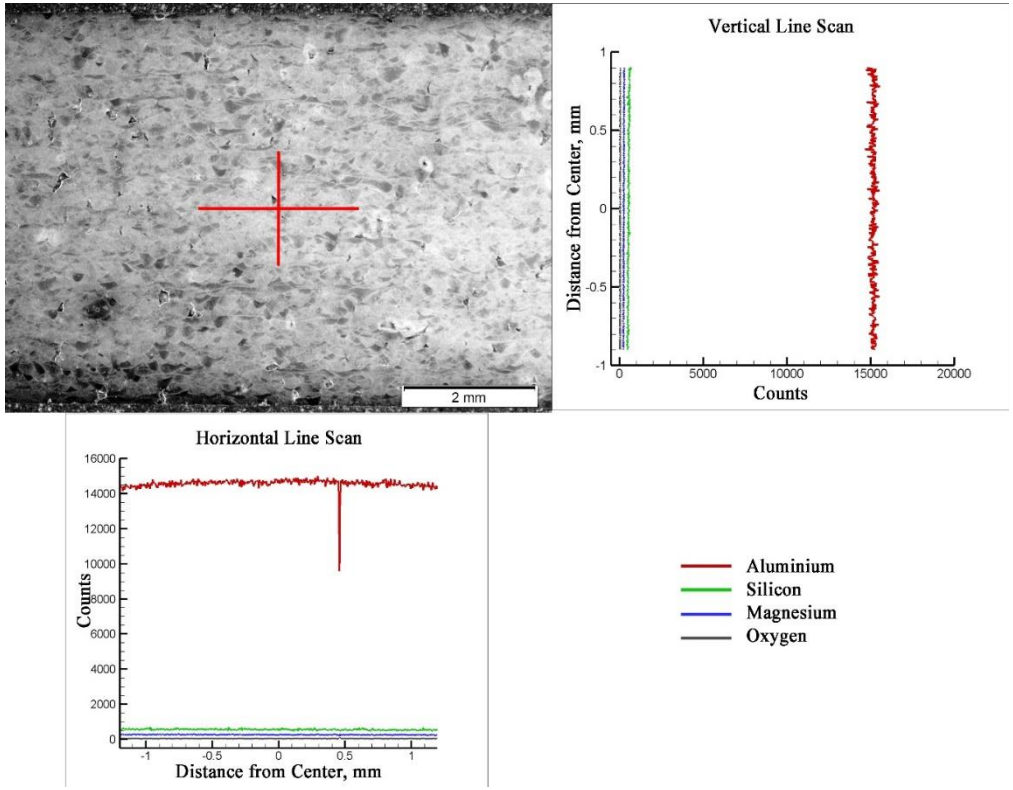

As-received SLM of $AlSi_{10}Mg$ with low VED.

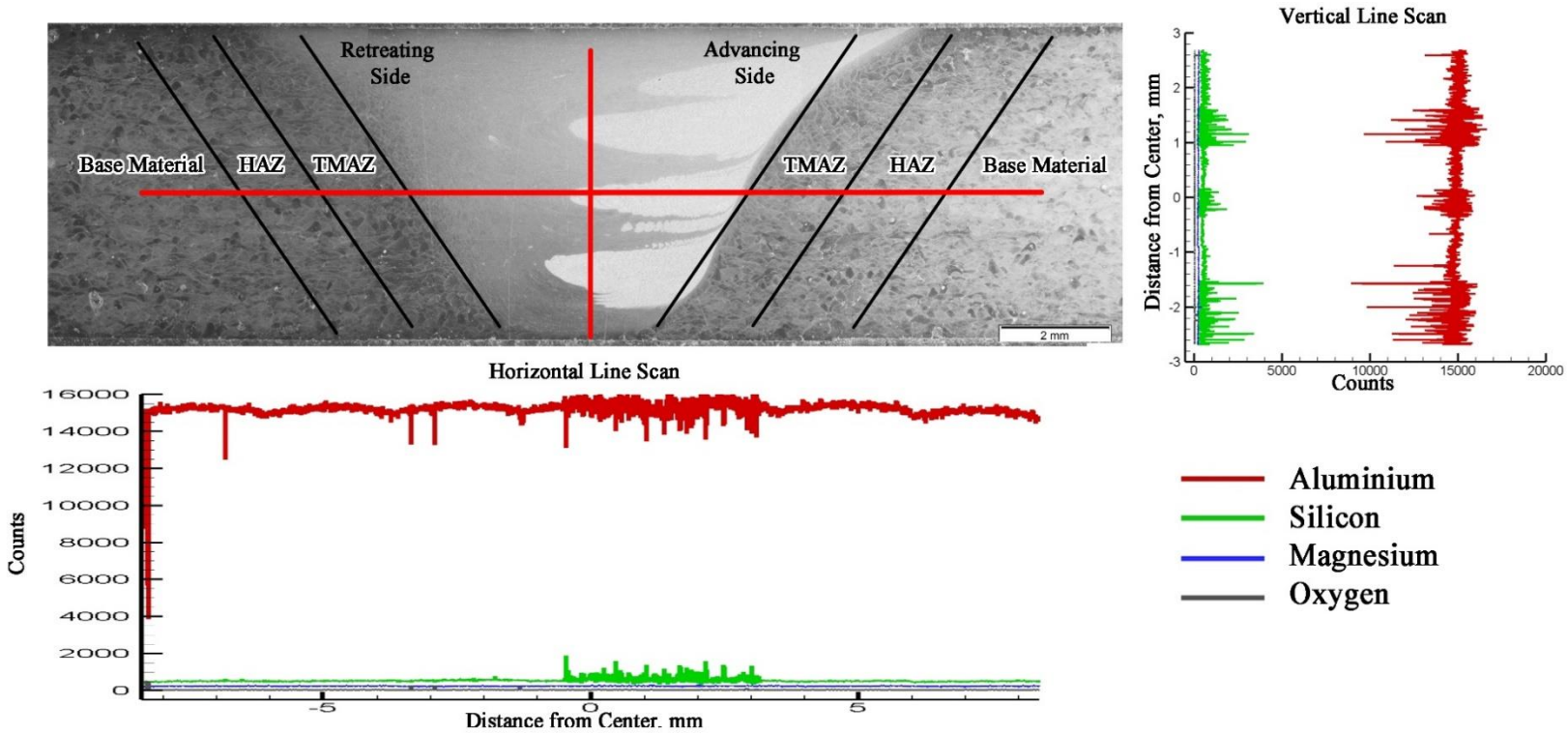

FSW with low heat input of SLM of $AlSi_{10}Mg$ with low VED.

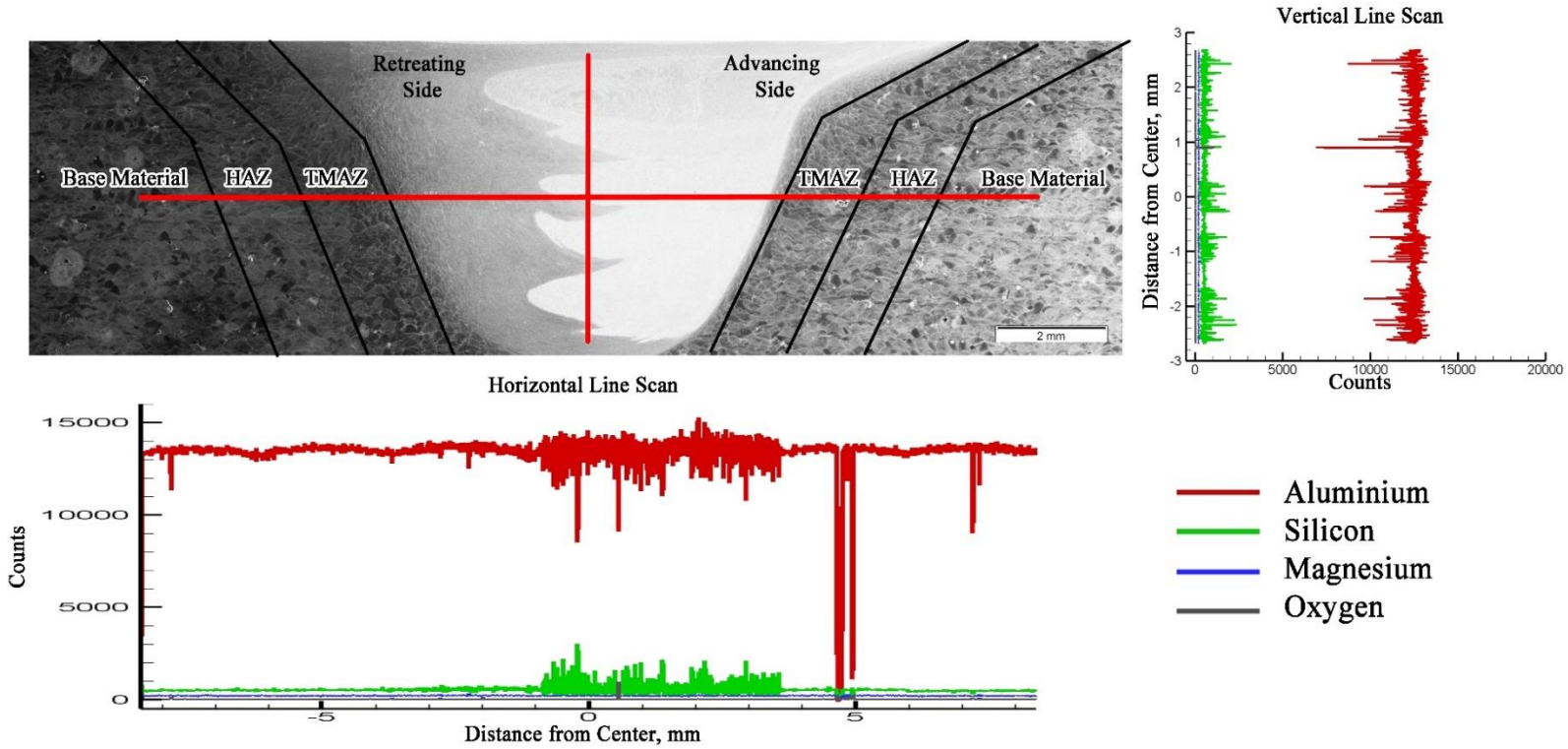

FSW with high heat input of SLM of $AlSi_{10}Mg$ with low VED.

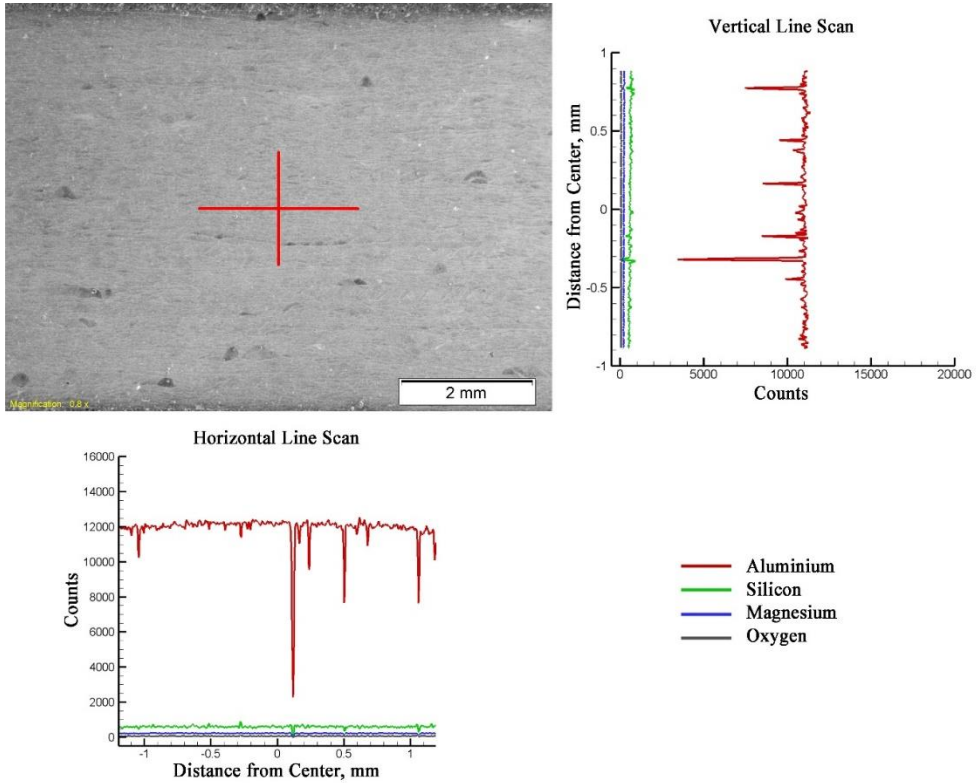

As-received SLM of $AlSi_{10}Mg$ - 2% wt. nAl_2O_3 with high VED.

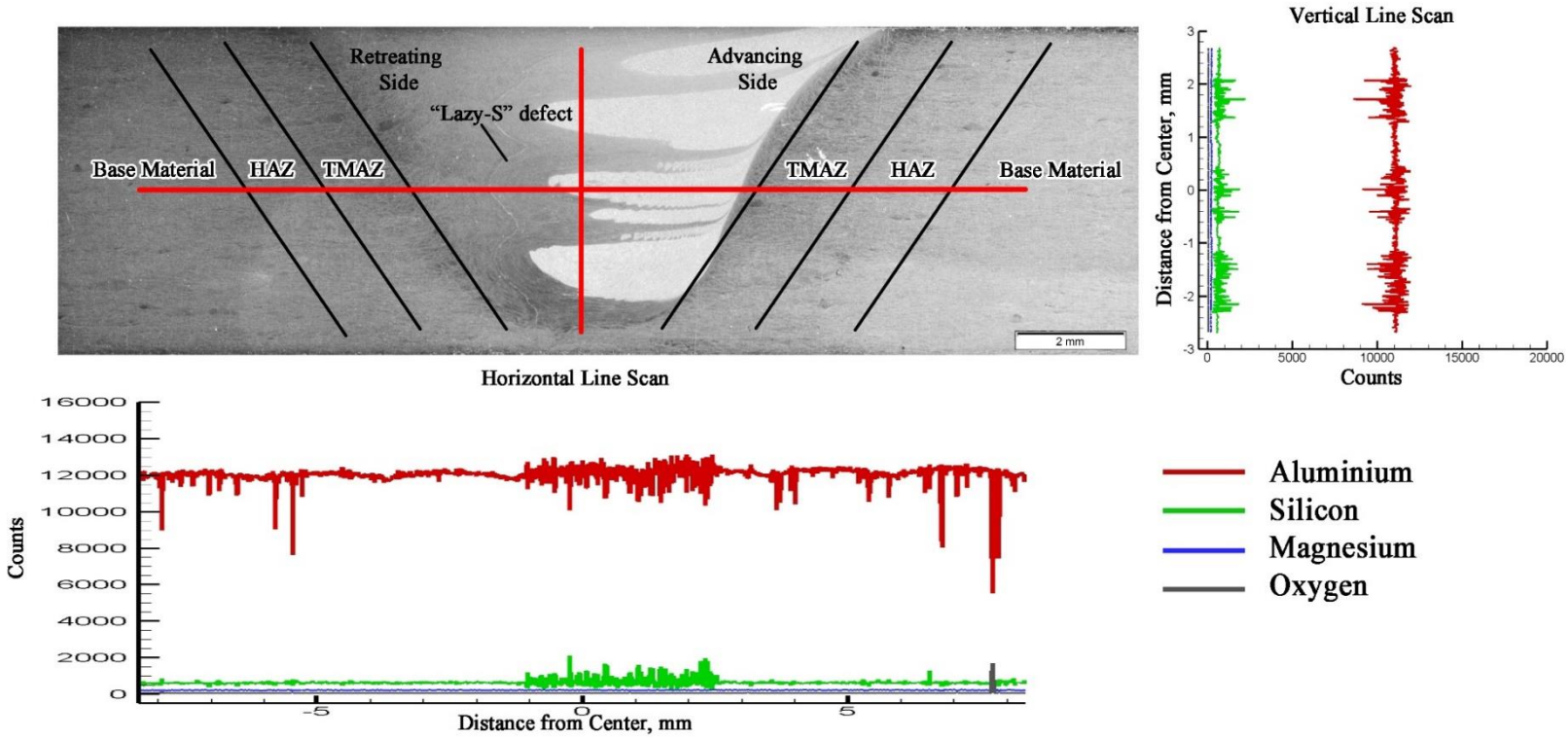

FSW with low heat input of SLM of $AlSi_{10}Mg$ - 2% wt. nAl_2O_3 with high VED.

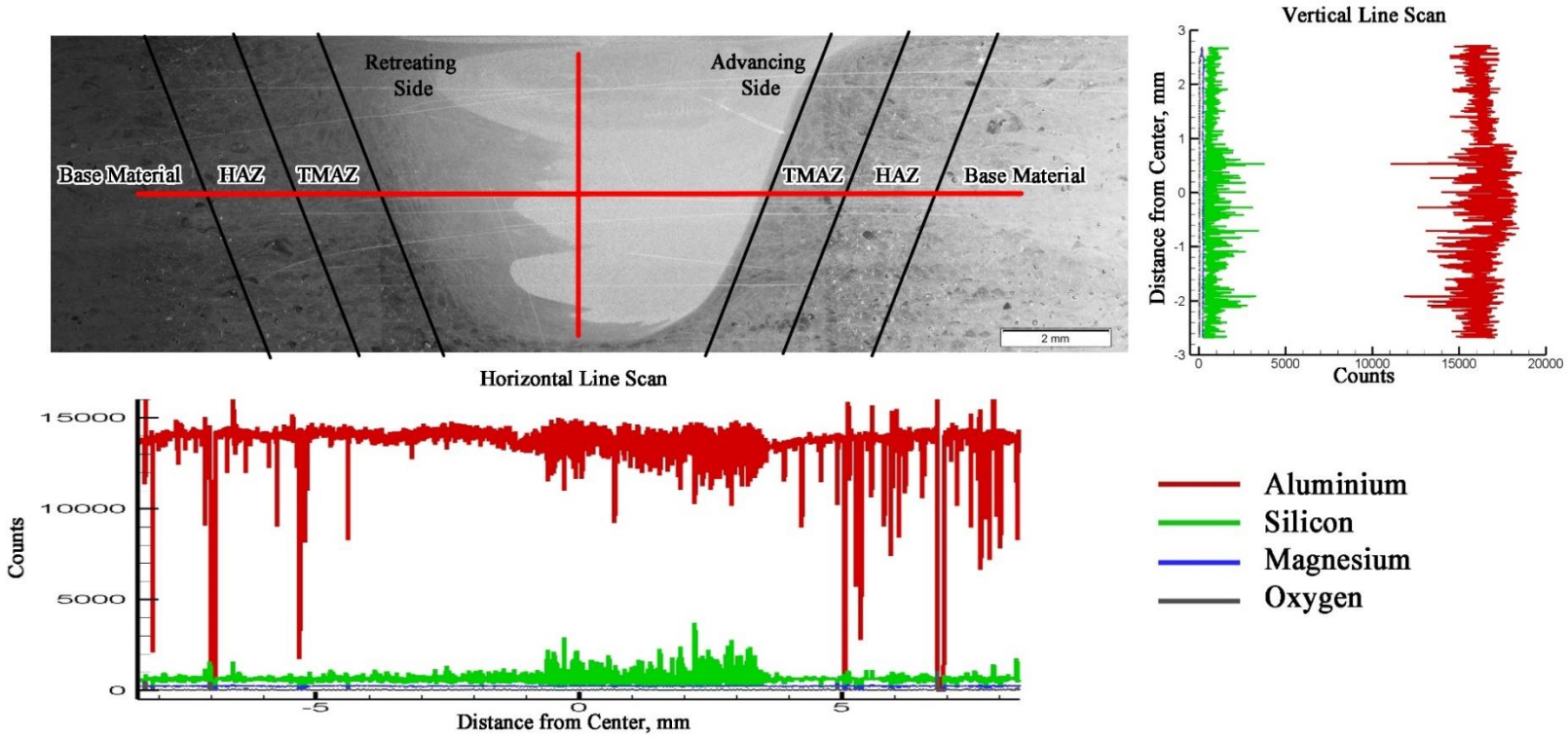

FSW with high heat input of SLM of $AlSi_{10}Mg$ - 2% wt. nAl_2O_3 with high VED.

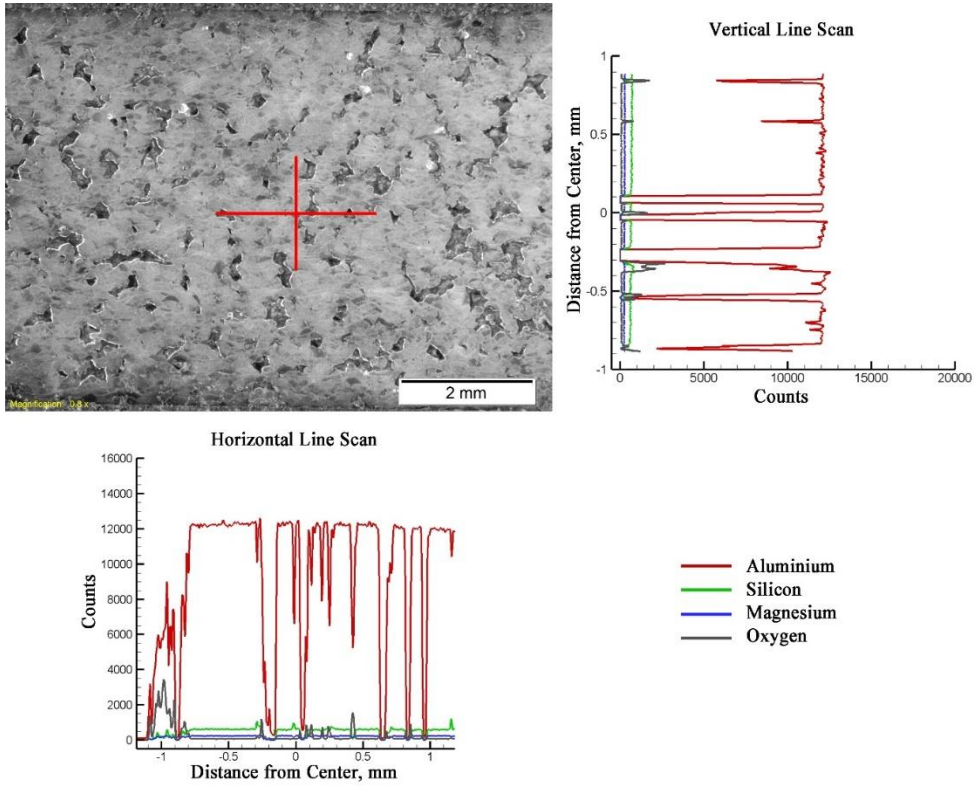

As-received SLM of $AlSi_{10}Mg$ - 2% wt. nAl_2O_3 with low VED.

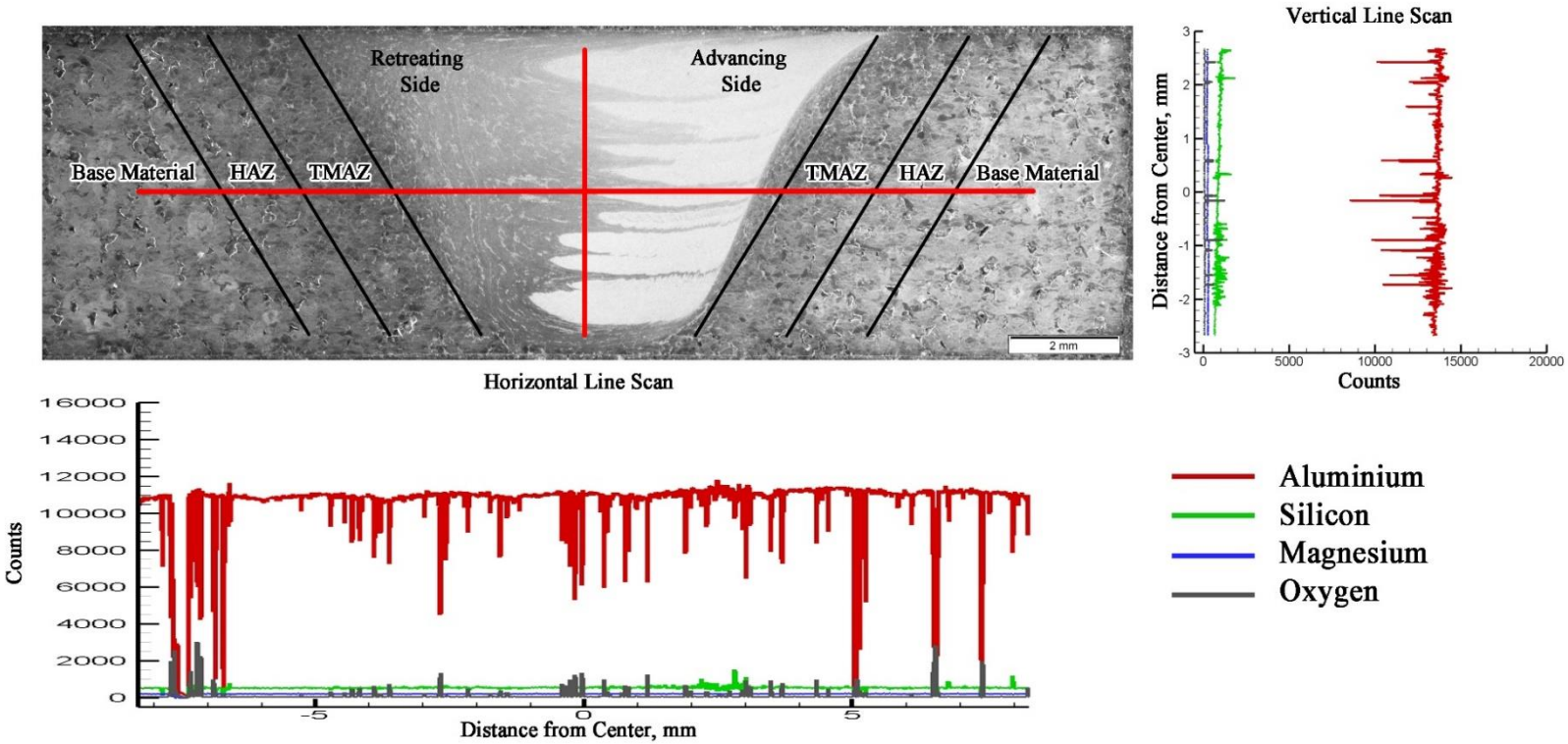

FSW with low heat input of SLM of $AlSi_{10}Mg$ - 2% wt. nAl_2O_3 with low VED.

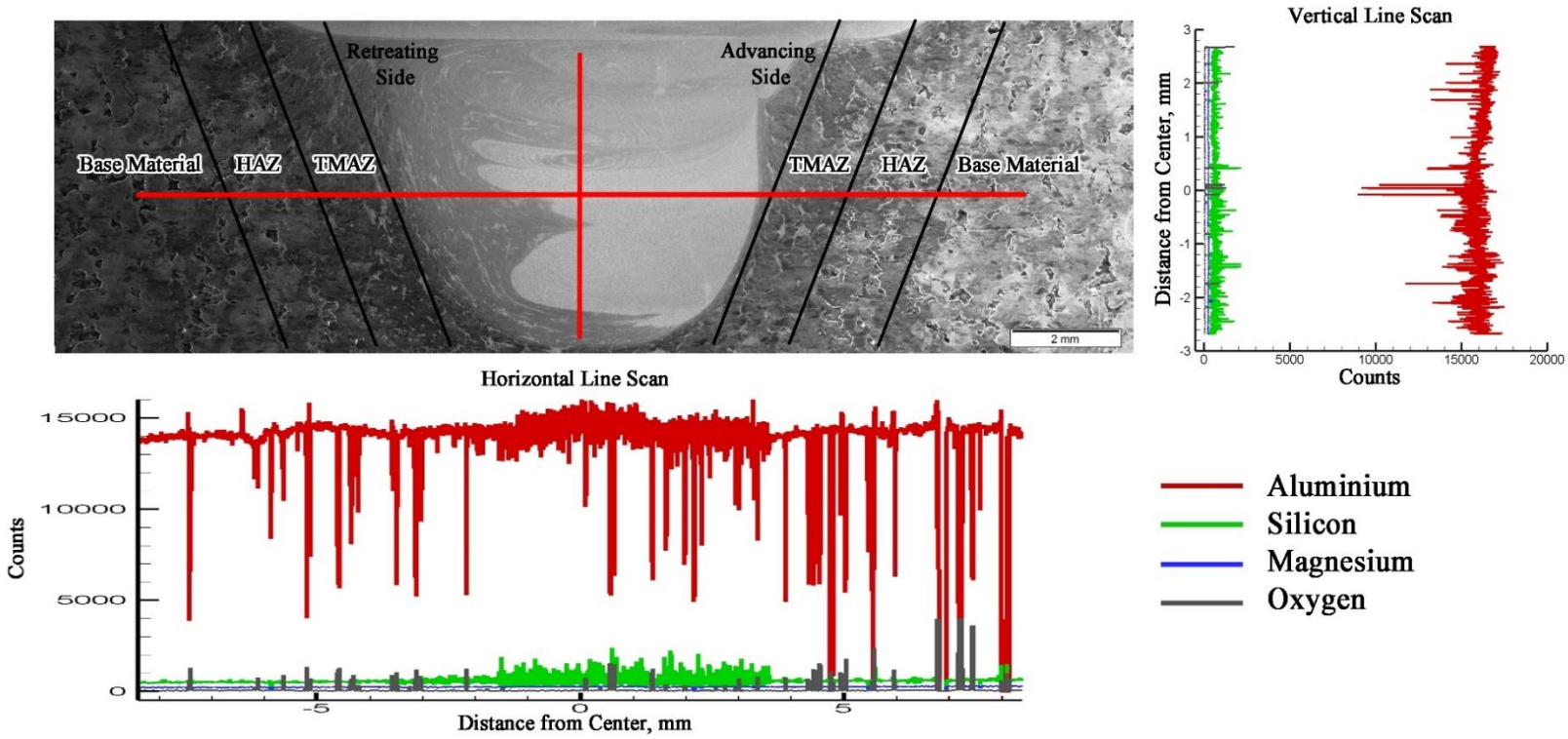

FSW with high heat input of SLM of $AlSi_{10}Mg$ - 2% wt. nAl_2O_3 with low VED.

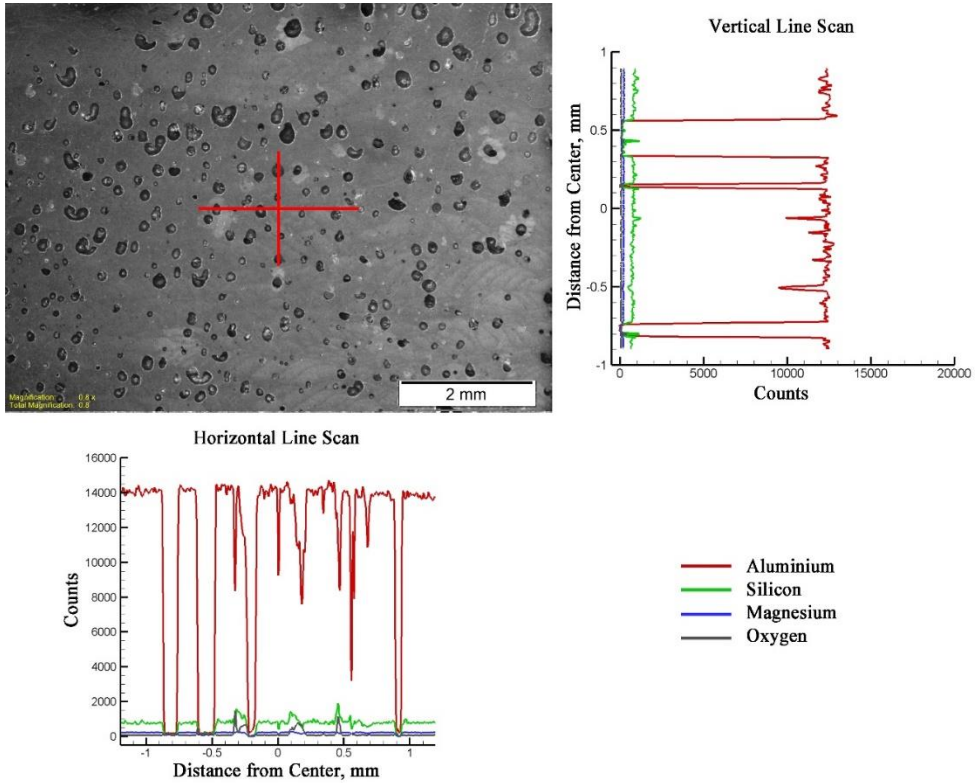

as-received SLM of $AlSi_{10}Mg$ - 5% wt. nAl_2O_3 with high VED.

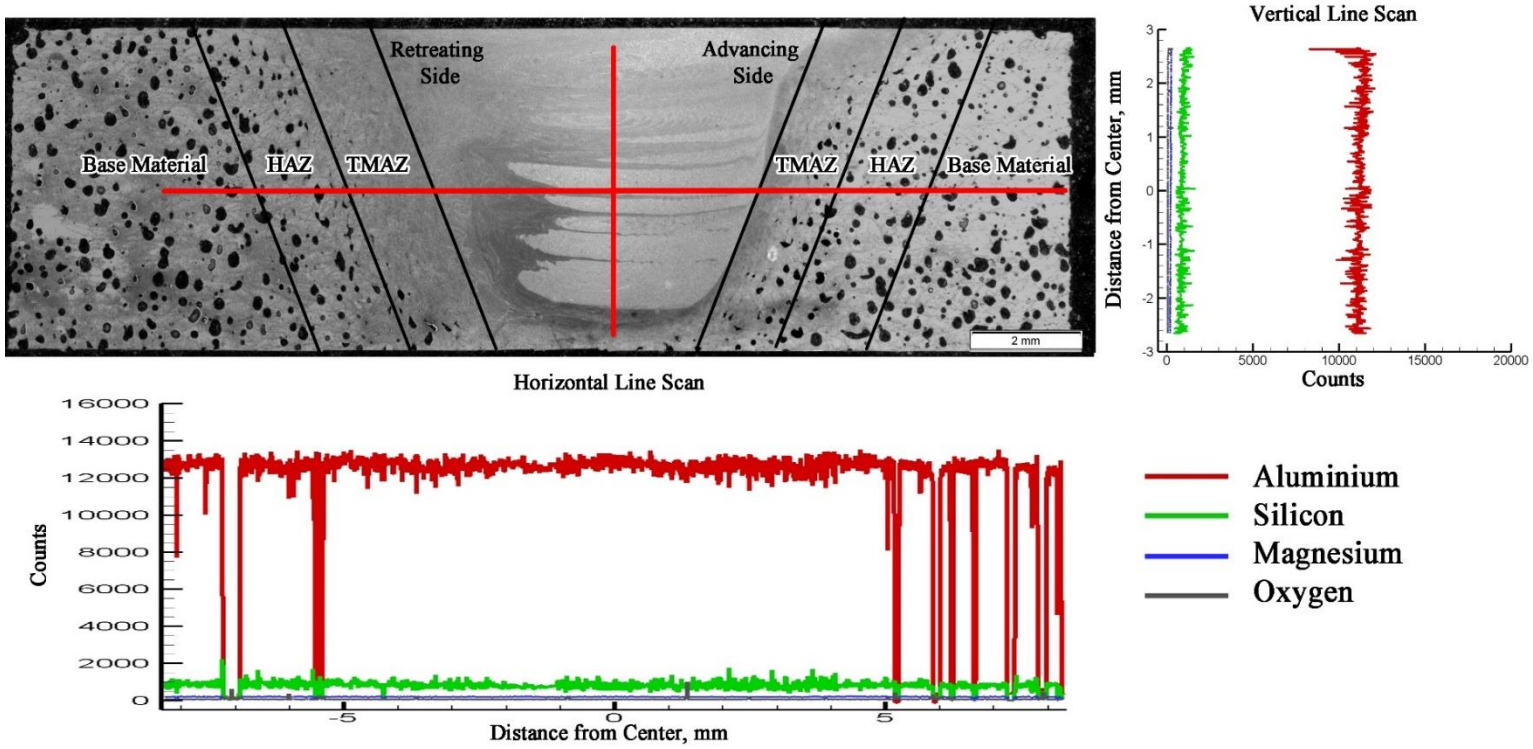

FSW with low heat input of SLM of $AlSi_{10}Mg$ - 5% wt. nAl_2O_3 with high VED.

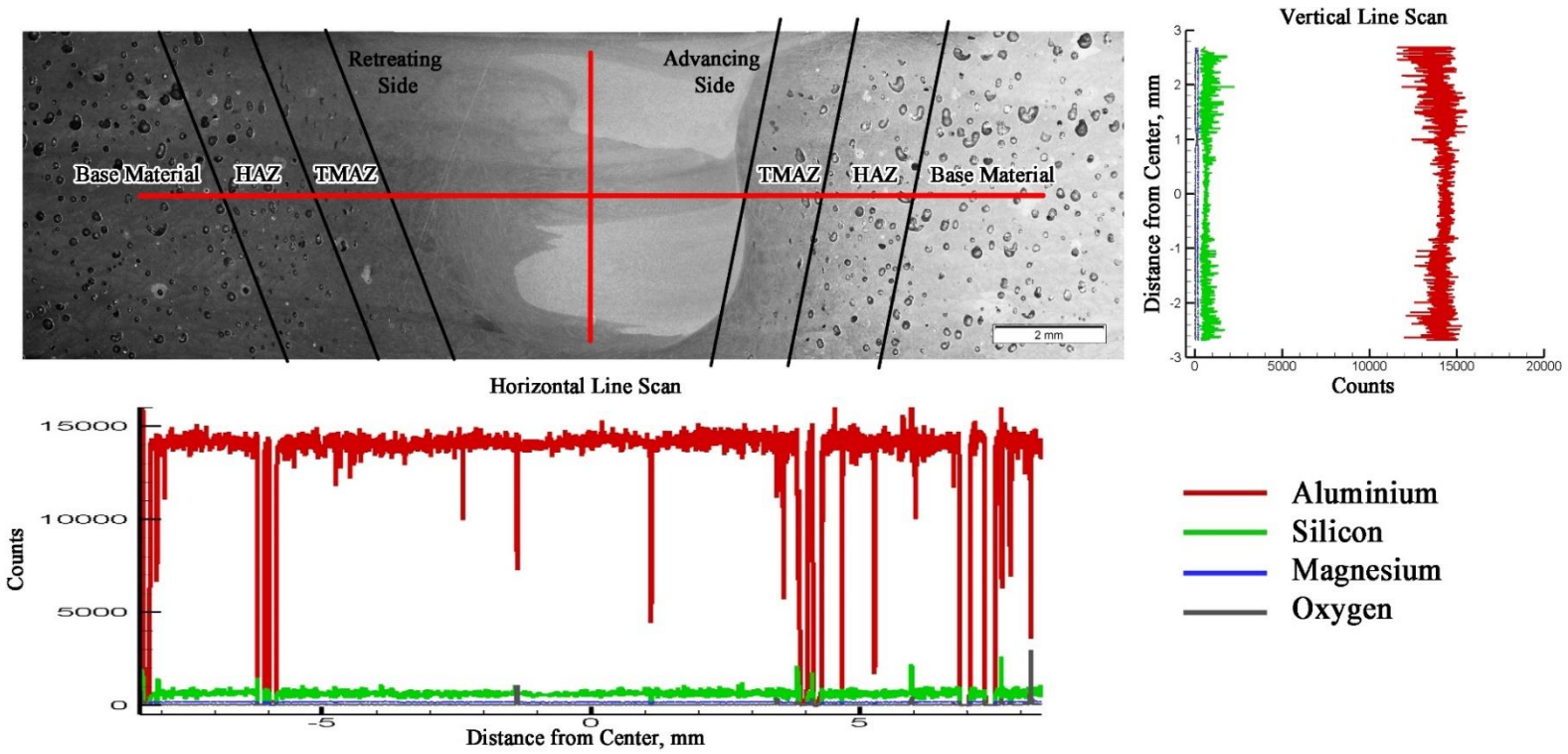

FSW with high heat input of SLM of $AlSi_{10}Mg$ - 5% wt. nAl_2O_3 with high VED.

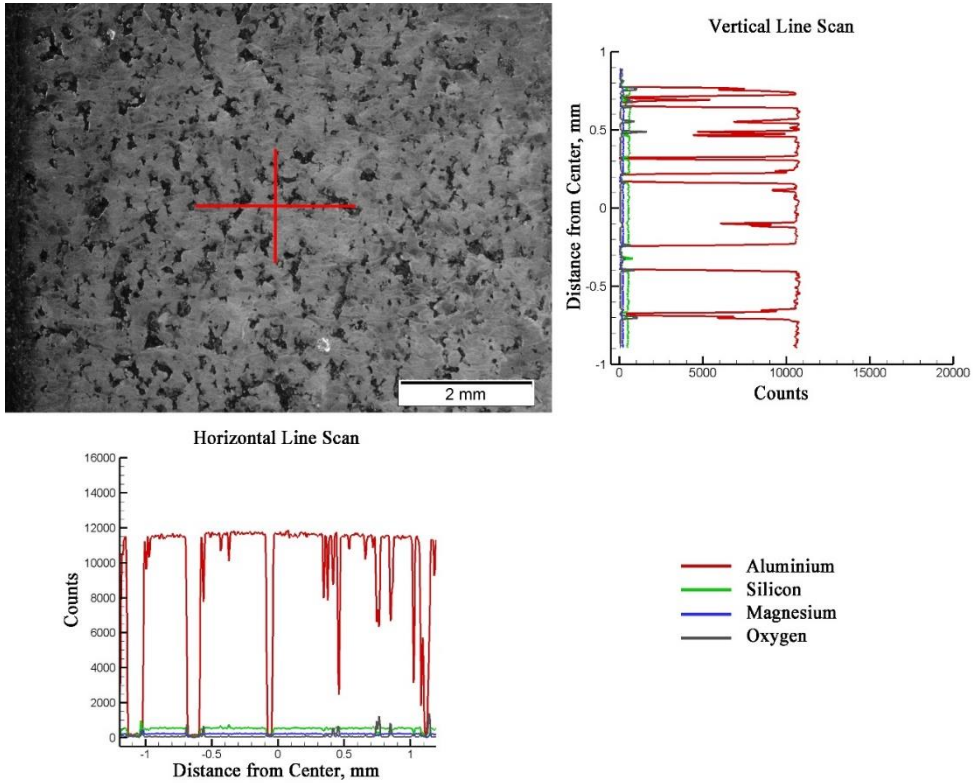

As-received SLM of $AlSi_{10}Mg$ - 5% wt. nAl_2O_3 with low VED.

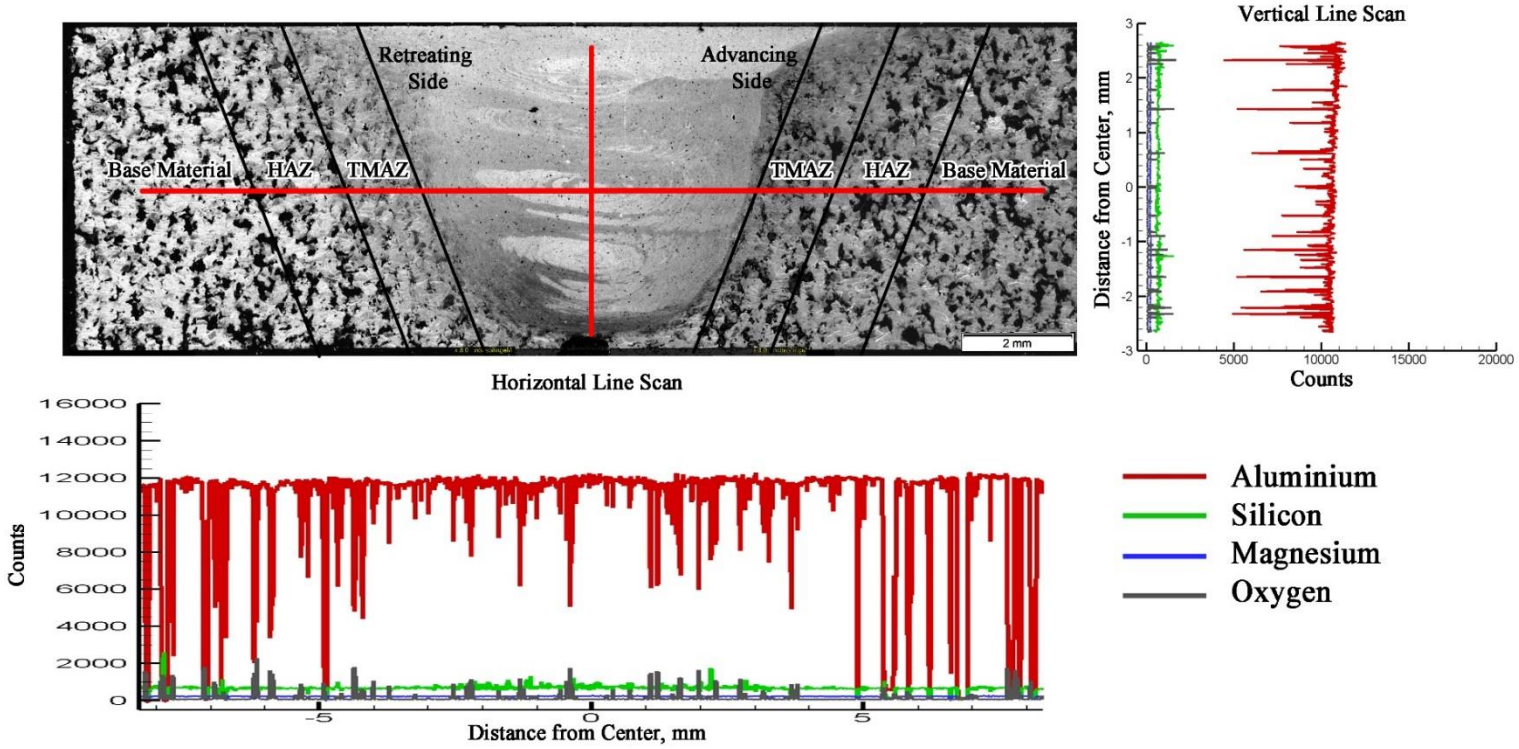

FSW with low heat input of SLM of $AlSi_{10}Mg$ - 5% wt. nAl_2O_3 with low VED.

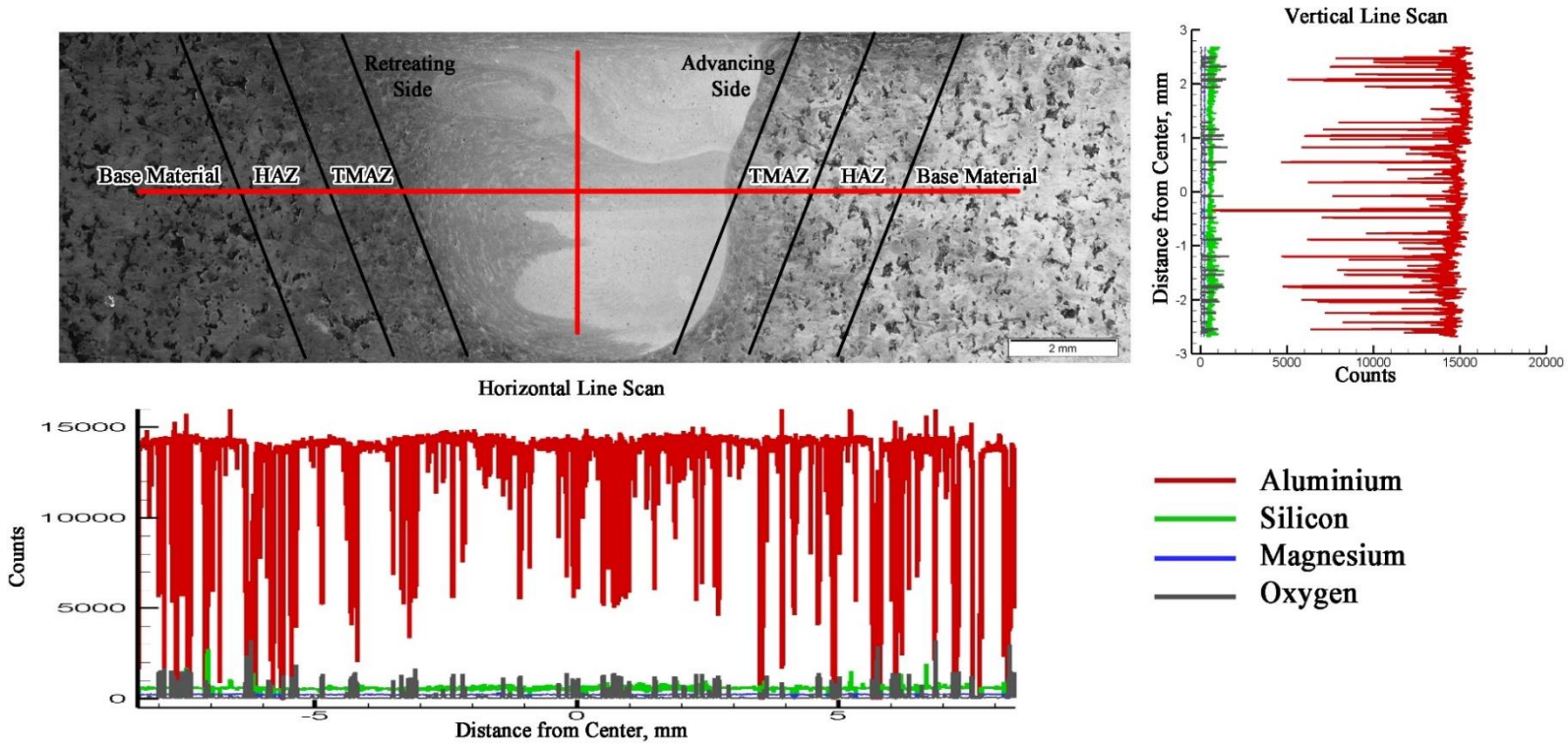

FSW with high heat input of SLM of $AlSi_{10}Mg$ - 5% wt. nAl_2O_3 with low VED.

Appendix B

Micro-Computerized Tomography (Micro CT) Scan Results

This appendix contains the micro CT scan images of all the samples in this study.

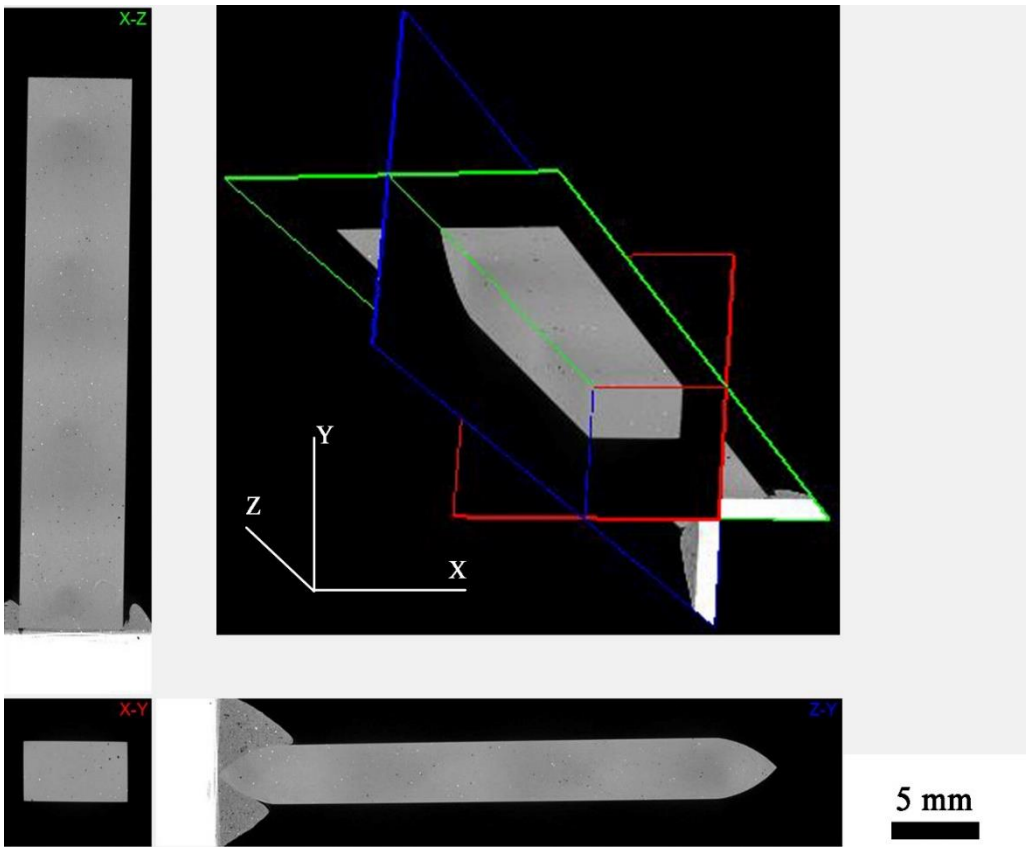

As-received SLM of $AlSi_{10}Mg$ with high VED.

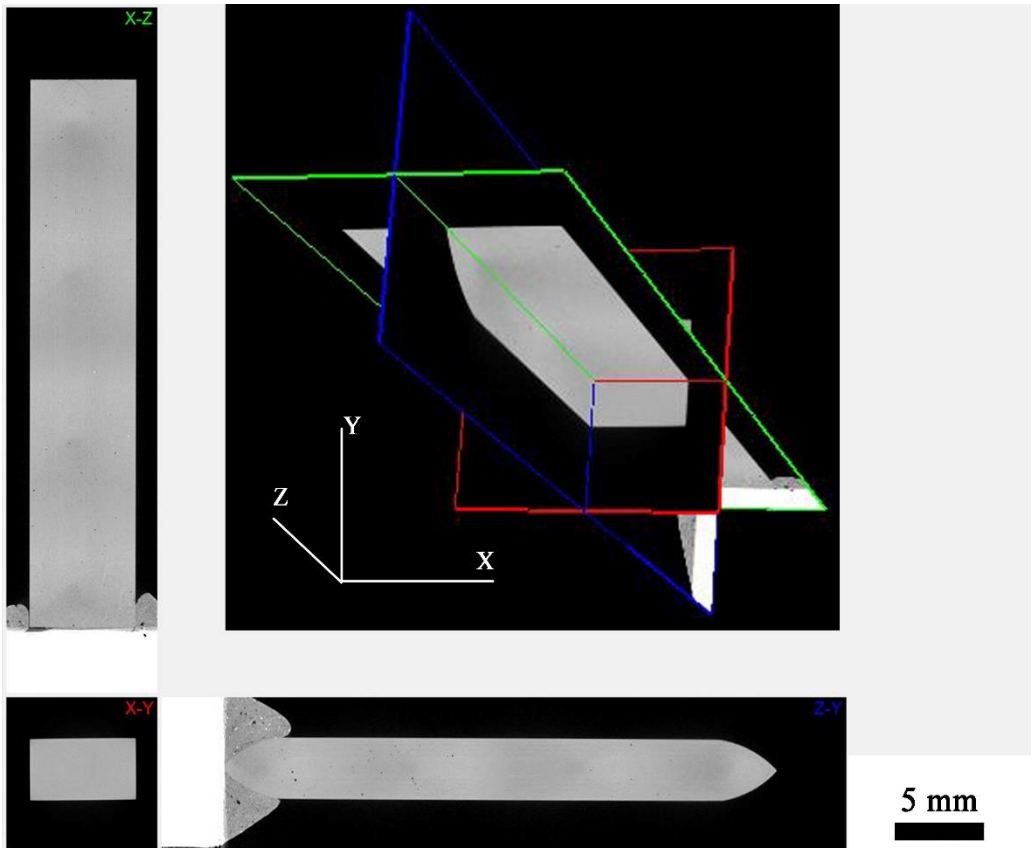

FSW with low heat input with low tilt angle of SLM of $AlSi_{10}Mg$ with high VED.

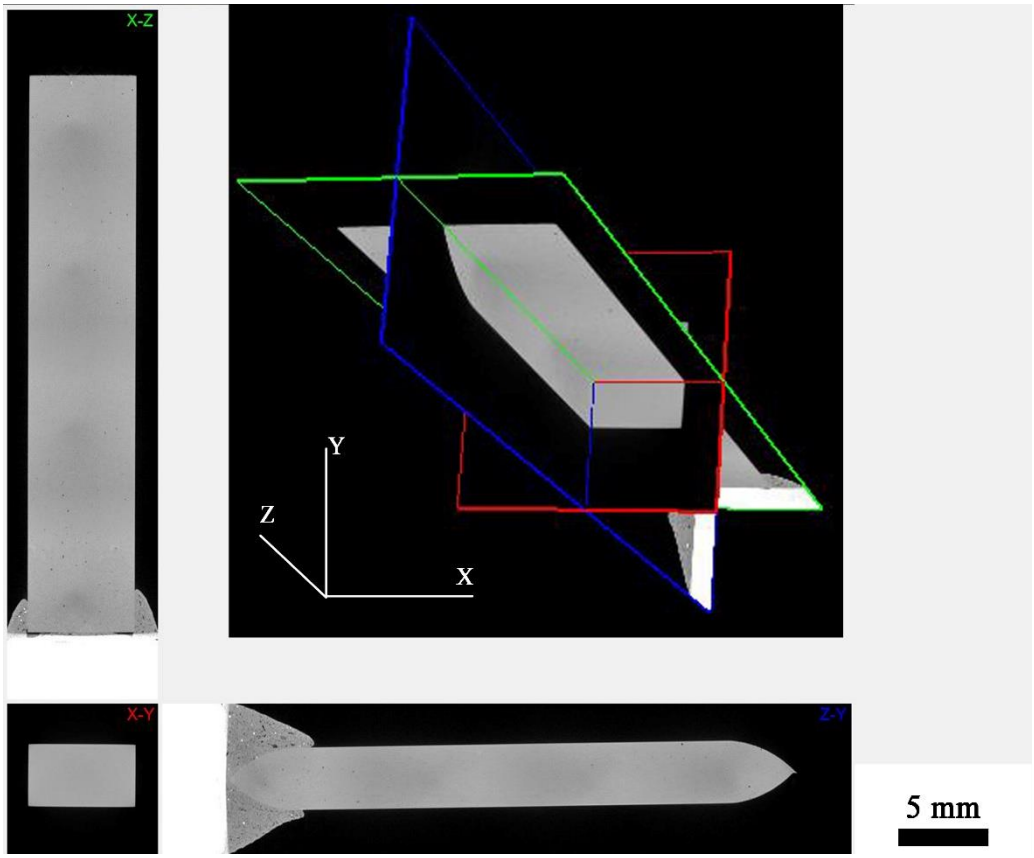

FSW with high heat input with low tilt angle SLM of $AlSi_{10}Mg$ with high VED.

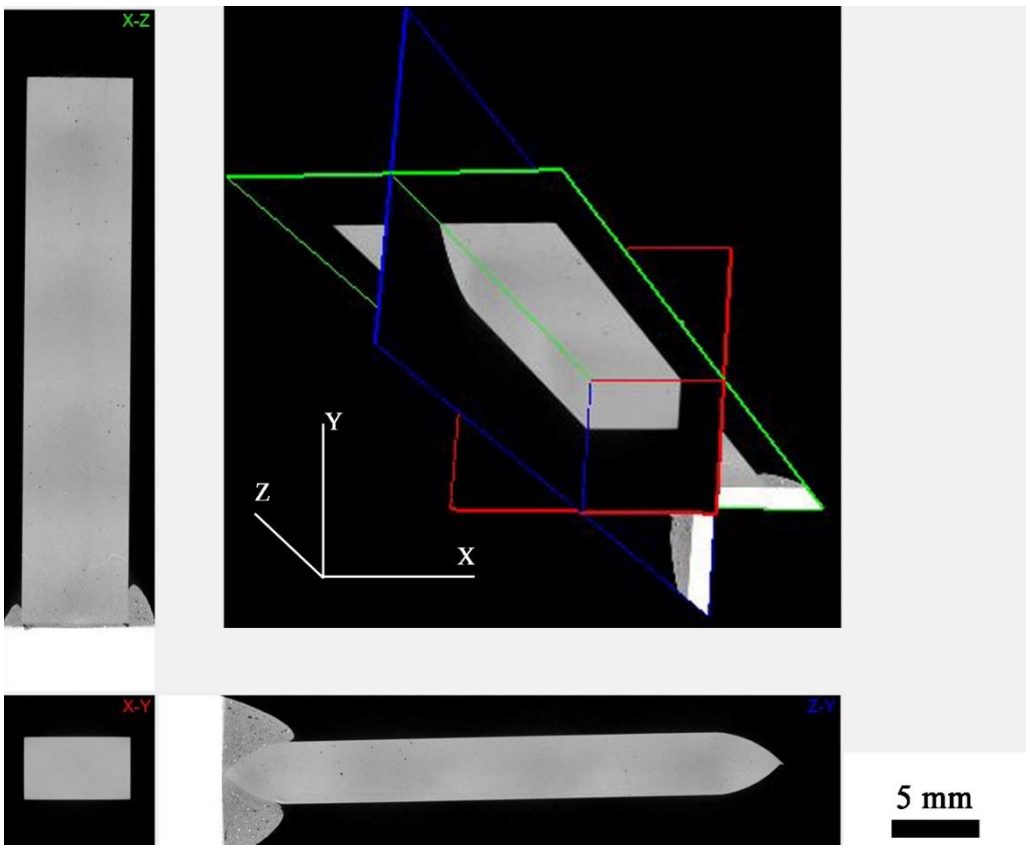

FSW with low heat input with high tilt angle of SLM of $AlSi_{10}Mg$ with high VED.

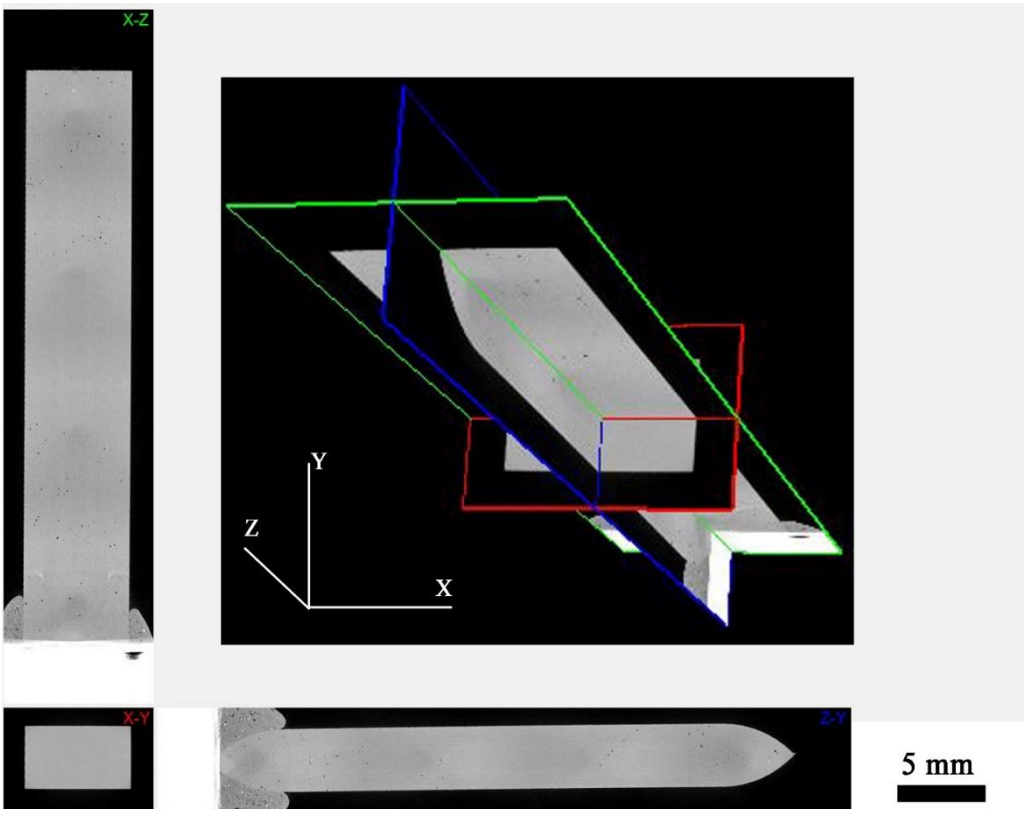

FSW with high heat input with high tilt angle of SLM of $AlSi_{10}Mg$ with high VED.

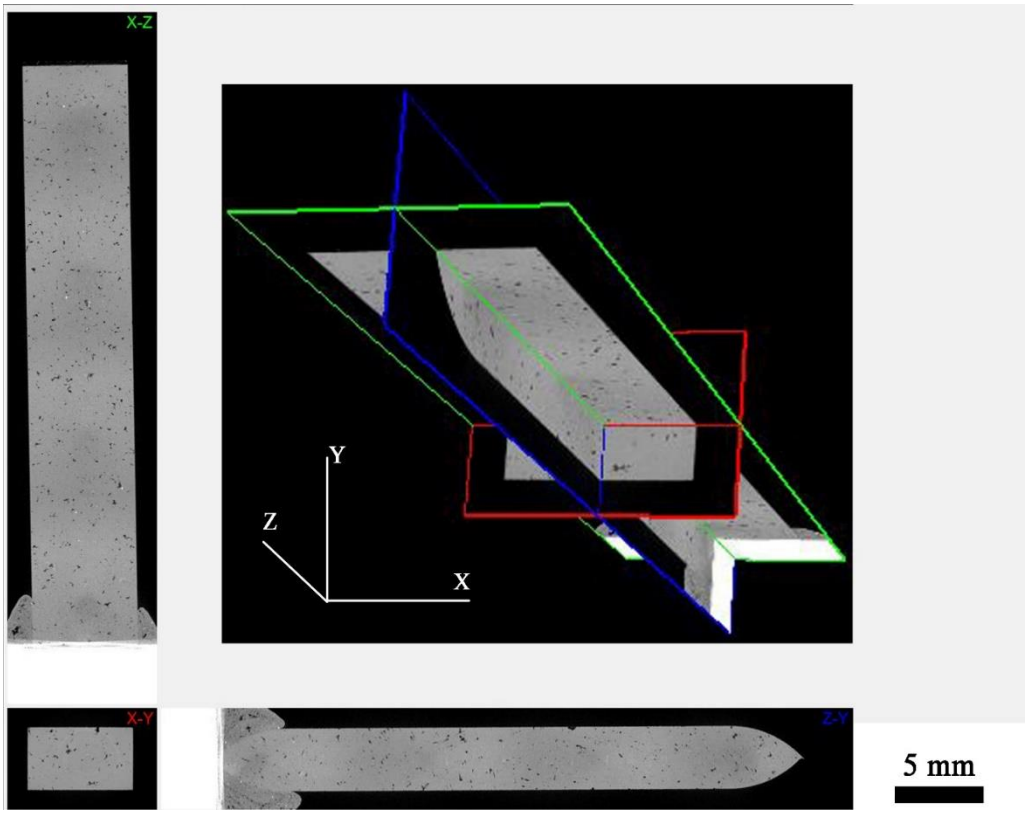

As-received SLM of $AlSi_{10}Mg$ with low VED.

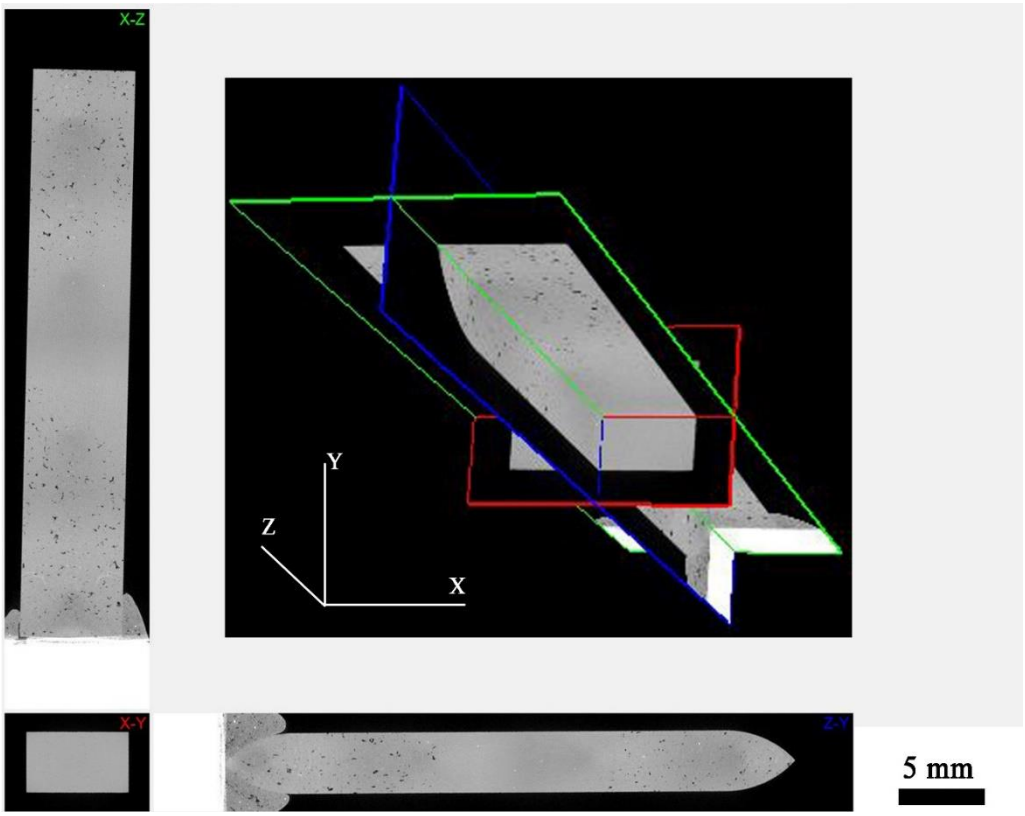

FSW with low heat input of SLM of $AlSi_{10}Mg$ with low VED.

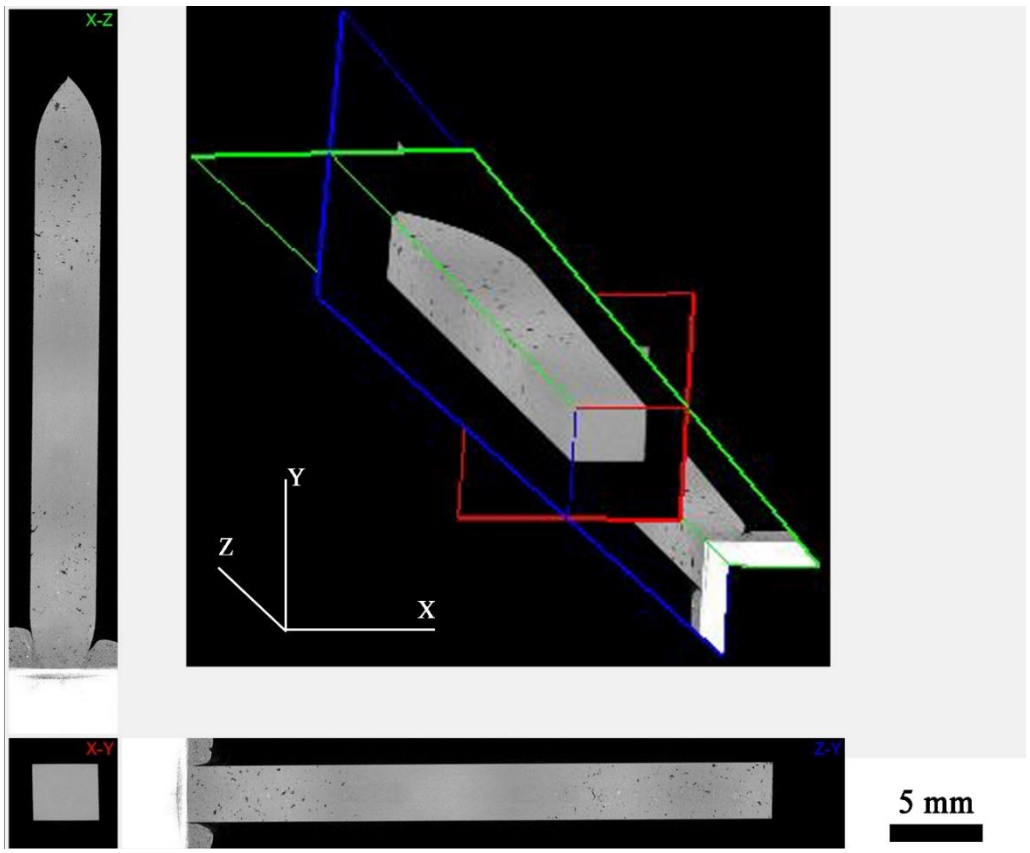

FSW with high heat input of SLM of $AlSi_{10}Mg$ with low VED.

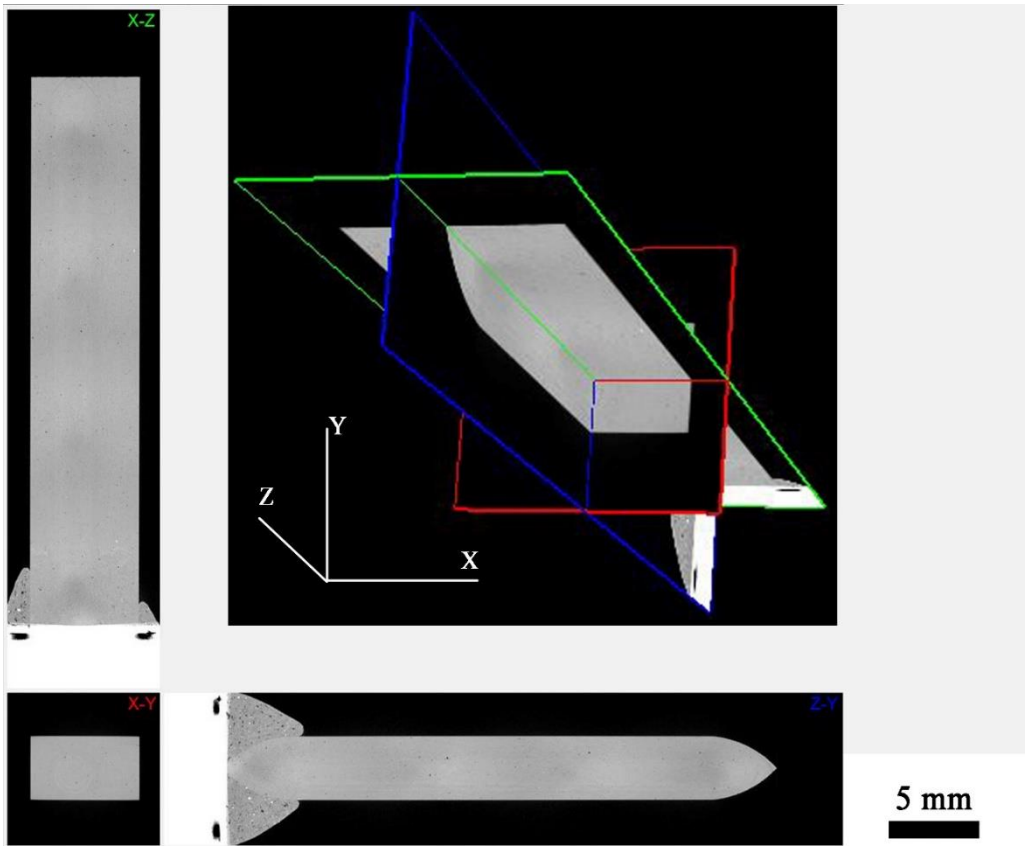

As-received SLM of $AlSi_{10}Mg$ - 2% wt. nAl_2O_3 with high VED.

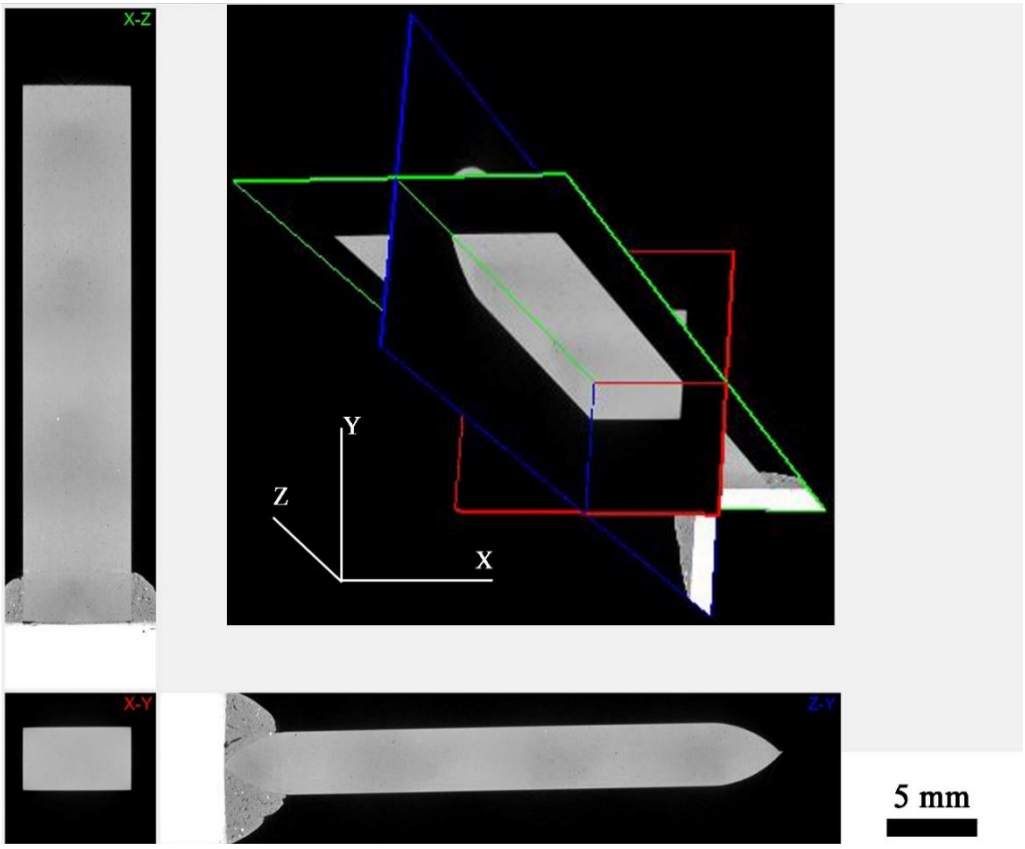

FSW with low heat input of SLM of $AlSi_{10}Mg$ - 2% wt. nAl_2O_3 with high VED.

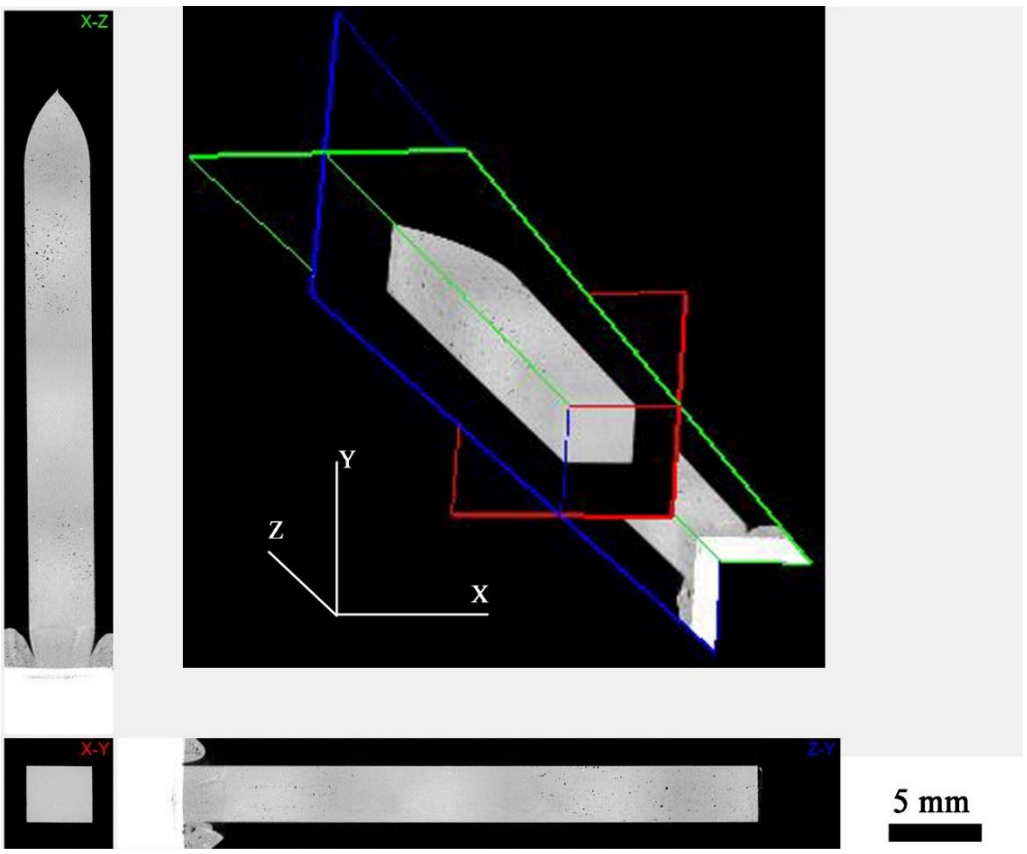

FSW with high heat input of SLM of $AlSi_{10}Mg$ - 2% wt. nAl_2O_3 with high VED.

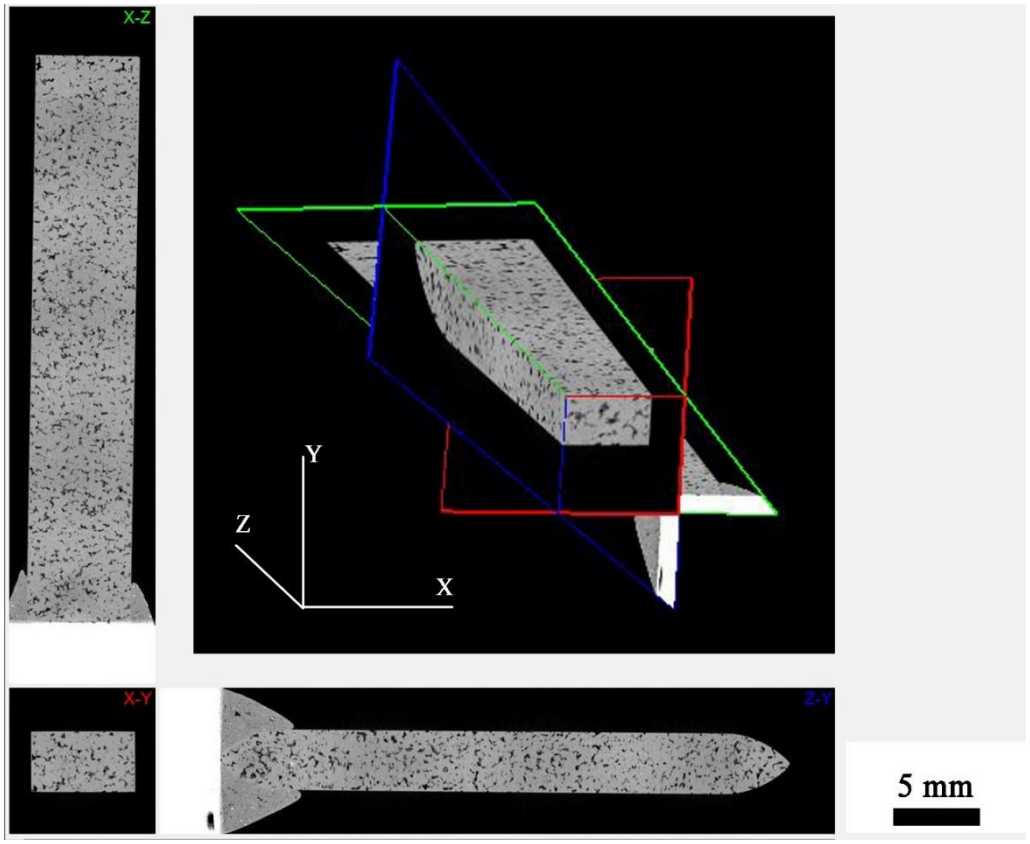

As-received SLM of $AlSi_{10}Mg$ - 2% wt. nAl_2O_3 with low VED.

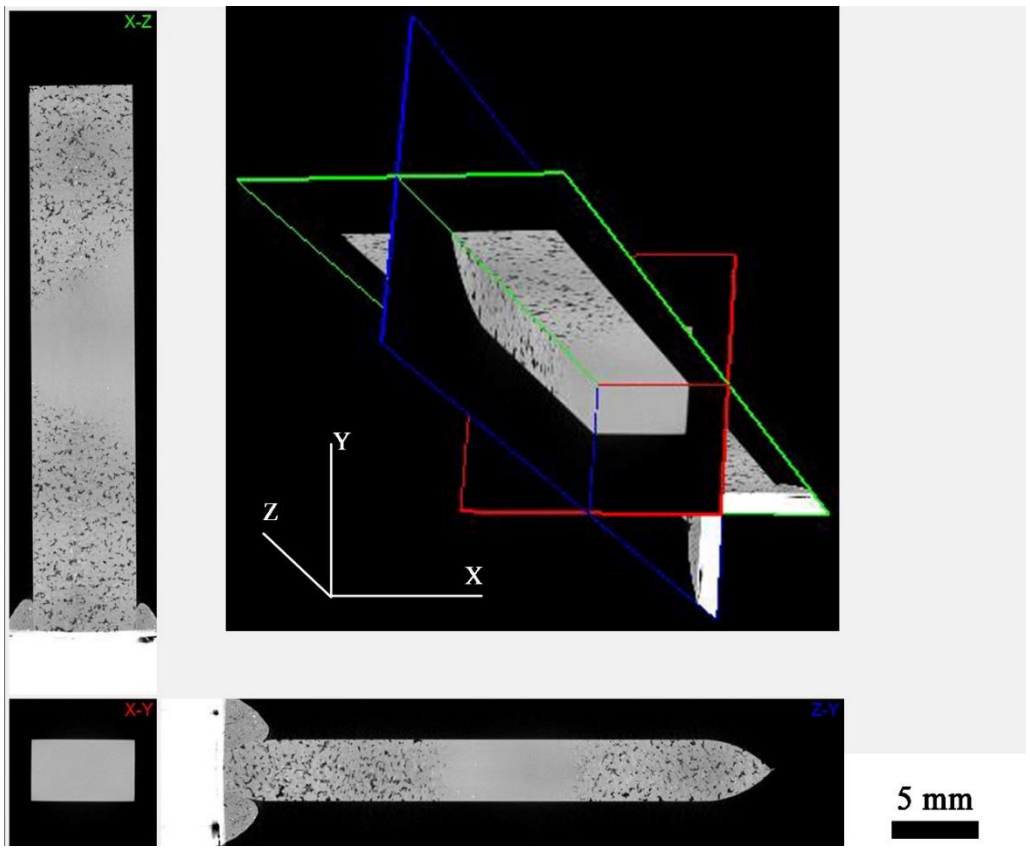

FSW with low heat input of SLM of $AlSi_{10}Mg$ - 2% wt. nAl_2O_3 with low VED.

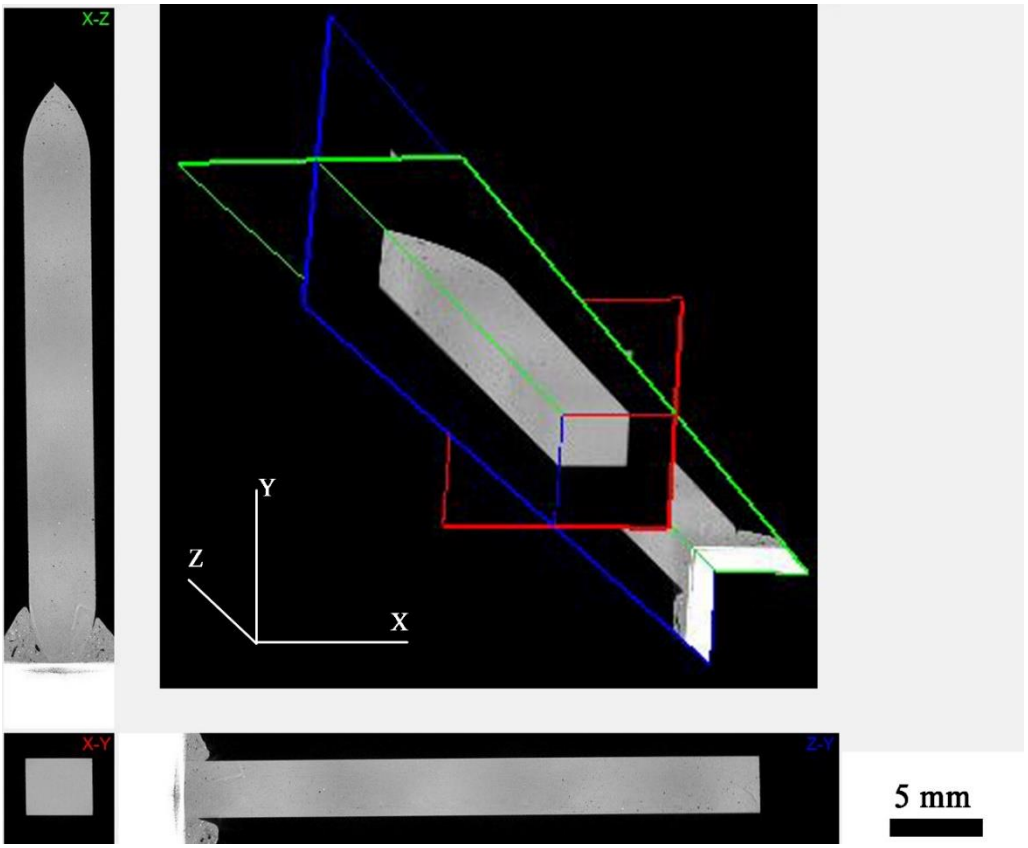

FSW with high heat input of SLM of $AlSi_{10}Mg$ - 2% wt. nAl_2O_3 with low VED.

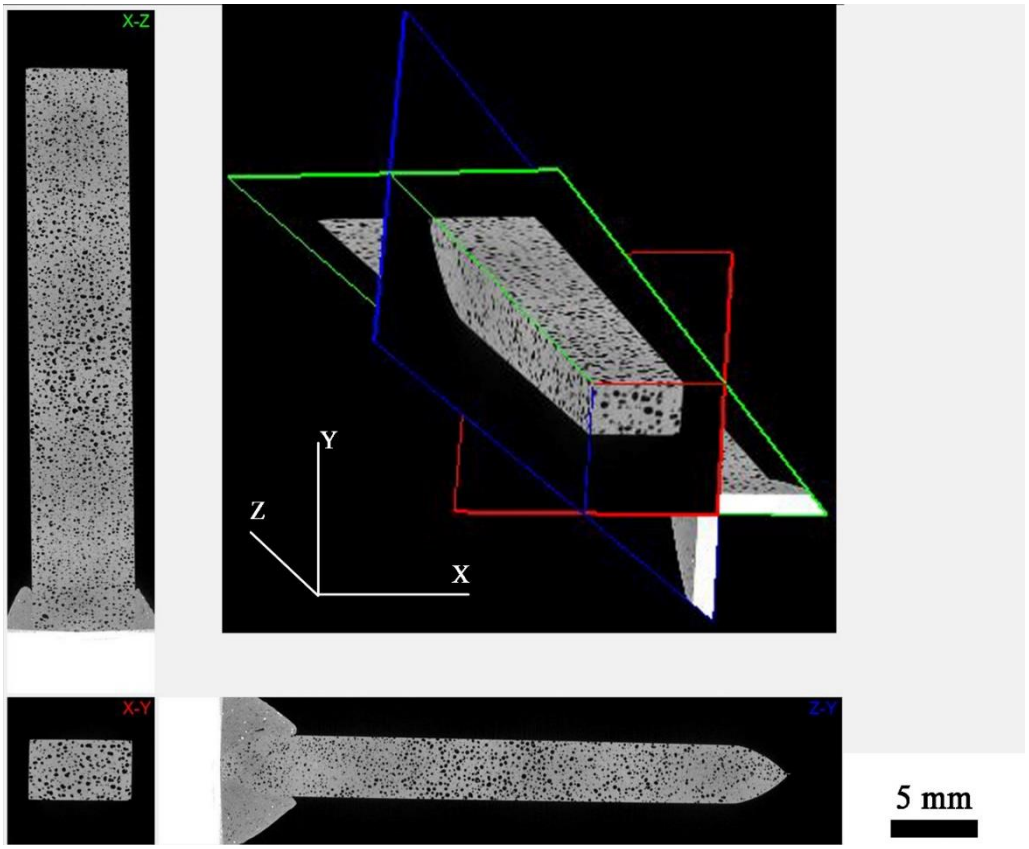

As-received SLM of $AlSi_{10}Mg$ - 5% wt. nAl_2O_3 with high VED.

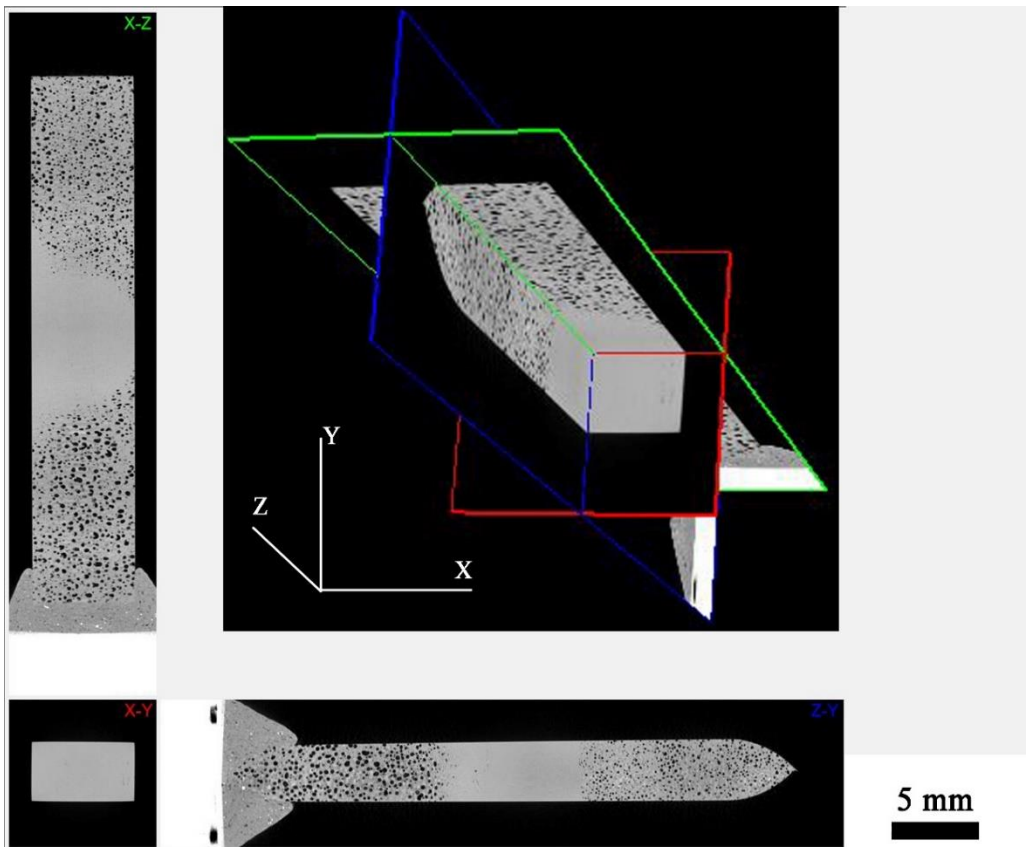

FSW with low heat input of SLM of $AlSi_{10}Mg$ - 5% wt. nAl_2O_3 with high VED.

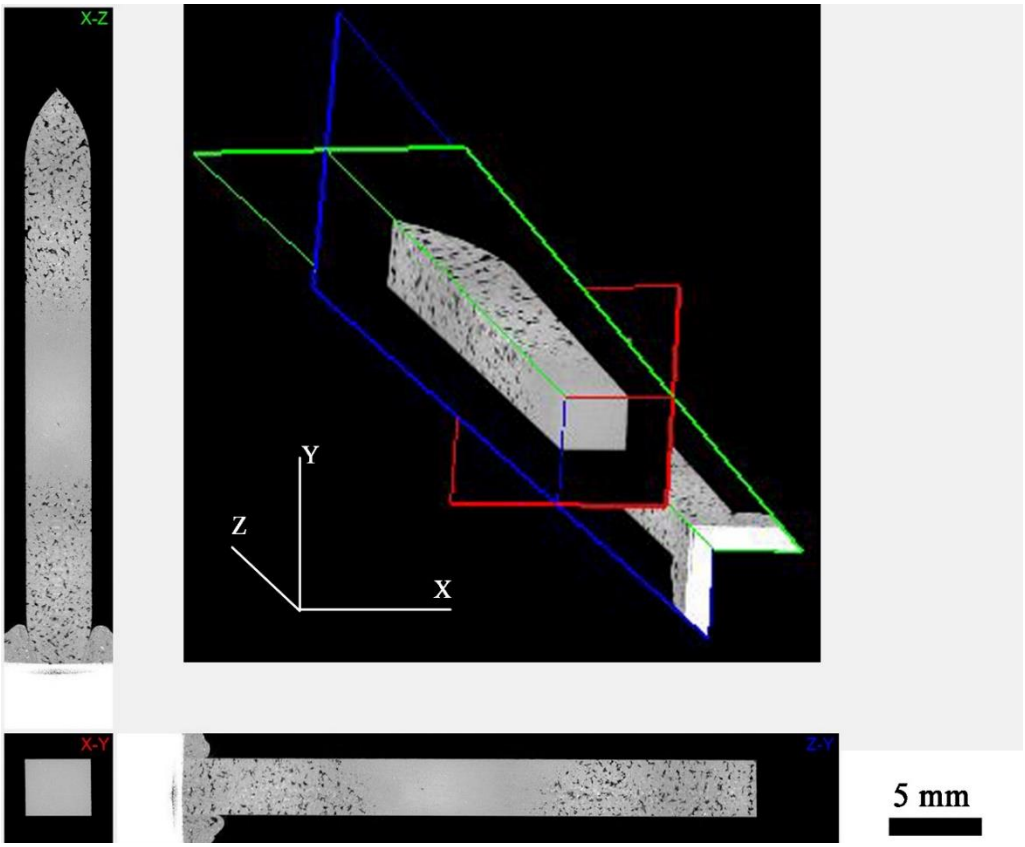

FSW with high heat input of SLM of $AlSi_{10}Mg$ - 5% wt. nAl_2O_3 with high VED.

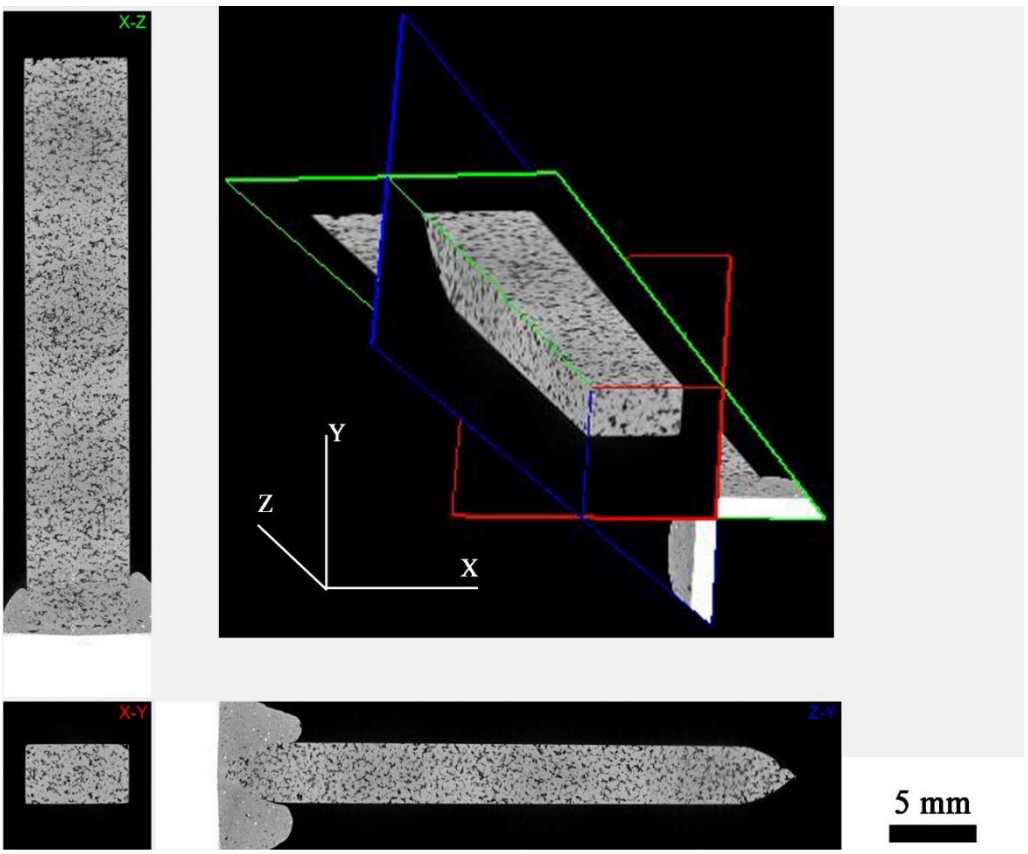

As-received SLM of $AlSi_{10}Mg$ - 5% wt. nAl_2O_3 with low VED.

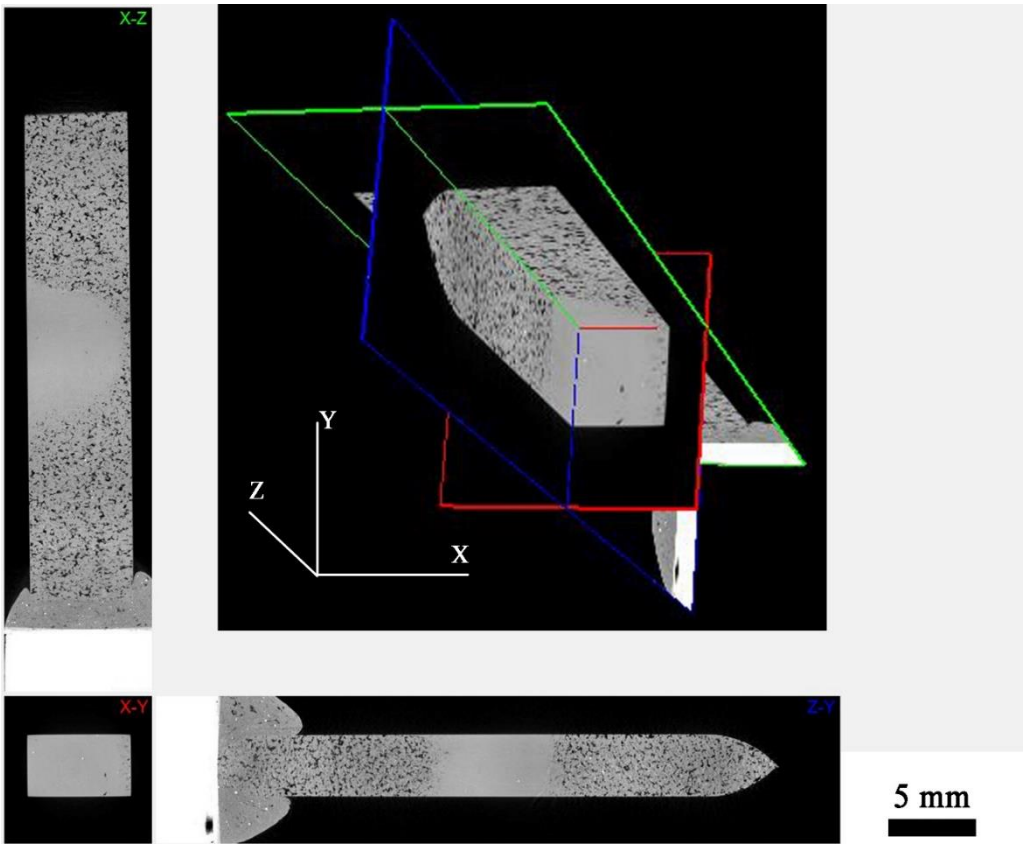

FSW with low heat input of SLM of $AlSi_{10}Mg$ - 5% wt. nAl_2O_3 with low VED.

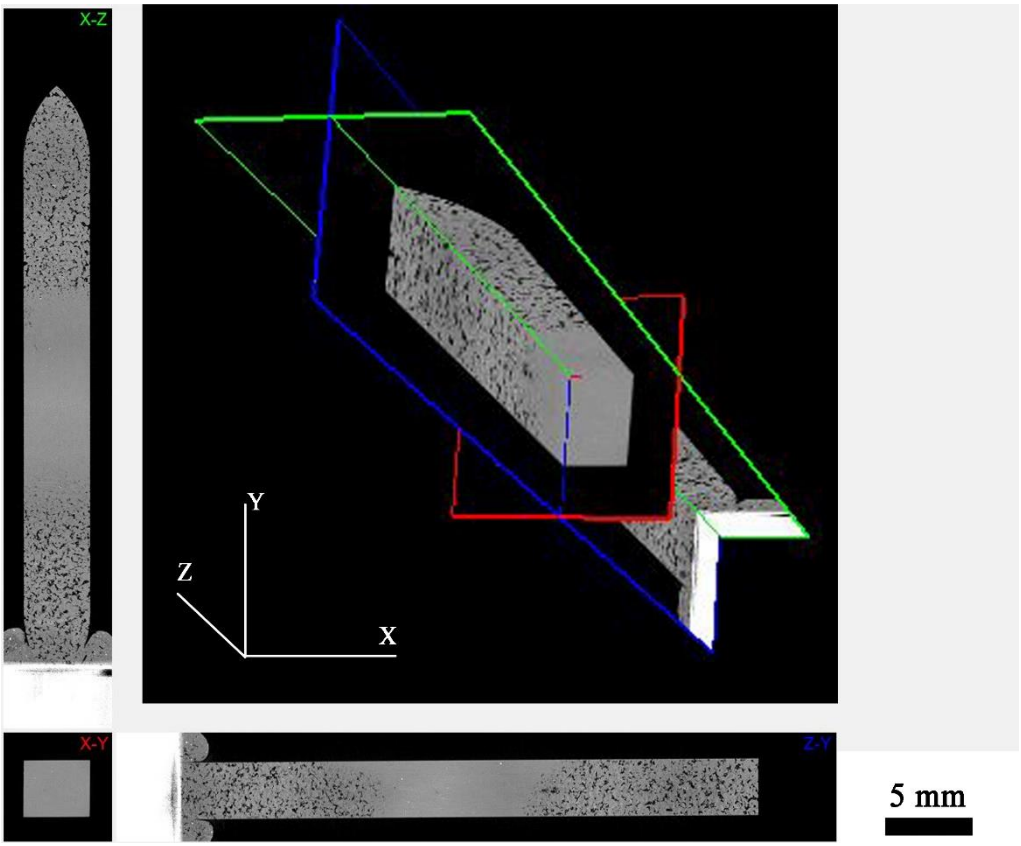

FSW with high heat input of SLM of $AlSi_{10}Mg$ - 5% wt. nAl_2O_3 with low VED.

Appendix C

Tensile Test Results

This appendix contains the tensile test results of all the samples in this study.

Tensile Properties of Al base metal and various composites produced by FSP.

Types of tensile coupons tested	Ultimate Tensile Strength (MPa)	Yield Strength (MPa)	Elongation (%)
As-received AA6061-O*	125	55	25
As-received AA6061-T6*	310	276	12
FSPed Al	193±3	95±4	18±2
Al-CNTs	178±28	112±2	10±5
Al-Al_2O_3	228±2	111±2	24±1
Al- Al_2O_3-CNTs	236±3	163±4	4±1

*Tensile property values for AA6061-O and AA6061-T6 base metal are from ASM Handbook [54].

The tensile result of various aluminium alloy and its composites for chapter 5.

	0.2% Yield Strength (MPa)	UTS (MPa)	Elongation (%)
Rolled sheet of AA6061-O	55	125	25
Rolled sheet of AA6061-T6	276	310	12
SLM of Al - 4% vol. nAl_2O_3 [57]	110	160	5
SLM of $AlSi_{10}Mg$ with high VED	275 ± 6	439 ± 13	6 ± 2
SLM of $AlSi_{10}Mg$ with low VED	265 ± 4	355 ± 8	3 ± 1
SLM of $AlSi_{10}Mg$ - 2% wt. nAl_2O_3 with high VED	215 ± 3	363 ± 10	5 ± 1
SLM of $AlSi_{10}Mg$ - 2% wt. nAl_2O_3 with low VED	168 ± 2	175 ± 3	1 ± 1
SLM of $AlSi_{10}Mg$ - 5% wt. nAl_2O_3 with high VED	111 ± 5	194 ± 21	3 ± 1
SLM of $AlSi_{10}Mg$ - 5% wt. nAl_2O_3 with low VED	105 ± 4	105 ± 9	1 ± 1

Tensile results of various aluminium alloys with and without FSW for chapter 6.

	0.2% Yield Strength (MPa)	UTS (MPa)	Elongation (%)	Weld Efficiency (%)
Rolled sheets of AA6061-O [54]	55	125	25	
Rolled sheets of AA6061-T6 [54]	276	310	12	
SLM fabricated $AlSi_{10}Mg$	275 ± 6	439 ± 13	6 ± 2	
FSW of rolled sheets AA6061-T6 **[219]**	148	232	6	64.2
FSW of $AlSi_{10}Mg$ with RS = 1200 rpm, TS = 3 mm/s, TA = 2.5°	110 ± 3	131 ± 5	2 ± 1	29.17
FSW of $AlSi_{10}Mg$ with RS = 1200 rpm, TS = 1 mm/s, TA = 2.5°	128 ± 2	235 ± 5	6 ± 1	52.24
FSW of $AlSi_{10}Mg$ with RS = 600 rpm, TS = 1 mm/s, TA = 4.5°	148 ± 3	237 ± 4	7 ± 1	53.9
FSW of $AlSi_{10}Mg$ with RS = 1200 rpm, TS = 1 mm/s, TA = 4.5°	146 ± 5	240 ± 8	8 ± 1	54.7

Tensile results of various aluminium alloys with and without FSW for chapter 7.

	0.2% Yield Strength (MPa)	UTS (MPa)	Elongation (%)	Weld Efficiency (%)
Rolled sheets AA6061-T6 (as-received)	276	310	12	
FSW of rolled sheets AA6061-T6 **[219]**	148.3	231.6	5.9	64.2
SLM of $AlSi_{10}Mg$ with high VED (as-received)	275±6	439±13	6±2	
FSW with low heat input on SLM of $AlSi_{10}Mg$ with high VED	148±3	237±4	7±1	53.9
FSW with high heat input on SLM of $AlSi_{10}Mg$ with high VED	146±5	240±8	8±1	54.7
SLM of $AlSi_{10}Mg$ with low VED (as-received)	265±4	355±8	3±1	
FSW with low heat input on SLM of $AlSi_{10}Mg$ with low VED	146±1	238±2	6±1	67.0
FSW with high heat input on SLM of $AlSi_{10}Mg$ with low VED	140±1	240±2	5±1	67.8

Tensile results of SLM of $AlSi_{10}Mg$ - 2% wt. nAl_2O_3 with and without FSW for chapter 7, where YS is yield strength, UTS is the ultimate tensile strength, EL is the elongation, and WE is the weld efficiency.

Material and Process	YS (MPa)	UTS (MPa)	EL (%)	WE (%)
SLM of $AlSi_{10}Mg$ - 2% wt. nAl_2O_3 with high VED (as-received)	215±3	363±10	5±1	
FSW with low heat input on SLM of $AlSi_{10}Mg$ - 2% wt. nAl_2O_3 with high VED	145±1	235±1	6±1	64.8
FSW with high heat input on SLM of $AlSi_{10}Mg$ - 2% wt. nAl_2O_3 with high VED	136±1	243±2	10±2	66.8
SLM of $AlSi_{10}Mg$ - 2% wt. nAl_2O_3 with low VED (as-received)	168±2	175±3	1±1	
FSW with low heat input on SLM of $AlSi_{10}Mg$ - 2% wt. nAl_2O_3 with low VED	128±4	146±10	3±1	83.3
FSW with high heat input on SLM of $AlSi_{10}Mg$ - 2% wt. nAl_2O_3 with low VED	124±2	135±5	3±2	77.1

Tensile results of SLM of $AlSi_{10}Mg$ - 5% wt. nAl_2O_3 with and without FSW for chapter 7, where YS is yield strength, UTS is the ultimate tensile strength, EL is the elongation and WE is the weld efficiency.

	YS (MPa)	UTS (MPa)	EL (%)	WE (%)
SLM of $AlSi_{10}Mg$ - 5% wt. nAl_2O_3 with high VED (as-received)	111±5	194±21	3±1	
FSW with low heat input on SLM of $AlSi_{10}Mg$ - 5% wt. nAl_2O_3 with high VED	102±1	169±3	5±1	87.1
FSW with high heat input on SLM of $AlSi_{10}Mg$ - 5% wt. nAl_2O_3 with high VED	95±2	164±4	3±1	84.5
SLM of $AlSi_{10}Mg$ - 5% wt. nAl_2O_3 with low VED (as-received)	105±4	105±9	1±1	
FSW with low heat input on SLM of $AlSi_{10}Mg$ - 5% wt. nAl_2O_3 with low VED	91±1	91±3	1±1	86.9
FSW with high heat input on SLM of $AlSi_{10}Mg$ - 2% wt. nAl_2O_3 with low VED	97±1	103±3	2±1	98.2